NATIONAL TECHNICAL UNIVERSITY OF ATHENS
SCHOOL OF APPLIED SCIENCES
DEPARTMENT OF PHYSICS
HIGH ENERGY PHYSICS LABORATORY

Study of Rare Decays of B Hadrons and Development of a Data Viewer Application of the Detector Control System in the ATLAS Detector

A dissertation presented by

Charilaos Tsarouchas

to
The Department of Physics
for the degree of
Doctor of Philosophy
in the subject of

Physics

National Technical University of Athens
April 2012

Study of Rare Decays of B Hadrons and Development of a Data Viewer Application of the Detector Control System in the ATLAS Detector

PhD THESIS

Charilaos A. Tsarouchas

Advisors: Theodoros Alexopoulos   Stefan Schlenker
Professor, NTU-Athens   Scientist, CERN

Exam committee:

....

Theodoros Alexopoulos   Evangelos Gazis   Georgios Tsipolitis

Professor NTUA   Professor NTUA   Associate Professor NTUA

....

Dr. Sandro Palestini   Dr. Stefan Schlenker   Christina Kourkoumelis   Dimitris Fassouliotis

Senior Staff Physicist, CERN   Scientist, CERN   Prof., NKUA   Assist. Prof., NKUA

Athens, (April of 2012)

....
Charilaos A. Tsarouchas

ΕΘΝΙΚΟ ΜΕΤΣΟΒΙΟ ΠΟΛΥΤΕΧΝΕΙΟ
ΣΧΟΛΗ ΕΦΑΡΜΟΣΜΕΝΩΝ ΜΑΘΗΜΑΤΙΚΩΝ
ΚΑΙ ΦΥΣΙΚΩΝ ΕΠΙΣΤΗΜΩΝ

Μελέτη Σπανίων Τρόπων Διάσπασης Αδρονίων B
και Εφαρμογές Οπτικοποίησης Δεδομένων Συστήματος
Αυτομάτου Ελέγχου στο πείραμα ATLAS

ΔΙΔΑΚΤΟΡΙΚΗ ΔΙΑΤΡΙΒΗ

ΧΑΡΙΛΑΟΥ Α. ΤΣΑΡΟΥΧΑ

Διπλωματούχου Φυσικού Εφαρμογών Ε.Μ.Π.

ΕΠΙΒΛΕΠΩΝ :
Θ. ΑΛΕΞΟΠΟΥΛΟΣ
Καθηγητής Ε.Μ.Π.

ΑΘΗΝΑ, Απρίλιος 2012

ΕΘΝΙΚΟ ΜΕΤΣΟΒΙΟ ΠΟΛΥΤΕΧΝΕΙΟ
ΣΧΟΛΗ ΕΦΑΡΜΟΣΜΕΝΩΝ ΜΑΘΗΜΑΤΙΚΩΝ
ΚΑΙ ΦΥΣΙΚΩΝ ΕΠΙΣΤΗΜΩΝ

Μελέτη Σπανίων Τρόπων Διάσπασης Αδρονίων *B*
και Εφαρμογές Οπτικοποίησης Δεδομένων Συστήματος
Αυτομάτου Ελέγχου στο πείραμα ATLAS

ΔΙΔΑΚΤΟΡΙΚΗ ΔΙΑΤΡΙΒΗ

ΧΑΡΙΛΑΟΥ Α. ΤΣΑΡΟΥΧΑ

Διπλωματούχου Φυσικού Εφαρμογών Ε.Μ.Π.

ΤΡΙΜΕΛΗΣ ΣΥΜΒΟΥΛΕΥΤΙΚΗ ΕΠΙΤΡΟΠΗ:
1. Θεόδωρος Αλεξόπουλος, Καθ. Ε.Μ.Π.
2. Ευάγγελος Γαζής, Καθ. Ε.Μ.Π.
3. Γεώργιος Τσιπολίτης, Αν. Καθ. Ε.Μ.Π.

ΕΠΤΑΜΕΛΗΣ ΕΞΕΤΑΣΤΙΚΗ ΕΠΙΤΡΟΠΗ:
1. Θεόδωρος Αλεξόπουλος, Καθ. Ε.Μ.Π.
2. Ευάγγελος Γαζής, Καθ. Ε.Μ.Π.
3. Χριστίνα Κουρκουμέλη, Καθ. Ε.Κ.Π.Α.
4. Γεώργιος Τσιπολίτης, Αν. Καθ. Ε.Μ.Π.
5. Δημήτρης Φασουλιώτης, Επ. Καθ. Ε.Κ.Π.Α.
6. Sandro Palestini, Sen. St. Physicist, CERN
7. Stefan Schlenker, Scientist, CERN

ΑΘΗΝΑ, Απρίλιος 2012

....
Χαρίλαος Α. Τσαρουχάς

Contents

Acknowledgements

Firstly, I would like to express my thankfulness to the high energy physics group of the National Technical University of Athens, for the valuable support since my undergraduate years. First and foremost, I would like to express my gratitude to Theodoros Alexopoulos the professor who first introduced me to the subject of High Energy Physics, encouraged me in my initial steps and imparted his passion of working as an experimental physicist. The wonderful working environment in his office will stay in my memory forever. I am thankful to Georgios Tsipolitis for the –always to the point– comments he gave me during some of my master and PhD presentations. I am indebted to Evangelos Gazis for his valuable advices and help and also for introducing me to the high energy group of the university of Lund where I spend half a year of my PhD. Finally, I would like to thank Sotiris Vlachos for supervising me and introducing me to the High Energy Physics world of CERN, when I first visited the laboratory as summer student back in 2005.

Working in the central Detector Control System (DCS) group of ATLAS with Stefan Schlenker as a supervisor was a real privilege for me. His good overview in a wide range of activities and studies was inspiring and his flexible way of thinking and solving the various problems as they appeared, was always an excellent example to follow. In particular, I would like to thank Stefan Schlenker for always protecting the delicate balance of my working time between the technical DCS tasks and the physics analysis duties and for generously offering, the required time for writing my PhD thesis properly.

I owe sincere and earnest thankfulness to Alex Cerri. In the first year, during the CERN ATLAS team (CAT) meetings, he explained to me many experimental High Energy Physics techniques. Later on, he was accepting me in his office, almost in a daily basis, answering with patience my numerous questions and managing at the same time to develop my analytic thought. His scientific approach to the analysis problems was always stimulating and his collaborative working spirit has affected me deeply.

Additionally, among the people of the CERN ATLAS group, I would like to express my gratitude to Sandro Palestini for his valuable advice, help and support from my initial steps in the ATLAS collaboration.

I am heartily thankful to my colleagues and friends, Stefanos Leontsinis, George Iakovidis and Konstantinos Karakostas for helping me spot the various flaws of the document of the thesis, Aisling Vaughan for correcting the language in native English, and Sotiris Fragiskos, for sharing with me many different good latex techniques and for remarkably upgrading the final style of this document.

I would like to thank my parents Eleni and Antonis and my brother Christoforos, for their constant support. The warm childhood moments in our home, will stay in my memory through all my life.

I want to dedicate this thesis to Olga, my friend, partner and wife. I am thankful to life for bringing us together.

Most of us do elementary particle physics neither because of the intrinsic interestingness of the phenomena we study, nor because of the practical importance of what we learn, but because we are pursuing a reductionist vision. All the properties of ordinary matter are what they are because of the principles of atomic and nuclei physics, which are what they are because if the rules of the Standard Model of elementary particles, which are what they are because... Well, we don't know, this is the reductionist frontier, which we are currently exploring.

Steven Weinberg

Chapter 1

Μελέτη Σπανίων Τρόπων Διάσπασης B Αδρονίων

Η διδακτορική διατριβή αποτελείται απο τρείς θεματικές ενότητες:

1. Μελέτη του σωματιδίου χ_b και της διάσπασής του σε δυο J/ψ με χρήση δεδομένων του ανιχνευτή ATLAS από συγκρούσεις πρωτονίων στον LHC.

2. Μελέτη της σπάνιας διάσπασης $B_s^0 \to \mu^+\mu^-$ και υπολογισμός του άνω ορίου του $\mathrm{Br}(B_s^0 \to \mu^+\mu^-)$ με χρήση δεδομένων του ανιχνευτή ATLAS από συγκρούσεις πρωτονίων στον LHC.

3. Ανάπτυξη εφαρμογής οπτικοποίησης δεδομένων του συστήματος αυτόματου ελέγχου του ανιχνευτή ATLAS.

1.1 Μελέτη του Σωματιδίου χ_b και της Διάσπασής του σε δυο J/ψ με Χρήση Δεδομένων του Ανιχνευτή ATLAS από Συγκρούσεις Πρωτονίων στον LHC.

Στα πλαίσια του Καθιερωμένου Προτύπου, έχουν αναπτυχθεί διάφορα θεωρητικά μοντέλα για μια ποσοτική περιγραφή της παραγωγής καταστάσεων βαρέων κουαρκόνιουμ (ένα quark και το anti-quark του σε μια δέσμια κατάσταση) τα οποία όμως δεν επαληθεύονται ακριβώς από το πείραμα. Τα αποτελέσματα μιας πρώτης προσπάθειας εξήγησης άμεσης παραγωγής J/ψ βασιζόμενη στο Color Singlet Model (CSM), απέκλιναν από τα πειραματικά δεδομένα κατά μία τάξη μεγέθους. Ένα άλλο μοντέλο, το Color Octet Model (COM) έδωσε καλύτερα αποτελέσματα, αλλά η εγκάρσια πόλωση του J/ψ που προέβλεπε, δεν έχει επαληθευτεί. Λίγο αργότερα, διορθώσεις ανωτέρας τάξης (Next-to-Leading Order, NLO) στο CSM που έγιναν, απέφεραν καλύτερα θεωρητικά αποτελέσματα και ξανάδωσαν αξιοπιστία σε αυτό το μοντέλο, αλλά και πάλι τα πειραματικά αποτελέσματα δεν δείχνουν να συμπίπτουν σε όλες τις περιπτώσεις. Μετρήσεις διπλής παραγωγής κουαρκόνιουμ, που μελετούνται σε αυτή την ενότητα, αναμένεται να δώσουν πολύ ισχυρούς περιορισμούς στα υπάρχοντα μοντέλα και πιστεύεται ότι θα συμβάλουν σε μια καλύτερη αντίληψη της δημιουργίας καταστάσεων κουαρκόνιουμ.

Για τις ανάγκες της ανάλυσης, δημιουργήθηκαν δεδομένα προσομοίωσης του σήματος (100 000 γεγονότα) και χρησιμοποιήθηκαν όλα τα δεδομένα συγκρούσεων pp στον LHC κατά το 2010 και 2011. Στη συνέχεια ακολούθησε η ανακατασκευή των διασπάσεων και εφαρμόστηκε μια πρώτη εύλογη προεπιλογή γεγονότων. Μελετήθηκαν γεγονότα τα οποία περιλαμβάνουν 4 ή περισσότερα

μιόνια, απαιτώντας δύο από αυτά να είναι combined (να έχουν συνδυαστεί στον εσωτερικό ανιχνευτή τροχιών και στον ανιχνευτή μιονίων). Οι τροχιές όλων των μιονίων στον εσωτερικό ανιχνευτή έχουν ελεγχθεί ότι πληρούν κάποια κριτήρια ποιότητας και ανήκουν στην περιοχή $|\eta| < 2,5$. Τα J/ψ που έχουν ανακατασκευαστεί, έχουν $\chi^2/\mathrm{ndf} < 15$, ορμή $p_T > 3\,\mathrm{GeV}/c$ και ανήκουν στην περιοχή $|\eta| <$ $2,5$. Τέλος, τα ανακατασκευασμένα υποψήφια γεγονότα χ_b έχουν $\chi^2/\mathrm{ndf} < 15$, ορμή $p_T > 8\,\mathrm{GeV}/c$ και ανήκουν και αυτά στην περιοχή $|\eta| < 2,5$. Μελέτες σκανδαλισμού έδειξαν ότι το βέλτιστο trigger για τη συγκεκριμένη ανάλυση είναι το *EF_2mu4_Jpsimumu*[1].

Ο ρυθμός διάσπασης του συγκεκριμένου καναλιού υπολογίζεται σύμφωνα με την σχέση

$$\mathrm{Br}(\chi_b \to J/\psi J/\psi) = \mathrm{N}_{\chi_b} \frac{1}{L_{int}\sigma(pp \to \chi_b + X)A\epsilon}$$

όπου,

N_{χ_b}: ο αριθμός των χ_b σωματιδίων (εξάγεται με χρήση δεδομένων συγρούσεων προτονίων του ΛΗ¨)

L_{int}: η integrated luminosity

$\sigma(pp \to \chi_b + X)$: η ενεργός διατομή παραγωγής χ_b στις συγκρούσεις του LHC (προέρχεται απο θεωρητικές μελέτες)

$A\epsilon$: το γινόμενο των γεωμετρικών αποδοχών του ανιχνευτή και των αποδοτικοτήτων της ανακατασκευής των χ_b σωματιδίων (ο υπολογισμός γίνεται με χρήση δεδομένων προσομοίωσης).

Η διάσπαση που μελετάται έχει ώς προιόντα 2 J/ψ. Το υπόβαθρο του χ_b μπορεί να προέρχεται είτε απο διάσπαση όπου το 1 J/ψ δεν είναι πραγματικό (fake), είτε πιό σπάνια απο διασπάσεις όπου τα δυο J/ψ δεν είναι πραγματικά (double-fake), είτε (αμελητέας συνεισφοράς) από άλλες διασπάσεις συντονισμού (resonances) με πραγματικά J/ψ στην περιοχή του σήματος.

Δεδομένου του πολύ μικρού αριθμού υποψήφιων χ_b, αναπτύχθηκε μια προσεκτική μελέτη όλων των μεταβλητών διαχωρισμού σήματος – υποβάθρου. Για τον διαχωρισμό σήματος υποβάθρου, μια εκτεταμένη ανάλυση οδηγεί στη μέγιστη δυνατότητα διαχωρισμού. Το πρώτο στάδιο αυτής της ανάλυσης περιλαμβάνει τον ορισμό των μεταβλητών διαχωρισμού, οι οποίες επιλέγονται με τα παρακάτω κριτήρια:

το secondary vertex αναμένεται να βρίσκεται πολύ κοντά στο primary vertex αφού τα σωματίδια χ_b διασπώνται σε ελάχιστο χρονικό διάστημα αφότου δημιουργηθούν. Αντίθετα, το υπόβαθρο προέρχεται απο διασπάσεις άλλων B σωματιδίων που όπως είναι γνωστό έχουν σχετικά μεγάλο χρόνο ζωής και ταξιδεύουν μερικά δέκατα του mm προτού διασπαστούν.

Η δυναμική των υποψήφιων σωματιδίων του σήματος και του υποβάθρου, αναμένεται να έχουν διαφορετικές συμμετρίες στην τελική κατάσταση. Τα χ_b σωματίδια διασπώνται ακριβώς μετά την δημιουργία τους και η διάσπαση δεν έχει κάποιον συγκεκριμένο προσανατολισμό. Αντίθετα, τα B σωματίδια του υποβάθρου αναμένονται να ταξιδεύουν για λίγο και μάλιστα κατά την κατεύθυνση που ενώνει το primary με το secondary vertex.

χαρακτηριστικά της αδρονοποίησης των χ_b σωματιδίων μπορούν να καταδείξουν αν το γεγονός περιλαμβάνει σήμα ή όχι. Στην περίπτωση του σήματος, τα J/ψ της διάσπασης του χ_b είναι σχετικά απομονωμένα από άλλες τροχιές σωματιδίων που προέρχονται από το primary vertex.

Οι τελικές κατανομές διαχωρισμού συγκεντρώνονται στον πίνακα 1.1.

Η επόμενη μελέτη, μετά την επιλογή των μεταβλητών διαχωρισμού, έχει να κάνει με τη βελτιστοποίηση των τομών. Η επιλογή του βέλτιστου σημείου τομής γίνεται με τη χρήση κατάλληλων

---

[1]EF_2mu4_Jpsimumu: απαιτεί δύο μιόνια, $4\,\mathrm{GeV}/c$ το καθένα, που πυροδοτούν όλα τα στρώματα σκανδαλισμών και επιπλέον απαιτεί η αναλλοίωτη μάζα των δύο μιονίων να είναι συμβατή με τη μάζα του J/ψ.

Μεταβλητές	Περιγραφή
α_{2D}	Αν $\boldsymbol{x}$ είναι το διάνυσμα από το primary vertex (PV) στο secondary vertex (SV), τότε α_{2D} είναι η γωνία στο επίπεδο xy ανάμεσα στο $\boldsymbol{x}$ και $\boldsymbol{p}^B$ (χρησιμοποιείται η απόλυτη τιμή).
t_0 significance	το μήκος διάσπασης $t_0 = L_{xy}M_B/p_T^B$ διαιρούμενο με την αβεβαιότητά του, σ_{t_0}.
χ^2_{xyz}, χ^2_z	χ^2 υπολογισμένο μεταξύ του PV και SV αντίστοιχα στα x, y, z και z.
Isolation $(I_{\Delta R \leq 0,7})$	Ο λόγος του p_T^B ως προς το άθροισμα των p_T^B συν τα p_T όλων των τροχιών που ικανοποιούν $p_T > 0,5\,\mathrm{GeV}/c$ μέσα σ' έναν κώνο $\Delta R < 0,7$ από την κατεύθυνση του μεσονίου B, αποκλείοντας τα προϊόντα διάσπασης του μεσονίου B.
p_T^B	Η ορμή του μεσονίου B στο επίπεδο xy.
χ^2/ndf	Υπολογισμός του χ^2 του fit των τεσσάρων μιονίων στο secondary vertex

Table 1.1: *Οι μεταβλητές διαχωρισμού που χρησιμοποιήθηκαν στην ανάλυση του* $Br(\chi_b \to J/\psi J/\psi)$.

εκτιμητών. Στη συγκεκριμένη ανάλυση χρησιμοποιήθηκε ο εκτιμητής $\mathcal{P} = \epsilon/(1 + \sqrt{N_{\mathrm{BGR}}})$, όπου N_{BGR} είναι ο αριθμός των γεγονότων υποβάθρου στην περιοχή του σήματος, και ο οποίος εκτιμητής έχει αποδειχτεί ότι είναι ο καταλληλότερος για την εξαγωγή ορίου κατά τη διαδικασία της βελτιστοποίησης [1]. Ο υπολογισμός των βέλτιστων σημείων τομών (cuts) των μεταβλητών διαχωρισμού, γίνεται λαμβάνοντας υπόψη τα αποτελέσματα του εκτιμητή $\mathcal{P}$ ταυτόχρονα και για τις 6 μεταβλητές. Οι τιμές των βέλτιστων τομών (cuts) συγκεντρώνονται στον Πίνακα 1.2.

Μεταβλητή	**Τομή**
t_0 significance	1,89
χ^2_{xyz}	3,57
χ^2_{ndf}	5,26
α_{2D}	0,04
p_T	14473 MeV/c
Isolation $I_{\Delta R \leq 0,7}$	0,70

Table 1.2: *Ο πίνακας των μεταβλητών διαχωρισμού με τη μέγιστη διαχωριστική δύναμη και οι αντίστοιχες βέλτιστες τομές τους.*

Η αναμενόμενη τιμή των γεγονότων υποβάθρου στην περιοχή του σήματος, N_{χ_b}, υπολογίζεται από την εφαρμογή των βέλτιστων σημείων των τομών στις αντίστοιχες μεταβλητές διαχωρισμού και στην συνέχεια fit στα πλευρικά δεδομένα και αναγωγή στην περιοχή του σήματος (sideband interpolation). Με χρήση των δεδομένων του 2011, παρατηρούμε $3,02 \pm 0,58$ γεγονότα υποβάθρου στην περιοχή του σήματος.

Μια πρώτη εκτίμηση της ευαισθησίας της ανάλυσης όσο αναφορά την συγκεκριμένη διάσπαση μπορεί να γίνει με σύγκριση της effective cross section $\sigma_{eff} = N/L_{int}$ μεταξύ των δεδομένων προσομοίωσης και των πραγματικών δεδομένων. Ο θεωρητικός υπολογισμός του effective cross

section με χρήση δεδομένων προσομοίωσης δίνει $\sigma_{eff}^{MC} = [0,23 - 1,47]\,\text{fb}$ ενώ για τα πραγματικά δεδομένα η μετρούμενη τιμή είναι $\sigma_{eff}^{data} = (0,58 \pm 0,001)\,\text{fb}$.

Αν αναλογιστούμε τη συνεισφορά του χ_{b2} καταλαβαίνουμε ότι η ανάλυση έχει πλέον αποκτήσει την απαιτούμενη ευαισθησία και μπορεί να χρησιμοποιηθεί για την εξαγωγή ενός άνω ορίου με τα δεδομένα του 2011 ενώ υπάρχουν βάσιμες προσδοκίες για παρατήρηση της συγκεκριμένης διάσπασης με τα γεγονότα του 2012.

1.2 Υπολογισμός του Ορίου του $\text{Br}(B_s^0 \to \mu^+\mu^-)$ με τον Ανιχνευτή ATLAS

Οι διαδικασίες ουδετέρων ρευμάτων που αλλάζουν το flavour των κουαρκ (flavour changing neutral currents) καταστέλλονται πολύ στα πλαίσια του Καθιερωμένου Προτύπου (ΚΠ) και γι αυτό η μελέτη τους είναι ιδιαίτερης σημασίας για την αναζήτηση νέας φυσικής. Το καθιερωμένο πρότυπο προβλέπει ένα ρυθμό διάσπασης του $B_s^0 \to \mu^+\mu^-$ υπερβολικά μικρό ($(3,5 \pm 0,3) \times 10^{-9}$) [2]. Αυτή η διαδικασία όμως ενδέχεται να ενισχύεται από συζεύξεις από άλλα σωματίδια εκτός του ΚΠ (π.χ. υπερ-συμμετρικά σωματίδια). Γι αυτόν τον λόγο ο υπολογισμός ανωτάτων ορίων στον ρυθμό διάσπασης του $B_s^0 \to \mu^+\mu^-$ είναι μεγάλης σημασίας στο ερευνητικό πρόγραμμα του CERN.

Η ανάλυση που απαιτείται για τον υπολογισμό του άνω ορίου του $\text{Br}(B_s^0 \to \mu^+\mu^-)$ είναι αποτέλεσμα συνεργασίας πολλών ερευνητών. Ο συγγραφέας συνέβαλε σημαντικά σε κάποια κομμάτια της ανάλυσης. Για λόγους πληρότητας όλα τα στάδια της ανάλυσης αναφέρονται στη διδακτορική διατριβή, με τις λεπτομέρειες που αντιστοιχούν στη δουλειά του συγγραφέα να έχουν καταγραφεί ενδελεχώς, ενώ λεπτομέρειες της υπόλοιπης ανάλυσης μπορούν να βρεθούν στο [3].

Ο ρυθμός διάσπασης $\text{Br}(B_s^0 \to \mu^+\mu^-)$ στην ανάλυση που ακολουθεί υπολογίζεται ως αναφορά μια άλλη διάσπαση $B^\pm \to J/\psi K^\pm$, με σκοπό την ελαχιστοποίηση των συστηματικών σφαλμάτων των γεωμετρικών αποδοχών του ανιχνευτή και των αποδοτικοτήτων της ανακατασκευής των σωματιδίων, παρέχοντας ταυτόχρονα μικρές στατιστικές αβεβαιότητες.

Ο ρυθμός διάσπασης του συγκεκριμένου καναλιού υπολογίζεται σύμφωνα με τη σχέση

$$\text{Br}(B_s^0 \to \mu^+\mu^-) = \text{Br}\left(B^\pm \to J/\psi\,K^\pm\right)\frac{f_u}{f_s}\,\frac{N_{B_s^0}}{N_{B^\pm}}\,\frac{A_{B^\pm}\epsilon_{B^\pm}}{A_{B_s^0}\epsilon_{B_s^0}}$$

όπου f_u/f_s ο λόγος των κατακερματισμών (fragmentations) των u και s quark, A οι αποδοχές και ϵ η αποδοτικότητα της ανακατασκευής των γεγονότων. Η ανάλυση που ακολουθείται είναι *τυφλή ανάλυση* (blind analysis) που σημαίνει οτι η περιοχή σήματος $[5066,\ 5666]\,\text{MeV}/c^2$ δεν αποκαλύπτεται παρά μόνο όταν η μέθοδος υπολογισμού του άνω ορίου έχει πλήρως καθοριστεί, για την αποφυγή ασυνείδητων μεροληψιών.

Η μέτρηση του $\text{Br}(B^\pm \to J/\psi\,K^\pm)$, f_u/f_s προέρχονται από το Particle Data Group (PDG) [4] και πρόσφατες μετρήσεις του πειράματος LHCb αντίστοιχα.

Τα $N_{B_s^0}$ και $N_{B^\pm}$ είναι ο αριθμός των B_s^0 και $B^\pm$ αντίστοιχα που υπολογίζονται κατά το στάδιο της ανακατασκευής των σωματιδίων.

Το $A_{B^\pm}\epsilon_{B^\pm}/A_{B_s^0}\epsilon_{B_s^0}$ υπολογίζεται από τα δεδομένα προσομοίωσης.

Για την ανάλυση χρησιμοποιήθηκαν πραγματικά δεδομένα από pp συγκρούσεις σε ενέργεια $\sqrt{s} = 7\,\text{TeV}$ που αντιστοιχούν σε μια $L_{\text{int}} = 2,4\,\text{fb}^{-1}$ και δεδομένα προσομοίωσης για το σήμα (200 000 γεγονότα) και για το κανάλι αναφοράς (500 000 γεγονότα). Μια προεπιλογή των γεγονότων περιλαμβάνει:

- γεγονότα που πυροδοτούν το trigger EF_2mu4[2]

- γεγονότα με μιόνια που έχουν συνδυαστεί από τον εσωτερικό ανιχνευτή τροχιών και τον ανιχνευτή των μιονίων (combined muons)[3]

- γεγονότα στα οποία το χ^2/ndf του B vertex είναι μικρότερο του 2, όπου χ^2 είναι η κατανομή χ^2 που χρησιμοποιήται στην στατιστική και ndf είναι ο αριθμός των ανεξαρτήτων μεταβλητών που χρησιμοποιούνται κατά τον προσδιορισμό του χ^2.

- γεγονότα στα οποία τα υποψήφια σωματίδια B έχουν ορμή $p_T > 8$ GeV/c και $|\eta| < 2,5$.

Το υπόβαθρο αποτελείται από τρία μέρη. Πραγματικά μιόνια ($bb \rightarrow \mu^+\mu^- X$) που είναι το κύριο υπόβαθρο και υπολογίζεται από τα πλευρικά δεδομένα με αναγωγή στην περιοχή του σήματος (side-band interpolation). Ψεύτικα μιόνια με Br($B_s^0 \rightarrow \mu^+_{\text{fake}}\mu^-_{\text{fake}}$) ~ 10^{-9} που είναι κοντά στα επίπεδα του σήματος. Πραγματικά και ψεύτικα μιόνια ($B \rightarrow \mu K \nu$) με αμελητέα συνεισφορά.

Όπως έχει προαναφερθεί, η πληροφορία των γεωμετρικών αποδοχών και αποδοτικοτήτων της προσομοίωσης υπολογίζεται με βάση τα δεδομένα προσομοίωσης. Για να εξασφαλιστεί ότι τα δεδομένα προσομοίωσης μπορούν να είναι αξιόπιστα, έχει αναπτυχθεί μια λεπτομερής μελέτη [5]. Οι τομές (cuts) που χρησιμοποιούνται στο στάδιο της δημιουργίας εισάγουν μια μεροληψία στις κινηματικές επιλογές του χώρου των φάσεων. Οι αντίστοιχες διορθώσεις υπολογίζονται συγκρίνοντας τα bins των (η, p_T) από τα ιστογράμματα των αρχικών δειγμάτων MC προσομοίωσης με τα bins των (η, p_T) ιστογραμμάτων ειδικών δειγμάτων MC χωρίς τομές (cuts). Μια δεύτερη μεροληψία έχει να κάνει με το γεγονός ότι η φύση δεν μπορεί να περιγραφεί επακριβώς από κανένα παραγωγό γεγονότων προσομοίωσης. Σε αυτή την περίπτωση οι διορθώσεις προέρχονται από σύγκριση των ιστογραμμάτων (η, p_T) του σήματος αναφοράς MC με τα bins των (η, p_T) των ιστογραμμάτων του σήματος αναφοράς από πραγματικά δεδομένα. Το αποτέλεσμα είναι ένα 'οδηγούμενο από σήμα' (Data Driven-DD) βάρος γεγονότος που προσδιορίζεται από μια επαναλαμβανόμενη μέθοδο. Σε όλες τις υπόλοιπες μελέτες, τα γεγονότα διορθώνονται σύμφωνα με τα βάρη:

$$W(\eta, p_T) = W^{\text{GL}}(\eta, p_T) W^{\text{DD}}(p_T) W^{\text{DD}}(\eta)$$

Για το διαχωρισμό σήματος υποβάθρου, μια εκτεταμένη ανάλυση οδηγεί στη μέγιστη δυνατότητα διαχωρισμού. Το πρώτο στάδιο αυτής της ανάλυσης περιλαμβάνει τον ορισμό των μεταβλητών διαχωρισμού. Οι μεταβλητές επιλέγονται με τα παρακάτω κριτήρια:

Το secondary vertex αναμένεται να βρίσκεται μακριά από το primary vertex στο σήμα (αφού τα σωματίδια B ταξιδεύουν σχετικά μεγάλο χρονικό διάστημα πριν διασπαστούν) ενώ το αντίθετο αναμένεται για το υπόβαθρο.

Η δυναμική των υποψηφίων σωματιδίων του σήματος και του υποβάθρου, αναμένεται να έχουν διαφορετικές συμμετρίες στην τελική κατάσταση. Για παράδειγμα, το B σωματίδιο του σήματος αναμένεται να ταξιδεύει περίπου στην ίδια κατεύθυνση με την κατεύθυνση της ευθείας που ενώνει το primary με το secondary vertex (δηλαδή η pointing angle είναι μικρή) ενώ το αντίθετο αναμένεται για το σωματίδιο του υποβάθρου.

---

[2]EF_2mu4: Απαιτεί δύο μιόνια, 4 GeV/c το καθένα, να πυροδοτεί όλα τα στρώματα σκανδαλισμών (level triggers),

[3]combined muons: αν η τροχιά του μιονίου που έχει ανακατασκευαστεί στο φασματόμετρο μιονίων ταιριάζει με μία τροχιά του εσωτερικού ανιχνευτή, τότε οι τροχιές αυτές συνδυάζονται σε μία τροχιά μιονίου που χαρακτηρίζεται ως combined muon. Με το συνδυασμό των δύο ανεξάρτητων αυτών πληροφοριών, πετυχαίνουμε καλύτερη ανάλυση και καλύτερη απορριπτική ισχύ πλαστών μιονίων (fake muons),

Πληροφορία από την πλήρη ανακατασκευή του γεγονότος μπορεί να προσφέρει έναν επιπλέον τρόπο για τον διαχωρισμό σήματος – υποβάθρου. Για παράδειγμα, τροχιές σωματιδίων που δεν ανήκουν στο σωματίδιο B, αναμένονται να βρίσκονται πιο κοντά στο secondary vertex στην περίπτωση του υποβάθρου από ότι στην περίπτωση του σήματος.

Τέλος, χαρακτηριστικά της αδρονοποίησης των B σωματιδίων μπορούν να καταδείξουν αν το γεγονός περιλαμβάνει σήμα ή όχι. Στην περίπτωση του σήματος, τα προϊόντα της διάσπασης B είναι σχετικά απομονωμένα από άλλες τροχιές σωματιδίων που προέρχονται από το primary vertex.

Με βάση τα παραπάνω μελετήθηκαν αρχικά 28 μεταβλητές διαχωρισμού. Ένας τέτοιος μεγάλος αριθμός μεταβλητών όμως θα προκαλούσε προβλήματα σε οποιονδήποτε ταξινομητή στη φάση της βελτιστοποίησης. Γι' αυτό το λόγο αναπτύχθηκε μια μεθοδολογία η οποία, βασιζόμενη στους πίνακες συσχετισμού των μεταβλητών και στις καμπύλες Receiver Operating Characteristic, ROC[4], αποφέρει τη μεγαλύτερη δυνατότητα διαχωρισμού με το μικρότερο δυνατό αριθμό μεταβλητών διαχωρισμού. Ο πίνακας 1.3 που ακολουθεί συγκεντρώνει τις τελικές μεταβλητές διαχωρισμού που χρησιμοποιήθηκαν καθώς και τους ορισμούς τους.

Μεταβλητές	Περιγραφή
α_{2D}	Αν $\boldsymbol{x}$ είναι το διάνυσμα από το primary vertex (PV) στο secondary vertex (SV), τότε α_{2D} είναι η γωνία στο επίπεδο xy ανάμεσα στο $\boldsymbol{x}$ και $\boldsymbol{p}^B$ (χρησιμοποιείται η απόλυτη τιμή).
ΔR	Η γωνία $(\Delta\phi^2 + \Delta\eta^2)^{1/2}$ ανάμεσα στα $\boldsymbol{x}$ και $\boldsymbol{p}^B$.
L_{xy}	βαθμωτό γινόμενο στο επίπεδο xy, $\boldsymbol{x} \cdot \hat{\boldsymbol{p}}^B$.
t_0 significance	το μήκος διάσπασης $t_0 = L_{xy}M_B/p_T^B$ διαιρούμενο με την αβεβαιότητά του, σ_{t_0}.
χ^2_{xy}, χ^2_z	χ^2 υπολογισμένο μεταξύ του PV και SV αντίστοιχα στα x, y και z.
Isolation ($I_{\Delta R \leq 0,7}$)	Ο λόγος του p_T^B ως προς το άθροισμα των p_T^B συν τα p_T όλων των τροχιών που ικανοποιούν $p_T > 0,5\,\text{GeV}/c$ μέσα σ' έναν κώνο $\Delta R \leq 0,7$ από την κατεύθυνση του μεσονίου B, αποκλείοντας τα προϊόντα διάσπασης του μεσονίου B.
$\lvert d_0^{\max} \rvert, \lvert d_0^{\min} \rvert$	Μέγιστη και ελάχιστη vertex impact parameter στο επίπεδο xy των προϊόντων διάσπασης του μεσονίου B ως προς το primary vertex (χρησιμοποιείται η απόλυτη τιμή).
$\lvert D_{xy}^{\min} \rvert, \lvert D_z^{\min} \rvert$	Ελάχιστη απόσταση της πιο κοντινής απόστασης στο xy επίπεδο μεταξύ του secondary vertex και των άλλων τροχιών (χρησιμοποιείται η απόλυτη τιμή).
p_T^B	Η ορμή του μεσονίου B στο επίπεδο xy.
$\lvert p_L^{\max} \rvert, \lvert p_L^{\min} \rvert$	Μέγιστη και ελάχιστη ορμή των δυο μιονίων στην κατεύθυνση του μεσονίου B.

Table 1.3: *Οι μεταβλητές διαχωρισμού που χρησιμοποιήθηκαν στην ανάλυση του $Br(B_s^0 \to \mu^+\mu^-)$.*

---

[4]Οι καμπύλες ROC σχετίζονται με το λόγο κέρδους προς κόστος. Στις αναλύσεις Φυσικής Υψηλών Ενεργειών το κέρδος έχει να κάνει με την απόρριψη του υποβάθρου, ενώ το κόστος έχει να κάνει με την την αποδοτικότητα του σήματος.

Όπως αναμενόταν θεωρητικά, η μεταβλητή της απομόνωσης (isolation) αποδείχτηκε και πειρα-ματικά ότι είναι μία από τις πιο καλές μεταβλητές όσον αφορά τη δύναμη διαχωρισμού. Είναι ευρέως γνωστό όμως ότι η συγκεκριμένη μεταβλητή υποφέρει αρκετά από το φαινόμενο pile-up (πολλαπλές ανελαστικές συγκρούσεις στο ίδιο γεγονός). Γι αυτό τον λόγο, χρησιμοποιήθηκε ένας νέος ανθεκτικός στο pile-up ορισμός του isolation και σε μια ειδική μελέτη εξετάστηκε η αποδοτικότητά του ως προς την πολλαπλότητα των σημείων συγκρούσεων της δέσμης (Primary Vertex, PV) του γεγονότος. Τα αποτελέσματα της μελέτης ξεπερνάνε τις καλύτερες προσδοκίες. Η μελέτη έδειξε ότι ο νέος αυτός ορισμός του isolation είναι πραγματικά ανεξάρτητος του αριθμού των PV του γεγονότος.

Αφού έχουν ορισθεί οι μεταβλητές διαχωρισμού, το επόμενο βήμα είναι ο ορισμός της μεθόδου διαχωρισμού σήματος – υποβάθρου. Η ανάλυση κάνει χρήση ταξινομητών πολλών μεταβλητών (multivariate analysis) όπου εκτεταμένες μελέτες έδειξαν ότι ο ταξινομητής Boosted Decision Tree (BDT) δίνει τα καλύτερα αποτελέσματα. Αρχικά επιλέγοντας 3 μόνο μεταβλητές (isola-tion, t_0, $|\alpha_{2D}|$) τα αποτελέσματα του ταξινομητή συγκρίθηκαν με αυτά μιας μεθόδου "cut and count" και βρέθηκαν να είναι ίδια στα πλαίσια των σχετικών σφαλμάτων τους. Στη συνέχεια, προσθέτοντας περισσότερες μεταβλητές διαχωρισμού στον ταξινομητή, εξακριβώθηκε η βαθμιαία καλύτερη συμπεριφορά του. Τελικά ένας έλεγχος, χρησιμοποιώντας ειδικά δημιουργημένα γεγονότα προσομοίωσης σήματος στα $6,5\,\mathrm{GeV}/c^2$, έδειξε ότι το αποτέλεσμα του ταξινομητή είναι ανεξάρτητο της μάζας, αποδεικνύοντας ότι η χρήση του δεν θα προκαλέσει κάποια μεροληψία. Ο αριθμός γεγονότων του $B^\pm$ μετα τα αντίστοιχα cuts, είναι ένα από τα στοιχεία υπολογισμού του Br($B_s^0 \to \mu^+\mu^-$). Η τελική τιμή για το $N_{B^\pm}$ είναι αποτέλεσμα ενός binned maximum likelihood fit, το οποίο γίνεται στις διαφορετικές περιοχές διακριτικής ικανότητας της μάζας (mass resolution). Ο αριθμός γεγονότων του $B^\pm$ μετα τα αντίστοιχα cuts, καταγράφεται στον πίνακα 1.4.

Category	yield ± stat. ± syst.	rel. stat.	rel. syst.	χ^2 fit prob.
1	$4928 \pm 67 \pm 37$	$1,6\,\%$	$0,9\,\%$	$41\,\%$
2	$1407 \pm 39 \pm 23$	$2,8\,\%$	$1,6\,\%$	$93\,\%$
3	$1126 \pm 34 \pm 19$	$3,0\,\%$	$1,7\,\%$	$21\,\%$
All	$6968 \pm 86 \pm 88$	$1,2\,\%$	$1,3\,\%$	$82\,\%$

Table 1.4: *Ο αριθμός γεγονότων του $B^\pm$ για τις τρεις διαφορετικές περιοχές διακριτικής ικανότητας της μάζας.*

Το τελικό βήμα είναι ο υπολογισμός του ίδιου του ορίου Br($B_s^0 \to \mu^+\mu^-$). Ένα τελευταίο στοιχείο του υπολογισμού είναι ο αριθμός γεγονότων του σήματος για το B_s^0, το οποίο προϋποθέτει αποκάλυψη της περιοχής της αναλλοίωτης μάζας στην περιοχή του σήματος. Τα υποψήφια γεγονότα B_s^0 της περιοχής του σήματος για τις τρεις διαφορετικές οικογένειες αναλλοίωτης μάζας είναι 2/1/0 αντίστοιχα. Η εξαγωγή του ορίου γίνεται με τη μέθοδο των $95\,\%$ CLs [6] και αποφέρει το ανώτατο όριο Br($B_s^0 \to \mu^+\mu^-$) = $2,2 \times 10^{-8}$.

1.3   Εφαρμογή Οπτικοποίησης Δεδομένων του Συστήματος Αυτομάτου Ελέγχου του Ανιχνευτή ATLAS

Το σύστημα αυτομάτου ελέγχου (Detector Control System - DCS), είναι το υπεύθυνο σύστημα για την ασφαλή και συνεκτική λειτουργία του ανιχνευτή. Επιβλέπει το hardware του ανιχνευτή, δίνει on-line πληροφορία για τις λειτουργικές παραμέτρους του, ενημερώνει για τυχόν προβλήματα και αποθηκεύει χρήσιμη πληροφορία σε μια βάση δεδομένων. Το DDV (DCS Data Viewer), είναι μια διαδικτυακή εφαρμογή οπτικοποίησης δεδομένων του συστήματος αυτομάτου ελέγχου. Έχει μια αρχιτεκτονική υπηρέτη–πελάτη (server–client) και αρθρωτό και ευέλικτο σχεδιασμό. Είναι σχεδιασμένο ώστε να εξυπηρετεί όλη την επιστημονική κοινότητα του ανιχνευτή (εμπειρογνώμονες και απλούς χρήστες) και είναι προσβάσιμο από το διαδίκτυο εντός και εκτός CERN. Οι προδιαγραφές της εφαρμογής είναι :

- Ανεξαρτησία από λειτουργικό σύστημα και περιηγητή διαδικτύου (browser)

- Χρόνος έναρξης περίπου 10 s

- Τυπικός χρόνος λήψης δεδομένων περίπου 10 s

- Εξαγωγή ρυθμίσεων σε XML file

- Απόδοση γραφημάτων, χρήση πολλαπλών αξόνων, πίνακες, ROOT, ASCII

- Προστασία βάσης δεδομένων από υπερβολική χρήση

Ο πρώτος τρόπος αναπαράστασης των δεδομένων είναι με τη βοήθεια γραφικών παραστάσεων και ιστογραμμάτων. Αυτή είναι η βασική διεπιφάνεια επαφής με τον χρήστη. Ένας δεύτερος τρόπος αναπαράστασης των δεδομένων είναι με τη βοήθεια καταλόγων. Στην πρώτη στήλη αναφέρεται το όνομα των δεδομένων που θέλουμε να δούμε. Σε μια δεύτερη στήλη αναφέρεται η τιμή των δεδομένων και σε μια τρίτη στήλη αναφέρεται ο χρόνος που γράφτηκε η τιμή αυτή. Αυτή η διεπιφάνεια αρχικά δημιουργήθηκε με την τεχνολογία των java applets αλλά στη συνέχεια τροποποιήθηκε και χρησιμοποιήθηκε η τεχνολογία java-script, η οποία είναι ανεξάρτητη περιηγητή. Τέλος ο τρίτος τρόπος που ο χρήστης μπορεί να έχει εποπτεία των δεδομένων είναι με αρχεία ROOT και ascii. Ο βασικός τρόπος πλοήγησης στα δεδομένα DCS του ανιχνευτή είναι με χρήση των miller column. Για περαιτέρω φιλική χρήση όμως, υπάρχει και μια μηχανή αναζήτησης, όπου ο χρήστης πληκτρολογεί το επιθυμητό πρότυπο ή σχηματισμό (pattern) και η μηχανή αναζήτησης επιστρέφει όλα τα δεδομένα που αντιστοιχούν σε αυτό το πρότυπο. Αξίζει να σημειωθεί ότι η μηχανή αναζήτησης υποστηρίζει και regular expressions για πιο σύνθετες αναζητήσεις. Το DDV είναι πλέον ένα επίσημο service του ανιχνευτή ATLAS και αυτό που επίσημα προτείνεται για κάθε αναζήτηση δεδομένων του ανιχνευτή. Εξυπηρετεί 150 περίπου ενεργούς χρήστες και, εκτός από τον ανιχνευτή ATLAS, χρησιμοποιείται από το πείραμα COMPASS, ενώ εκφράζεται έντονα το ενδιαφέρον για τη χρήση του και από όλα τα υπόλοιπα πειράματα του LHC.

Chapter 2

Elementary Particle Physics at the LHC

Elementary particle physics addresses a fundamental question: *what is the universe made of*? It aims to explore the elementary building blocks of matter and the fundamental interactions amongst them. The belief that everything is made from few basic elements can be traced to the ancient texts of Greeks, Indians and Chinese from over two thousand years ago. Today, these fundamental questions are addressed by particle physics and the Large Hadron Collider (LHC), together with its' detectors, is a new experimental apparatus to put our current theories under test.

2.1   Elementary Particles

It is well known that all matter is composed of a small number of fundamental particles. These fundamental particles can be categorized into three groups, the *leptons*, the *quarks* and the *mediators*.

The leptons carry integral electric charge and are divided into three *generations*. The first generation of leptons includes the well known *electron* and the $e-$neutrino, ν_e. The *muon* and the *tau* are also leptons, heavier replicas of the electron. The second generation of leptons includes the *muon* and the ν_μ and the third generation of leptons includes the *tau* and the ν_τ.

The *quarks* carry fractional electric charges, $+2|e|/3$ or $-|e|/3$. Similarly with the leptons, there are six *flavours* of quarks divided into three generations. The quark symbols for the different flavours are u for *up*, d for *down*, s for *strange*, c for *charm*, b for *bottom* and t for *top*. The name "quark" was coined by Gell-Mann who in 1964, suggested that all the different particles that had been discovered until then, (e.g. n, p, Σ^0) are composed of more elementary constituents [7]. In the beginning, the quark model faced fundamental theoretical objections, such as the violation of the Pauli principle (e.g. the u quarks in Δ^{++} seemed to be in the same state) and the fact that never has been observed an unbound quark state. It was the *colour hypothesis* (each quark has three colours —introduced by W. Greenberg) [8], the assumption of *quark confinement* and finally the discovery of the J/ψ meson [9, 10] resulting in what is known as *November Revolution* [11] that finally rescued the quark model. Nevertheless the unusual quark terminology reflects how seriously people took the quark model in its inception [12].

Upon this, Feynman and Stuckelberg in 1940 [13] presented an insightful interpretation of the negative-energy states appearing in Dirac's relativistic formula $E^2 - p^2c^2 = m^2c^4$. The negative-energy solution is interpreted like the positive-energy states of the positive energy

solution. In light of this interpretation, every particle is considered to have its own *antiparticle*, which is like a mirror image that has the same mass but an opposite charge. Therefore, there exist six anti-leptons and six anti-quarks which come in three different colours.

Generation	Flavour	Charge	Mass (MeV/c^2)
leptons			
first	e	-1	0.51
	ν_e	0	0
second	μ	-1	105.69
	ν_μ	0	0
third	τ	-1	1776.99
	ν_τ	0	0
quarks			
first	d	-1/3	5
	u	2/3	2
second	s	-1/3	100
	c	2/3	1290
third	b	-1/3	4670
	t	2/3	172900

Table 2.1: *The elementary particles of the Standard Model (SM) (adapted from [4]).*

2.2 Fundamental Forces

The elementary particles interact in four fundamental ways, which, are described in terms of the exchange of particles, that is *electromagnetic*, *strong*, *weak*, and *gravitational*. The electromagnetic force is the force that keeps the electrons around the nuclei and links the atoms in molecule structures. The theory that describes the electromagnetic force is the Quantum Electrodynamics (QED) and its mediator is the photon. The strong force is the force that keeps the quarks inside the nucleus, it is described by Quantum Chromodynamics (QCD), with the *gluon* as a mediator. It is named *strong* force as its strength is much higher, when compared with the rest of the forces. The weak force is responsible for the radiative decay of subatomic unstable particles. It is derived from the theory of flavour dynamics and its mediators are the *W* and *Z* bosons. Lastly, the gravitational force is the one that keeps the planets in their orbits. It is described by the general theory of relativity, although the quantum theory of gravity has not yet been been developed and its mediator, the *graviton*, is a purely theoretical particle. In elementary particle physics, the gravitational force is not taken into account with respect to the other forces due to its extremely small strength.

2.3 The Standard Model

The Standard Model [14] is the collection of the theories, emerged between 1960 and 1970 , concerning the electromagnetic, weak, and strong nuclear interactions of the subatomic particles (quarks and leptons). All the fundamental interactions in this model derive from one simple requirement, namely that the theory is invariant under local gauge transformations.

Force	Mediator	Charge	Mass (MeV/c^2)
Strong	gluons	0	0
Electromagnetic	photon	0	0
Weak	W bosons	±1	80.42
	Z boson	0	91.19

Table 2.2: *The fundamental forces and their mediators in the Standard Model (adapted from [?]).*

2.4 Quantum Field Theory and Gauge Freedom

Quantum field theory (QFT) is the natural language used in particle physics, which provides theoretical framework that combines quantum mechanics with special relativity and is used in the Standard Model. In QFT, the classical distinction of particles and fields does not exist any more, the particles are not localised entities like they are in classical mechanics, but they are considered to be the excited states of a field. Furthermore, in QFT, the forces between particles are mediated by other particles. For example the electromagnetic interaction between two electrons is mediated by the exchange of a photon.

In QFT the *Lagrangian* formulation is adopted due to its obvious theoretical advantages. The dynamics of a system are summarised in a Lagrangian $\mathcal{L}$ (a Lagrangian density, to be precise) that is a function of the fields and their space-time derivatives:

$$\mathcal{L}(x) = \mathcal{L}(\phi, \partial_\mu \phi)$$

Since QFT is a relativistic theory, the calculus of variations is performed more naturally using the Euler-Lagrange equation and the motion of the field is described by:

$$\partial_\mu \left(\frac{\partial \mathcal{L}}{\partial(\partial_\mu \phi)} \right) = \frac{\partial \mathcal{L}}{\partial \phi}$$

A very important phenomenon associated with QFT is the gauge freedom and the corresponding field theory is called *gauge* theory. In gauge theories the Lagrangian is invariant under a continuous group of *local* transformations that can be thought of abstract "changes of coordinates". It is believed that all the fundamental interactions in nature are described by gauge theories [15].

2.4.1 Quantum Electrodynamics

The Dirac Lagrangian that describes the free spin-1/2 electron is:

$$\mathcal{L} = i\hbar c \overline{\psi} \gamma^\mu \partial_\mu \psi - mc^2 \overline{\psi} \psi$$

If we demand that this $\mathcal{L}$ is invariant under a local phase transformation, $\psi \rightarrow e^{i\theta(x)}\psi$, or, using a terminology from group theory, $\psi \rightarrow U\psi$, $U^\dagger U = 1$, $U = e^{i\theta}$, we are forced to introduce in the initial $\mathcal{L}$ a vector field A^μ. Furthermore, to satisfy a globally invariant $\mathcal{L}$, the new field A^μ has to be massless. Finally the complete $\mathcal{L}$ becomes:

$$\mathcal{L} = \underbrace{\left[i\hbar c \overline{\psi} \gamma^\mu \partial_\mu \psi - mc^2 \overline{\psi} \psi \right]}_{\text{electrons}} - \underbrace{\left[\frac{1}{16\pi} F^{\mu\nu} F_{\mu\nu} \right]}_{\text{EM component}} - \underbrace{\left(q\overline{\psi} \gamma^\mu \psi \right) A_\mu}_{\text{photons}}$$

The $\mathcal{L}$ is invariant under the so-called *covariant derivative*

$$\mathcal{D}_\mu = \partial_\mu + i\frac{q}{\hbar c}A_\mu$$

It describes Dirac spinor fields ψ (e.g. electrons) interacting with vector massless Maxwell fields (photons), whereas the middle term is the free photon Lagrangian.

2.4.2 Quantum Chromodynamics

The free Lagrangian for a quark flavour (e.g. u) is

$$\psi = \begin{pmatrix} \psi_r \\ \psi_b \\ \psi_g \end{pmatrix}, \qquad \overline{\psi} = \begin{pmatrix} \bar{\psi}_r & \bar{\psi}_b & \bar{\psi}_g \end{pmatrix}$$

where r, g, b are the three colours of quarks.

In a similar way to QED, we demand the $\mathcal{L}$ to be invariant under the local SU(3) gauge transformations $\psi \to S\psi$.

$$\psi \to S\psi, \qquad S \equiv e^{-iq\tau\lambda(x)/\hbar c}$$

By replacing the ordinary derivative with the covariant one $\mathcal{D}_\mu = \partial_\mu + i\frac{q}{\hbar c}\lambda A_\mu$ and introducing the vector fields A_μ (eight of them), the modified $\mathcal{L}$ becomes:

$$\mathcal{L} = \underbrace{\left[i\hbar c\overline{\psi}\gamma^\mu\partial_\mu\psi - mc^2\overline{\psi}\psi \right]}_{\text{quarks}} - \underbrace{\left[\frac{1}{16\pi}F^{\mu\nu}F_{\mu\nu} \right]}_{\text{free gluon Lagrangian}} - \underbrace{\left(q\overline{\psi}\gamma^\mu\lambda\psi \right)A_\mu}_{\text{gluons}}$$

and is invariant under SU(3) transformations.

This describes the equivalent mass Dirac fields which are the quarks [*up, down, strange, charm, bottom, top*, where each of them has an intrinsic property of colour (r, g, b)], interacting with eight massless vector fields (the eight gluons), and the middle term represents the free gluon Lagrangian.

2.4.3 Electroweak Unification and Symmetry Breaking

The weak interaction is a fundamental force in nature, responsible for the decay of charged pions or muons for example. There are two kinds of weak interactions, *charged* (mediated by W) and *neutral* (mediated by Z).

In 1960, Glashow, Weinberg and Salam [16] proposed the electroweak theory which is a unification of electromagnetic and weak forces. Despite the existence of W and Z [17], an open question on how the mediators of the weak force actually acquire their mass remains.

If we assume [18] a Lagrangian:

$$\mathcal{L} = \frac{1}{2}(\partial_\mu\phi)^*(\partial^\mu\phi) + \frac{1}{2}\mu^2(\phi^*\phi) - \frac{1}{4}\lambda^2(\phi^*\phi)^2$$

where $\phi = \phi_1 + i\phi_2$ is a single complex field, and if we require local gauge transformations

$$\phi \to e^{i\theta(x)}\phi$$

and replace the normal derivative with the covariant

$$\mathcal{D}_\mu = \partial_\mu + i\frac{q}{\hbar c}A_\mu$$

we get the following Lagrangian

$$\mathcal{L} = \frac{1}{2}\left[\left(\partial_\mu - \frac{iq}{\hbar c}A_\mu\right)\phi^*\right]\left[\left(\partial^\mu + \frac{iq}{\hbar c}A^\mu\right)\phi\right] + \frac{1}{2}\mu^2(\phi^*\phi) - \frac{1}{4}\lambda^2(\phi^*\phi)^2 - \frac{1}{16\pi}F^{\mu\nu}F_{\mu\nu}$$

If we additionally select a convenient gauge

$$\theta = -\arctan\left(\frac{\phi_2}{\phi_1}\right)$$

and introduce the fields

$$\eta = \phi_1 - \frac{\mu}{\lambda}, \qquad \varrho = \phi_2$$

which are fluctuations around the ground state, we end up with the final Lagrangian

$$\mathcal{L} = \left[\frac{1}{2}(\partial_\mu\eta)(\partial^\mu\eta) - \mu^2\eta^2\right]$$
$$+ \left[-\frac{1}{16}F^{\mu\nu}F_{\mu\nu} + \frac{1}{2}\left(\frac{q\mu}{\hbar c\lambda}\right)^2 A_\mu A^\mu\right]$$
$$+ \frac{\mu}{\lambda}\left(\frac{q}{\hbar c}\right)^2 \eta\left(A_\mu A^\mu\right) + \frac{1}{2}\left(\frac{q}{\hbar c}\right)^2 \eta^2 A_\mu A^\mu - \lambda\mu\eta^3 - \frac{1}{4}\lambda^2\eta^4$$
$$+ \left(\frac{\mu^2}{2\lambda}\right)^2$$

This Lagrangian describes a massive scalar field η (the Higgs particle) interacting with a massive gauge field A^μ. As it can be seen, the first term of the final Lagrangian is a fere Klein-Gordon Lagrangian for the Higgs field, which evidently carries a mass $m_\eta = \sqrt{2}\mu\hbar/c$. This shows that the mass of Higgs m_η, is sensitive to the shape of the potential and therefore the mass of the Higss particle itself can not be determined by the theory.

2.5 New Physics

At present we can fairly say that the SM stands triumphant. It is a remarkable achievement of particle physics that has been successfully tested over the past 30 years and shows excellent agreement with numerous experimental measurements of electroweak and strong interactions.

Notwithstanding this, there are a number of shortcomings and problems that appear in the SM. We have yet to understand the true mechanism responsible for the mass of the weak interaction gauge bosons $W^\pm$ and Z^0. The Higgs mechanism would provide an elegant explanation for this but there is as yet no experimental verification to prove it. Furthermore, the *hierarchy problem*[1] the huge gap between the Plank and the GUT scale (grand unification energy) is not yet understood. In addition, gravity is not incorporated into the same theoretical framework with the other fundamental interactions and, even worse, the SM deals only with $\sim 5\%$ of the matter of the universe, while astronomical evidence indicates that the *Dark Matter* and *Dark Energy* account for the remaining 95%.

---

[1]The hierarchy problem is one of the puzzles of the modern theoretical physics, where two widely separated scales are evident, when one compares the relative strength of the fundamental forces. On the one hand, there is the Plank scale (10^{19}GeV) associated with the gravitational interactions and on the other hand, there is the electroweak scale associated with the masses of $W\pm$ and Z^0 (~ 100) GeV. The question arises; how these particles can be so light when the Plank scale is so big?

Paradoxically, the flaws of the SM lead to the development of promising theories of new physics (NP) that aim to explain phenomena beyond the scope of the SM. The following paragraphs highlight some of the possible discoveries of new physics at the LHC era and the latest relevant experimental results.

2.5.1 The Higgs Boson

The Higgs mechanism is a helpful mechanism that deals with the masses of $W^{\pm}$ and Z^0 based on a theory where the lagrangian is invariant under local phase transformations. In this model a complex scalar doublet *Higgs field* is introduced in addition to the fermion and boson gauge fields. The dominant production mechanism at hadron colliders, is *gluon fusion*, $g + g \rightarrow h$, via a quark loop, while other modes like *W–Z* bremsstrahlung or *W/Z* fusion are expected. There are many different decay modes of the Higgs particle, the branching ratios of which are depending a lot on the mass of the Higgs particle(see Image 2.1). The $H \rightarrow b\bar{b}$ dominates in low mass ranges ($< 130\,\text{GeV}/c^2$), but it suffers from high QCD background. Nevertheless, other channels with smaller rates, but easier experimental observation (such as $H \rightarrow \gamma\gamma$) can be used in the searches. In the intermediate mass range ($130 - 180\,\text{GeV}/c^2$) the preferable search is done using the $H \rightarrow WW^*, H \rightarrow ZZ^*$ decays. Finally the same decays dominate in high mass ranges ($180 - 1000\,\text{GeV}/c^2$) both the gauge bosons are allowed to be *on shell* [2]. Unfortunately, until now the Higgs boson remains unobserved.
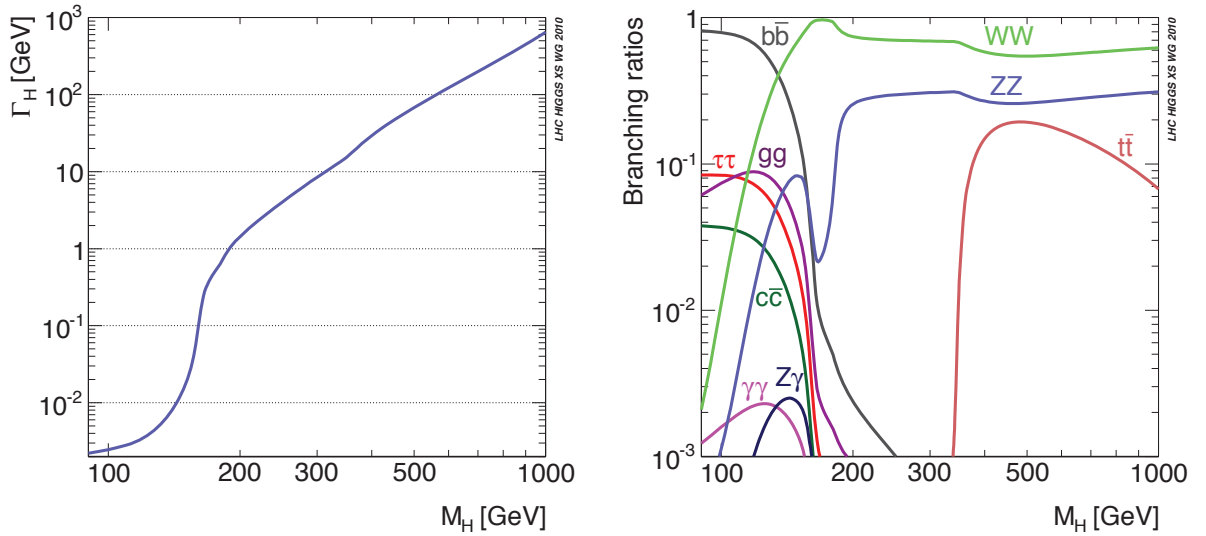
Figure 2.1: *Scatter plot of the decay width (left) and of the branching ratios (right) of the SM Higgs as a function of its mass.*

Constraints

As it is shown above, the value of the mass of the Higgs cannot be determined by theory, but it can be theoretically constrained within an upper limit $< 1\,\text{TeV}/c^2$ due to unitarity arguments [19, 20]. Experimentally, intervals in the mass region have also been excluded. The first experimental constraints came from studies at LEP with a lower bound of Higgs mass, while

---

[2]The term on shell indicates that the mass of the particle is on the hyperboloid of the energy-momentum space defined by the equation in four momentum notation) $E^2 - p_{m_\mu}p^\mu = m^2$.

recent Tevatron [21] results excluded even more regions. Nevertheless, the most stringent constraints come from LHC. During the writing of this thesis the latest results of the Higgs boson search at the LHC were given in [22]. Below is a summary of the most important experimental constraints.

Experimental Constraints by LEP

The mass of the scalar boson is greater than $114.4\,\text{GeV}/c^2$ at 95% CL [23].

Experimental Constraints by Tevatron

The final study [22] includes all Higgs decays amongst which $H \to b\bar{b}$ and $H \to WW^*$ are the dominant ones. The region that is excluded is the $[147, 179]\,\text{GeV}/c^2$, while the region $[115, 140]\,\text{GeV}/c^2$ shows a data excess greater than 2σ. Finally CDF [24] and D0 [25] observe an excess in the $b\bar{b}$ channel with a mass $\sim 125\,\text{GeV}/c^2$.

Experimental Constraints by LHC

Studies at LHC using all 2011 data [22], show that it is preliminary to draw any conclusions for the existence or not theHiggs particle. There is no hint of an excess in the channels $H \to WW^*$, $H \to b\bar{b}$, $H \to \tau\tau$. On the contrary, the channel $H \to \gamma\gamma$ shows an excess slightly bigger than 2.8σ at a mass of $125\,\text{GeV}/c^2$ in ATLAS and 2.9σ at $125\,\text{GeV}/c^2$ in CMS. Moreover, the channel $H \to ZZ^*$ shows an excess of 2.16σ at $125\,\text{GeV}/c^2$ in ATLAS and 2.5σ at $119.5\,\text{GeV}/c^2$ at CMS. As far as the combined results are concerned, ATLAS shows an excess of 2.5σ at $126\,\text{GeV}/c^2$ while the CMS shows an excess of 2.8σ at $125\,\text{GeV}/c^2$. When the *look elsewhere effect*[3] is taken into account, the signal drops by $\sim 10\%$. However, this effect is questioned when the excess appears at roughly the same mass in the same decay channels in both experiments. In the current scheme of things, the combined significant excess is consistent with a signal expectation, but the fact that the observation hints do not appear in all decay channel remains puzzling. Provided that the LHC will perform the collected statistics by the end of the year (as expected during 2012), this will be enough to prove the existence or *in*existence of the Higgs boson.

2.5.2 Supersymmetry

Supersymmetry [26] (SUSY) is a proposed symmetry where every fundamental matter particle has a massless shadow force carrier particle and every force carrier particle has a massive shadow matter particle. It is a symmetry between particles and force carriers. If SUSY is a truly fundamental symmetry, it can potentially address several unresolved theoretical problems. The supersymmetric extension of the SM could be extremely promising to describe Nature, in that;

- The *hierarchy problem* is tackled since SUSY allows the theory to have two stable but separate mass scales.

- The electroweak symmetry breaking emerges directly from the theory and accommodates for the quark, leptons and bosons masses.

- The lightest supersymmetric particle is colourless, neutral and stable, an attractive candidate for Dark Matter.

---

[3]The look elsewhere effect is a technique in the statistical analysis of an experiment, that quantifies the probability that a statistically significant observation is coming from an occasional random fluctuation

- The matter-antimatter asymmetry observed in the universe can be explained.

Unfortunately, at present, even the latest LHC results do not show any experimental evidence of supersymmetry, even in the hypothesis of the minimal supersymmetric version of the SM [27]. According to the latest LHC studies [28], there is no evidence of SUSY and the search limits are pushed towards $M_{\text{SUSY}} > \sim 1\,\text{TeV}/c^2$. Moreover, there is no sign of SUSY from indirect measurements of flavour physics that push the search limits even further to $M_{\text{SUSY}} > \sim 10\,\text{TeV}/c^2$. As a result, it can be asserted that any expectations for early discoveries were too optimistic, while there is still plenty of room where (heavy) SUSY could hide.
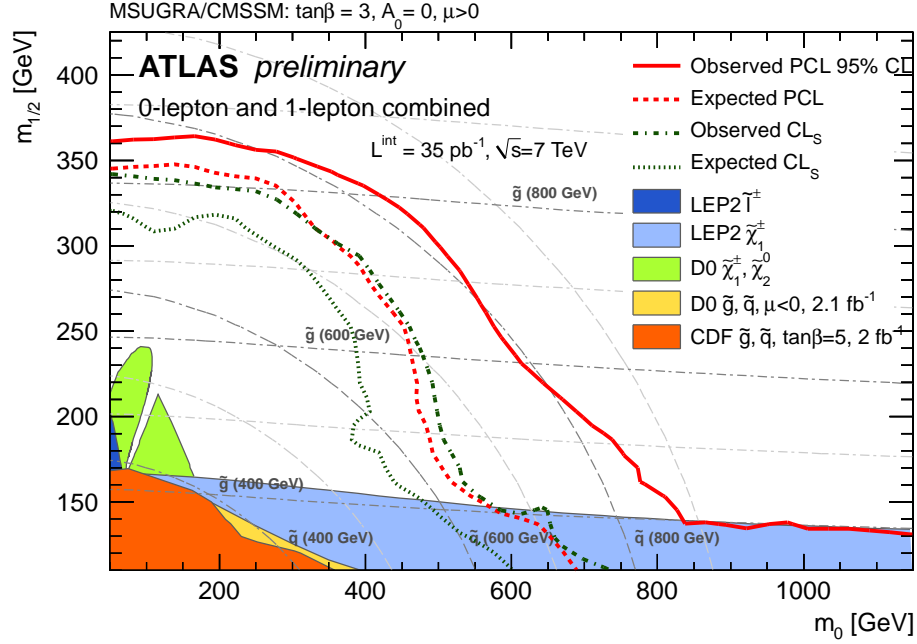
Figure 2.2: *No evidence of SUSY in 2010 searches in the m_0, $m_{1/2}$ plane. (m_0: common scalar particle mass (sleptons, squarks), $m_{1/2}$ common fermion particle mass (gauginos)).*

Chapter 3

The Large Hadron Collider and the ATLAS Detector

This chapter aims to describe the main parts of the experiment that produce the data used in this thesis. In contrast with *most* areas of physics, where the experimental apparatus covers the size of a table or a room, the apparatus in high energy physics is colossal and staggeringly complicated. The "experimental setup" is composed of two main parts, an accelerator that accelerates the hadrons and a detector that records the debris of the collisions.

3.1   The Large Hadron Collider

The Large Hadron Collider (LHC) [29], is the world's highest energy particle accelerator, the largest and the most complex scientific instrument ever built. It is hosted in a ring of 27 km diameter, built 50 to 175 m below the outskirts of Geneva, Switzerland. The LHC is a multinational project with ~10.000 members drawn from different universities, research centres and laboratories from over 100 countries. The aim of the LHC is to shed light upon some of the most fundamental questions of physics, such as what is the origin of mass, whether hidden symmetries and extra spatial dimensions exist in the universe and what is the dark matter.

In its designed operation, pp collisions will take place at a centre of mass energy of $\sqrt{s} = 14$ TeV, reaching an instantaneous luminosity of

$$L = \frac{n_{\mathrm{b}} N_{\mathrm{L}} N_{\mathrm{R}} f_{\mathrm{rev}}}{A_{\mathrm{T}}^{\mathrm{eff}}} \sim 10^{34} \; \mathrm{cm}^{-2}\mathrm{s}^{-1}$$

where $f_{\mathrm{rev}} = c/27$ km $\sim 10^4$ Hz, $\sigma_{\mathrm{b}} = 16$ µm and $A_T^{\mathrm{eff}} = 4\pi\sigma_{\mathrm{b}}^2$ is the effective transverse area of the proton-beam. In each proton-beam store, 2808 bunches are injected into the LHC ring, which at 7 TeV, the current energy, results in a total energy of LHC beam equal to $2808\times1.15\times10^{11}\times7$ TeV $= 362$ MJ.

The proton bunches reach the LHC at 450 GeV/proton, after being accelerated from a complex of older CERN accelerators, as shown in Figure 3.1. Initially, the protons are accelerated linearly by a *linear accelerator* (LINAC2) to 50 MeV. After which, they enter the *Proton Synchrotron Booster* (PSB) which increases their energy to 1.4 GeV. Following PSB they enter into the *Proton Synchrotron* (PS), which further increases their energy up to 25 GeV and finally they are fed into the *Super Proton Synchrotron* (SPS), increasing their energy up to 450 GeV.

Six detectors are located underground at six points of the LHC ring, as shown in Figure 3.2. Two of them, *ATLAS* [30] and *CMS* [31], are general purpose detectors that have been
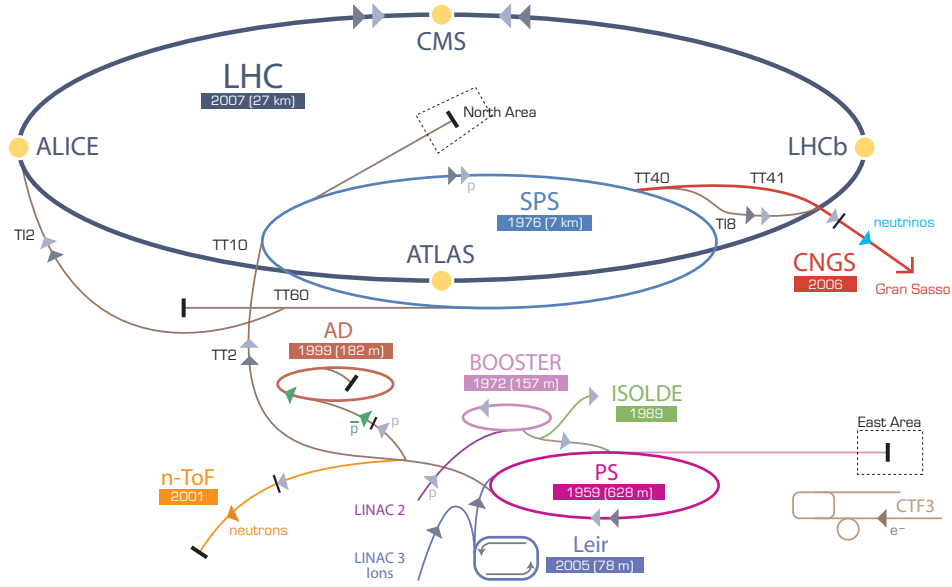
Figure 3.1: *The LHC accelerator complex.*

designed for a variety of physics studies. The *ALICE* [32] experiment is specialised to study the properties of quark–gluon plasma, that is believed to have existed in the early universe,whereas the *LHCb* [33] experiment is dedicated to studies of b-quark properties. Finally, in the very forward region, close to the beam axis, there are two smaller detectors *TOTEM* [34] and *LHCf* [35] that aim to study physics processes .

The tunnel that hosts the LHC is the same as the one used for the *Large Electron Positron* Collider (LEP). Electron-positron colliders are suitable for precision measurements and stringent tests of fundamental principles, Moreover, they cannot compete with the energies needed at the LHC, due to the electromagnetic radiation that is produced, when charged particles accelerate radially, as in the case of particle accelerators. This radiation is called *synchrotron radiation* (similar to the cyclotron radiation, which appears when the particles are moving in non-relativistic speeds). The energy loss per revolution is $P = 2(e^2 c \gamma^4)/(3 \cdot 4\pi\epsilon\rho^2)$, where $\gamma = E/m_0 c^2$ and ρ is the radius of the accelerator, meaning that the radiation loss increases proportionally to the fourth power of the beam energy and the electrons lose energy about 10^{13} times faster than the protons. Thus, synchrotron radiation is the main reason that all future accelerators are designed to be linear accelerators.

Hadron colliders offer several advantages over electron colliders, namely the ability to undertake simultaneous studies in a wide energy interval without needing precise tuning. This is because the centre of mass energy of the colliding partons is $\sqrt{s'} = \sqrt{abs}$, where a, b are the traverse momentum fractions carried by the colliding protons; which means (in cases of small fractions) that at $\sqrt{s} = 14\,\text{TeV}$, particles in the order of TeV can be produced. Moreover, hadron collisions are the only way to study parton-parton collisions, like gluon-gluon collisions. As shown in Figure 3.3, the cross-section of several processes rises quickly with $\sqrt{s}$. At the nominal LHC energies, cross-sections of new physics processes are expected to reach the wanted values. Moreover, the data analysis in hadron colliders is more complicated because multiple parton collisions can result in complicated final states (where many uninteresting processes happen most of the time) and the centre of mass frame of the colliding partons is not at rest at

the lab frame.
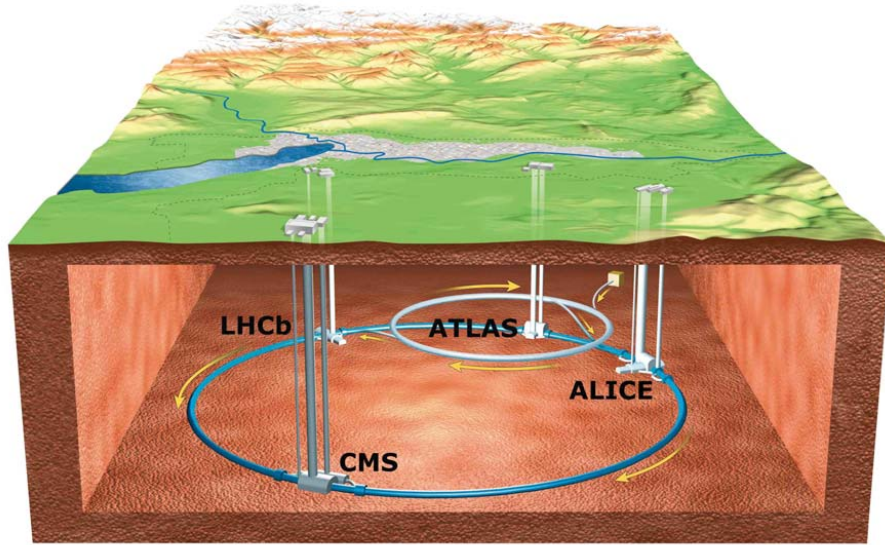
Figure 3.2: *The LHC ring and the position of its four big experiments.*

3.2 A Toroidal LHC Apparatus (ATLAS)

The ATLAS detector [30] is a general purpose detector designed for physics studies at the Large Hadron Collider. The ATLAS experiment, by reconstructing the interactions of the debris of the proton-proton collisions aims to exploit the full physics potential of the LHC and to answer some of the most fundamental questions in nature today [36].

3.2.1 Overview of the ATLAS Detector

A particle physics detector, like the ATLAS [30], has to be able to detect the particles that emerge from the proton-proton collisions as precisely and as efficiently as possible. It has to be able to make detections with high accuracy in a wide range of energies of the produced particles and to be as hermetically sealed as possible. The ATLAS detector is a cylindrical detector 44 m in length, 25 m in diameter and weighs 7000 tons (see Figure 3.6). The experimental apparatus can be divided into three main regions, a central region called *barrel* and two *end-cap* regions, one on each side. The very centre of the detector, where the two proton-beams of LHC collide, is called the Interaction Point (IP). Moving outward from the interaction point, the detector consists of a tracking system able to measure the directions and momenta of the charged particles. The calorimeter system measures the energies of the electrons, photons and hadrons. The muon spectrometer measures the momentum and position of the muons that have enough energy to reach it. Furthermore, a magnet system provides a magnetic field, allowing the tracker and the muon spectrometer to perform measurements of the momentum of charged particles. The performance challenges are summarized in table 3.1 and they are driven by the strict physics requirements. Such requirements include efficient reconstruction of charged particles and precise reconstruction of secondary vertices. Electromagnetic and hadronic calorimeters are

expected to provide accurate identification and measurements for the electrons, photons and the jets accordingly. Muon momentum resolution in a big range of muon momenta and low rate of misidentified muons is very important too. All sub-detectors are expected to offer almost full coverage in azimuthal angle and be as hermetic as possible.

Detector Component	Resolution
Tracker	$\sigma_{p_{\mathrm{T}}}/p_{\mathrm{T}} = 0.05\% p_{\mathrm{T}} \oplus 1\%$
Electromagnetic Calorimeter	$\sigma_E/E = 10\% E \oplus 0.7\%$
Hadronic Calorimeter (barrel, end-caps)	$\sigma_E/E = 50\% E \oplus 3\%$
Hadronic Calorimeter (forward)	$\sigma_E/E = 100\% E \oplus 10\%$
Muon Spectrometer	$\sigma_{p_{\mathrm{T}}}/p_{\mathrm{T}} = 10\%$ at $1\,\mathrm{TeV}$

**Table 3.1:** *The performance challenges of the various ATLAS detectors [37].*

3.2.2 Coordinate System

The ATLAS coordinate system is presented below. All quantities measured by the detector are based on this coordinate system.

- The interaction point is the origin of the coordinate system

- The z-axis is oriented along the beam axis, as shown in Figure 3.4.

- The x-axis points towards the centre of LHC

- The y-axis points upwards

- The xy plane is called the *transverse plane* and it is perpendicular to the beam direction

- The side A/C of the detector is the side with positive/negative z

- r is the radial distance to the beam axis

- ϕ is the azimuthal angle, as shown in Figure 3.5.

- θ is the polar angle, as shown in Figure 3.5.

- *rapidity* is defined as $y = \frac{1}{2}\ln\left(\frac{E+p_z}{E-p_z}\right)$, where E, p_z is the energy and the momentum along the $z-$axis of the particle accordingly. This is preferred over the polar angle θ because the particle production, as a function of rapidity, is approximately constant.

- In the limit that the particle is travelling, with the speed of light or the mass of the particle is nearly zero, the *pseudorapidity* is numerically close to the *rapidity* and is defined as $\eta = -\ln[\tan(\theta/2)]$, where θ is the polar angle. The η combined with ϕ are used to define a position in the detector.

- Distance ΔR in the $\eta\phi$ plane is defined as $\Delta R = \sqrt{(\Delta\eta)^2 + (\Delta\phi)^2}$, where η, ϕ are the pseudorapidity and the azimuthal angle accordingly.
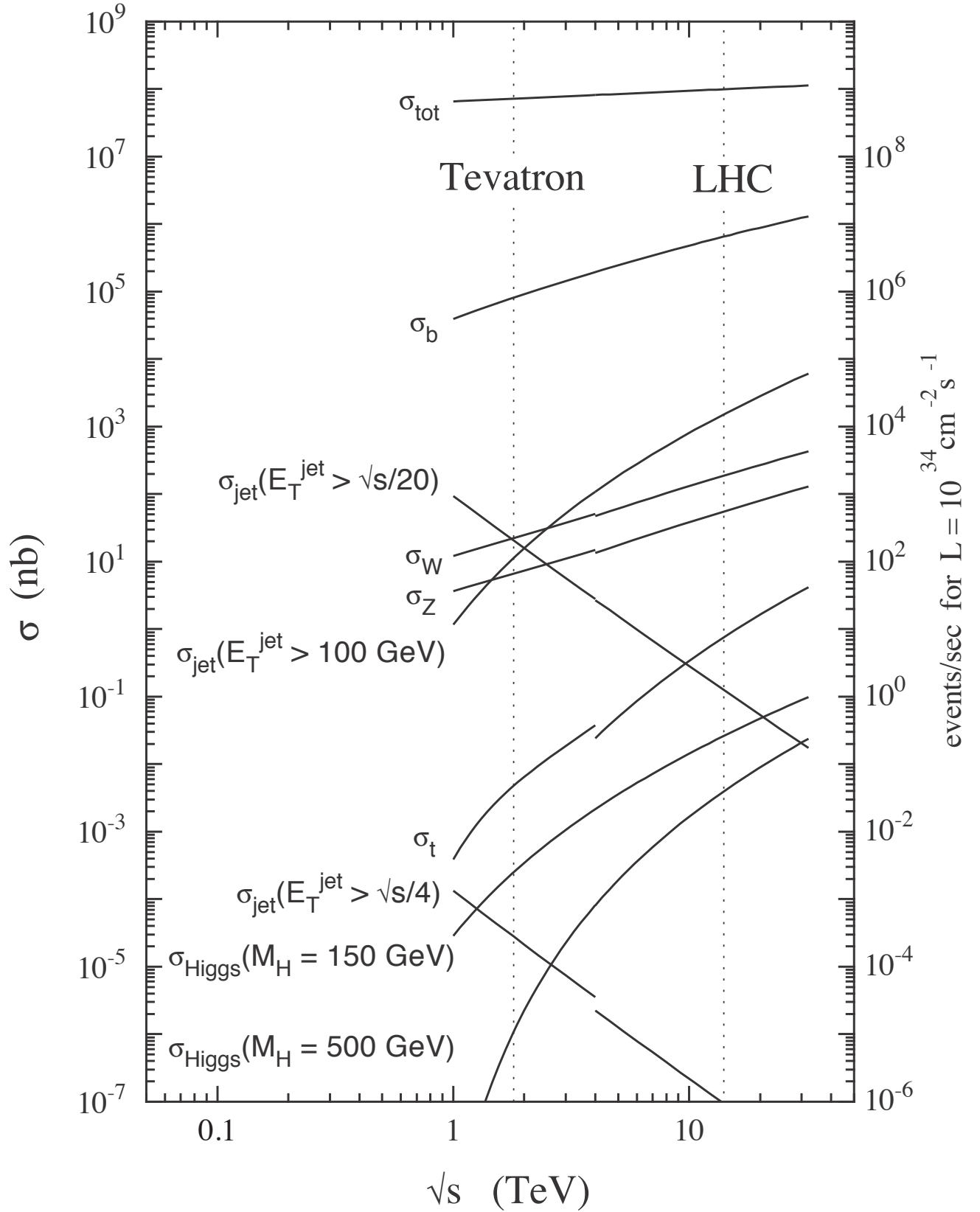
Figure 3.3: *The most important processes in proton (anti)-proton collisions as a function of centre of mass energy.*
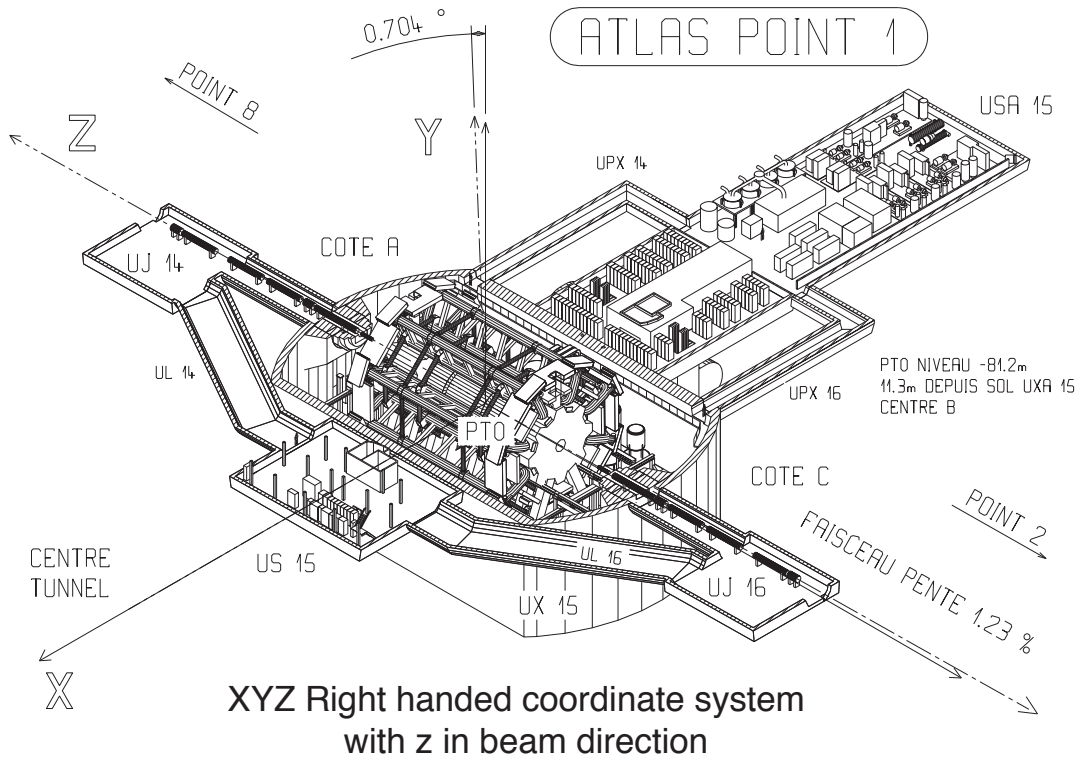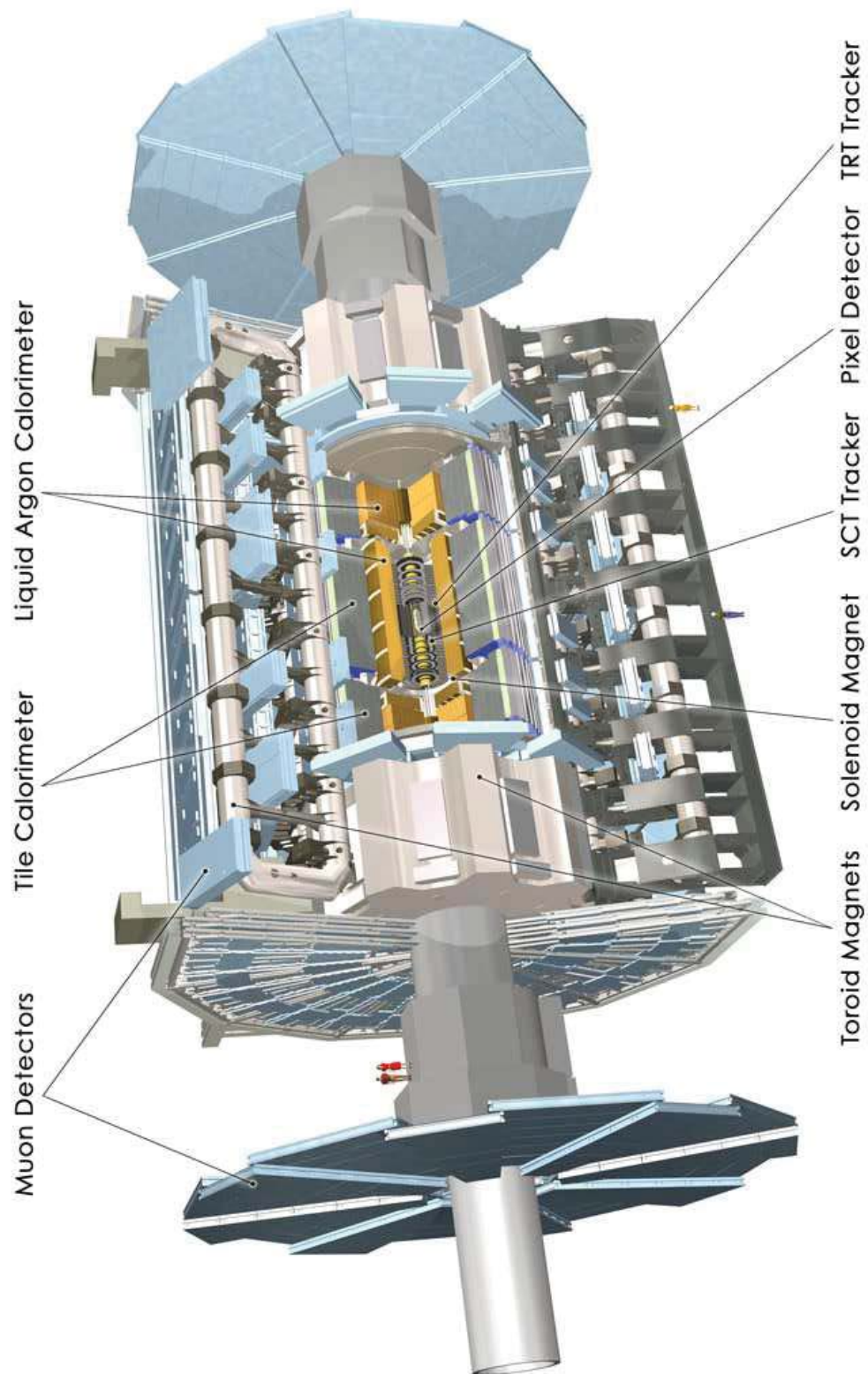
Figure 3.4: *The coordinate system of the ATLAS detector.*
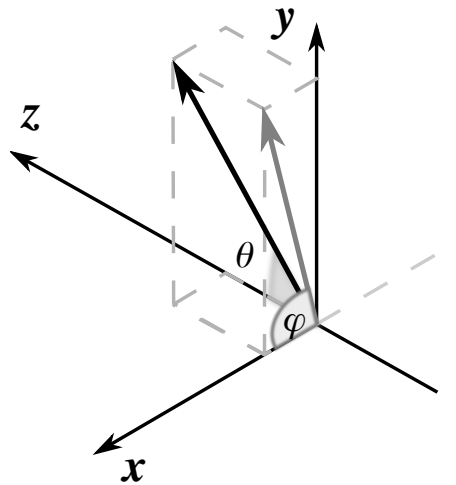
Figure 3.5: *The cartesian and spherical coordinate system of the ATLAS detector, showing the polar angle θ and the azimuthal angle φ.*

Figure 3.6: *A schematic view of the ATLAS detector with its main components.*

3.2.3   Inner Detector

The *Inner Detector* (ID) [38] lies in the innermost part of the ATLAS detector, which surrounds the beam line, as shown in Figure 3.7. The diameter of the ID is 2.1 m and its length is 6.2 m, providing an angular coverage up to $|\eta| < 2.5$. The ID is surrounded by a superconducting solenoid magnet that provides a magnetic field strength of 2 T in the centre of the detector and it is crucial for the momentum measurements and the charge identification. The Inner Detector systems are largely based on silicon micro-strip detectors and high-resolution semiconductor pixels at the smallest radii.

In design conditions, approximately every 25 ns, 1000 particles will emerge from the LHC collisions creating a high occupancy environment. The main challenges for the ID at such particle rates is the radiation tolerance, the control of ageing effects and the efficient pattern recognition in both ϕ and z-coordinates. Considering the different flux of particles at increasing radii, three technologies are composing the ID. Moving from the innermost region outwards, these are the *silicon pixel*, the *silicon micro-strip* and the *transition radiation tracker*.

The Pixel Detector   (PIX) [39] is the one closest to the interaction point. It consists of three concentric cylinders around the beam pipe with inner radii 5.1, 8.9 and 12.3 cm, respectively. In order to face the high particle densities in that region, the cell size of the pixel detector is $50 \times 400 \, \mu m^2$, segmented in $R\phi$ and z, which gives an occupancy of about 10^{-4} per pixel per bunch crossing. A charged particle that transverses the pixel detector creates electron-hole pairs that drift towards a readout electrode and, in the case the collected charge is larger than a specific threshold, the charge deposition is recorded. The resolution of the pixel technology is $10 \, \mu m$ in the $R\phi$ plane and $115 \, \mu m$ in the z-coordinate.

One of the most important parts for physics analysis (especially *B* Physics) of the Pixel Detector is the *B layer* —the barrel layer that is closest to the beam pipe. Particles that are produced promptly in the interaction point can be distinguished from short lived particles — like the *B* hadrons— by accurate reconstruction of the primary and secondary vertices, thus a suitable detector as close as possible to the interaction point is of utmost importance.

The Semiconducting Tracker   (SCT) [40] surrounds the PIX and consists of four barrel layers and nine disks in each end-cap. The cylinders cover an area of pseudorapidity $|\eta| < 1.1 - 1.4$ and radii 30-51 cm, while the end-caps cover an area of pseudorapidity range $1.1 - 1.4 < |\eta| < 2.5$ and radii extending to 56 cm. There are 8448 identical rectangular-shaped barrel sensors with size 64.0×63.6 mm and 80 mm strip pitch, all 285 mm thick, while in end-caps there are five slightly different sensor sizes so as to accommodate the more complex geometry. Each SCT module has an intrinsic accuracy of $17 \, \mu m$ in $R\phi$, $580 \, \mu m$ in z and is equipped with two silicon strip layers. The strips are placed at a small angle with respect to the z−axis (stereo angle of 40 mrad) in order to improve the position resolution along the z-axis.

The Transition Radiation Tracker   (TRT) is situated in the outermost region of the ID (beyond 56 cm). In addition to its tracking capabilities, the TRT provides particle identification (PID) [41] (e.g. electron identification is possible since emission of transition radiation is much more likely for an electron than for a pion). The tracker is composed of a barrel and two symmetrical end-cap configurations that consist of about 300,00 carbon-fiber straws of 1.5 m length, parallel to the beam axis. The straws are filled with a gas mixture of 70% Xe, 27% CO_2, 3% O_2 which is ionized when a charged particle traverses through and the resulting free electrons drift towards the wire where they are amplified and read out. The average number

of TRT hits per track is around 34, except for the low acceptance region between barrel and end-caps. It provides only $R\phi$ information, with a resolution of $130\,\mu m$, which is larger than that of the silicon trackers, but this is compensated by the large number of hits per track.
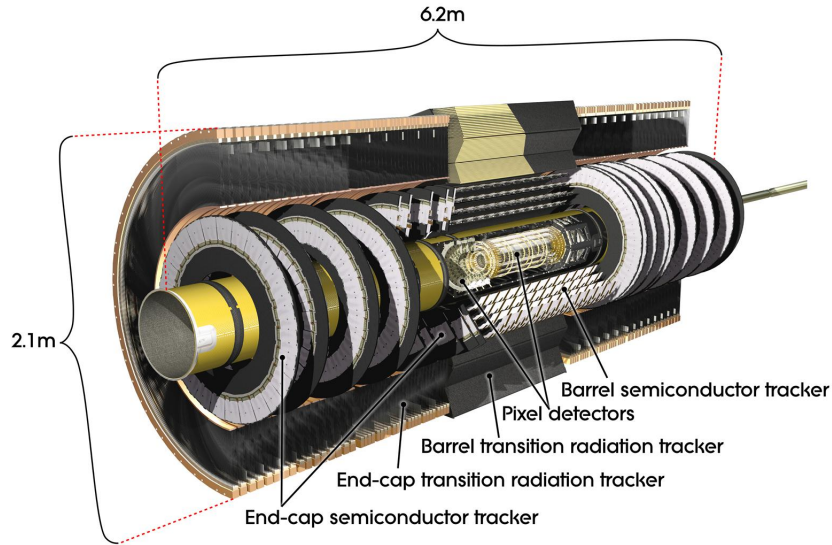
Figure 3.7: *The ATLAS inner detector. Note the pixel detector at the centre, the TRT at the exterior and the SCT barrel and end-caps in between.*
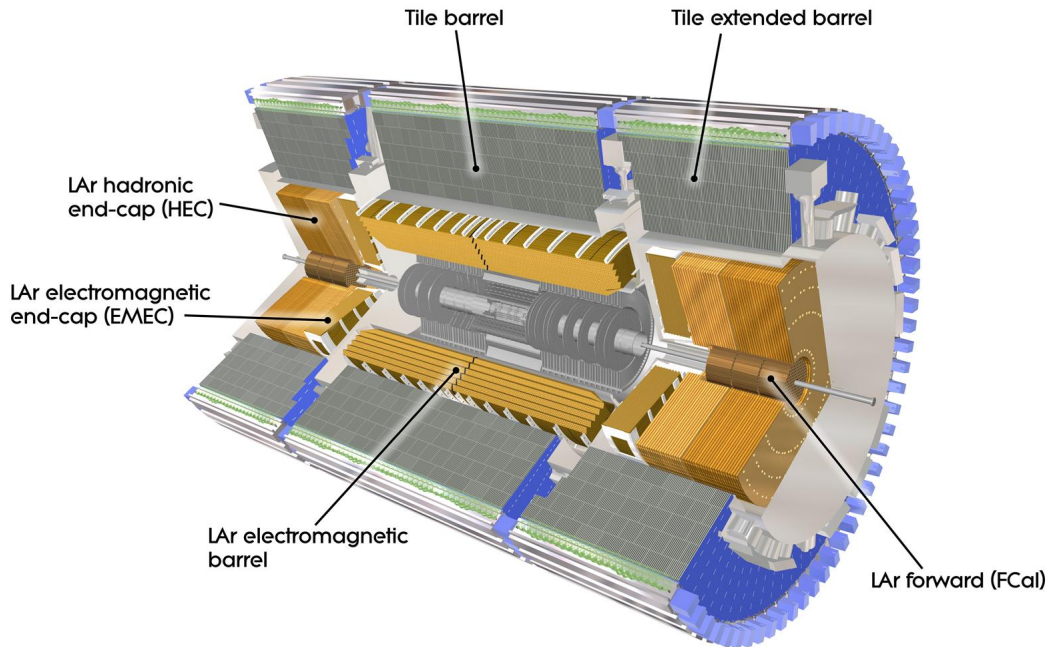
Figure 3.8: *The ATLAS calorimetry system.*

3.2.4   Calorimeters

The ATLAS calorimetry consists of an electromagnetic and a hadronic calorimeter (tile calorimeter) and it is located between the Inner Detector and the Muon Spectrometer, as shown in Figure 3.8. The task of the calorimeters is to measure the energy and the position of electrons and photons, the missing transverse momentum of the event, particle identification, the energy and direction of jets and to contribute to the event selection at the trigger level. The *electromagnetic calorimeter* covers the $|\eta| < 3.2$, the *hadronic barrel* and two extended barrel tile calorimeters cover the $|\eta| < 1.7$ while the *hadronic end-cap* calorimeters extend the calorimeter region over $|\eta| < 4.9$. Calorimeters will play a crucial role in discovering new physics (NP) in LHC, as they measure quantities that are potentially good NP signatures, such as the Higgs mass reconstruction in the $\gamma\gamma$ channel, or the observation of significant missing transverse energy originating from non-interacting supersymmetric particles. Often, the total thickness of a calorimeter is expressed in units of *radiation length* X_0. Radiation length represents the traverse distance in matter over which the electron energy drops by a factor of $1/e$ (due to bremsstrahlung and e^+e^- pair production). Therefore, if a material consists of a single type of nuclei, the radiation length X_0 can be approximated by the following expression:

$$X_0 = \frac{716.4A}{Z(Z+1)\ln(287/Z)}\,\mathrm{g\,cm^{-2}}$$

where Z is the atomic number and A the mass number of the nucleus.

The Electromagnetic Calorimeter (ECAL) is composed of a barrel and two end-caps and measures the energy of photons and electrons. The absorber material is Pb and the active material is liquid argon. The purpose of the Pb, is to cause particle showers, when these interact with liquid argon this cause electron ionisation thereby allowing the electrons to be collected in the electrode. The geometry of the calorimeter layers follows an accordion shape which allows for complete ϕ coverage and no azimuthal cracks. The total thickness of the ECAL is 22/26 X_0 (radiation length) in the barrel/end-cap.

The ECAL is composed of 3 parts with different granularity. The inner part has thickness of $5X_0$ and the segmentation is $\Delta\eta \times \Delta\phi = 0.03 \times 0.1$. The middle part is segmented in zones with $\Delta\eta \times \Delta\phi = 0.025 \times 0.025$ has the highest granularity and absorbs the majority of the particles of the event. The outer part is segmented with $\Delta\eta \times \Delta\phi = 0.05 \times 0.025$ and its thickness is 2-12 X_0. The trigger towers used in the trigger system are absorbed by grouping the high granular calorimeter cells. The overall energy resolution $\Delta E/E$ is

$$\frac{\Delta E}{E} = \frac{10\%}{\sqrt{E}} \oplus 0.5\%$$

The Hadronic Calorimeter (HCAL) is composed of a barrel and several end-cap parts and aims to measure the jet energy and direction. It is divided into two independent technologies, the *Tile Calorimeter* in the $|\eta| < 1.7$ region and the *Liquid Argon Calorimeter* in the $1.5 < |\eta| < 3.2$ region. The *Tile* Calorimeter uses plastic scintillator tiles as active material, which produce the input signals of the photomultipliers, while the absorber material is iron. It consists of three barrel parts, the central barrel ($|\eta| < 1$) and two extended barrels ($0.8 < |\eta| < 1.7$). The granularity is (0.1×0.1) for the central and the first extended barrel and 0.1×0.2 for the second outmost extended barrel.

The *liquid argon* hadronic end-cap calorimeter uses liquid argon as active material and copper as the absorber. Each end-cap part is composed of two wheels and each wheel is built

from 32 identical modules. The granularity of the end-cap is 0.2×0.2 and the energy resolution $\Delta E/E$ is

$$\frac{\Delta E}{E} = \frac{50\%}{\sqrt{E}} \oplus 3\%$$

The Forward Calorimeter (FCAL) covers the region $3.1 < |\eta| < 4.9$. Its thickness is 10 absorption lengths and it is segmented in three parts. The first part is made of copper and is optimised for electromagnetic calorimetry, while the other two parts are made by tungsten rods, designed to measure the energy coming from hadronic interactions. In the forward region the energy resolution $\Delta E/E$ is

$$\frac{\Delta E}{E} = \frac{100\%}{\sqrt{E}} \oplus 10\%$$

3.2.5 Muon Spectrometer

The muon spectrometer [42] provides triggering of high p_T muon events and detects muons with high resolution momentum on a broad p_T range. It consists of a barrel part that covers the area of $|\eta| < 1.05$ and two end-cap parts that cover the area $1.05 < |\eta| < 2.7$. In the barrel the chambers are placed in three concentric cylindrical layers (stations) in radius equal to 5 m, 7.5 m and 10 m with respect to the z-axis. In the end-caps, the chambers are arranged in four disks placed at a distance of 7 m, 10 m, 14 m and 21.5 m with respect to the interaction point (see Figure 3.9).

Muons in the p_T range 3 GeV/c to 1 TeV/c are measured with high efficiency and high resolution. In the case of low p_T muons the resolution deteriorates due to the multiple scattering effects and the fluctuations in the energy loss within the calorimeters whereas in the case of high p_T muons, the wire chamber resolution and the relative alignment of chambers, are the principal causes for the resolution to degrade (see Figure 3.12). There are two types of muon chambers, *Trigger* chambers (technologies of *Resistive Plate Chambers* and *Thin Gap Chambers*) and *Precision Tracking* chambers (*Monitored Drift tubes* and *Cathode Strip Chambers*).
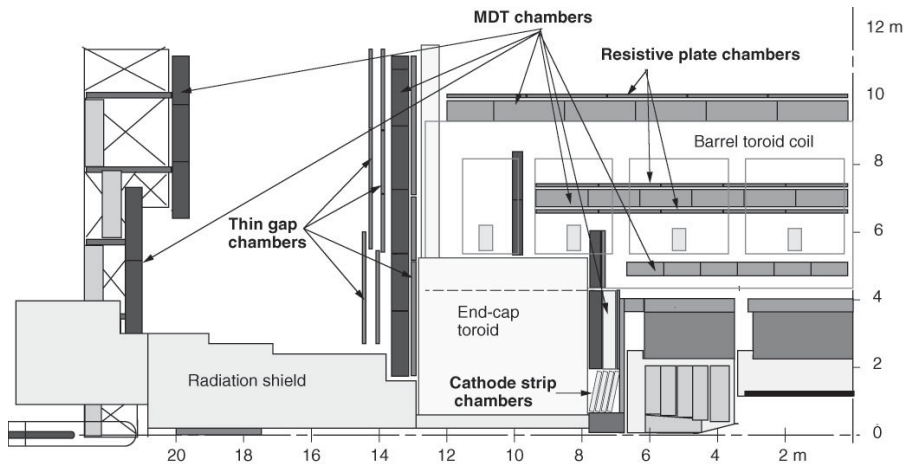

Figure 3.9: *Side-view of one quadrant of the ATLAS muon spectrometer.*

The Monitored Drift Tubes (MDTs) (see Figures 3.10, 3.11) are aluminium tubes of 3 cm diameter and of 0.9 m to 6.2 m length, filled with Ar:CO$_2$ (93% : 7%) operated at a pressure of 3 bar and a high voltage of 3080 V. The cathode is the tube itself, while the anode is a wire in the middle of the tube. When a muon passes through the tube, primary ionization electrons will drift to the positively charged electrode while positive ions, will move to the cathode. They tubes are oriented orthogonally with respect to the beam axis, allowing measurement of $r\eta$ coordinates. One MDT chamber is composed of two multi-layers of MDT tubes and each multilayer consists of three (middle/outer stations) or four (inner station) layers. The spatial resolution of a tube is ∼ 80 μm while the overall precision of the plane transverse to the anode wires is ∼ 40 μm. The basic detection element is a cylindrical aluminium drift tube of 30 mm diameter and a W-Re central wire of 50 μm diameter see Figure 3.10. The MDT detector system consists of 1,150 chambers containing a total of 354,000 drift tubes.
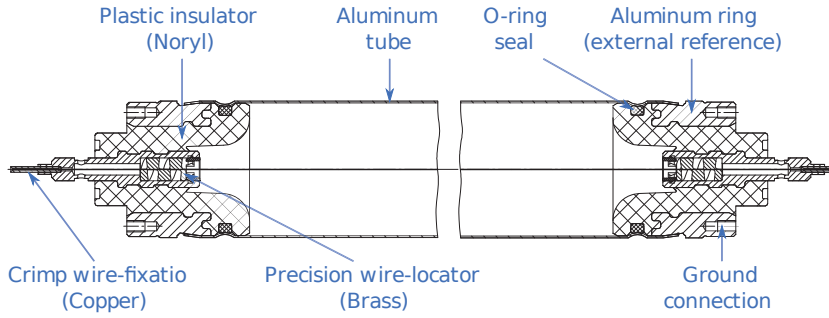
Figure 3.10: *A cylindrical aluminium drift, the basic detection element of MDD chambers*
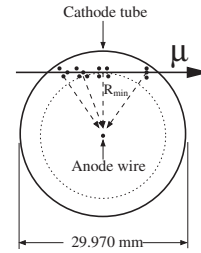
Figure 3.11: *Cross section of the tube.*

The Cathode Strip Chambers (CSCs) are muon-tracking chambers located in the high pseudorapidity region (2.0 < |η| < 2.7). The CSCs are multi-wire proportional chambers with an anode pitch of 2.54 mm and a cathode strip readout with a pitch of 5.4 mm. They use a gas mixture of Ar:CO$_2$, (80% : 20%). The precision measurement of the ϕ-coordinate is achieved by charge interpolation of the distributed charge measurement on the cathode strips with a resolution of 60 μm. The measurement of the η-coordinate comes from the readout of strips that are orthogonal to the cathode strips and its resolution is 5 mm.

The Resistive Plate Chambers (RPCs) are used for the muon trigger system in the barrel region. There are three layers of RPCs located between the eight coils of the superconducting barrel toroid magnet, consisting of two parallel highly resistive plates separated by 2 mm and enclosing a gas volume filled with an appropriate non flammable and low cost gas mixture, C$_2$H$_2$F$_4$: iC$_4$H$_1$O:SF$_6$, (94.7% : 5% : 0.3%). The external plate is covered with a thin graphite layer that allows uniform distribution of the high voltage along the plates. During nominal operation, a strong and uniform electric field of about 4.9 kV/mm is pervading the chambers volume, which permits a time resolution of 1.5nsec. A time resolution that good is achieved as all electron primary clusters from avalanches produce one signal simultaneously without drifting (line in MDTs). The readout strips have a typical width of 30 mm and are split in two orthogonal to each other plates measuring η and ϕ. The measurement of the ϕ-coordinate coming from the RPC has a resolution of 10 mm and is of significance importance a MDT chambers cannot measure this coordinate.

Thin Gap Chambers (TGCs) are used for the muon trigger system in the end-cap region. There are nine TGC layers, seven of which are located in the end-cap outside of the MDT middle station and the remaining two are located in front of the innermost tracking layer. TGCs are multi-wire proportional chambers with wire-to-wire pitch of 1.8 mm and wire-to-cathode pitch of 1.4 m. The two cathode graphite planes are equipped on the external surface with strips that are placed orthogonally with respect to the wires. The gas mixture, $CO_2 : n-C_5H_{12}$, (44% : 45%), is highly quenching and allows operation in quasi-saturate mode with a time resolution of 4 ns. The measurement of the ϕ-coordinate is carried out by the strips with a resolution at 3-7 mm, while the measurement of the r-coordinate is done with the wires and its resolution is 2-6 mm.

Muon Chambers			Resolution		
Type	**Function**	z	r	ϕ	**Time**
MDT	tracking	35 μm	-	-	-
CSC	tracking	-	40 μm	5 mm	7 ns
RPC	trigger	10 mm	-	10 mm	1.5 ns
TGC	trigger	-	$2 - 6$ mm	$3 - 7$ mm	4 ns

Table 3.2: *Summary of the resolution in z, r, ϕ and time (when applicable) of the different muon technologies.*
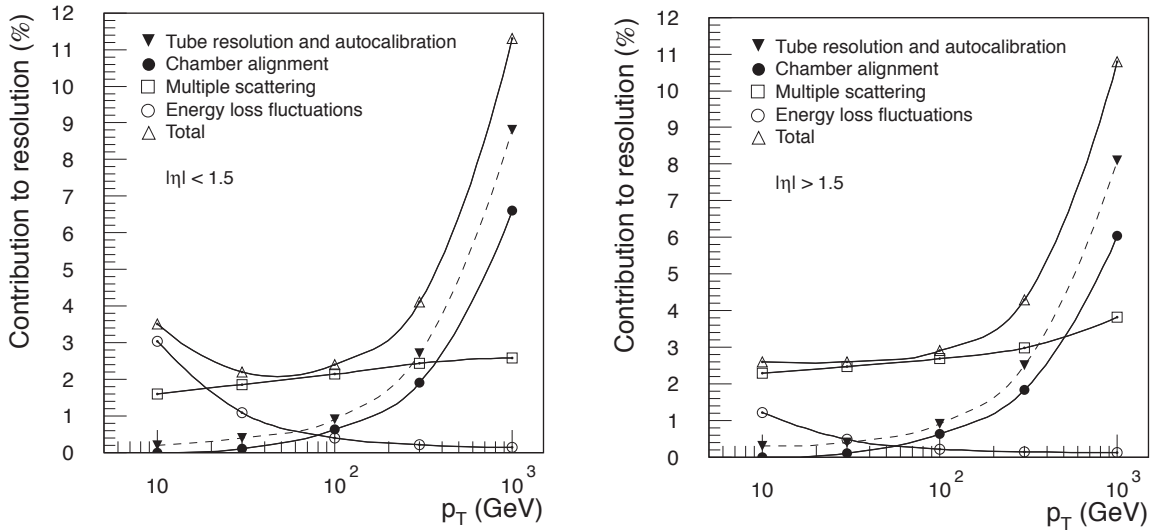
Figure 3.12: *Contributions to the $\Delta p_T/p_T$ as a function of p_T in barrel (left) and in end-cap (right), (adapted from [43]).*

3.2.6 Magnet System

The ATLAS experiment has a magnet system that provides the bending power needed for the momentum measurements. The system is composed of a central solenoid and three super-conductive air core toroid systems which assure minimum multiple scattering and provide good momentum resolution.

The central solenoid is located around the Inner Detector and provides a 2 T axial field in the tracker. It is 5.3 m long with a radius of 1.2 m and operates at 4.5° K. The coil together with its supporting structure and the material budget of the detector has to be minimised so that particle absorption is avoided.

The toroid systems consist of eight coils providing a non-uniform magnetic field up to 4 T in the Muon Spectrometer. A barrel toroid covers the barrel area and has 25.3 m length and 9.4/20.1 inner/outer diameter. The end-cap toroid is rotated by 22.5° with respect to the barrel toroid maximizing in this way the bending power in the barrel-end-cap boundary region (see Figure 3.13).

The magnet is operated at a nominal current of 20.4 kA and it is kept at 4.5° K temperature, by using liquid helium circulating around the coils.
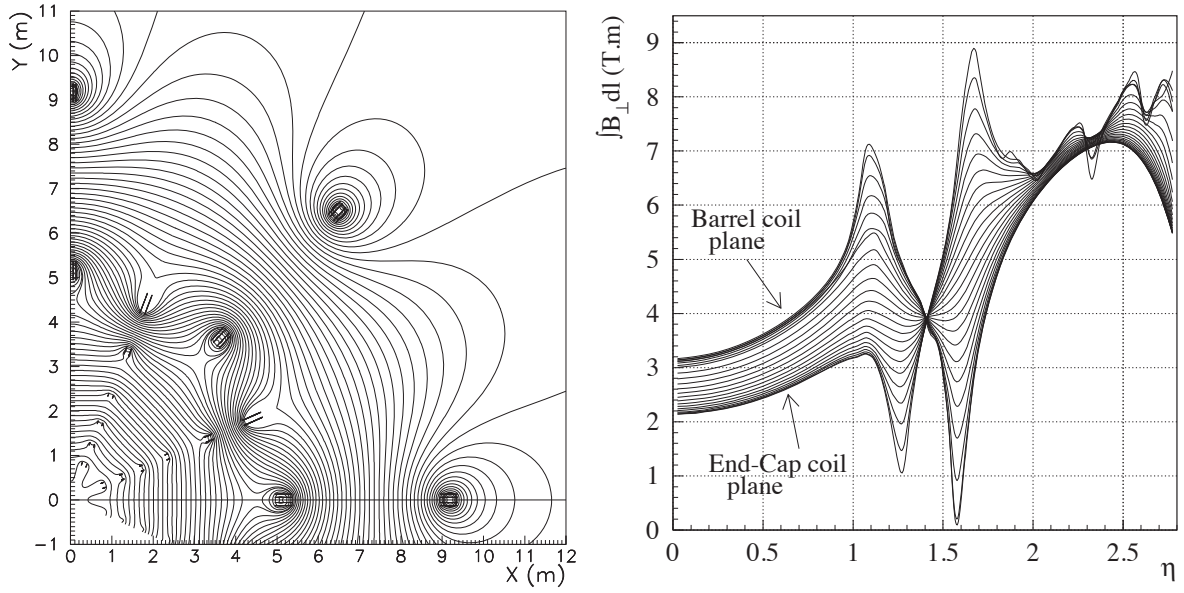
Figure 3.13: *The magnetic field lines in the transverse plane (left) and the bending power of the azimuthal component of the magnetic field as a function of pseudorapidity (right), (adapted from [44]).*
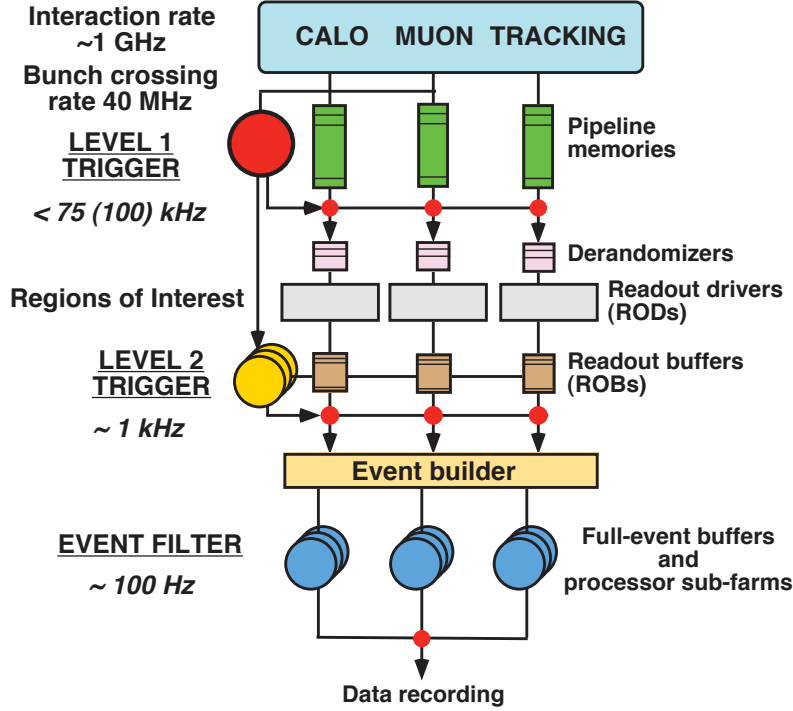
3.2.7 The ATLAS Trigger

At the current luminosity LHC produces 0.2 billion of proton-proton events per second. On the other hand, the processing power and the storage capabilities set a limit of ~ 100 selected events per second. This huge reduction factor in the rate (order of $\sim 10^7$) is achieved by the *trigger* system [45].

The ATLAS trigger system consists of three levels, as shown in Figure 3.14. The *level 1* trigger is a hardware level trigger, based on custom built processors and designed to make decisions within 2.5 μs.The information used comes from the calorimeters and/or the muon system and the selection is based in the presence of electrons, photons, tau leptons, jets, missing transverse energy and muons. The level 1 trigger has its *trigger menu* (a set of predefined level 1 triggers), which is containing information concerning the thresholds of trigger objects pre-scales [1] and

---

[1]the trigger pre-scale is a technique that ensures that the trigger system remains alive even at high

trigger object combinations to be used for the decisions. The regions of the detector where the trigger objects appear is called *Region of Interest* (RoI). As long as an event is triggered at level 1, the event data are stored in the front-end buffers and sent to the read-out drivers, where it is further processed from the higher level triggers.

Figure 3.14: *Architecture of the ATLAS trigger system with the numbers of event rates at the different trigger levels (adapted from [46]).*

The *level 2* trigger uses software algorithms that run in a large computing farm of several thousands commercial processors which are interlinked by a fast network. The level 2 trigger uses the level 1 RoIs and performs a partial reconstruction of the event. It also uses information of the inner detector by reconstructing tracks and vertices online with the full granularity of the readout. The full processor power is based on complex algorithms make decisions reducing the trigger rate to ~3.5 kHz. The data are sent from the readout servers to the event builders for further analysis.

The last in the trigger chain is the *event filter*. It uses the level 2 RoIs and the full detector granularity to process the entire event. The events of interest to the different physics analysis are separated to *event streams*. The level 2 and the event filter are known as *high-level* trigger.

Finally it is important to note that during data collection many conditions are not stable. In that, parts of the detector may go off (e.g. trip of a muon detector channel) or beam condition changes may occur. Therefore it is critical that the trigger system is flexible and sufficiently robust enough in order to manage such real-time changes.

---

luminosity running. If a specific trigger is prescaled e.g. at the value 2, that means that only one every two events that fire this trigger will be recorded.

B-triggers at ATLAS   At the LHC design energy, about 1% of collisions contain a $b\bar{b}$ pair. Besides, the ATLAS BPhysics program is quite broad, including studies of CP violation (e.g. $B_s^0 \to J/\psi K_s^0$, $B_s^0 \to J/\psi \phi$), rare decays ($B_{s,d}^0 \to \mu^+\mu^-(X)$), B_s^0 oscillations ($B_s^0 \to D_s^-\pi^+$) and various cross-section measurements.

On the other hand, the bandwidth of the recording of BPhysics events is limited, accounting only for $5-10\%$ of the total ATLAS trigger resources. Therefore, BPhysics triggers need to be efficient for BPhysics channels and also highly selective [47].

The core of the B-Trigger is the *level 1* muon trigger, which is based on a measurement of the muons' transverse momentum. The efficiency of the muon trigger plateaus at $\sim 85\%$, while the main background is due to real muons from π and K decays.

Single Muon Trigger   The *level 1* muon trigger selection is based on the detectors RPC (barrel) and TGC (end-cap) and requires a coincidence of hits in the different trigger stations within a predefined angular region [48]. If the candidate muon has energy between 4 to 10 GeV, it usually produces hits in the two inner muon stations and the triggers that are activated are *low-$p_{\rm T}$* triggers. In the other case that the muon is energetic enough (over 10 GeV), it produces hits in all three muon stations and *high-$p_{\rm T}$* triggers are activated. The *level 1* trigger provides for each muon candidate a region of interest (RoI) around its path.

The *level 2* muon selection uses the RoI of *level 1* as starting point and reconstructs the muon in the spectrometer, using information from the MDT chambers. The result is a new trigger object which is finally matched to the ID track information coming from pixels and SCT.

Finally the *Event Filter* studies the complete event data with a series of reconstruction and decision (hypothesis) algorithms and refines the *level 2* selection reducing the trigger by almost an order of magnitude.

Di-muon Triggers   The starting point is a *di-muon level 1* trigger which produces two RoIs. In each RoI the candidate muon is reconstructed by the *level 2* trigger separately. Finally, the two muons are combined and a mass cut is applied in their resonance. This trigger is known as *topological di-muon trigger*.

An alternative approach for the selection of di-muon events uses one muon RoI, as shown in Figure 3.15. Here the starting point is a single RoI in *level 1* and the search of a second muon is performed in a wider η and ϕ region. In this approach, the ID tracks are reconstructed and extrapolated to the muon spectrometer to tag muon tracks. Usually with this approach, low $p_{\rm T}$ J/ψs are reconstructed since the second muon is not explicitly required at *level 1*.
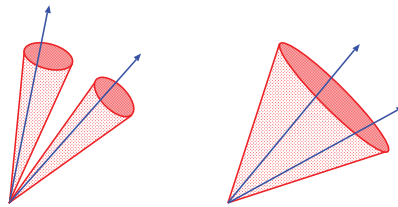
Figure 3.15: *The selection mechanism for the topological trigger (left) and the single RoI trigger (right) are shown schematically. In the analysis of χ_b the topological di-muon trigger EF_2mu4_Jpsimumu is used.*

3.2.8   Full Chain of Data Analysis

The production and analysis of the data in ATLAS is performed in a number of well defined steps. Initially, the raw data of the detector are produced in *bytestreams* which are then converted to object oriented in binary format data, known as Raw Data Objects (RDO). Next, the RDO are converted into high energy physics objects (muons, electrons, tracks) to a new format called Event Summary Data (ESD). Since ESDs contain all available information (including detector hits and reconstruction algorithms) their size per event is quite big for data analysis. For this reason ESDs are distilled to the Analysis Data Objects (AOD) which contain only the necessary information for data analysis maintaining a reasonable size per event. More details about the full ATLAS analysis chain can be found in [49].

3.2.9   Detector Alignment

The high accuracy in different measured parameters, motivated by the physics studies in ATLAS, require a highly sophisticated alignment system. In the inner detector the precision requirements of the silicon sensors alignment is below $10\,\mu m$ [50]. The alignment of the different tracking sub-systems is done at three levels of granularity, based on several alignment approaches. Firstly, the big structures (barrels, end–caps) are aligned. Secondly, the different layers of the barrels and the disks of the end–caps are aligned and finally the PIX and SCT sub–detectors are aligned module by module while the TRT sub–detector is aligned wire by wire. Furthermore, the accuracy of the muon momentum measurements requires an alignment of the muon spectrometer which chambers' position must be known to better than $50\,\mu m$. In order to achieve such precision, the muons spectrometer uses a combination of optical and track based alignment [51]. The alignment system of the muon spectrometer is divided in two main parts, barrel alignment and end–cap alignment. The barrel alignment system consists of two optical sensor types which capture an image of a target through a lens. The end–cap alignment system, follows the same technique but with a different arrangement of sensors because of its different geometry.

3.2.10   Data and the GRID

Since the design phase of LHC, it became clear that the amount of data produced at nominal operation could not be handled by the CERN on–site facilities and thus, a sophisticated infrastructure for distribution, processing and storage of data has to be implemented. This service, named *grid* [52], is now available and operational. The grid is distributed in different centres called *Tiers*. Tier–0 is an on–site CERN computer centre that keeps a primary backup and distributes the data further in Tier–1 centres around the world. Tier–1 centres keep a second copy of the data, support the grid and allow data access to physics analysis groups of the experiments. Tier–2 centres receive data from Tier–1 centres and they consist of one or more computing facilities. They are over 160 Tier–2 centres concentrate on simulation and end–user analysis. Finally, smaller computing centres called Tier–3 are integrated in the grid and provide access to grid facilities to individual scientists.

Part I

Bottomonium to Double Quarkonia

Chapter 4

Quarkonium the "Atom" of a Heavy Quark and a Heavy Antiquark

Quarkonium is a meson that is composed of a quark and an antiquark. Typical quarkonia are the bound state of the c quark and its antiquark, the ψ states (*charmonium*) and the b quark and its antiquark, the Y states (*bottomonium*), as described in Figure 4.1. Bound states composed by the heavier quark t and its antiquark cannot be actually seen, since the *"top"* decays by weak interactions before it can form a bound state. Finally, bound states composed of lighter quarks, u, d, s, are not quarkonia either, since their binding energy is comparable to their mass (expressed in energy units); so the physical states of such mesons, which we observe in the experiments, are just mixtures of light quark states.

4.1   Bound States and Fundamental Forces

For all fundamental interactions, the most convenient system for investigating the forces of nature is a bound system if two objects are attracting each other [53]. Gravitational force at astronomical distances holds objects together like the moon and the earth. In smaller ranges ($\sim 10^{-10}$ m), the electromagnetic force dominates and due to this force the electrons are bound to the nucleus. The bound system of an electron and a proton - the simplest atom, the hydrogen - is proved to be an essential testing ground of electromagnetic force. In even smaller distances ($\sim 10^{-15}$ m), strong interactions bind quarks into nucleons. In this case, a convenient context of investigating strong force was more difficult to be found. Contrary to the simplest atom, the simplest nucleon like the well known proton is a three body system that makes its study more complicated. Unfortunately the discovery of two body (quark - antiquark) systems like the light π mesons did not facilitate the study. In these systems the complication comes from the relativistic velocities of the quarks [54].

The first bound system which served as a test ground for the string force was discovered only in 1974 and it is the bound system of the heavy c quark and its antiquark (ψ states) [55]. This system can be studied as a non relativistic system. Only three years later, a heavier and even less relativistic system was discovered composed of the quark b and its antiquark (Y states). This is the system that is studied in this thesis.
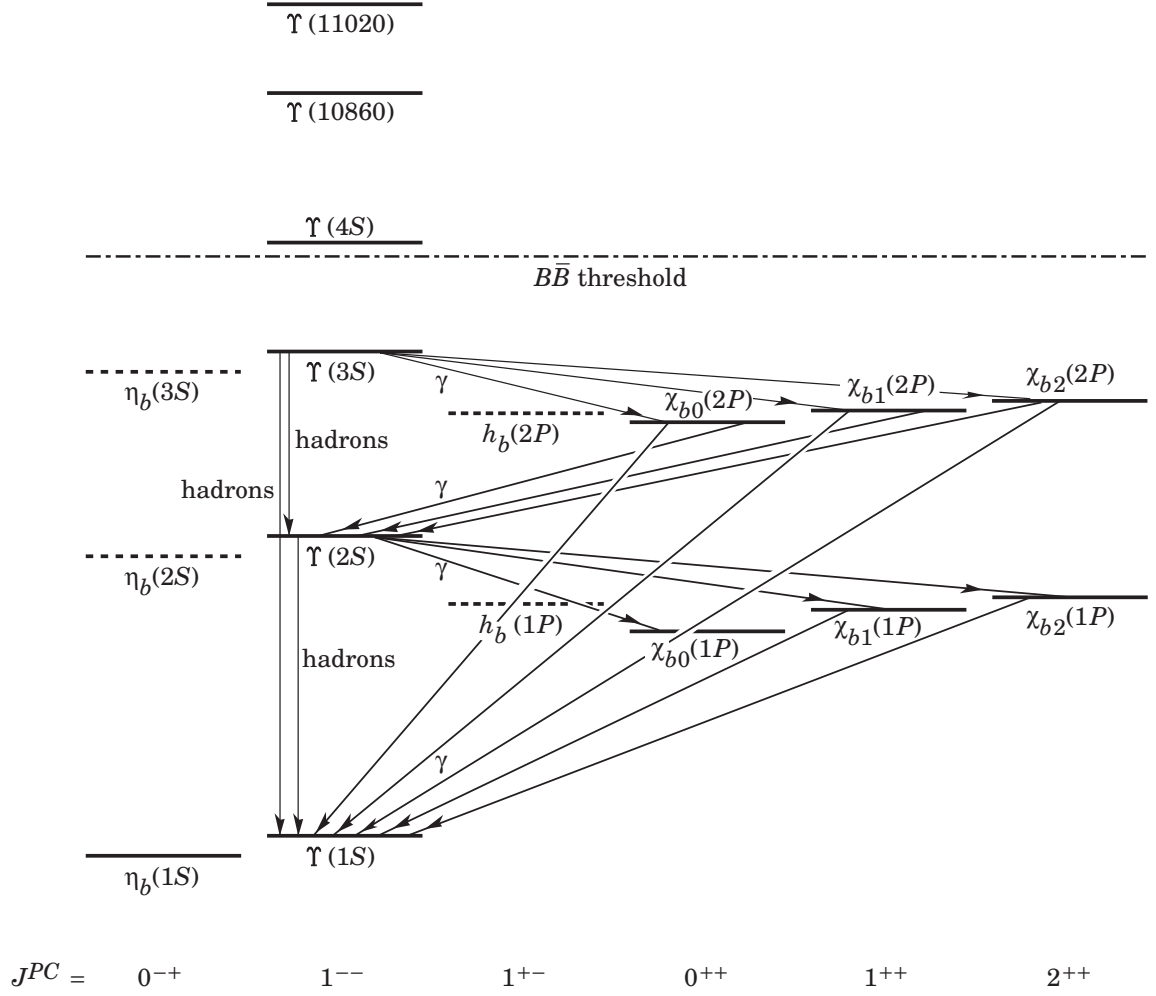
Figure 4.1: *The bottomonium system.*

4.2 The Bottomonium System

In order to understand the full structure of the bottomonium spectrum (the same apply to charmonium), one has to take into consideration the corrections induced by the spinning and the orbital motion of the quarkonium. By using the "kets" representation $|m\,s\rangle$ where s is the spin and m is the projection of the s in the z-axis, the quarkonium system is composed of the spin states $|m_1\,s_1\rangle$ and a $|m_2\,s_2\rangle$. The explicit decomposition into specific states of total spin momentum $|m\,s\rangle$ is derived by the formula:

$$|m_1\,s_1\rangle|m_2\,s_2\rangle = \sum_{m=|m_1-m_2|}^{(m_1+m_2)} C_{ss_1s_2}^{mm_1m_2}|m\,s\rangle$$

where $s = s_1 + s_2$ and $C_{ss_1s_2}^{mm_1m_2}$ are the *Clebsch-Gordan coefficients*.

By using the addition rule of momenta of quantum mechanics we get the possible values of $s = 0$ and $s = 1$ for the two spin-1/2 states. Taking this into consideration and consulting the
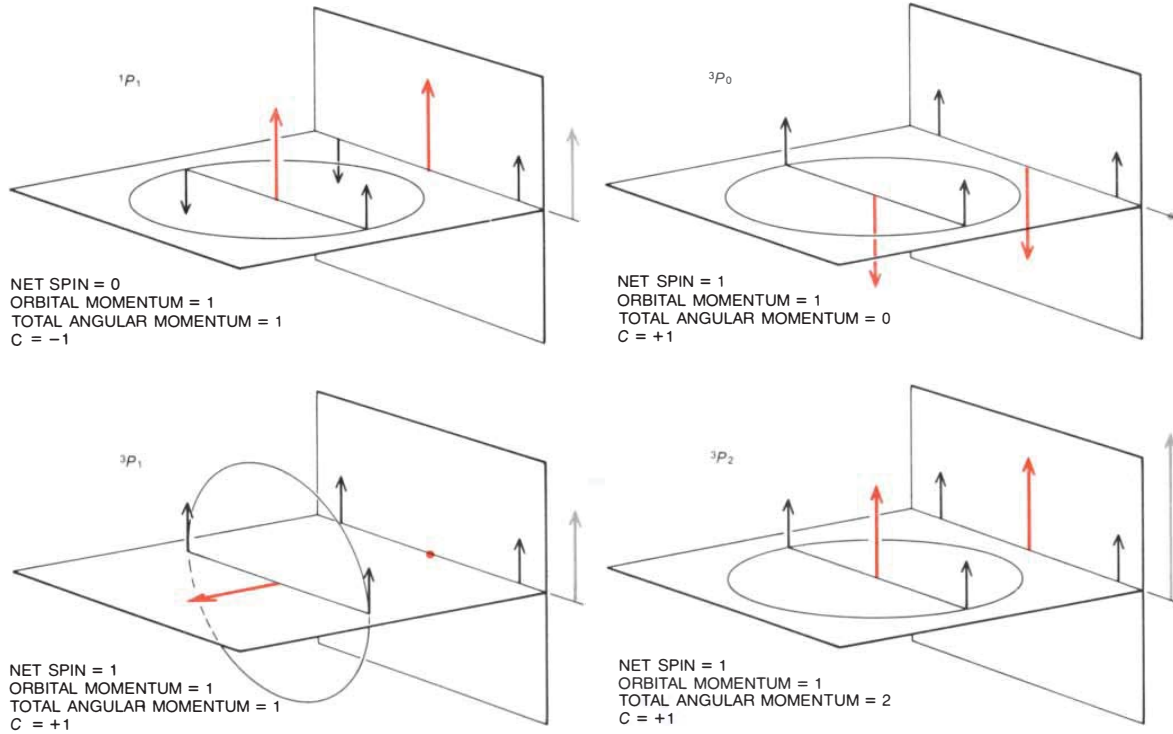
Figure 4.2: *The angular momentum of a bound system analysed by means of vectors projected onto a plane [53].*

Clebsch-Gordan $\frac{1}{2} \times \frac{1}{2}$ tables we find:

$$|\tfrac{1}{2}\ \tfrac{1}{2}\rangle|\tfrac{1}{2}\ \tfrac{1}{2}\rangle = |1\,1\rangle$$
$$|\tfrac{1}{2}\ \tfrac{1}{2}\rangle|\tfrac{1}{2}\ -\tfrac{1}{2}\rangle = \tfrac{1}{\sqrt{2}}|1\,0\rangle + \tfrac{1}{\sqrt{2}}|0\,0\rangle$$
$$|\tfrac{1}{2}\ -\tfrac{1}{2}\rangle|\tfrac{1}{2}\ \tfrac{1}{2}\rangle = \tfrac{1}{\sqrt{2}}|1\,0\rangle - \tfrac{1}{\sqrt{2}}|0\,0\rangle$$
$$|\tfrac{1}{2}\ -\tfrac{1}{2}\rangle|\tfrac{1}{2}\ -\tfrac{1}{2}\rangle = |1-1\rangle$$

If we group the three spin-1 states we get the triplet

$$|1\,1\rangle = |\tfrac{1}{2}\ \tfrac{1}{2}\rangle|\tfrac{1}{2}\ \tfrac{1}{2}\rangle$$
$$|1\,0\rangle = \tfrac{1}{\sqrt{2}}|\tfrac{1}{2}\ \tfrac{1}{2}\rangle|\tfrac{1}{2}\ -\tfrac{1}{2}\rangle + \tfrac{1}{\sqrt{2}}|\tfrac{1}{2}\ -\tfrac{1}{2}\rangle|\tfrac{1}{2}\ \tfrac{1}{2}\rangle$$
$$|1-1\rangle = |\tfrac{1}{2}\ -\tfrac{1}{2}\rangle|\tfrac{1}{2}\ -\tfrac{1}{2}\rangle$$

and the state that is left is the spin-0 state, the singlet

$$|0\,0\rangle = \tfrac{1}{\sqrt{2}}|\tfrac{1}{2}\ \tfrac{1}{2}\rangle|\tfrac{1}{2}\ -\tfrac{1}{2}\rangle - \tfrac{1}{\sqrt{2}}|\tfrac{1}{2}\ -\tfrac{1}{2}\rangle|\tfrac{1}{2}\ \tfrac{1}{2}\rangle$$

As we notice in a single state s=0 the spins are oppositely aligned. On the other hand, when $s = 1$ we obtain the triplet and the spins are aligned as much as they are allowed by their quantum nature.

The angular momentum of a bound system can be analysed by means of vectors projected onto a plane [53]. The spin of the quark is 1/2 and it is represented by the black arrows.

The orbital momentum is 1 ($l = 1$) and it is represented by the coloured arrows. The total angular momentum is composed of the projection of the net spin of the two quarks and the projection of the angular momentum in the plane, as illustrated in Figure 4.2. It should be clarified thought that in the schematics, the quark spin vectors are designed so to reproduce the net quark spin of the bound state and they are as parallel as it is allowed by their quantum mechanic nature[1]. From the same schematics we can derive the charge-conjugation number (C) by adding the absolute values of the projections of the net spin and the orbital angular momentum. Information concerning the different quantum states of the bottomonium system can be found in Table 4.1.

Notation of the States   The notation of the quarkonium states is borrowed from the notation of atomic spectra. Firstly it is noted the principal quantum number $n = 1, 2, 3 \ldots$, that describes the energy of the quantum state. Then it is noted the quantum number of the orbital angular momentum $l = 0, 1, 2, \ldots, n-1$. This quantum number is used to be noted by the letters S ($l = 0$), P ($l = 1$), D ($l = 2$), ... In the bottomonium system the lowest-energy state is the $1S$ which is the known Y. Except for the principal quantum number and the orbital quantum number, the quarkonium notation includes information of the net spin of the quarks and the total angular momentum. An upper script in the principal quantum number declares the net spin of the two muons ($2s + 1$, where s is the net spin of quarks). A subscript in the quantum number of the orbital angular momentum declares the total angular momentum J. The final symbolism of a quantum quarkonium state is $n^{2s+1}l_J$. The charge conjugation, C, the operator that converts each particle to its antiparticle is exactly conserved in this framework and its value is given by $C = (-1)^{L+S}$. Finally the parity P operation that flips the sign of the spatial coordinates, is also conserved and its value is given by $P = (-1)^{L+1}$.

4.2.1   A Non-Relativistic System

Heavy quark bound states like the bottomonium are non-relativistic systems. This happens because their binding energy is small compared to their mass. The total energy of the bottomonium state is composed of the rest energies of the b quark and the $\bar{b}$ antiquark, the kinetic energy of the quarks and their potential energy

$$E_{\text{total}} = (E_{\text{rest}}^b + E_{\text{rest}}^{\bar{b}}) + (K^b + K^{\bar{b}}) + Y(b\bar{b})$$

From the *Virial Theorem* it is known that for a stable system the mean kinetic and potential energy satisfy the relation $\langle T \rangle = -\frac{1}{2}\langle U \rangle$. This is a general theorem that covers phenomena from astronomy to the theory of gasses. In our case, by taking this theorem into consideration, we expect that the binding and the kinetic energy of the system should be comparable in size. Therefore it remains only to compare the rest energy of the b quarks with the potential energy of the system in order to understand whether the system is relativistic or not. The mass of the b quark is ~ 4.67 GeV/c^2, while the $q\bar{q}$ binding energy are of the order of few hundred MeV. This is a quite good evidence that the bottomonium system is non relativistic.

---

[1]When a momentum vector l has specified projection l_z = max = l in the z-axis, the other two components l_x and l_y do not have specified value, so we cannot say that the vector l is completely aligned with the z-axis.

Meson	Mass(MeV/c^2)	Width(keV/c^2)	spectroscopic notation	J^{PC}
η_b	9388.0 ± 2.7	-	1^1S_0	0^{-+}
$Y(1S)$	9460.3 ± 0.26	54.02 ± 1.25	1^3S_1	1^{--}
$\chi_{b0}(1P)$	$9859.44 \pm 0.242 \pm 0.41$	-	1^3P_0	0^{++}
$\chi_{b1}(1P)$	$9892.78 \pm 0.26 \pm 0.31$	-	1^3P_1	1^{++}
$\chi_{b1}(1P)$	$9912.21 \pm 0.26 \pm 0.31$	-	1^3P_2	2^{++}
$Y(2S)$	10023.26 ± 0.31	31.98 ± 2.63	2^3S_1	1^{--}
$\chi_{b0}(2P)$	$10232.5 \pm 0.4 \pm 0.5$	-	2^3P_0	0^{++}
$\chi_{b1}(2P)$	$10255.46 \pm 0.22 \pm 0.5$	-	2^3P_1	1^{++}
$\chi_{b1}(2P)$	$10268.65 \pm 0.22 \pm 0.5$	-	2^3P_2	2^{++}
$Y(3S)$	10355.2 ± 0.5	20.32 ± 1.85	3^3S_1	1^{--}

Table 4.1: *Table with information of bottomonium system. The state 1^3S_1 corresponds to Y which is the lowest energy state n = 1, its net spin =1 ($2s+1$ = 3), its orbital angular momentum is 0 (the bound state is a sphere that oscillates radially with the same width and phase) and its total angular momentum is 1. The state 2^3P_0 is the χ_{b0} particle which will be the bottomonium state to be studied from ATLAS LHC data in this thesis. As we can see, its principal quantum number is 2 (not the lowest energy state), its net spin =1, the orbital angular momentum of the system is 1 (this is the reason that χ_{b0} belongs to a triplet) and the total angular momentum J = 0.*

4.2.2 Potential Model

The observed spectrum energy levels of a quarkonium system show remarkable resemblance with the ones of positronium which is a compelling evidence that the quarkonium system is the states of a bound quark-antiquark pair. This can be understood in terms of a non relativistic treatment [56]. The phenomenological way to describe the quarkonium system is to solve the relativistic Schrödinger equation with the corresponding $q\bar{q}$ potential.

The quarks are bound by the strong force. Unlike systems like the positronium, where the force in action is the electromagnetic force and the energy levels can be calculated with great precision, in quarkonium systems the strong force is not only stronger than the electromagnetic force but also more complex. As we know from electromagnetism, a bound state is described completely when we know the energy and the angular momentum. Unfortunately, the exact form of the potential between two quarks is unknown and neither is known the strong analogue to magnetism that could be used to obtain the spin couplings [?].

Since we do not know what is the potential in work, we can start making some estimated guesses. Like quantum electrodynamics (QED) where the dominant interaction is mediated by the exchange of a photon, in quantum chromodynamics (QCD) the dominant interaction is dominated by the exchange of a gluon. Therefore in the case of short distances, we expect a coulomb like potential, something that has been experimentally proven in measurements of 2-jet cross sections in hadron colliders [57]. In the case where the quarks are apart, we do not

understand what is the form of the potential is, but if we take into consideration that no particle with color charge has ever been seen in isolation (*quark confinement*), we must expect that it should increase in some form without limit. In the literature, one can meet different choices of the dependence of distance of this second term of the potential, which can be logarithmic, linear or a harmonic oscillator potential.

A choice of the potential of the quarkonium model will finally look like:

$$V(r) = -\frac{A}{r} + Br$$

The "coulomb plus linear" potential is known as Cornell potential, initially developed by Cornell group in order to reproduce the charmonium spectrum [58]. For this potential, the Schrödinger equation cannot be solved analytically and the constants A, B are usually determined by solving the Schrödinger equation numerically and then fitting the data.

The method described above, leads to a purely phenomenological potential. Another way to derive the potential is to use perturbative QCD for the short range part while keeping the phenomenological long range part so that confinement is satisfied. This potential has the form has the form (see chapter 8 in [?])

$$V_r = -\frac{4}{3}\frac{a_s}{r} + Br$$

As we notice the "Coulomb plus linear" potential is spin independent which means that is not sufficient to reproduce the quarkonium spectrum in detail. In order to describe fine structure, we have to take into consideration the *spin-spin* interactions, *spin-orbit* interactions and *tensor terms*.

One has to introduce the total spin $S = s_1 + s_2$, the total angular momentum $L = r \times p$ and the tensor operator

$$S_{12} = 12\left[\frac{(s_1 \cdot r)(s_2 \cdot r)}{r^2} - \frac{1}{3}(s_1 \cdot s_2)\right]$$

Spin - spin coefficient

$$S^2 = S(S+1) = (s_1 + s_2)^2 = s_1(s_1+1) + s_2(s_2+1) + 2s_1 \cdot s_2$$

$$\Rightarrow s_1 \cdot s_2 = \frac{1}{2}[S^2 - s_1(s_1+1) - s_2(s_2+1)]$$

$$\overset{s_1=s_2=\frac{1}{2}}{\Rightarrow} s_2 \cdot s_2 = -\frac{3}{4} \quad \text{for } S = 0 \text{ (singlet)}$$

$$s_1 \cdot s_2 = +\frac{1}{4} \quad \text{for } S = 1 \text{ (triplet)}$$

Spin - orbit coefficient

$$J^2 = j(j+1) = (L+S)^2 = L^2 + S^2 + 2(L \cdot S) = l(l+1) + s(s+1) + 2(L \cdot S)$$

$$\Rightarrow L \cdot S = \frac{1}{2}[j(j+1) - l(l+1) - s(s+1)]$$

Tensor coefficient

Using $s_1 \cdot s_2 = \frac{1}{2}S^2 - \frac{3}{4}$, for the tensor coefficient we get:

$$S_{12} = \frac{4}{(2l-1)(2l+3)}\left[S^2L^2 - \frac{3}{2}L \cdot S - 3(L \cdot S)^2\right]$$

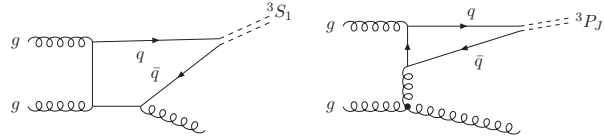Finally the spin dependent interactions can be added and form the spin-potential term:

$$V_{\text{spin}}(r) = V_{LS}(r)(\boldsymbol{L} \cdot \boldsymbol{S}) + V_T(r)\left[S(S+1) - \frac{3(\boldsymbol{S}\cdot\boldsymbol{r})(\boldsymbol{S}\cdot\boldsymbol{r})}{r^2}\right] + V_{SS}(r)\left[S(S+1) - \frac{3}{2}\right]$$

4.3 Quarkonium Production Mechanisms

According to the QCD factorisation theorem [59] the production of quarkonia is believed to be separated in two parts. The first part deals with the production of the $q\bar{q}$ pair where the distance scale of the pair creation is much smaller than the physical size of the meson and it is subject of perturbative QCD calculations. The second non perturbative part deals with the interactions of the long lived quark pair with the medium before the final formation of the QCD bound states. Although the first models were developed in the seventies, the experimental data and the theoretical predictions still show disagreements in some areas, proving that the production mechanisms of quarkonia are still only partially understood.

4.3.1 Singlet Model

This is the first and most natural model to describe quarkonia production. According to this model, the quark pair that produces the quarkonium physical state has the same quantum numbers as the physical (color singlet) state itself. [60–62]. The model name *color singlet model (CSM)* takes the name of the color singlet state. The corresponding Feynman diagrams of this model are shown in Figure 4.3. This model works well in low energy experiments, in J/ψ production in deep

Figure 4.3: *Leading order singlet n^3S_1 (left), leading order triplet n^3P_J (left).*

inelastic scattering and e^+e^- annihilation. First discrepancy with experimental data came from the Tevatron - CDF data where the ψ' cross section was measured to be more than one order of magnitude higher than the theoretical calculations [63].

4.3.2 Colour Evaporation Model

The color evaporation model [64] (CEM) appeared a little bit after the CSM. According to this model, any $q\bar{q}$ pair without being compulsory produced in a color singlet state, can end up in a physical quarkonium meson via soft interactions with the colour field. In many cases CEM gives reasonable agreement with data, including CDF data, but still there are results that the theory-experiment discrepancy is big. An example of failure of the model is the prediction of the ratio of the triplet J=0,1,2 χ states [65].

4.3.3 Colour Octet Model

The concept of *colour octet model (COM)* developed in the nineties [66] is similar to the one of CEM. The $q\bar{q}$ pairs produced in the hard process do not have to be in a colour singlet state but they can end up to a physical meson through radiation of soft gluons.

The COM is based on the fact that the heavy quark system is a non relativistic system and it is developed in the framework of the Non-Relativistic QCD (NRQCD). The Feynman diagrams describing the colour of the COM and its difference with the CSM is displayed in Figure 4.4. A big difference between the COM and the CEM is the pre-

Figure 4.4: *Difference between the CSM model (left) and the NRQCD COM (right) [67].*

dictions concerning quarkonia polarisation[2]. In CEM, as the radiation of the quark pair during soft interactions are uncontrolled, the net polarization of the quarkonia cannot be predicted. On the other hand, in COM through the NRQCD model, we can systematically calculate the polarization, which serve as a good test bed of the validity of the theory [68]. Unfortunately in some cases the model shows a discrepancy with the experimental data of CDF [69].

4.4 Bottomonium into Double Charmonium

Since the mass of the bottomonium is much heavier than the mass of the charmonium, the bottomonium can decay into not only light hadrons but also charmonium states. Such decays can contribute to studies of the dynamics of hard exclusive processes and the structure of the charmonium mesons.

4.4.1 Discrepancies in Double Charmonium Production

Prompt charmonium observation via double $c\bar{c}$ production in e^+e^- offers a very good opportunity to study perturbative and non perturbative effects in QCD. Cross section measurements $e^+e^- \to J/\psi\, c\bar{c}$ in Belle and BaBar collaborations revealed big discrepancies between theory and experimental results [**?**, 70, 71].

In 2002, the Belle collaboration performed studies of prompt J/ψ production via double $c\bar{c}$ production in e^+e^- continuum. In this process the one $c\bar{c}$ pair fragments into J/ψ meson while the other $c\bar{c}$ pair fragments into a charmonium or a charmed meson. According to contemporary theoretical calculations, we expect that $\sigma[e^+e^- \to J/\psi\, c\bar{c}] \sim 0.07$ pb [72–74], see Figures 4.5, 4.6. The cross section measured by Belle collaboration was an order of magnitude larger indicating that other contributions to the cross section were missing in the theory. In the same round of analysis of the double charmonium production, Belle measured:

$$\sigma[e^+e^- \to J/\psi\,\eta c] \times B(\eta_c \to\geq 4\ \text{charge}) = 0.0033^{+0.07}_{-0.06} \pm 0.009\,\text{pb},$$

$$\sigma[e^+e^- \to J/\psi\, D^*X] = 0.53^{+0.19}_{-0.15} \pm 0.14\,\text{pb},$$

$$\sigma[e^+e^- \to J/\psi\, c\bar{c}]/\sigma[e^+e^- \to J/\psi\, X] = 0.59^{+0.15}_{-0.13} \pm 0.14$$

---

[2]The spin alignment of the parent vector quarkonium state can be determined by measuring the polarisation parameter α in the distribution. $\mathrm{d}N/\mathrm{d}cos\theta^* = C\frac{3}{2\alpha+6}(1 + \alpha\cos^2\theta^*)$. The variable θ^* is defined by the direction of the positive muon in the positive quarkonium decay frame and the quarkonium momentum direction in the laboratory frame ($-1 < \theta^* < 1$). The factor $\frac{3}{2\alpha+6}$ is used to normalise the distribution to unit. The parameter α is defined as $\alpha = \frac{\sigma_T-2\sigma_L}{\sigma_T+2\sigma_L}$ where the σ_T and σ_L are the transversely and longitudinally polarised quarkonia respectively. If the quarkonium state is unpolarised, the variable $\alpha = 0$.
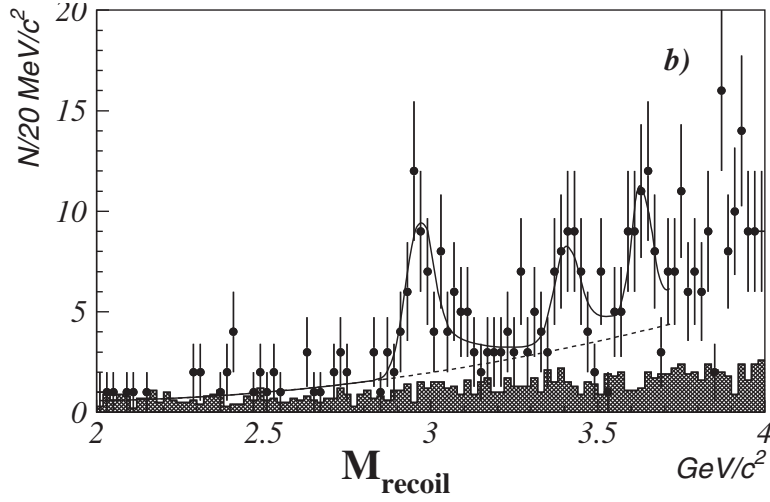
Figure 4.5: *Belle measurement. The distribution of the measured recoil mass ($M_{recoil} = [(\sqrt{s} - E_{J/\psi}^{*2}) - P_{J/\psi}^{*2}]^{1/2}$). The peak around 3.0 GeV/c^2 is the evidence for the process $e^+e^- \to J/\psi\eta_c$ while additional peaks of the χ_{c0}, $\eta_c(2S)$ are visible.*

(Since the η_c branching fractions are poorly known, the η_c decay products are expressed in terms of charged particles.)

Three years later, in 2005, BaBar collaboration publishes similar measurements of double charmonium production in e^+e^- annihilation. The main result obtained are:

$$\sigma[e^+e^- \to J/\psi \, c\bar{c}] \times B(\eta_c \to \geq 2\,\text{charge}) = 17.6 \pm 2.8^{+1.5}_{-2.1}\,\text{fb}$$

$$\sigma[e^+e^- \to J/\psi \, \eta_c(1s)] = 10.3 \pm 2.5^{+1.4}_{-1.8} \pm 0.009\,\text{pb},$$

The results (see Table 4.2) of these two experiments are inconsistent with the current theoretical expectation, which proved to be one of the largest disagreements in the Standard Model for the process of electron–positron annihilation to double charmonium (e.g. $e^+e^- \to J/\psi \, \eta_c$).

$J/\psi \, c\bar{c}$	η_c	χ_{c0}	$\eta(2D)$
BaBar	$17.6 \pm 2.8^{+1.5}_{-2.1}$	$10.3 \pm 2.5^{1.4}_{1.8}$	$16.4 \pm 3.7^{2.4}_{-3}$
Belle	$25.6 \pm 2.8 \pm 3.4$	$6.4 \pm 1.7 \pm 1.0$	$16.5 \pm 3.0 \pm 2.4$
NRQCD [?]	2.31 ± 1.09	2.28 ± 1.03	$0.960.45$
NRQCD [?]	5.5	6.9	3.7

Table 4.2: *Experimental results of BaBar and Belle collaboration against theoretical predictions of NRQCD [?, ?] This striking difference between theory-experiment was a puzzling problem for few years of the standard model in double charmonium production.*

For a number of years, the theoreticians were puzzled by the double charmonium processes that were produced in B factories, like $e^+e^- \to J/\psi \, \eta_c$. In trying to resolve this discrepancy, studies that took into consideration the next to leading order (NLO) QCD showed that the $O(a_s)$ corrections reduce the discrepancy between theory-experiment. Parallel to the NLO corrections, a number of other studies [75–79] took into consideration the relativistic corrections and the discrepancy became even smaller. It is claimed [80] that combining the two corrections mentioned
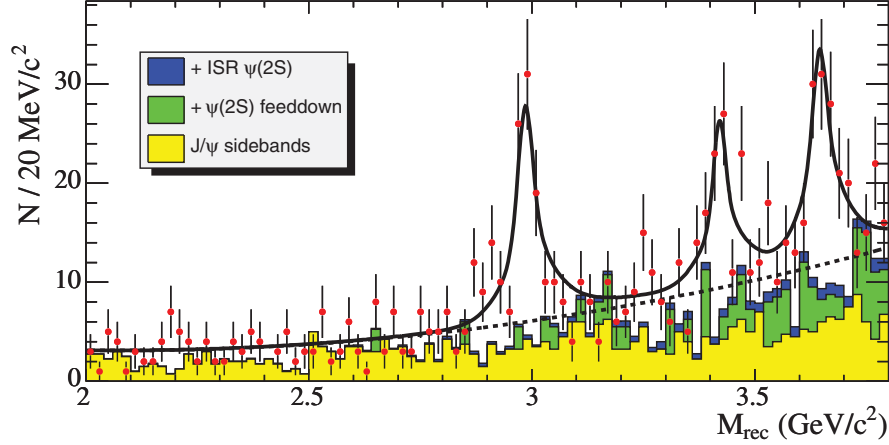
Figure 4.6: BABAR *measurement. The recoil mass distribution (solid curve), of $\eta_c(1S)$ around 3 GeV/c^2 while the χ_{c0} and $\eta_c(2S)$ are visible in the fit.*

above the theoretical-experimental discrepancy is resolved for the exclusive $e^+e^- \rightarrow J/\psi\,\eta_c$. In the same work though, the authors tried to apply the same corrections in the inclusive processes $e^+e^- \rightarrow J/\psi\,c\bar{c}$ but the relativistic corrections were negligible and the discrepancy was not resolved in this case. In the same period, other authors with similar or even more refined calculations came to similar results [81] proving that the understanding of double charmonium production stands in a more sticky ground.

4.4.2 Bottomonium Decays in Double Charmonium

Since bottomonium is heavier than charmonium, double charmonium production can happen in bottomonium decays too. In the recent years, a very big theoretical progress has been noticed in understanding the charmonium production of exclusive hadronic processes. Studies of these processes, parallel to the studies of e^+e^- annihilation that discussed in the previous section, can give an insight in the dynamics of hard exclusive processes and the structure of quarkonium mesons. Moreover, exclusive bottomonia decays offer a very important advantage. Since the initial bottomonia states have different quantum numbers, double charmonium production can be studied for processes that were suppressed in *B* factories.

Some very recent theoretical studies [82] [83] applying the so called light cone formalism and relativistic and electromagnetic corrections respectively, claim that the total branching ratio of $\chi_{b0,b2} \rightarrow J/\psi J/\psi$ is in an order that can marginally be seen with the data that would be selected in the first year of nominal LHC operation (the most popular theoretical values of the expectation of the branching ratio are found in Table 4.3). This work done in this thesis, aims for an experimental verification of the above theoretical predictions, using ATLAS LHC data.

studies from theory	Br($\chi_{b0} \rightarrow J/\psi J/\psi$)	Br($\chi_{b2} \rightarrow J/\psi J/\psi$)
[82]	9×10^{-5}	11×10^{-5}
[83]	0.5×10^{-5}	3.4×10^{-5}

Table 4.3: *Theoretical prediction for exclusive bottomonia decays into pairs of charmonium mesons (the state χ_{b1} is highly suppressed).*

4.4.3 Motivations of studies of Bottomonium in Double Charmonium Decays

The double charmonium production is still not well understood and remains one of the most challenging problems of heavy quarkonium physics. Better understanding of double charmonium production could shed some light in the understanding of physics of hard exclusive processes which will improve our knowledge of strong interaction dynamics in hard exclusive processes. The studies of double charmonium production in bottomonium decays [84] are offering a ground for studying the dynamics of hard processes and the structure of $c\bar{c}$ mesons. Finally, another advantage of bottomonium decays is that the quantum numbers of the initial state of the meson can lead to studies of final states that are suppressed in the e^+e^- collisions of B factories.

In the following chapter, it will be presented a study which evaluates the sensitivity of the ATLAS detector of reconstruction of di-onia resonances using 2010 and 2011 LHC ATLAS data.

Chapter 5

Study of the Decay $\chi_b \to J/\psi J/\psi$

The analysis presented follows a "cut and count" approach with a nominal blinded signal region in invariant mass, in order to avoid biases. The strategy of the analysis is graphically displayed in Figure 5.1. The χ_b data are split into two parts, including data from the mass signal region (DATA$_{\text{sig}}$) and data from the side-bands region (DATA$_{\text{bands}}$). The even number side-band (see 5.5) events are reserved for the definition of the analysis (selection of discriminating variables, optimisation of cuts), while the odd number side-band events are exclusively used for the background interpolation in the signal region. As long as all the analysis steps are properly defined, the number of observed events in the signal region (N_{OBS}) is extracted using the data of the signal region (DATA$_{\text{sig}}$) after applying the cuts. Finally, an estimation of the signal events N_{SIG} in the signal region is performed using the N_{OBS} and the N_{BGR}. The baseline approach for the extraction of the limit is a Rolke [85] based statistical extraction that uses the observed number of events in the signal region N_{OBS} and the expected number of the background events in the signal region N_{BGR}.
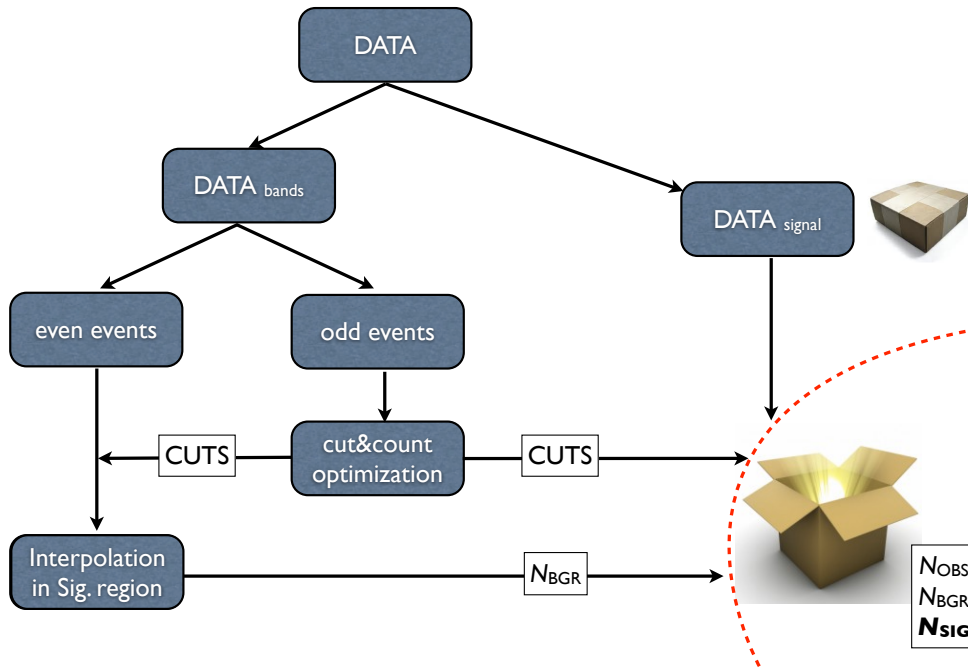
Figure 5.1: *The different steps of the analysis methodology.*

5.1   Simulation of the Signal Events

The generation process is $\chi_{b0} \rightarrow J/\psi J/\psi \rightarrow \mu^+\mu^-\mu^+\mu^-$ where Pythia [86] (v. 6.40) is used. The exact details of the generation are described below [87].

The processes that produce the χ_{b0} meson are the following

- $gg \rightarrow \chi_{b0} + g$

- $gg \rightarrow \chi_{b0} + q$

The available decay modes in Pythia are

- $\chi_{b0} \rightarrow Y\gamma$

- $\chi_{b0} \rightarrow gg$

Since the $\chi_{b0} \rightarrow J/\psi J/\psi$ decay mode is not included in Pythia, the following approximation is used:

1. The decay channel is chosen with probability 100% to be the $\chi_{b0} \rightarrow Y\gamma$.

2. The decay products are replaced with J/ψ, $Y \rightarrow J/\psi$ and $\gamma \rightarrow J/\psi$.

3. Each $J/\psi \rightarrow \mu^+\mu^-$ with 100% probability.

The generation file, except for the generation procedure, includes information concerning generation level trigger cuts which are applied by a selection algorithm developed in ATLAS BPhysics group, called *BSignal Filter*[1] [88]. The BSignal Filter is a trigger provided by the BPhysics ATLAS group and simulates the LV1, LV2 triggers. This Filter works the following way:

1. It loops over all HEP MC particles and if any of them pass the LV1 criteria (particle is muon, kinematic cuts) a flag that correspond to LV1 trigger is raised, a counter is incremented and the muon bar code is recorded.

2. If LV1 flag is raised, it goes through a second loop over the particles in order to check if LV2 is triggered. If the particle is muon, the bar code is checked to ensure it is the LV1 muon. If any found, the LV2 flag is raised and the counter is incremented.

3. If both LV1 and LV2 are passed the algorithm search for B-particles, extracts them and store them to an ntuple. If not, the event is rejected.

4. After all processing of all the event a summary report is printed.

5.2   Analysis on the Generated Events

---

[1]The BSignal filter, is a generator level trigger that acts after the end of the Pythia circle and filters out all the generated events that do not satisfy the minimum momentum criteria. These cuts simulate the ATLAS trigger cuts that happen during the reconstruction of the event. Therefore, the original production cross section has to be corrected so to include the rejection factor of the BSignal filter.

This paragraph discusses a first study using the generated data.

Figure 5.2: *The number of generated muons per event.*

All the generated particles have a characteristic id (the pdg id) and carry information concerning their "mother" particles and their "daughter" particles. In addition to the signal particles, other particles are also produced in the event that originate from the hadronization of the quark or the gluon. The distribution in Figure 5.2 is the number of muons in the event. Since in the final state of the decay each J/ψ decays to two muons, as a result each event is expected to have at least four muons.

The events with muon multiplicity more than four, include muons originating from the hadronization of the gluon or the quark. Other interesting distributions of the generated events (see Figure 5.3) deal with the transverse momentum of the reconstructed particles. The impact of the BSignal Filter on the p_T distribution of the muons is obvious. For example, in the transverse momentum of muons, the observed edges at $4\,\mathrm{GeV}/c$ and $6\,\mathrm{GeV}/c$ are due to the BSignal Filter.
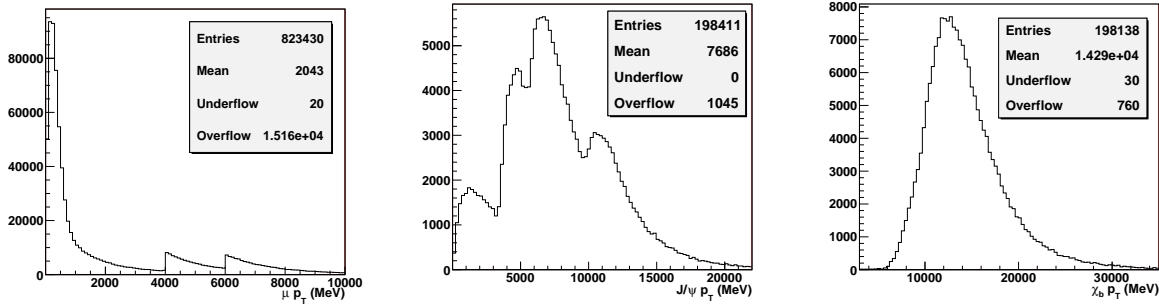
Figure 5.3: *The transverse momentum of muons, J/ψ and χ_b using the "true" information of the generated events, without taking into account the detector acceptance and efficiencies. The presence of BSignal Filter in the distribution of the p_T is obvious, by the appearance of the artificial steps at 4000, 6000 MeV/c.*

5.3 Off-line Reconstruction

5.3.1 Reconstruction of Muons

The muons produced in a collision, firstly pass through the *Inner Detector* (ID), subsequently they reach the *Electromagnetic* and *Hadronic Calorimeter* and if their energy is high enough, they reach the *Muon Spectrometer* (MS). A muon that leaves hits both in the ID and in the MS is refitted to a common track and is called a *combined muon*. The muons of lower energy that are not reconstructed in the MS since they do not leave the necessary hits in the muon chambers are called *tagged* muons. In ATLAS there are two muon reconstruction chains that use different pattern recognition strategies, the *STACO* and the *MUID* [89, 90]. This analysis uses muons reconstructed with the STACO algorithm.

5.3.2   Reconstruction of J/ψ

The J/ψs used in the analysis are reconstructed with the algorithm *VKalVrt* [91]. Some loose pre-selection criteria are applied that deal with the quality of the vertex fit (χ^2/ndf $<$ 200), the invariant mass of the reconstructed J/ψ (3000 MeV/c^2 $< m_{J/\psi} <$ 3200 MeV/c^2) and the charge of the muons (opposite charge). For background studies, a looser cut in the invariant mass of the J/ψs is applied (2700 MeV/c^2 $< m_{J/\psi} <$ 3500 MeV/c^2).

5.3.3   Reconstruction of χ_b

In the case that the event has more than one reconstructed J/ψ, the four tracks associated with the J/ψs are fitted to a common vertex. There are no χ^2/ndf or invariant mass pre-selections in the reconstruction phase. For reasons that will be developed in the next sections there are two χ_b reconstructed versions of the same candidate saved in each event. In the first version the J/ψs of χ_b are constrained to the world average J/ψ mass while in the second there is no such constraint in the fit.

5.4   Pre-selection of Candidates

A first loose pre-selection is applied to the candidate events providing a first reasonable skimming. All events are selected using the *EF_2mu4_Jpsimumu* di-muon trigger, that requires 2 muons of 4 GeV/c, each triggering at all trigger levels. At least two of the four χ_b muons, that are reconstructed in the MS, should be matched in the ID. All χ_b properties are based in the fit and the common vertex is required to satisfy χ^2/ndf $<$ 6. Furthermore the reconstructed χ_b candidates are required to have $p_T >$ 8 GeV/c and $|\eta| <$ 2.5. If the event includes more than one primary vertices the one closest to the beam-line direction of the χ_b vertex is chosen. The reconstructed J/ψs of the χ_b are required to have χ^2/ndf $<$ 15, $p_T >$ 3 GeV/c and $|\eta| <$ 2.5. Finally the ID tracks of the χ_b muons satisfy the *Muon Combined Performance (MCP)* group [92] conventions:

- Number of (PIX, SCT, TRT) hits is greater than (0, 5, 0)

- Less than two Pixel and SCT holes

- If more than 5 TRT hits $|\eta| <$ 1.9, require 90% outliers

- More than 5 TRT hits with 90% outliers for $|\eta| <$ 1.9

The distribution of the pre-selection variables before and after the cuts, can be found in Appendix A.2 in page 146. The reconstruction efficiency drops, after applying the pre-selection cuts, to 25% and 22% for the MC signal and data, respectively. In the case of signal the drop in the efficiency is exclusively due to the track quality criteria.

5.5   Signal, Blind and Side-band Regions

In order to avoid any bias during the optimization phase of the analysis a *blind* region around the χ_b invariant mass is defined. This region stays unrevealed until the end of the analysis where all the analysis steps are properly defined. The **blind** region is chosen to be the $\sim \pm 3\sigma$ region around the mean value of the reconstructed χ_b signal invariant mass in the case of the *unconstrained* fit. This region is [9280, 10480] MeV/c^2.

Apart from the blind region, a **signal** region is chosen to be the $\sim \pm 3\sigma$ region around the mean value of the reconstructed χ_b signal invariant mass in the case of a *constrained* fit. The signal region is $[9690, 9994]$ MeV/c^2.

The *side-bands* regions are selected following the standard method:

1. Side-bands should be broad enough so that enough statistics is included in the left and the right side-band.

2. Side-bands should be preferably in regions that are no other resonances. In case we know that there are other resonances in the bands region, any fits performed in these regions should take into consideration these resonances.

The **left side-band** for the χ_b invariant mass is in the range of $[6680, 9280]$ MeV/c^2 and the **right side-band** is in the range of $[10480, 13080]$ MeV/c^2. The signal, blind, side-bands regions are shown in Figure 5.4.
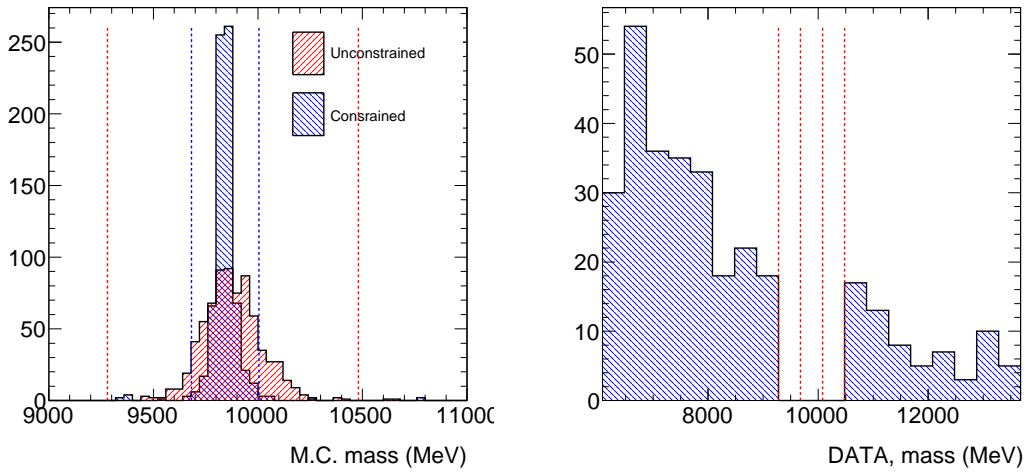
Figure 5.4: *Blind, signal and side-bands regions. In the simulated signal distribution (left) the region between the red lines is the blind region, while the region between the blue lines is the signal region.The side-bands region and the 3-bins blind region are displayed in the distribution of the invariant mass of the data (right).*

5.6 Binning

A correct *binning* of the invariant mass histogram is also important so that the blind, the signal and the side-bands regions are properly defined. The limits of the regions referred above are extracted taking into consideration a proper histogram binning.

1. The χ_b mean mass value is obtained from the MC signal histogram, $\chi_b^{\mathrm{mean}} \approx 9880$ MeV/c^2 and $\chi_b^{\mathrm{RMS}} \approx 150$ MeV/c^2.

2. A $\approx 3\sigma$ blind mass region is defined $[9880 - 3 \times 200, 9880 + 3 \times 200] = [9280, 10480]$ MeV/c^2 using $\sigma = 200$ MeV/c^2 (a bit broader than the χ_b^{RMS}).

3. A $\approx 16\sigma$ symmetric side-band mass region is defined $[9880 - 16 \times 200, 9880 + 16 \times 200] = [6680, 13080]$ MeV/c^2.

trigger correlation matrix				
	before preselection		after preselection	
	MC signal	data	MC signal	data
passed EF_2mu4_Jpsimumu	1122	730	736	314
passed EF_2mu4_Bmumu	645	152	422	66
passed both	381	79	286	43

Table 5.1: *The correlation matrix of the most popular triggers in the analysis of $\chi_b \to J/\psi J/\psi$.*

The final mass histogram has 19 bins, the bin width is 400 MeV/c^2 and the blind region includes exactly 3 bins, the 9th, the 10th and the 11th.

5.7 Trigger Selection in χ_b Studies

Single muon triggers are excluded from χ_b studies. The low p_T single muon triggers that can possibly be used are highly preselected while the rest of the single muon triggers are too high p_T triggers with small efficiencies.

Among the *di-muon* triggers, the natural candidates in the χ_b analysis are the *EF_2mu4_Jpsimumu* and the *EF_2mu4_Bmumu*[2]. A dedicated study is performed aiming to show which of these two triggers is more suitable. The results are summarised in table 5.1.

The most appropriate trigger is the **EF_2mu4_Jpsimumu**. The reasons are:

- The *EF_2mu4_Bmumu* is fired by too few events ($N_{\text{events}} = 66$).

- In both before and after the preselection, most of the events that pass the *EF_2mu4_Bmumu*, pass also the trigger. For the case of MC before pre-selection is 59% while after is 67%. For the case of data before the pre-selection is 52% while after it is 65%. *EF_2mu4_Jpsimumu*.

5.8 Isolation Variable

The decay products of a *B*-hadron are kinematically isolated from other tracks originating from the same primary vertex as the *B*-hadron. Therefore the *isolation* variable, $I_{\Delta R}$, is defined as:

$$I_{\Delta R} = \frac{p_T^{B_s}}{p_T^{B_s} + \sum_{\text{tracks}}^{\Delta R \leq 0.7} p_T}$$

where p_T^B is the transverse momentum of the *B*-meson and the $\sum_{\text{tracks}}^{\Delta R \leq 0.7} p_T$ is the transverse momenta of all tracks within a cone $\Delta R \leq 0.7$ from the direction of the *B*-meson, excluding its decay products.

The isolation is a potentially good discriminating variable for the χ_b analysis. However, it is well known that the *isolation* variable is strongly dependent on pile-up and though it deserves special treatment.

---

[2]EF_2mu4_Jpsimumu or EF_2mu4_Bmumu require two 4 GeV/c muons at all trigger levels, with the additional loose invariant mass cuts, compatible with a J/ψ or a B meson, accordingly.

Definition with χ^2 compatibility	
Isolation_10_Chi2_6_Loose	Isolation_7_Chi2_6_Loose
Isolation_10_Chi2_6_Medium	Isolation_7_Chi2_6_Medium
Isolation_10_Chi2_6_MediumPt05	Isolation_7_Chi2_6_MediumPt05
Isolation_10_Chi2_6_Tight	Isolation_7_Chi2_6_Tight
Isolation_10_Chi2_6_TightPt5	Isolation_7_Chi2_6_TightPt5
Definition without χ^2 compatibility	
Isolation_10_Chi2_NO_Loose	Isolation_7_Chi2_NO_Loose
Isolation_10_Chi2_NO_Medium	Isolation_7_Chi2_NO_Medium
Isolation_10_Chi2_NO_MediumPt05	Isolation_7_Chi2_NO_MediumPt05
Isolation_10_Chi2_NO_Tight	Isolation_7_Chi2_NO_Tight
Isolation_10_Chi2_NO_TightPt5	Isolation_7_Chi2_NO_TightPt5

Table 5.2: *The various definitions of the enhanced Isolation variable.*

A detailed study has been carried out to redefine the track selection within the *isolation* cone so to avoid additional interference [93]. In order to constrain the impact of the pile-up, additional selection criteria have been added and a χ^2-like quantity discriminates the tracks originating from the same vertex as the B-hadron while the efficiency is comparable to the one of the original definition. The parameters of the new *isolation* definition are

- ΔR of the *isolation* cone,

- p_T of tracks inside the *isolation* cone,

- χ^2 test of compatibility of tracks with the *B*-hadron vertex.

For the needs of such analysis, a wide range of *isolation* definitions has been studied grouped in the table below:

The various *isolation* definitions of the table 5.2 can be summarised in the expression: *Isolation_X_chi2_Y_Z* where

X = [10,7], are the possible values of the ΔR of the cone (multiplied by 10)

Y = [6, NO], are the possible values of the χ^2 track-vertex compatibility test. If the value is 6 the χ^2 test of the compatibility of the track to the χ_b vertex should have a result less than 6. If Y=NO, there is no χ^2 test.

X = [Loose, Medium, MediumPt5, Tight, TightPt5], indicates how energetic can be the track within the cone in order to be included in the sum of their momenta ($\Sigma_{\text{tracks}\Delta R}$)

A dedicated study based on the concepts of separation capabilities is performed that evaluates which of the *isolation* definitions offers the best separation power . The definitions with Y=NO are not taken into account since by construction we know that they are worse candidates as pile-up dependent. The remaining definitions are grouped into smaller groups and with the help of *ROC* curves the definition that satisfies the best signal-background discriminations chosen. The selection procedure of the choice of the variables with the best discriminating power has been developed in the section 7.6.6, while all the relevant plots of the comparisons

of this study can be found in A.3.

Group 1

Isolation_7_Chi2_6_Medium, Isolation_7_Chi2_6_MediumPt05, Isolation_7_Chi2_6_Tight, Isolation_7_Chi2_6_TightPt05

Among the ROC curves of the first group the curve which corresponds to the Isolation_7_Chi2_6_Medium, is higher than the rest in almost all signal efficiency range that means that it offers the best separation power within this group.

Group 2

Isolation_10_Chi2_6_Medium, Isolation_10_Chi2_6_MediumPt05, Isolation_10_Chi2_6_Tight, Isolation_10_Chi2_6_TightPt05

Among the ROC curves of the second group the curve which corresponds to the Isolation_10_Chi2_6_Medium, is higher than the rest in almost all signal efficiency range that means that it offers the best separation power within this group. The mixing of the lines in some areas reflect the low statistics of our samples.

Group 3

Best of group 1, best of group 2, Isolation_7_Chi2_6_Low, Isolation_10_Chi2_6_Low, Isolation_10_Chi2_6_Tight, Isolation_10_Chi2_6_TightPt05

Among the ROC curves of the third group the curves which corresponds to the Isolation of *Medium* type, are higher than the rest in high signal efficiencies, while the curves which correspond to the Isolation of *Low* type are higher in low efficiency ranges.

The definitions of *Isolation_10_6_Low* and *Isolation_7_6_Medium* offer the best separation capabilities in high a low signal efficiency range accordingly. Nevertheless, these two variables are expressing substantially the same thing and the separation gain obtained by using both of them is marginal. It is decided that the definition of *Isolation_7_6_Medium* is the one that is used in this analysis.

5.9   Selection of Discriminating Variables of χ_b

The choice of the discriminating variables is based on few basic principles that underline the physics of the signal and the background and they are listed below:

- The χ_b particle is a heavy particle that is produced at the interaction point and has a very short lifetime. On the other hand, many di-onia events include J/ψs that are coming from b-particles which travel long before their decay. In such cases, good separation variables should reflect the distance between the primary interaction point (PV) and the secondary χ_b candidate vertex (SV).

- The discriminating variables should reflect the distance of the J/ψ vertices. The vertices of the two J/ψs that are the decay products of the χ_b should coincide, while the ones originating from the background are expected to be rather separated.

- The dynamics of the system are expected to be different between signal and background. If x is the vector from the primary to the secondary vertex, the direction of the momentum of the χ_b is expected to be very close to the direction of the x. In the case of the background, the two directions are not expected to be correlated.

- The decay products of a B-hadron are kinematically isolated from other tracks originating from the same primary vertex.

5.9.1 Definitions of Possible Discriminating Variables

What follows is the list of the discriminating variables that are studied and can possibly be used in this analysis. The corresponding distributions of these variables can be found in A.4.

- Pointing angle in 2D (α_{2D}) and 3D (α_{3D})
  If x is the vector from the Primary Vertex point to the Secondary Vertex point, then α_{2D} is the angle between the x and the momentum vector, p, of the B-meson. It is calculated in the transverse plane (α_{2D}) and in the 3-dimensional space (α_{3D}).

- $\Delta R = \sqrt{(\varphi_x - \varphi_p)^2 + (\eta_x - \eta_p)^2}$
  It is the distance ΔR in the $\eta\phi$ plane, where ϕ is the azimuthal angle and η is the pseudo-rapidity.

- $\chi^2(\text{PV} - \text{SV})$
  This variable is derived from the position and the covariance matrix information of the Primary (PV) and Secondary Vertex (SV). It is χ^2-like variable, under the hypothesis that the primary and B-meson vertex coincide. It is computed separately in the 3-dimensional space (χ^2_{xyz}), in the transverse plane (χ^2_{xy}), and along the z-direction (χ^2_z).

- Isolation
  It is defined as the ratio of p_T^B over the sum of p_T^B and of the transverse momenta of all tracks within a cone $\Delta R < 0.7$ from the direction of the B-meson, excluding its decay products. Two definitions of the isolation variable are studied, one including the χ^2 compatibility cut and one not including it.

- $L_{xy} = x \cdot \hat{p}_B$
  Where x is the vector from the Primary to the Secondary Vertex and $\hat{p}_B$ is the unitary momentum vector of the B-meson. The L_{xy} significance, which is $L_{xy}/\sigma_{L_{xy}}$, is calculated, too.

- Proper Time and Proper Time significance
  The proper time is defined as $t_0 = L_{xy}M_B/p_T$, where p_T, M_B are the transverse momentum and the mass of the B-meson, respectively. The Proper Time significance, t_0/σ_{t_0}, is calculated as well, where σ_{t_0} is the error of the proper time.

- χ^2 of the vertex fit of the B-meson

- Transverse Momentum, p_T, is the momentum of the B-meson in the xy plane.

5.9.2 Correlations of Separation Variables

The study of the correlations of the separation variables offers an insight in the separation capabilities of the variables. Different correlation schemes between the signal and the background point to variables that hide good separation capabilities. On the other hand, similar correlation schemes are also proven to be useful indications, since they point to variables that hold similar physical meaning and though can be eliminated without any loss of separation power. Many of the separation variables candidates, by construction are correlated while others are completely

independent and uncorrelated. Besides some variables may are correlated in the case of signal and uncorrelated in the case of background and vice versa. The *Correlation matrix* is a matrix that groups the *correlation coefficients* of all the variable pairs offering an overview of their dependence.

The *correlation coefficient* is a dimensionless measure of the level of correlation of two variables x and y. It is defined as follows

$$\rho_{xy} = \frac{\sigma_{xy}^2}{\sigma_x \sigma_y}$$

where $\sigma_{xy}^2 = V_{xy} = E[(x - \mu_x)(y - \mu_y)]$ is the covariance of two random variables x, y

and $\sigma_x^2 = E[(x - \mu_x)^2]$, $\sigma_y^2 = E[(y - \mu_y)^2]$ are the variances of the variables x, y.

The *correlation matrix* is a matrix that groups the correlation coefficients of all the variable pairs and offers an overview of their dependence. The correlation matrix of the final discriminating variables for the signal and the background are shown in Figure 5.5.
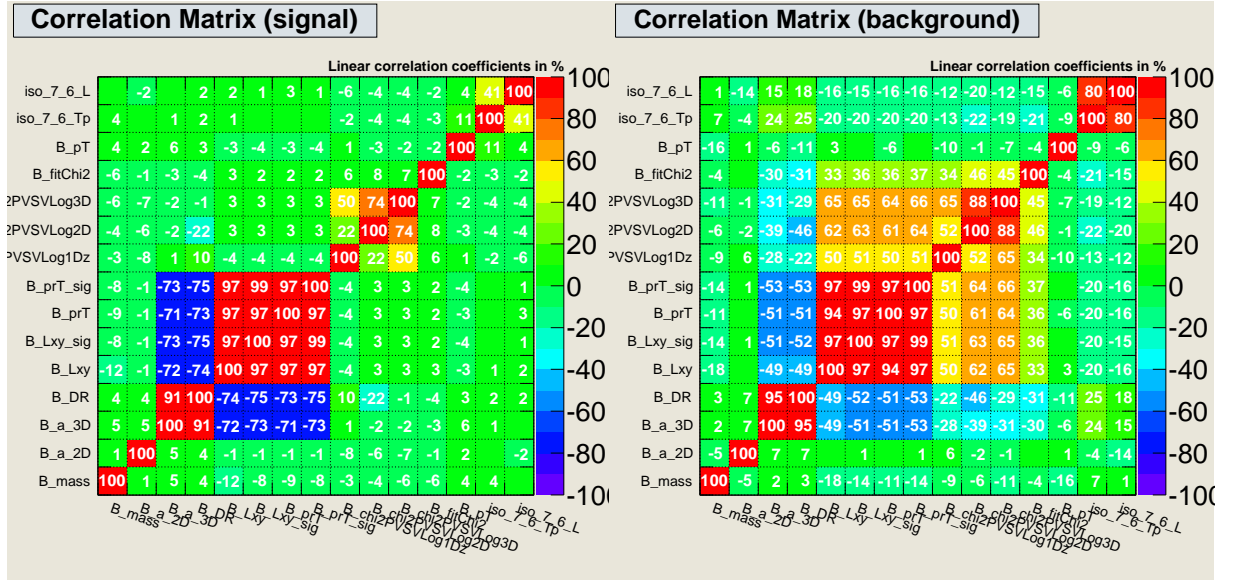
Figure 5.5: *The correlation matrix of all the possible discriminating variables for the signal (left) and the background (right).*

From the correlation matrix for signal, we can see the following facts:

- all variables are uncorrelated with mass,

- the variables of opening angles (α_{2D}, α_{3D}) and ΔR can be grouped together since they are highly correlated,

- the variables L_{xy}, L_{xy} significance, proper time t_0, proper time significance can be grouped together since they are highly correlated,

- the variables χ_z^2, χ_{xy}^2, χ_{xyz}^2 can be grouped together since they are highly correlated.

Furthermore, from the correlation matrix of the background we can see the following:

- the discriminating variables in the case of the background are more correlated than in the case of signal,

- except for the principle strong correlations, there are secondary weaker correlations between several groups of variables,

- all variables are substantially uncorrelated with the mass of χ_b.

5.9.3 Separation Capabilities of Discriminating Variables

The big number of discriminating variables (15) in χ_b study can potentially cause difficulties in the optimisation step. Furthermore many of these variables are highly correlated, share the same physical meaning and the use of all of them does not contribute further in the signal-background discrimination. The study of the correlation matrices done in the previous paragraph is a useful method that regroups properly the separation variables in smaller groups which each one of them contains highly correlated variables.

In this paragraph a ranking of the variables based on their separation power is performed within each group. The aim is to reduce the final number of separation variables without any loss of discriminating power. The ranking of the variables is done with the help of ROC curves and the method is explained in section 7.6.6.

Group 1: opening angle calculated in 2D (α_{2D}), calculated in 3D (α_{3D}) and ΔR
   Among the ROC curves of this group, the one that corresponds to the $|\alpha_{2D}|$ is higher than the rest in almost all signal range showing that he $|\alpha_{2D}|$ offers the best separation power within the group.

Group 2: L_{xy}, L_{xy} significance, proper time t_0, proper time t_0 significance
   Among the ROC curves of this group, the curve that corresponds to the t_0 significance is higher than the rest in high signal efficiency range. In the small signal efficiency range the lines are overlapped and in this case we use the *log(background efficiency) versus log(signal efficiency)* curves. In this region the line that is lower to the rest offers the best separation power, and it corresponds to the t_0 significance again. Finally, the t_0 significance offers the best separation power within this group.

Group 3: χ_z^2, χ_{xy}^2, χ_{xyz}^2
   Among the ROC curves of this group, the one that corresponds to the χ_{xyz}^2 is higher than the rest in almost all signal efficiency range showing that the χ_{xyz}^2 offers the best separation power within this group.

Group of Isolation
   As it is shown in the section 5.8, among all the different definitions of the isolation variables the *Isolation_7_6_Medium* is the one chosen to be used in this analysis.

Group of remaining variables
   The rest of the separation variables (p_T, χ^2/ndf) are independent and will be used as discriminating variables (ndf is the number of independent parameters available to fit a model to the data.).

5.10   Final List of Separation Variables

The final list of separation variables are presented in 5.6 and their definitions are summarised in table 5.3.

Variable	Description
α_{2D}	If $\boldsymbol{x}$ is the vector from the Primary Vertex point to the Secondary Vertex point, then α_{2D} is the angle between the $\boldsymbol{x}$ and the momentum vector, $\boldsymbol{p}$, of the B-meson.
t_0 significance	Proper decay length $t_0 = L_{xy} M_B / p_T^B$, divided by its uncertainty, σ_{t_0}.
χ^2_{xyz}	χ^2 computed between the measured PV and SV positions respectively in x, y, z.
Isolation $(I_{\Delta R \leq 0.7})$	Ratio of $|p_T^B|$ over the sum of $|p_T^B|$ and of transverse momenta of all tracks within a cone $\Delta R \leq 0.7$ from the direction of the B-meson, excluding its decay products.
p_T^B	The transverse momentum of the B-meson.
χ^2/ndf	χ^2 of the χ_b vertex.

Table 5.3: *The final list of discriminating variables.*
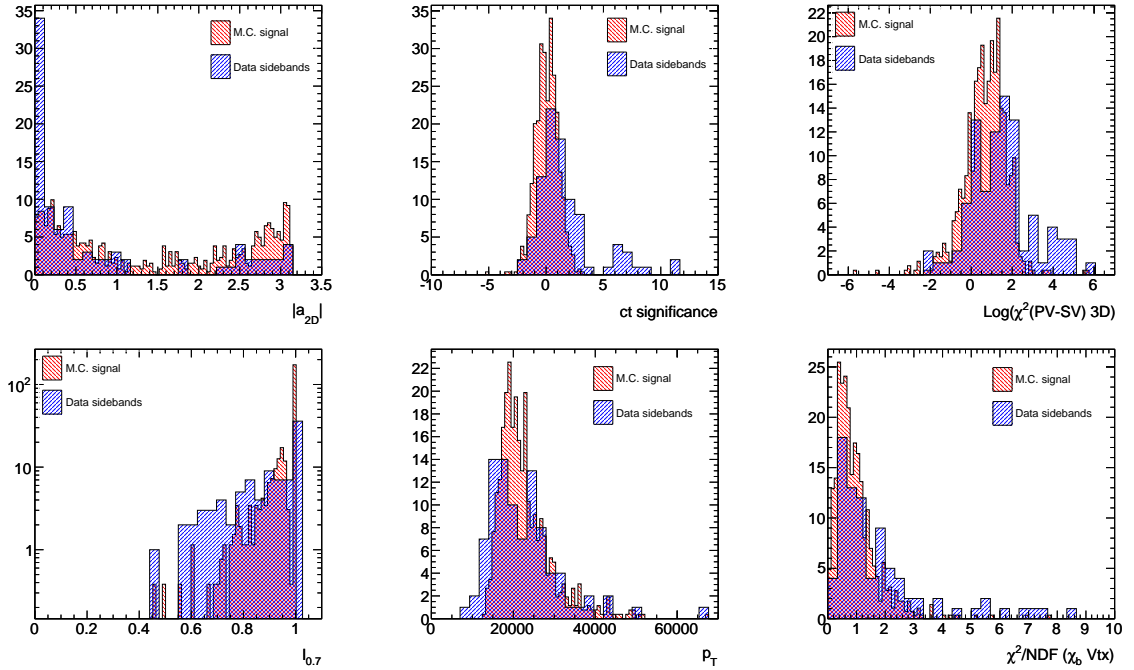
Figure 5.6: *The variables displayed here are the α_{2D}, t_0 significance, χ^2_{xyz}, Isolation, p_T^B, χ^2/ndf*

5.11   Optimisation of Cuts

The cut points of the discriminating variables, in the optimisation step, are chosen in a way so as to achieve the maximum rejection of the background and in the same time the maximum efficiency of the signal. During this step, the range of each of the separation variables is divided into 20 equal slices and for each sub-range the left point has been used as a cut value. The result is a 6×20 grid that allows a contemporary scan of the selection variables, taking into consideration possible correlations. In each grid point a carefully chosen *estimator* is calculated which values will be used for the extraction of the optimal cut points of the selection variables.

There are several definitions of estimators, the most popular of them (a nice comparison is referred in [1]) are listed below:

1. $\mathcal{P} = S / \sqrt{B + S}$

   where S is the number of signal events and B is the number of background events in the signal region. This estimator is not a good choice since it cannot be maximised if the cross-section of the signal is unknown.

2. $\mathcal{P} = S / \sqrt{B}$

   where S is the number of the signal events and B is the number of the background events in the signal region. This estimator performs badly when the value of B is small. Since in the χ_b study, the number of background events in the signal region is expected to be very small, this definition of the estimator is proved to be a bad choice.

3. $\mathcal{P} = \epsilon_{\text{SIG}} / \left(\alpha/2 + \sqrt{B} \right)$ (Figure of Merit (FoM) proposed by Punzi [1])

   where ϵ_{SIG} is the efficiency of the signal, B is the number of background events in the signal region and $\alpha = 2$ corresponds to the 95% CL. This estimator is not suffering from the problems referred above and it is proven to give the best limit when it is used in the step of optimisation.

An example of the optimisation of the cut of the L_{xy} variable with the use of the Punzi FoM is shown in Figure 5.7. The distribution of the signal and the background is sliced in 20 bins (left plot). In each bin, the background rejection and the signal efficiency is calculated (middle plot). For each bin, the estimator is calculated (right plot). The point that corresponds to the maximum value of the estimator is proven to be the optimal cut point, as shown in the right plot of Figure 5.7.

5.11.1   Factorisation

In case of a single variable, the optimisation is a straight forward procedure. The distribution has just to be split into few cut points and the estimator has to be calculated in each of them. In case of bigger number of separation variables, the theoretical approach remains the same but the calculation of the estimator, with a simultaneous scan of all the variables, can cause performance issues. More specifically in our case, where the number of discriminating variables is 6, it is observed that, even for a small number of cut points (20), the calculation of the estimator in each grid point needs a huge (order of months) processing time.This huge delay is observed even in the case that the number of variables is four. In order to conform this obstacle, the concept of the factorisation is introduced.

The calculation of the estimator is still performed in each grid point of a 6 dimensional grid, but instead of the deriving its value from the calculation of the full expression, the derivation
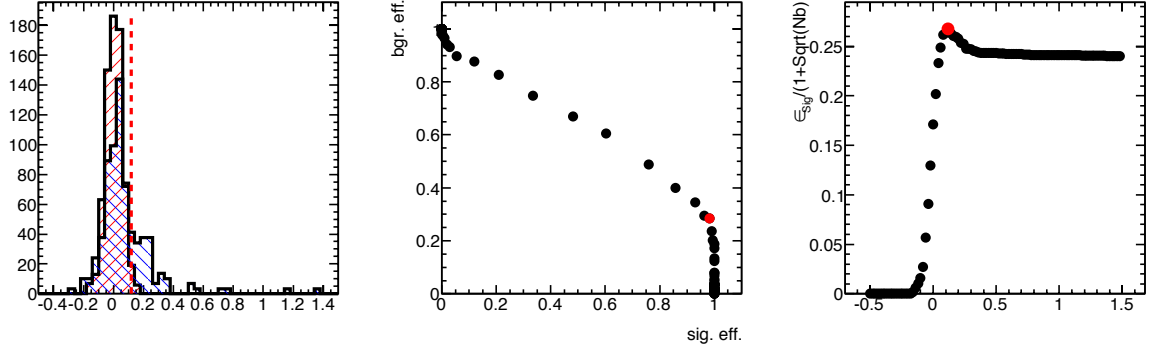
Figure 5.7: *Optimisation for the case of a single variable. The distribution of L_{xy} (left), the ROC curves (middle) and the estimator using the Punzi FoM (right). The optimal cut point corresponds to the maximum value of the estimator.*

comes from a simple product of recalculated efficiencies that have been factorised according to the correlation matrix of the variables.

The factorised efficiency of the signal is

$$\text{eff}_{\text{SIG}}\left(t_0, \alpha_{2D}, \chi^2_{3D}(\text{PV} - \text{SV}), \chi^2/\text{ndf}, p_T, I_{0.7}\right)$$
$$= \text{eff}_{\text{SIG}}(t_0, \alpha_{2D})\, \text{eff}_{\text{SIG}}(\chi^2_{3D}(\text{PV} - \text{SV}))\, \text{eff}_{\text{SIG}}(\chi^2/\text{ndf})\, \text{eff}_{\text{SIG}}(p_T)\, \text{eff}_{\text{SIG}}(I_{0.7})$$

The factorised efficiency of the background is

$$\text{eff}_{\text{BGR}}(t_0, \alpha_{2D}, \chi^2_{3D}(\text{PV} - \text{SV}), \chi^2/\text{ndf}, p_T, I_{0.7})$$
$$= \text{eff}_{\text{BGR}}(t_0, \alpha_{2D}, \chi^2_{3D}(\text{PV} - \text{SV}), \chi^2/\text{ndf})\, \text{eff}_{\text{BGR}}(p_T)\, \text{eff}_{\text{BGR}}(I_{0.7})$$

5.11.2 Validation of the Factorisation

Although the factorisation technique solves the performance issues, in order to be used in the analysis it has to be cross checked that quantitatively it gives the correct result. For this purpose, a dedicated test estimates the differences observed between the efficiencies calculated applying the factorisation method and the ones applying simple cuts (see Figure 5.8). Ideally a good behaviour of the factorisation would be graphically verified if the scatter plot of the efficiency using the factorisation method against the efficiency using simple cuts looks like the a line that connects the points (0,0) and (1,1). A more detailed test that can quantify the differences of the two methods, is achieved by plotting the value $0.5(\text{eff}_{\text{fact}} - \text{eff}_{\text{cuts}})/(\text{eff}_{\text{fact}} + \text{eff}_{\text{cuts}})$. The expected distribution is a gaussian with a mean value at 0 and a very small sigma. Looking at the distributions of this analysis, the mean value is indeed observed around 0 and the sigma is relatively small but there is a strange structure in the bottom of the gaussian. The plot on the right sheds some light by indicating that the strange behaviour comes from cases that the efficiency is small.

5.11.3 Final Cuts

By using the Figure of Merit of Punzi and the factorisation method described above, the optimal cuts of the discriminating variables of the analysis are extracted. In Figure 5.9, the red lines correspond to the output of the estimator when the optimization is done with the single variable
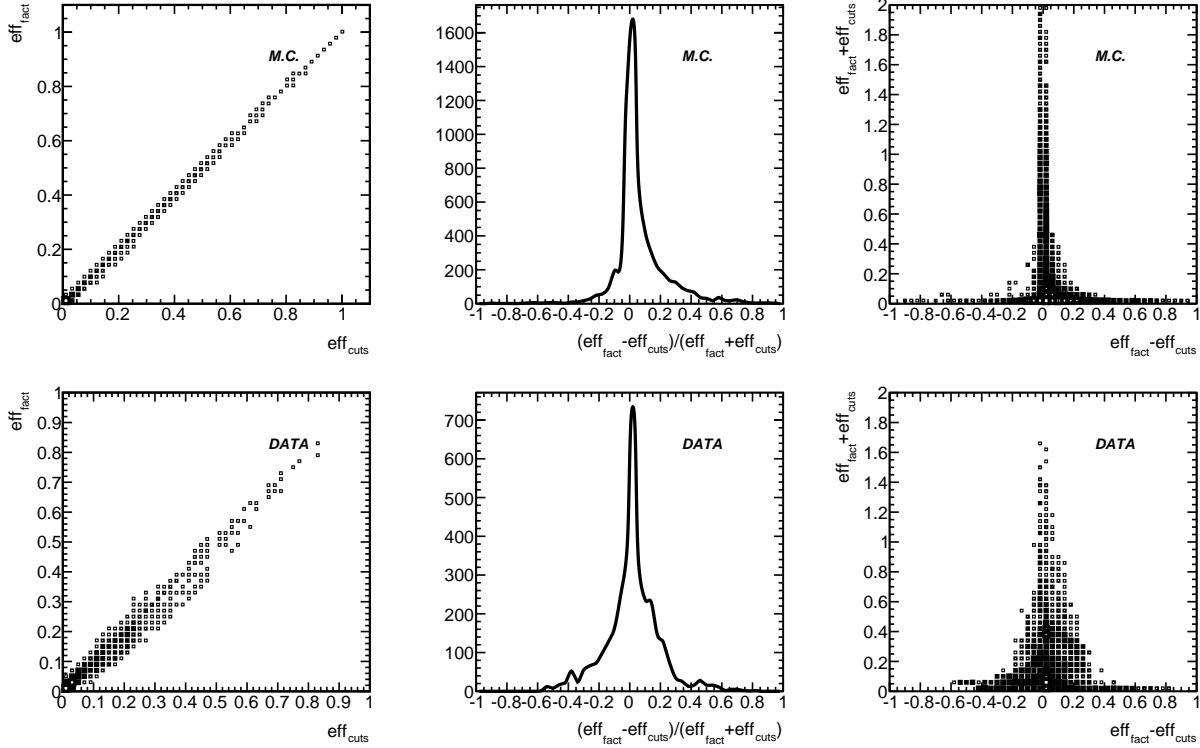
Figure 5.8: *Validation of the factorisation step. The top, bottom distributions correspond to simulated signal data and real data accordingly. The scatter plot on the left shows the correlation of the efficiency calculated from the factorisation and the one calculated from a straight forward calculation by applying the cuts. The distribution in the middle is the $0.5(\text{eff}_{fact}- \text{eff}_{cuts})/(\text{eff}_{fact}+\text{eff}_{cuts})$ and shows the percentage declination of the the efficiency calculated from the factorisation versus the one calculated from a straight forward calculation by applying the cuts. The scatter plot on the right shows that the main declinations in the efficiency calculations of the two methods appear in small signal efficiency range.*

while the black lines correspond to the output of the estimator when the optimisation is done using a 6 dimensional grid of all the discriminating variables together. The small shift of the limits offers a qualitative verification that the procedure of the optimisation works correctly. The cuts after the optimisation step become more loose than the ones derived from the single-variable optimisation, assuring in this way that no "hard" cuts are applied and the maximum efficiency of the signal is obtained with the simultaneous maximum rejection of the background.

5.12   Extraction of Limit Using 2010 Data

This paragraph presents the Upper Limit extraction on the branching ratio of $\chi_b \rightarrow J/\psi J/\psi$. The study makes use of an integrated luminosity $L_{int} = 0.04\,\text{fb}^{-1}$ that corresponds to the LHC 2010 data of pp collisions (details about the LHC data used can be found in A.1). Due to the small statistics, the limit is expected to be higher than the theoretically expected one, but it offers a first evaluation of the sensitivity of the analysis and proves that the various previous studies in the analysis stand in a solid ground. The extraction of the Upper Limit comes together with a Confidence Level (CL) that expresses the probability that by repeating the experiment, the
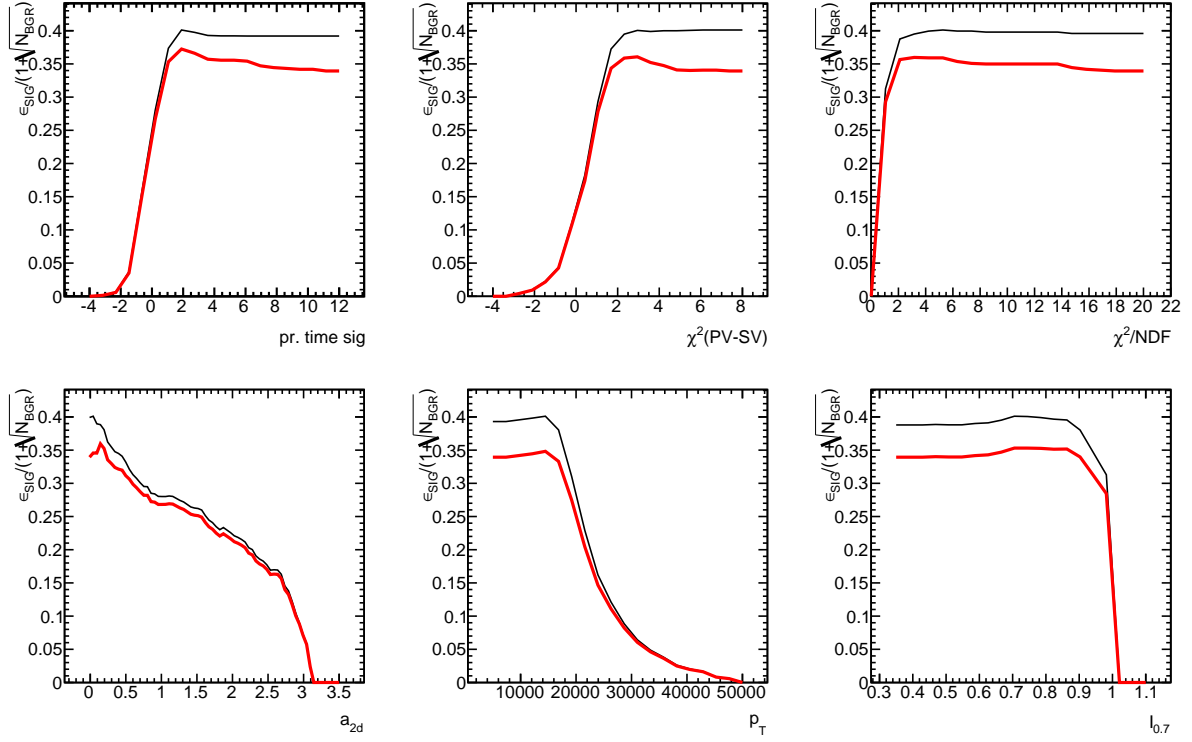
Figure 5.9: *The optimal cut points of the variables correspond to the maximum value of the estimator. In the case that the optimisation is done for each variable separately, the calculated estimators of the variables are displayed with red curves. In case the case that the optimisation is done using simultaneously and for all the variables together, the calculated estimators of the variables are displayed with black curves.*

outcome will fall in the same range.

The event selection of the $\chi_b \to J/\psi J/\psi$ is optimised based on a set of cuts derived from appropriate signal and background models (the efficiency of signal and background, as a function of the number of the applied cuts, is shown in Figure 5.10). Since the statistics of 2010 data is small, the optimisation of the appropriate cuts is performed using the data of 2011, by appropriately correcting the expression of the estimator, as follows:

$$\mathcal{P} = \frac{\epsilon_{\text{SIG}}}{\dfrac{\alpha}{2} + \sqrt{\dfrac{L^{2010}}{L^{2011}} N^B{}_{\text{SIG}}}}$$

where L^{2010}/L^{2011}, $N^B{}_{\text{SIG}}$, ϵ_{SIG}, α are the ratio of the integrated luminosity during the 2010 run and 2011 run, the number of background events expected in the signal region, the efficiency of the signal and α, a parameter of the estimator that defines the % Confidence Level (CL) in the extraction of the limit, accordingly.

The limit on the branching ratio, $\text{Br}(\chi_b \to J/\psi J/\psi)$, depends on the limit of the number of χ_b candidates, N_{χ_b}, through a multiplicative coefficient known as *Single Event Sensitivity* (SES), as shown in the following formula:

$$\text{Br}(\chi_b \to J/\psi J/\psi) = N_{\chi_b} \text{SES}$$

where SES is given by:

$$\text{SES} = \frac{1}{L_{\text{int}}\sigma(pp \to \chi_b + X)\text{Br}(J/\psi \to \mu^+\mu^-)\text{Br}(J/\psi \to \mu^+\mu^-)A\epsilon}$$

where L_{int} is the integrated luminosity, $\text{Br}(\chi_b \to J/\psi J/\psi)$ is the branching ratio of the decay of J/ψ to muons (two times because there are two J/ψs in the χ_b decay) and $A\epsilon$ is the product of the geometrical acceptance A by the total reconstruction efficiency ϵ of the χ_b decay.

The information needed for the final calculation is listed below:

- The integrated luminosity of pp collisions during 2010 data taking at LHC is $L_{\text{int}} \sim (0.04 \pm 0.0044)\,\text{fb}^{-1}$.

- The $\sigma(pp \to \chi_b + X) \sim (0.57 \pm 0.11)\,\mu\text{b}$ is the theoretical expectation of the production cross section of the χ_b [82].

- The $\text{Br}(J/\psi \to \mu^+\mu^-) = 0.0593 \pm 0.0006$ is the world average value of the branching ratio of the J/ψ to two muons [4].

- The product $A\epsilon$ is calculated from the simulation and found to be $\sim (6.6 \pm 0.25) \times 10^{-4}$. This is the ratio of the number of the reconstructed simulated signal events over the total number of the generated signal events.

The errors of the above quantities are propagated properly and result in $\delta(\text{SES}) \sim 0.21(\text{SES})$. The details that correspond to the numbers that are used in the extraction of the limit are listed below:

- The luminosity determination in ATLAS detector is achieved by the use of several detectors and multiple algorithms [94]. Each of the independent luminosity evaluation methods, has different acceptance, systematic uncertainties and sensitivity to background, but for a fixed value of inelastic pp collisions per bunch crossing, the absolute luminosities obtained using these different methods agree within ±2%. There are many factors that contribute to the systematic uncertainties of the absolute luminosity measurements, like uncertainties in the absolute bunch charge (beam intensity), different displacement of beams at each scan step, imperfect beam centring, choice of fit models of the scan data. Among them, the uncertainty in the bunch intensities is the dominant one and the common systematic uncertainty of the luminosity is ±11%. In the analysis the integrated luminosity is calculated with the ATLAS luminosity calculation tool [95]. As input in the calculation, it is used the *Luminosity Flag:OflLumi-7TeV-003, PhysicsTrigger:EF_2mu4_Jpsimumu, GRLfile:data10_7TeV_periodAllYear_-DetStatus_v21_pro05_CoolRunQuery-00-04-00 _muon.xml*. The output of the calculation is $40.0\,\text{pb}^{-1}$ (with negligible statistical uncertainties).

- The production cross-section of the χ_b is retrieved from the work done in [82] but the error of this number is not reported in any of the theoretical studies. The writer, few months ago, contacted the working group of [82] and asked for an update of the expected cross-section of the χ_b production at $7TeV$ with its corresponding error. Unfortunately, until the moment of the writing of this thesis, there is not any publication with the corresponding error but according to colleagues from the theory community of the ATLAS Bphysics and beyond, an estimation of the statistical uncertainty in the χ_b production cross-section is 20%. This is the dominant source of systematic uncertainties of this analysis.

The Br$(J/\psi \to \mu^+\mu^-)$ with its corresponding uncertainty is retrieved from PDG [4] and it is $(5.93 \pm 0.06)\%$.

The number of background events in the signal region is calculated by side-band interpolation. Different fit models can be used to evaluate the background in the signal region and the differences in their results are propagated accordingly as systematic uncertainties. In this measurement the fit model used is a linear function ($y = ax + b$) and we find that in the signal region $^{2010}N_{\text{sig. region}}$ =**0.76±0.89** events are expected to be background. No other model is used to fit the background and the final number is reported without systematic uncertainties in this round of the analysis. With the statistics of 2010 data and taking into consideration [77, 84], the theoretically expected number is $^{2010}N_{\chi_b}^{\text{theory}} = 0.02$.

The factor $A\epsilon$ refers to the detector acceptance and efficiencies in the reconstruction phase of the analysis. From the 100000 generated events, only 659 survived the acceptance of the detector, the pre-selections, the trigger and optimization cuts. The $A\epsilon$ is calculated by:

$$A\epsilon = \frac{N_{\text{reconstructed}}}{N_{\text{generated}}} = \frac{659}{100000} = 6.6 \times 10^{-3}$$

In the current round of the analysis, there is not any estimation of the systematic errors of $A\epsilon$ but instead, only the statistical error is propagated, $\delta(A\epsilon)_{\text{stat}} = 2.5 \times 10^{-4}$.

Errors on results in High Energy Physics are traditionally reported by using classical confidence intervals. There are several different techniques for constructing such intervals. Below, the most well-known ones are referenced.

A considerable dissatisfaction concerning the construction of the upper confidence limits has been noticed during the recent years, in the cases of Poisson processes with background, or of Gaussian errors with a bounded physical region. The Feldman Cousins technique (FC) [96] is a powerful technique, which, by using a particular choice of ordering, results in intervals which are never unphysical or empty.

The Rolke method [85] is based on a "profile likelihood" approach, where the profile likelihood is a likelihood which accounts for nuisance parameters. The resulting intervals for the parameters in almost all common cases, have the exact coverage probability for all values of the nuisance parameters. The signal in this approach is assumed to be distributed according to the Poisson distribution, while different assumptions can be made on the distribution of the nuisance parameters.

CLs [6] is a well-known technique for the extraction of the upper limit, motivated by the frequentist statistics. It is a well-known framework used for the combined searches at High Energy Physics experiments.

The FC approach works well in case of no (or negligible) uncertainties, therefore it cannot accommodate the uncertainty of the background estimation and SES. Due to that, the FC method is not chosen for our analysis.

In the analysis of the Br$(\chi_b \to J/\psi J/\psi)$, it is decided to be used the Rolke method since it offers a statistical treatment of the errors, its results are generally accepted from the scientific community and it does not require a difficult (and thus easy to errors) implementation, like the CLs technique.

The Rolke is a clear, easy to implement, method that treats correctly the uncertainties and it is the one used in the extraction of the Br$(\chi_b \to J/\psi J/\psi)$ limit. A number of *toy* experiments (1000) are performed to evaluate the upper limit expectations at 90% and 95% CL. The mean and median are reported in table 5.4.

CL %	Mean	Median
90	4.2×10^{-3}	3.2×10^{-3}
95	5.7×10^{-3}	4.6×10^{-3}

Table 5.4: *Mean and median upper limit of $Br(\chi_b \to J/\psi J/\psi)$ using LHC 2010 data.*
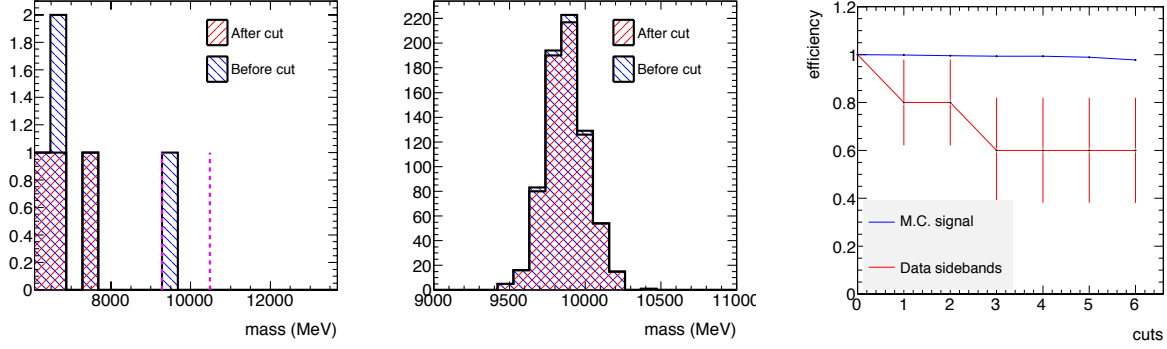
Figure 5.10: *The invariant mass distribution of the real data (left) and simulated signal events (right). The efficiency drop is negligible in the case of signal while it drops to the half in the case of the background. The blue and red curves of the right plot, display the drop of the efficiency as a function of the applied cut for the data and the simulated signal accordingly.*

5.13 Estimation of the Sensitivity of the Analysis Using 2011 Data

The integrated luminosity of LHC collected during 2010 was limited, and thus insufficient to make an observation. Experimentally, this is confirmed by the insignificant information extracted from the distribution of the invariant mass of the χ_b candidates. Nevertheless, the integrated luminosity of LHC collected during 2011, is two times of magnitude larger than the one of 2010, which permits the expectation of a meaningful study for the extraction of the limit of the $Br(\chi_b \to J/\psi J/\psi)$.

Although, at the current state of the analysis, the invariant mass distribution in the signal region is decided to stay unrevealed, the distribution of the sidebands can offer valuable information concerning the expected background yield. This information, together with the theoretical values of the χ_b production cross-section, $\sigma(pp \to \chi_b + X)$ and its branching ratio to J/ψs, $Br(\chi_b \to J/\psi J/\psi)$, can offer a realistic estimation of the sensitivity of the analysis.

At the moment, there is not any theoretical estimation of the $pp \to \chi_b X$ production and the $Br(\chi_b \to J/psiJ/psi)$ at 7 TeV. Nevertheless, taking into consideration [77, 84] and the current reconstruction efficiency of our analysis, the theoretically expected number is $^{2011}N_{\chi_b}^{theory} = 2.2$. Using the data 2011 and assuming a liner fit, the number of background events, after the proper cuts, in the signal region is calculated to be $^{2011}N_{\text{sig. region}}$ =**3.02±0.58** (we take into consideration that the study of the extraction of the yield uses only half of the statistics, since the other half is used during the study of cuts optimisation). The final distributions of data and signal MC of the invariant mass of the χ_b are shown in Figure 5.11. Details of the signal and background yield after progressive addition of the optimised cuts can be found in Table 5.5. In

CUT	N_{SIG}	signal $\varepsilon \pm \delta\varepsilon$	N_{BGR}	background $\varepsilon \pm \delta\varepsilon$	$N_{\text{BGR}}^{\text{sig}} \pm \delta\left(N_{\text{BGR}}^{\text{sig}}\right)$
No cut	722	1±0	78	1±0	2.5 ± 0.3
$+t_0$ sig	698	0.96±0.006	58	0.74±0.049	2.1±0.3
$+\chi_{3D}^2$	692	0.95±0.007	55	0.70±0.051	2.0±0.2
$+\chi^2$	690	0.95±0.007	53	0.67±0.052	2.0±0.3
$+\alpha_{2D}$	672	0.93±0.009	49	0.62±0.054	1.9±0.2
$+p_T$	659	0.91±0.010	45	0.57±0.055	1.6±0.3
$+I_{0.7}$	651	0.90±0.011	39	0.5±0.056	1.5±0.2

Table 5.5: *Information concerning the signal and background yields after progressive addition of the optimised cuts. The N_{SIG} and N_{BGR} are the numbers of signal and background candidates accordingly, that survive the cuts. The N_{BGR}^{sig} is the number of background events in the signal region.*
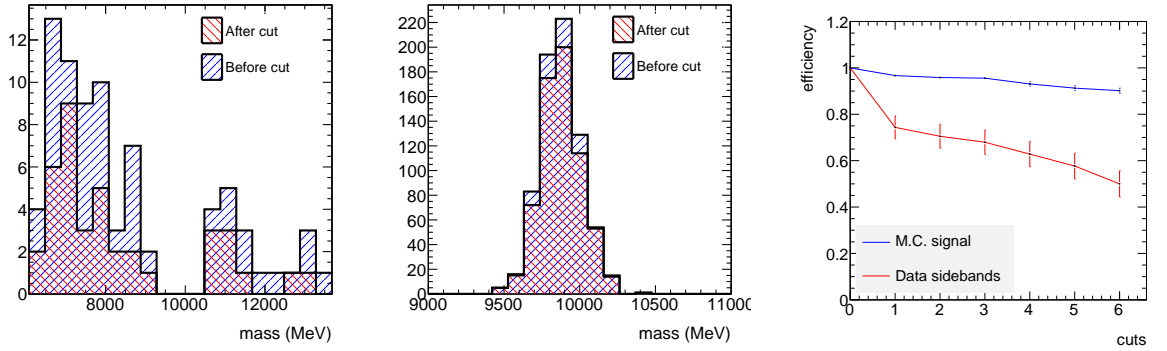
Figure 5.11: *The invariant mass distribution of the real 2011 data (left) and simulated signal events (right). The signal region in case of data remains blinded. After applying the optimised cuts, in case of the signal the efficiency drops slightly while in the case of the background, the efficiency drops to the half. The blue and red curves of the right plot, display the drop of the efficiency as a function of the applied cut for the data and the simulated signal accordingly.*

order to get an estimation of sensitivity of the analysis, the effective cross section for the signal and the background is compared, where the effective cross section σ' is given by $\sigma' = N/L_{int}$. In the case of background, the measured effective cross section $\sigma'_{bgr} = (0.58 \pm 0.01)$ fb while the theoretical value for the effective cross section of the signal based on [82] lie in the range $\sigma'_{bgr} = [0.23 - 1.47]$ fb. We conclude that the effective cross section of the measured background is comparable with the effective cross section of the expected signal, which indicates that the analysis has obtained the required sensitivity and the statistics of the LHC 2012 data (even a fraction of them) should lead to a first observation.

Part II

Rare B Decays

Chapter 6

Theoretical Motivations for the Studies of Rare B Decays

6.1 Introduction of Formalism

The weak interaction is a fundamental force of nature responsible for the decays of charged pions, muons and neutrons. There are two kinds of weak interactions: *charged* interactions, that are mediated by the $W^{\pm}$, and *neutral* interactions, that are mediated by the Z^0.

6.1.1 Charged Weak Interactions

Leptons experience weak interactions via the coupling of Ws to leptons. In such interactions an electron/muon/tau is converted into its associated neutrino $\nu_e/\nu_\mu/\nu_\tau$ with the emission (or absorption) of a W^- (or a W^+). In the case of leptons, the coupling of $W^{\pm}$ occurs strictly within a particular generation[1]. Since cross-generation mixing among the leptons does not appear, the conservation laws of electron number, muon number and tau number can be derived.

lepton generations	quark generations
$\begin{pmatrix} \nu_e \\ e \end{pmatrix}$, $\begin{pmatrix} \nu_\mu \\ \mu \end{pmatrix}$, $\begin{pmatrix} \nu_\tau \\ \tau \end{pmatrix}$	$\begin{pmatrix} u \\ d \end{pmatrix}$, $\begin{pmatrix} c \\ s \end{pmatrix}$, $\begin{pmatrix} t \\ b \end{pmatrix}$

This does not happen in the case of quarks, though. The coupling of W to quarks does not strictly respect the particle generation. In the opposite case, laws like "bottom-up" conservation would exist and, since a decay of a particle into lighter particles is prevented by a conservation law, particles like the lightest B-meson would not decay any more, leading to a very different world [100].

---

[1]In fact, recent results at Kamiokande [97] and SuperK [98, 99], show strong evidence for neutrino oscillations using atmospheric neutrinos. This means that neutrinos can convert from one flavour to another and the lepton numbers (electron, muon, tau) are not conserved. This discovery, suggests modest changes in the framework of charged weak interactions within the SM but we do not know exactly yet the form they will take.

Indeed there are plenty of experimental observations of cross-sectional coupling in quarks, as for example in the decay $\Lambda \rightarrow p + e^- + \bar{\nu}_e$. This kind of experimental observation was first addressed theoretically in 1963 by the work of Cabibbo [101], then, 7 years later by the GIM mechanism [102] and in 1973 by the work of Kobayashi and Maskawa [103]. The result of this work is the CKM matrix, which is a unitary matrix that keeps the information of the cross-generation couplings of quarks.

$$V_{\text{CKM}} = \begin{pmatrix} V_{ud} & V_{us} & V_{ub} \\ V_{cd} & V_{cs} & V_{cb} \\ V_{td} & V_{ts} & V_{tb} \end{pmatrix}, \qquad \begin{pmatrix} V_{d'} & V_{s'} & V_{b'} \end{pmatrix} = V_{\text{CKM}} \begin{pmatrix} V_d & V_s & V_b \end{pmatrix}$$

where

$\qquad |V_{ij}|^2$ is the probability of a transition from a quark i to a quark j

$\begin{pmatrix} V_d & V_s & V_b \end{pmatrix}$ are the states of a specific color (physical particles)

$\begin{pmatrix} V_{d'} & V_{s'} & V_{b'} \end{pmatrix}$ are the "corrected" states to be used in the weak interactions

The nine complex coupling numbers of the CKM matrix can be reduced to 3 real numbers, the generalised Cabibbo angles (θ_{12}, θ_{23}, θ_{13}), and an imaginary phase δ (since CKM matrix is a 3×3 unitary matrix). After this parametrisation, which is the standard parametrisation in the Particle Data Group, the matrix gets the form:

$$V_{\text{CKM}} = \begin{pmatrix} c_{12}c_{13} & s_{12}c_{13} & s_{13}e^{-i\delta_{13}} \\ -s_{12}c_{23} - c_{12}s_{23}s_{13}e^{i\delta_{13}} & c_{13}c_{23} - s_{12}s_{23}s_{13}e^{i\delta_{13}} & s_{23}c_{13} \\ s_{12}s_{23} - c_{12}c_{23}s_{13}e^{i\delta_{13}} & -c_{12}s_{23} - s_{12}c_{23}s_{13}e^{i\delta_{13}} & c_{23}c_{13} \end{pmatrix}$$

where

$$c_{12} = \cos\theta_{12} \quad \text{and} \quad s_{12} = \sin\theta_{12}$$

The V_{CKM} is the unique source of CP violation and the SM offers no insight on this. The values are experimentally calculated:

$$|V_{ij}| = \begin{pmatrix} 0.97428 & 0.2253 & 0.00347 \\ 0.2252 & 0.97345 & 0.0410 \\ 0.00862 & 0.0403 & 0.9991 \end{pmatrix}$$

6.1.2 Neutral Weak Interactions

Although the first theoretical expectation of neutral weak interactions appeared in 1961 by Glashow [104], in the theory of electroweak unification, experimental data of neutral weak interactions appeared only in 1973 in CERN through the reaction

$\quad \nu_\mu + e^- \rightarrow \nu_\mu + e^-, \qquad$ neutral weak interaction of leptons

$\quad \bar{\nu}_\mu + N \rightarrow \bar{\nu}_\mu + X, \qquad$ neutrino-quark process in neutrino-nucleon scattering

The unitarity of the V_{CKM} leads to

$$\Sigma_i V_{ij} V_{ik}^* = \delta_{jk}$$

Such relations can be geometrically represented by a triangle in the complex plane. One of these relations, specifically for $j = d$, $k = b$ is of particular interest for b-decays, where

$$V_{ud}V_{ub}^* + V_{cd}V_{cb}^* + V_{td}V_{tb}^* = 0$$

$$(\bar{\rho}, \bar{\eta})$$

α

$\dfrac{V_{ud}V_{ub}^*}{V_{cd}V_{cb}^*}$

$\dfrac{V_{td}V_{tb}^*}{V_{cd}V_{cb}^*}$

γ

β

$(0,0)$

$(1,0)$
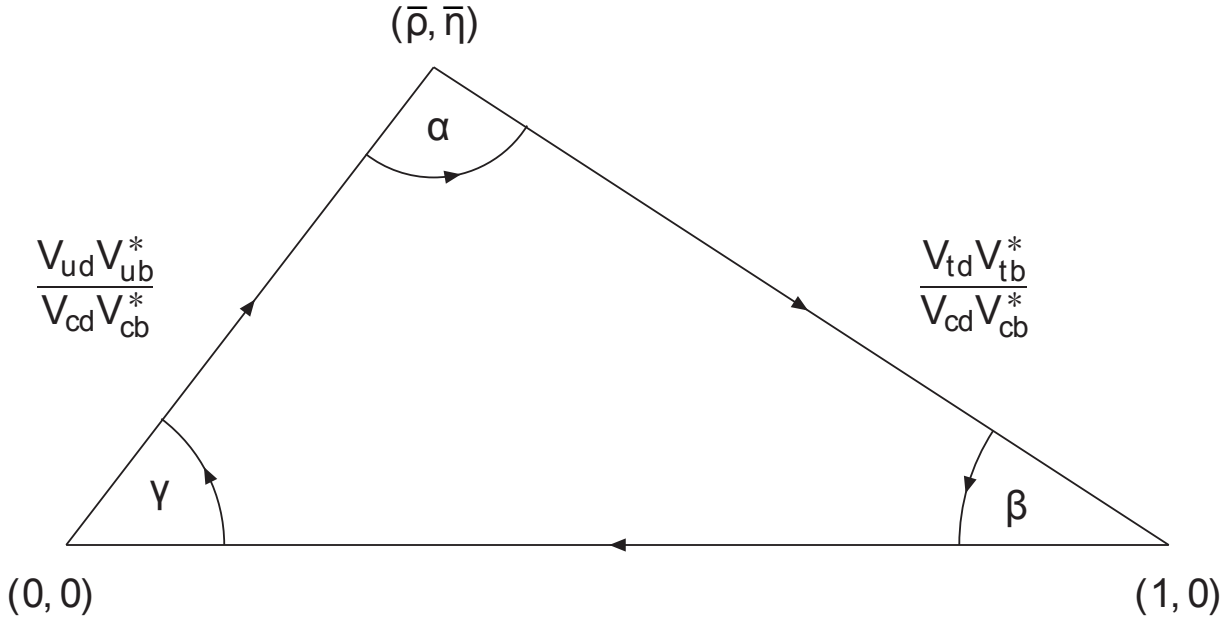
Figure 6.1: *The rescaled unitarity triangle. (V_{cd} is real and lengths are divided by $|V_{cd}V_{cb}^*|$) where the three vertices are fixed in $(0,0), (1,0), (\bar{\rho}, \bar{\eta})$ - Wolfenstein parameters [105].*

which is known as *unitarity triangle* (see Figure 6.1). The angles of the triangle are:

$$\alpha = \arg\left(\frac{-V_{td}V_{tb}^*}{V_{ud}V_{ub}^*}\right), \qquad \beta = \arg\left(\frac{-V_{cd}V_{cb}^*}{V_{td}V_{tb}^*}\right), \qquad \gamma = \arg\left(\frac{-V_{ud}V_{ub}^*}{V_{cd}V_{cb}^*}\right)$$

6.2   Flavour Changing Neutral Currents

A *flavour changing neutral current* (FCNC) is an interaction where the flavour of a quark or lepton changes via a coupling of a neutral boson. Since, within the Standard Model (SM), the rate of the FCNC is quite small, it offers a wonderful "smoking gun" of new physics in cases where it is measured to be substantially higher. This is because decays of e.g. $B_{d,s} \to \mu^+\mu^-$ can happen, but not at tree level. They can only be produced through loop processes (see Figure 6.2), which make them extremely rare. They are classified as

- $\Delta F = 1$ transitions (the flavour of a meson is changed by 1 unit).

- $\Delta F = 2$ transitions (the flavour of a meson is changed by 2 units, like in meson anti-meson transitions).

At loop level, the FCNC transitions are a set of triple and quartic effective vertices and are known as box and penguin diagrams, respectively.

The decay of $B_s^0 \to \mu^+\mu^-$ within the standard model is dominated by a Z boson penguin diagram and a box diagram with the exchange of two W bosons. As a purely leptonic decay, it has a quite simple theoretical description and a very clean experimental signature. Some of the Feynman diagrams that represent the corresponding loop process are displayed in Figure 6.2.
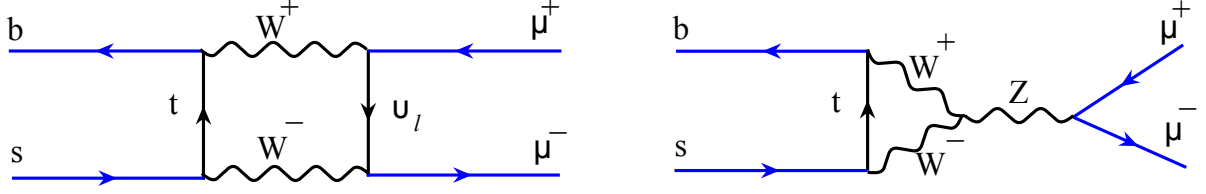
Figure 6.2: *Feynman diagrams of box (left) and penguin (right) processes.*

6.3   FCNC and New Physics

FCNC tests have already proved themselves as useful tools for shaping the SM. The GIM model [102] got a quantitative prediction after confirming that there are no FCNC transitions in $K_L \rightarrow \mu^+\mu^-$. Furthermore, "top-less" models were ruled out, since no NCFC process was observed in B-decays. Similarly, extensions to the SM can introduce new FCNC decays that have to be confirmed experimentally. The FCNC theories of NP include

- Supersymmetric models [106], where FCNC processes can be produced at a tree level diagram.

- Forth generation quark models where a fourth generation quark can lead in FCNC.

- Technicolor models [107] where FCNC appears in new Z couplings.

- Extra dimension models.

- Extra quark models [108] that can lead to FCNC tree processes.

6.3.1   Theoretical Expectations and Measurement of $\mathbf{Br}(B_s^0 \rightarrow \mu^+\mu^-)$

The theoretical prediction of the branching fraction is $\mathrm{Br}(B_s^0 \rightarrow \mu^+\mu^-) = (3.5 \pm 0.3) \times 10^9$ [2]. The latest results from the different experiments in Tevatron and LHC are summarised in table 6.1.

experiment	Br upper limit ($\times 10^{-8}$)	$L_{\mathrm{int}} \left(\mathrm{fb}^{-1} \right)$
D0 [109]	5.1	6.1
CDF [110]	4.0	7.0
CMS [111]	1.9	1.14
LHCb [112]	1.6	0.37
ATLAS [113]	2.2	2.4

Table 6.1: *The latest public results for the $Br(B_s^0 \rightarrow \mu^+\mu^-)$ at 95% CL upper limit presented by the collaborations D0, CDF, CMS, LHCb and ATLAS.*

6.3.2   Motivations for the Measurement of $\mathbf{Br}(B_s^0 \rightarrow \mu^+\mu^-)$

The $B_s^0 \rightarrow \mu^+\mu^-$ decay is allowed through FCNC transitions within the SM, as described in the Feynman diagrams in Figure 6.2. The decay is dominated by a Z/Higgs penguin diagram. A contribution of the box diagram is suppressed by a factor of $(M_W/m_t)^2$, where M_W, M_t are the

mass of the W-meson and top-quark, respectively and the decay is not allowed at tree level. Furthermore, the decay is helicity-suppressed by a factor $(m_l/m_{B_s^0})^2$.

In the LHC physics programme, since the Standard Model gives very precise predictions for rare decays, measurements like the $\mathrm{Br}(B_s^0 \to \mu^+\mu^-)$ provide an extremely sensitive testing ground for new physics. Indirect searches like these are complementary to the direct ones, they do not rule out new physics, but constrain theoretical models for it, and help set the direction for searches in all the LHC experiments. Moreover, since indirect searches can in principle be sensitive to much smaller scales than the direct ones are, they can address new physics models that cannot be proven experimentally with the current energy reach of the accelerator machines.

In the following chapter, it will be presented the the extraction of the upper limit of $\mathrm{Br}(B_s^0 \to \mu^-\mu^+)$ using $2.4\,\mathrm{fb}^{-1}$ of the 2011 ATLAS LHC data.

Chapter 7

Limit on $\mathrm{Br}(B^0_s \to \mu^+\mu^-)$ with the ATLAS Detector

This section documents a multi-bin analysis performed to search for $B^0_s \to \mu^+\mu^-$ decays. It is based on an integrated luminosity of $2.4\,\mathrm{fb}^{-1}$ collected by ATLAS in the first half of 2011 pp collisions ($\sqrt{s} = 7\,\mathrm{TeV}$) data taking period (details about the data used in B.1). It is important to note that the analysis presented here is the work result of several people, including the author which contributed extensively in some important parts. The parts that correspond to the work of the author will be documented in detail while the other parts will be outlined here, for the sake of completeness. References to detailed documentation will be provided when applicable. For a full detailed documentation of all parts one can refer to [3].

7.1 Analysis Methodology

The analysis is a study of the relative $\mathrm{Br}(B^0_s \to \mu^+\mu^-)$ with respect to a well-established reference signal. The reference channel is the $B^\pm \to J/\psi K^\pm$, chosen to minimise the systematic uncertainties in the evaluation of the relative efficiencies and acceptances. The $\mathrm{Br}(B^0_s \to \mu^+\mu^-)$ limit is calculated through the following formula

$$\mathrm{Br}(B^0_s \to \mu^+\mu^-) = N_{\mathrm{obs}}\,\mathrm{SES}$$

where N_{obs} is the number of observed events. The SES is the Single Event Sensitivity, given by

$$\mathrm{SES} = \mathrm{Br}_{\mathrm{ref}}(B^\pm \to J/\psi K^\pm)\,\frac{f_u}{f_s}\,\frac{1}{N_{\mathrm{ref}}}\,\frac{A_{\mathrm{ref}}\epsilon_{\mathrm{ref}}}{A\epsilon}$$

where $\mathrm{Br}_{\mathrm{ref}}(B^\pm \to J/\psi K^\pm)$, N_{ref}, A_{ref} and ϵ_{ref} are the branching ratio of the reference decay $B^\pm \to J/\psi K^\pm$, the number of $B^\pm$ candidates, the geometrical acceptance of the detector, the (reconstruction and trigger) efficiency respectively, while A and ϵ are the geometrical acceptance of the detector and the (reconstruction and trigger) efficiency, respectively. In addition, f_u/f_s is the ratio of the fragmentation functions of the u and s quarks.

The analysis that is performed is *blind*[1]. The signal region $[5066, 5666]\,\mathrm{MeV}/c^2$ is not revealed until the limit extraction method is completely defined. In order to avoid biases,

---

[1]An analysis is characterised as *blind* when certain information is not revealed to the people involved so that concious or sub-concious bias is prevented. In High Energy Physics, the *blind* analysis strategies became popular the recent years and they are used in measurements of very small expected signals

the odd-numbered side-band events are used in signal/background comparisons, multivariate classifier training and selection optimisation, while the even-number events are exclusively used for the final background interpolation and the extraction of the $B^{\pm}$ yield.

Finally, in order to maximally exploit the data information, the sample is divided into three subsets, according to the three mass resolution families (barrel, transition and end-cap, as will be described in Section 7.4). A Confidence Level (CLs)[2] statistical extraction method is used to set an upper limit of the branching ratio.

7.2   Pre-selection of Candidates

A preliminary selection is applied in the candidate events in order to provide a first reasonable skim of the events. The pre-selection cuts are explained below and they are summarised in table 7.1.

- All the accepted events are using a *di-muon* trigger (*EF_2mu4_Bmumu* or *EF_2mu4_Jpsimumu*[3] for the signal and reference channel respectively), which requires that two muons in the event have transverse momentum greater than 4 GeV/c.

- The two muons that belong to the B_s^0-meson are *combined* muons (inner detector hits matched to the muon spectrometer hits).

- The muons are reconstructed with the STACO [89] algorithm (detailed studies of STACO and MUID [90] performance show that the STACO algorithm collects the most wanted attributes).

- All the B-meson properties come from the vertex fit.

- The primary vertex information is extracted from the primary vertex that is closest to the B-meson vertex in the $z-$direction.

- Special attention is given to the selection of the tracks of the muons of the B-meson decay. Only the tracks that satisfy the standard quality criteria, defined by the Muon Combined Performance (MCP) group [92], are accepted. The MCP recommendations require that each combined muon has at least one Pixel b-layer hit, at least 2 Pixel hits, at least 6 SCT hits, at least 3 Pixel and SCT holes and at least 5 TRT hits with less than 90% outliers. Furthermore, the muons are required to have $p_{\text{T}} > 4\text{GeV}$

- the $\chi^2/$ndf of the B-meson vertex is less than 2.

- the B-meson candidates have $p_T^B > 8.0\,\text{GeV}/c$ and $|\eta| < 2.5$.

7.3   Background Contributions

The background of our signal can be split into two main parts, a non-resonant ($B \rightarrow \mu^+\mu^- X$) continuum background and a resonant part (details in appendix J of [3]). An interpolation of the **non-resonant** background is used to define the background in the signal region. The

---

[2]A popular statistical method to setup a limit in a rare physical process.

[3]EF_2mu4_Jpsimumu or EF_2mu4_Bmumu require two 4 GeV/c muons at all trigger levels, with the additional loose invariant mass cuts, compatible with a J/ψ or a B-meson, accordingly.

pre-selection cut	$B_s^0 \to \mu^+\mu^-$	$B^\pm \to J/\psi K^\pm$
fit χ^2/ndf	< 2	< 6
p_T^B	$> 8.0\,\mathrm{GeV}/c$	$> 8.0\,\mathrm{GeV}/c$
$|\eta|$	< 2.5	< 2.5
N combined muons	2	2

Table 7.1: *Summary of the pre-selection cuts of the signal and reference channels.*

events used are the even events, as the odd ones are used on the optimisation part. The **resonant** background is due to the B decay candidates containing either one or two erroneously identified muons (fake muons). Events with two fake muons, are due to two body hadronic B decays ($B \to hh$), e.g. $B_s \to K^+ p^-$, where both hadrons are misidentified as muons. The muon fake rates are extracted from a dedicated for this analysis MC study, which includes Pythia generated samples of $B \to hh$ events of the modes K^+K^-, $\pi^+\pi^-$, $K^+\pi^-$, $K^-\pi^+$. The results show good agreement with the data driven studies of [114] and are used in the evaluation of the $\mathrm{Br}(B_s-> hh) = 1.2 \times 10^{-9}$. It is shown that the double-fake events are the main source of resonant background and the dominant modes of this background are $B_s^0 -> p^+p^-$, $B_s^0 \to K^+p^-$, $B_s^0 \to K^-p^+$. The image 7.1 shows the track's $(p_T^{ID} - p_T^{MU})/p_T^{ID}$.
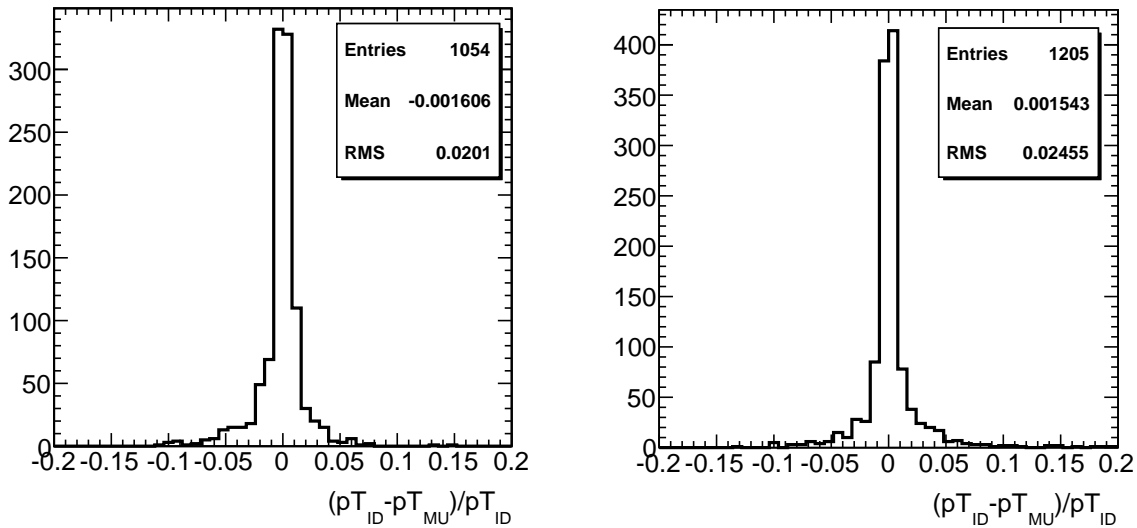
Figure 7.1: *Difference of the track p_T between the muon spectrometer and the inner detector, divided by the track p_T of the inner detector (MC on the left and data on the right).*

7.4 Mass Resolution Families

The different position resolution performance of the detector in the barrel and end-cap region (see Figure 7.2) is propagated to the mass resolution of the B_s^0. Three broad categories of events are identified. In the first family, both the B_s^0 muon tracks are detected in the barrel. In the second family, one muon track is detected in the barrel and the other one in the common transition region, or both muon tracks are detected in the common transition region. In the third family, at least one of the two muon tracks is detected in the end-caps, where

- barrel region: $0 < |\eta| < 1.0$

- transition region: $1.0 < |\eta| < 1.5$

- end-cap region: $1.5 < |\eta| < 2.5$

The selection of the signal and reference channel will be separately optimised for these three categories of events.
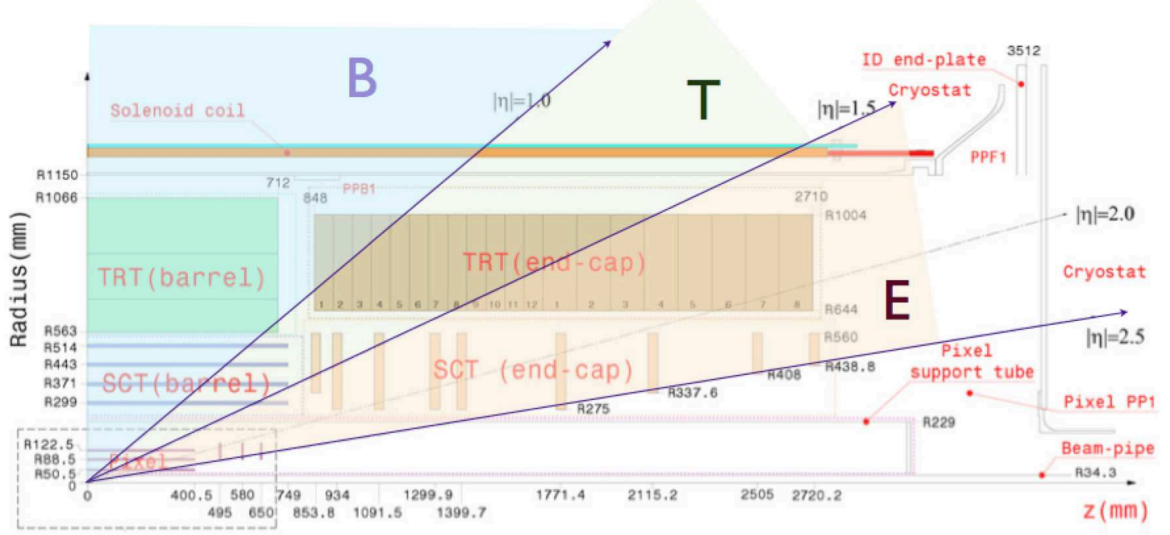
Figure 7.2: *The different pseudorapidity regions of the inner detector that attribute the different resolution families in the mass of the B_s^0.*

7.5   Monte Carlo Tuning

As explained in the analysis strategy, the acceptance and efficiencies that are used in the extraction of the limit, are determined by simulated events of the signal and the reference channel. In order to ensure that the generated simulated Monte Carlo (MC) samples are trustworthy, a detailed MC tuning study has been performed (details can be found in [5]).

7.5.1   Generator-Level Corrections

A first bias comes from the kinematic selections in the phase space of the generated samples of the $B^{\pm}$ and the B_s^0. These cuts are introduced in the generator-level for practical reasons, in order to enhance the production efficiency. The generated MC data used in this analysis include the selections:

- at least one muon with $p_T > 2.5\,\text{GeV}/c$ and $|\eta| < 2.5$

- all muons in the final state with $p_T > 0.5\,\text{GeV}/c$ and $|\eta| < 2.5$

- all hadrons in the final state with $p_T > 0.5\,\text{GeV}/c$ and $|\eta| < 2.5$

The corrections are calculated by comparing the η, p_T bins of the 2D histograms of the biased MC samples to the η, p_T bins of the 2D histograms of some unbiased (without a cut in η, p_T) MC samples generated specifically for this study (see the scatter plot in Figure 7.3). The result is an η, p_T histogram whose contents are the correction factors for each pair of η and p_T. In the remainder of the analysis, the events in each η, p_T bin are re-weighted according to the weight

$$W^{\text{GL}}(\eta, p_T) = \frac{1}{v_{ij}}$$

where v_{ij} is the content of the η, p_T bin of the generator-level correction histogram.

7.5.2 Data-Driven Corrections

Another bias in MC data comes from the fact that nature cannot be described perfectly by any MC generator. The physics models in the simulation of the events are inconsistent with respect to the data. In this case, the bias is addressed by a comparison of generator-level corrected MC events and data side-band subtracted events. The result are data-driven (DD) event weights that are determined with an iterative[4] method. Since the p_T and η of the B-meson are not correlated, two 1D histogram-weight-maps are constructed, one for η, W_η and one for p_T, W_{p_T} (see middle and right plot in Figure 7.3). For the rest of the analysis, the events are corrected accordingly to the weight

$$W^{\text{DD}}(\eta, p_T) = W^{\text{DD}}_{p_T} W^{\text{DD}}_\eta$$

Therefore, in all the studies that follow, an overall weight is assigned to each MC event:

$$W^{\text{GL}}(\eta, p_T) = W^{\text{GL}}(\eta, p_T) W^{\text{DD}}(\eta, p_T) = \frac{1}{v_{ij}} W^{\text{DD}}_{p_T} W^{\text{DD}}_\eta$$
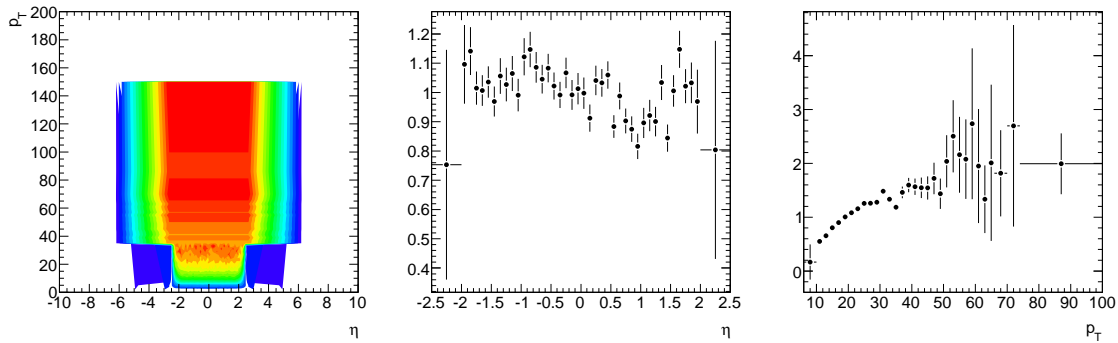
Figure 7.3: *The scatter plot that maps the GL corrections (left) and the histograms of the η and p_T (measured in GeV/c) DD correction in the middle and right accordingly.*

---

[4]Initially the generator level weights are calculated. Next, the Data Driven (DD) weights are calculated. These weights then are applied to the MC events, and the DD reweight procedure is repeated. These iterations stop until the weights stabilize.

7.6 Discriminating Variables and Separation Capabilities

7.6.1 Choice of Separation Variables

The final list of the signal-background separation variables is an important step which affects many other parts of the analysis and contributes directly to the extracted limit. A study of the selection of the discriminating variables needs careful and methodical treatment. Even within B physics studies the separation variables are not always the same; instead, they are chosen accordingly to the underlying physics of the signal and the background. In our study, the choice we made was shaped by four attributes of the underlying physics:

1. The secondary vertex is expected to be separated differently with respect to the primary vertex, depending on the case. For the signal, the B-particle is expected to travel with respect to the primary vertex before its decay and the secondary vertex is expected to be few millimetres away from the primary vertex. On the contrary, in the case of background there is no particle to travel like the B-meson and the secondary vertex is expected to coincide with the primary one. Taking the above into consideration, variables like the *proper time* of the particle or its L_{xy} are expected to be good discriminating variables.

2. The dynamics of the particles of the signal and the background are expected to have different symmetries in the final state, too. The B-particle of the signal is expected to travel in the same (or almost the same) direction with the direction of the vector that connects the primary and the secondary vertex. On the contrary, there is no special preference expected in the direction of the momentum of the B-meson candidate of the background. According to the above, variables like the *pointing angle* are good choices for the signal/background discrimination.

3. Information of the full reconstruction of the event can sometimes offer good insight for the separation of signal and background, too. Tracks that are not relevant to the B-meson decay, in the case of the background, are expected on average to be closer to the secondary vertex than the ones that come from the signal. Variables that reflect such separation are the $D^{\min}$ or $D^{\max}$ (see 7.6.2 for the definition).

4. Finally, hadronisation features of the B-meson can highlight differences between signal and background. In the case of signal, the decay products of the B-meson decay are isolated from other tracks that originate from the same vertex, while in the case of background this is not necessarily true. The *isolation* variable is probably the best candidate that deals with the hadronisation features.

7.6.2 Definitions of Possible Discriminating Variables

What follows is the list of the discriminating variables that are studied and can possibly be used in this analysis. All the corresponding distributions can be found in appendix B.2 in page 156.

- Pointing angle in 2D (α_{2D}) and 3D (α_{3D})
  If $\boldsymbol{x}$ is the vector from the Primary Vertex point to the Secondary Vertex point, then α_{2D} is the angle between the $\boldsymbol{x}$ and the momentum vector, $\boldsymbol{p}$, of the B-meson. It is calculated in the transverse plane (α_{2D}) and in the 3-dimensional space (α_{3D}).

- $\Delta R = \sqrt{(\varphi_x - \varphi_p)^2 + (\eta_x - \eta_p)^2}$
  It is the distance ΔR in the $\eta\phi$ plane, where ϕ is the azimuthal angle and η is the pseudo-rapidity.

- $\chi^2(\mathrm{PV} - \mathrm{SV})$
  This variable is derived from the position and the covariance matrix information of the Primary (PV) and Secondary Vertex (SV). It is χ^2-like variable, under the hypothesis that the primary and B-meson vertex coincide. It is computed separately in the 3-dimensional space (χ^2_{xyz}), in the transverse plane (χ^2_{xy}), and along the z-direction (χ^2_z).

- Impact parameter $d_0^{\min}$ and its significance
  The $d_0^{\min}$ is the impact parameter d_0, calculated in the transverse plane, that corresponds to the smaller value of the d_0 value of the two tracks of the B-meson. The impact parameter significance, $d_0^{\min}/\sigma_{d_0^{\min}}$, is calculated as well, where $\sigma_{d_0^{\min}}$ is the error of the impact parameter.

- Impact parameter $d_0^{\max}$ and its significance
  $d_0^{\max}$ is the impact parameter d_0, calculated in the transverse plane, that corresponds to the larger value of the d_0 value of the two tracks of the B-meson. The impact parameter significance, $d_0^{\max}/\sigma_{d_0^{\max}}$, is calculated as well, where $\sigma_{d_0^{\max}}$ is the error of the impact parameter.

- Isolation
  It is defined as the ratio of $|p_{\mathrm{T}}^B|$ over the sum of $|p_{\mathrm{T}}^B|$ and of the transverse momenta of all tracks within a cone $\Delta R < 0.7$ from the direction of the B-meson, excluding its decay products. Two definitions of the isolation variable are studied, one including the χ^2 compatibility cut and one not including it.

- Distance of Closest Approach (DCA) and its significance
  This variable is designed to exclude vertices compatible with the hypothesis of more than two charged tracks originating from them. We loop over the tracks in the event not used in the candidate reconstruction and select the one closest to the B-meson vertex in the transverse plane. The distance is calculated in the xy plane, $D_{xy}^{\min}$. The DCA significance, $D_{xy}^{\min}/\sigma_{D_{xy}^{\min}}$ is calculated as well, where $\sigma_{D_{xy}^{\min}}$ is the error of the DCA.

- Distances of Closest Approach along the z axis (ZCA) and its significance
  This variable is similar to the $D_{xy}^{\min}$ but it is calculated along the z axis, $D_z^{\min}$. The ZCA significance, $D_z^{\min}/\sigma_{D_z^{\min}}$ is calculated as well, where $\sigma_{D_z^{\min}}$ is the error of the ZCA.

- $L_{xy} = x \cdot \hat{p}_B$
  Where x is the vector from the Primary to the Secondary Vertex and $\hat{p}_B$ is the unitary momentum vector of the B-meson. The L_{xy} significance, which is $L_{xy}/\sigma_{L_{xy}}$, is calculated, too.

- Proper Time and Proper Time significance
  The proper time is defined as $t_0 = L_{xy}M_B/p_T$, where p_T, M_B are the transverse momentum and the mass of the B-meson, respectively. The Proper Time significance, t_0/σ_{t_0}, is calculated as well, where σ_{t_0} is the error of the proper time.

- χ^2 of the vertex fit of the B-meson

- Transverse Momentum, p_T, is the momentum of the B-meson in the xy plane.

- $p_{\text{lng}}^{\max}$ and $p_{\text{lng}}^{\min}$, calculated in 2D and 3D
  These are the maximum and minimum among the two B-meson daughters of the projection of the muon momentum to the B-meson momentum axis. The calculation is done in the transverse plane (2D) and in the 3-dimensional space (3D).

- p_{Trel} calculated in 2D and 3D
  p_{Trel} is the projection of the muon momentum to the axis that is perpendicular to the B-meson momentum axis. The value of the p_{Trel} is the same for both muons by definition. The calculation is done both in the transverse plane (2D) and in 3D.

7.6.3 Discriminating Variables which Deserve Special Treatment

Many of the discriminating variables are calculated during the reconstruction step in the ATLAS analysis framework ATHENA[5] [115] and they are used unchanged in the analysis (e.g. p_T^B). In comparison, some variables need careful treatment before they are ready to be used, while few other variables are derived exclusively offline using some basic reconstruction information. The relevant studies of the variables used in this analysis which deserve special treatment are listed below.

Impact Parameter

The information of the d_0 of the track is calculated in the reconstruction step with respect to the 0-point of the ATLAS coordinate system. On the other hand, the interaction point of the beam always has a small offset depending on the beam conditions. A proper correction of the d_0 has to be performed, as shown in Figure 7.4.

With the help of Figure 7.6 we see that

$$d_0' = (\boldsymbol{x}' \times \hat{\boldsymbol{p}}_{\text{track}}) \cdot \hat{\boldsymbol{z}}, \text{ the } d_0 \text{ calculated in ATHENA}$$
$$d_0 = (\boldsymbol{x} \times \hat{\boldsymbol{p}}_{\text{track}}) \cdot \hat{\boldsymbol{z}}, \text{ the corrected } d_0$$

The correction of the d_0 can be calculated using the following relations

$$\text{If} \quad d_0 = d_0' - d_0''$$
$$\text{where} \quad d_0'' = (\boldsymbol{a} \times \hat{\boldsymbol{p}}_{\text{track}}) \cdot \hat{\boldsymbol{z}} = \left((x-0, y-0) \times \hat{\boldsymbol{p}}_{\text{track}}\right) \cdot \hat{\boldsymbol{z}}$$
$$\text{and} \quad \boldsymbol{a} \times \hat{\boldsymbol{p}}_{\text{track}} = \begin{pmatrix} \hat{\boldsymbol{x}} & \hat{\boldsymbol{y}} & \hat{\boldsymbol{z}} \\ x-0 & y-0 & z-0 \\ \hat{\boldsymbol{p}}_x & \hat{\boldsymbol{p}}_y & \hat{\boldsymbol{p}}_z \end{pmatrix} = xp_y - yp_x$$
$$\text{then} \quad d_0 = d_0' - (xp_y - yp_x)$$

where $\boldsymbol{a}$ is the position of the primary vertex (PV) with respect to the nominal zero point of the ATLAS coordinate system.

Impact Parameter Error

In the ATHENA level reconstruction, access to the error of the d_0 parameter is possible. This error comes from the track information itself. Nevertheless, there is another factor that contributes in the uncertainty of the d_0, that has to do with the error of the measured position of the primary vertex (PV). The contribution of this uncertainty has to be first

---

[5]ATHENA is the ATLAS control and analysis framework. It provides the necessary interfaces and services for building HEP experiment frameworks in the domain of event data processing applications.
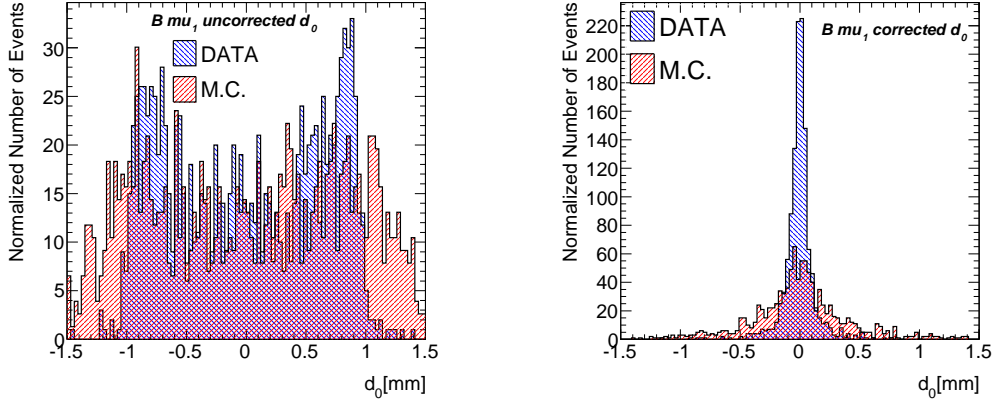
Figure 7.4: *The d_0 of the muon of the B particle before (left) and after (right) the correction.*

compared with the track d_0 error and then quadratically added in an overall d_0 error. The information of the uncertainty of the PV position is stored in the relevant covariant matrices and can be accessed in the ATHENA-level reconstruction step, too.

The schematics of Figure 7.7 help visualise the two error contributions. Finally, the PV error contribution can be calculated by multiplying the covariant matrix with a unit vector that has the PV as starting point and lies in the direction of d_0. The three contributions in the impact parameter error that are coming from the track, the primary vertex and their combination, is shown in Figure 7.5.
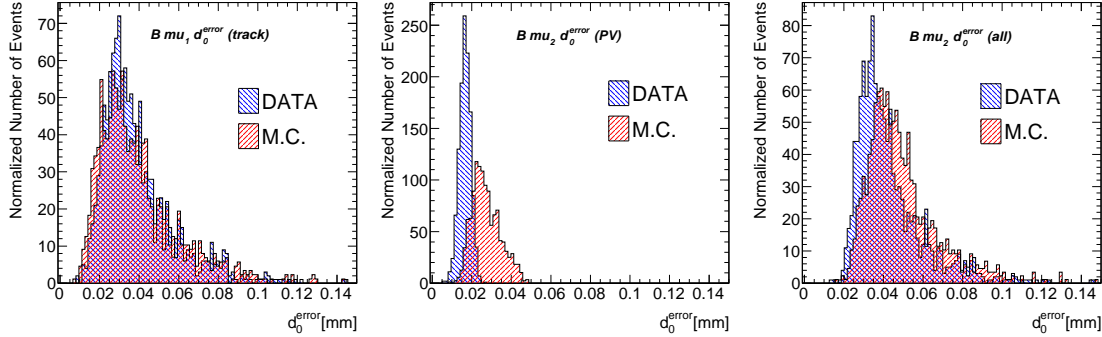
Figure 7.5: *The correction of the d_0 error of the muon. The d_0 error of the track (left) of the primary vertex (middle), of both track and primary vertex (right). The dominant contribution comes from the error of the track.*

7.6.4 Correlation of Separation Variables

After the definition of the discriminating variables, we continue with the study of their correlations. It should be mentioned that before the derivation of the correlation coefficients, two extra cuts —on top of the baseline cuts— were introduced: $L_{xy} > 0$ and $|\alpha_{2D}| < 1.5$. These cuts offer a more realistic picture of the correlations of the variables since they remove the correlation contribution coming from the negative range of variables like L_{xy} and pointing angle. The correlation coefficients are calculated for each pair of variables and are grouped in the matrices
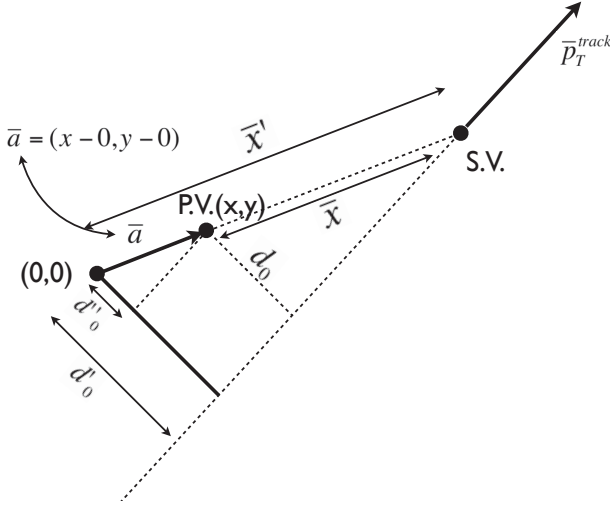
Figure 7.6: *Correction of the d_0.*   **Figure 7.7:** *Correction of the d_0 error.*
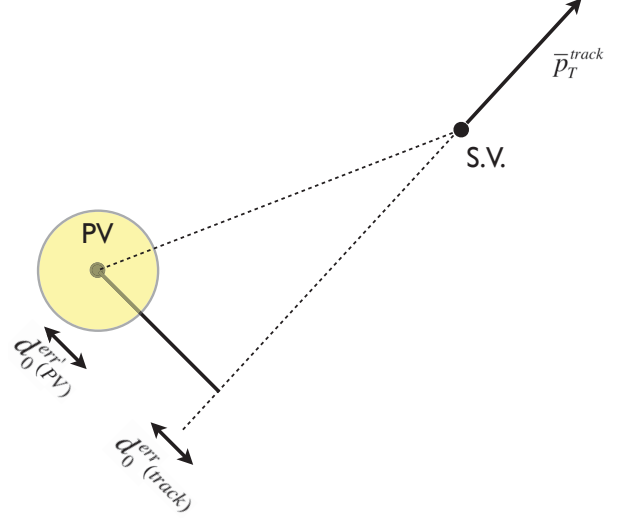
shown in Figure 7.8. The study of the correlation matrices for signal and background offers a better and faster insight in the separation capabilities of the variables and useful results can be drawn by looking into it:

- **Mass correlations**
  Any variable that is correlated with mass, should be discarded since it is biasing the result. The correlation matrix shows that p_{Trel} (calculated either in 2D or in 3D) is correlated with mass and therefore, it is not used as discrimination variable.

- **Highly correlated variables**
  Variables that are highly correlated are not independent variables and share similar physical meaning. In such cases, each group of highly correlated variables is studied separately. We remove from each of these groups the variables showing less separation power.

- **Discrepancy in correlation between signal and background**
  Variables which present different correlations in signal and background may offer good handles for signal/background discrimination. Figure 7.9 summarises the different cases of correlation discrepancies between signal and background.

7.6.5   Correlation Families

By looking into the scatter plots of all the variable pairs, similar correlation patterns appear, which allows us to group the correlations into 4 distinct correlation families.

family A

No real correlation for signal, nor for background. The small correlation that is observed is due to the RMS dependency of one variable with respect to the other variable.

family B

No real correlation for signal, nor for background. Variables are spread homogeneously in the scatter plot with different offsets. Discrepancy in correlation between signal and background comes from different offsets and different RMSs.
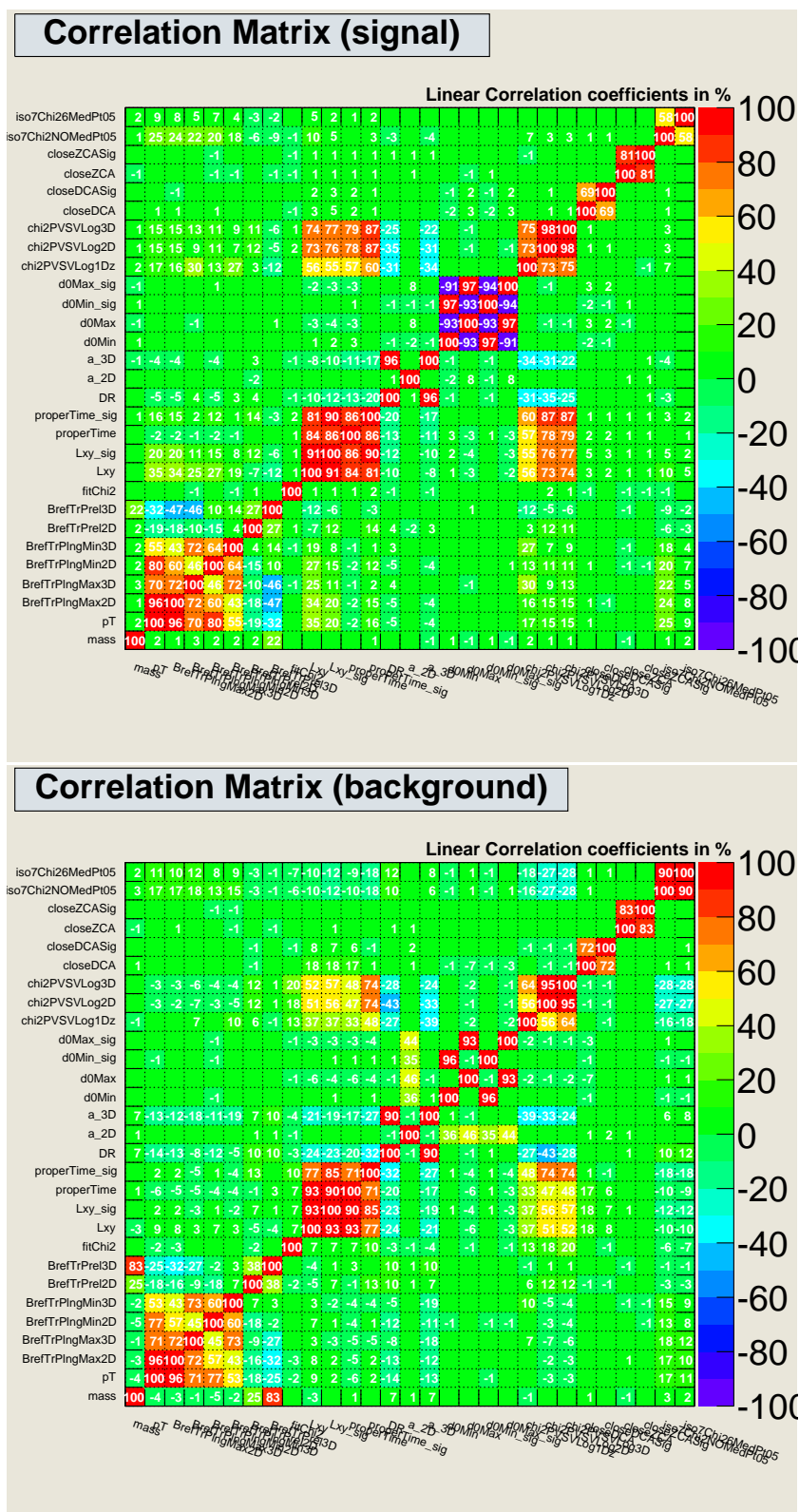
Figure 7.8: *Correlation matrix for the signal (top) and the background (bottom).*

family C

> Strong correlation in signal and in background. If there are several versions of such variables that are not independent to each other, we choose the one with the best separation power.

family D

> Strong (anti)correlation for signal, not correlation for background. Potentially good discrimination handles of the analysis.

7.6.6   Methodology of Selection of Separation Variables

The big initial number of possible discrimination variables (28 in this study) can potentially cause problems to the multivariate analysis classifiers. The study demonstrated in this section aims to reduce the number of discriminating variables without loss of separation power. The information needed comes from the correlation matrix and the signal/background efficiency curves. First, we look into the correlation matrix and we regroup the variables into smaller groups. Each of these groups contains highly correlated variables. Then, by inspecting the *ROC curves* and the *log-efficiency curves* (the definition of these curves can be found in Appendix B.3 in page 159) for every variable in each group, an evaluation concerning the separation power of the variables is made. Some variables are proposed to be kept while others are proposed to be discarded since they do not contribute more in the signal-background discrimination. Finally, taking into consideration the results coming from the small groups, a *final list* of discriminating variables is derived.

The schematics in Figure 7.10 illustrate the different cases which appear in the analysis. With the help of the schematics a set of decision rules concerning the maximum separation power is derived and it is explained below.

Case *A*

> - If variables that correspond to the blue and red curves are independent, we keep both variables since multivariate analysis will extract the maximum separation power found of both high and low signal efficiency ranges.
>
> - If variables that correspond to the blue and the red curves are not independent, we have to consult cases *a*, *b*. If *A* and *a* is true, we keep the variable that corresponds to the red curve, as in all signal efficiency range this variable offers better separation power.
>
> - If *A* and *b* is true, we keep both variables as multivariate analysis will extract the maximum separation power of both high and low signal efficiency ranges.

Case *B*

> We keep both variables as multivariate analysis will extract the maximum separation power of both high and low signal efficiency ranges.

The method that is described above, is applied in all the groups of the initial discriminating variables and a final list of the most powerful of them is extracted. Examples of application of this method can be found in B.3.
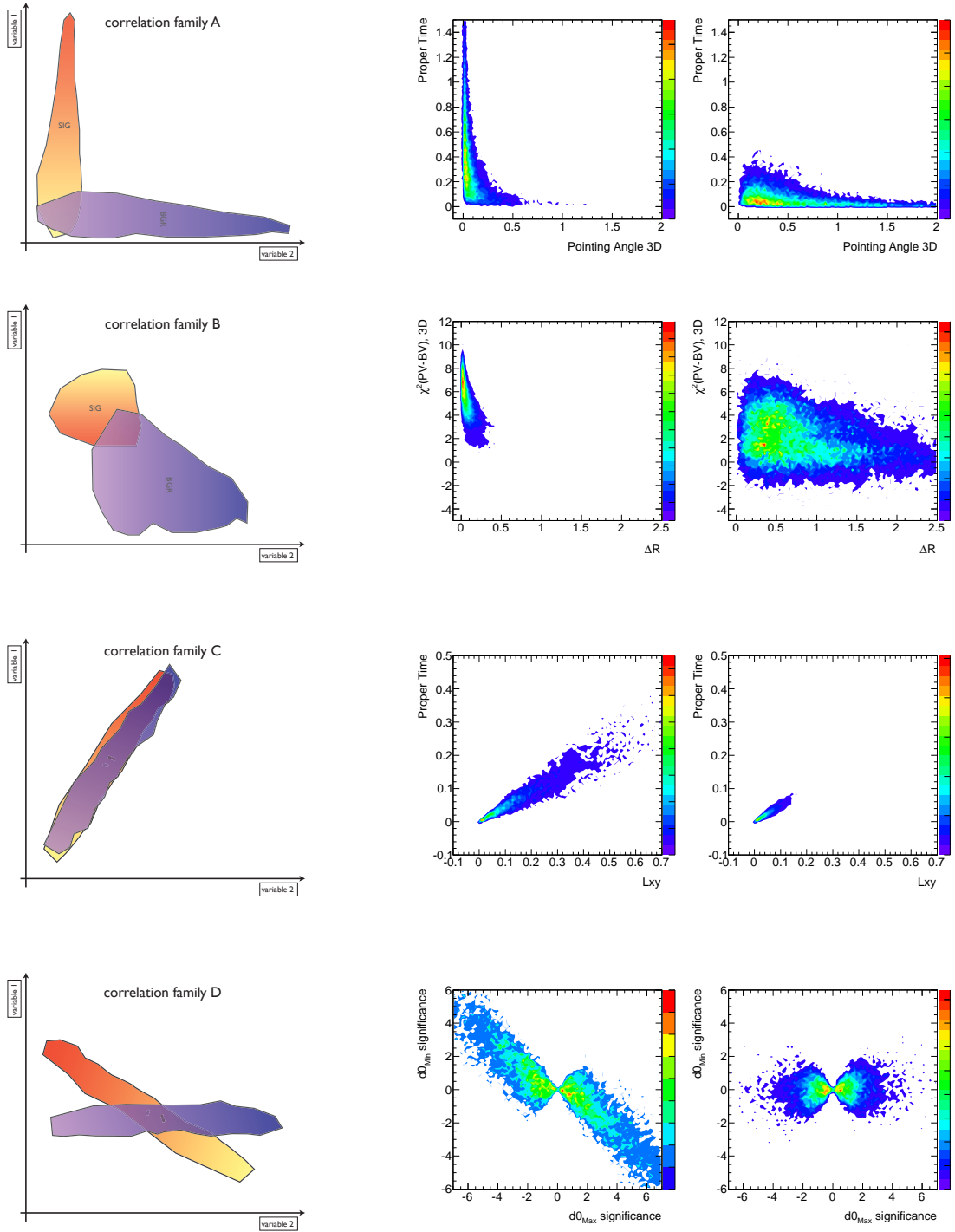
Figure 7.9: *The four correlation families of the variables that show some differences in their correlation between signal and background events. The plots on the left column represent schematically the four different cases, while the middle and right column are examples of each of these families for the signal and the background events, respectively.*
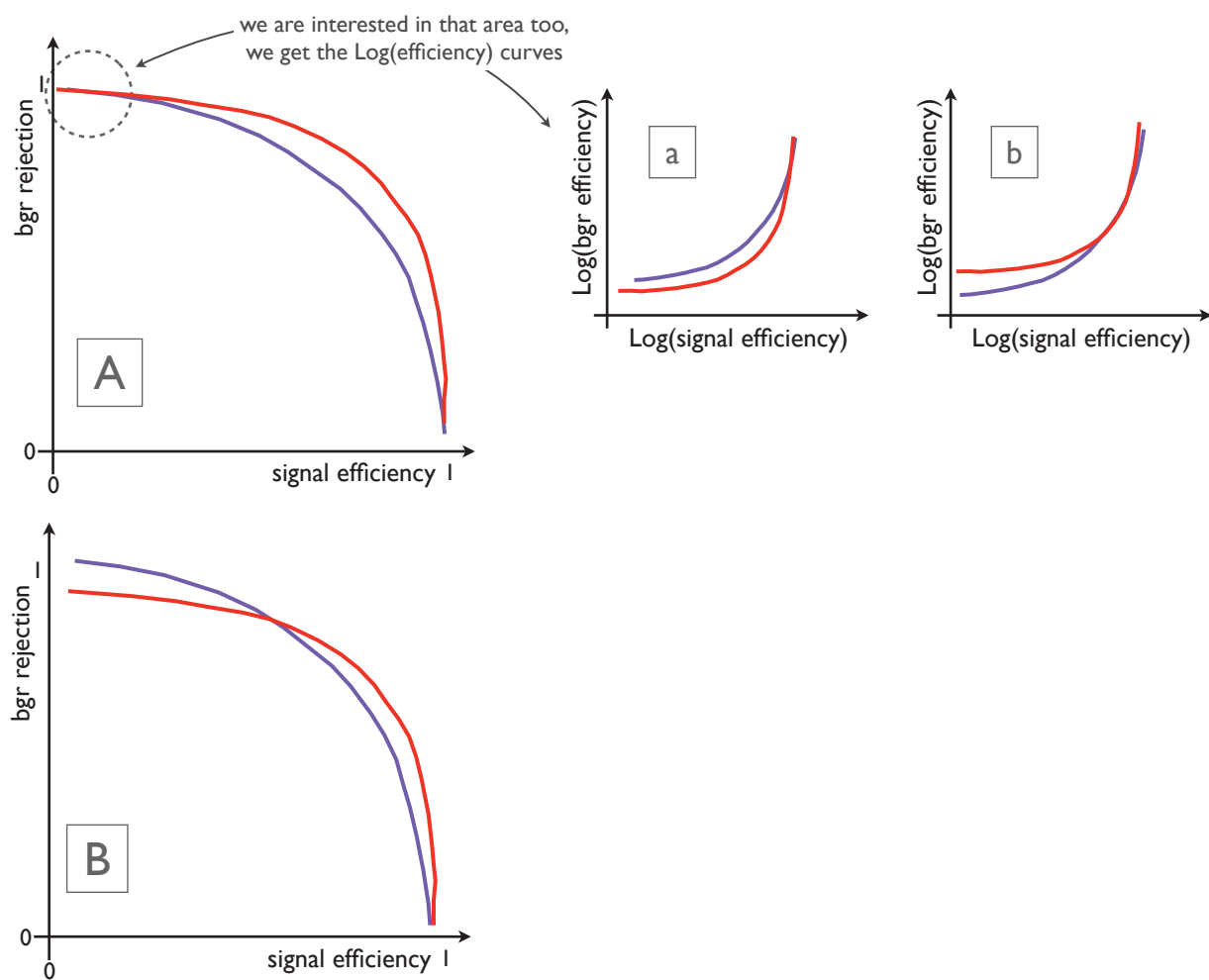
Figure 7.10: *Schematics for the different cases of the efficiency curves.*

7.6.7 The Final List of Discriminating Variables

According to the above studies, a final list of 14 discriminating variables is proposed. The variables with their definitions are summarised in table 7.2, while the signal/background distributions are shown in Figure 7.11.

Variable	Description
$|\alpha_{2D}|$	If $\boldsymbol{x}$ is the vector from the Primary Vertex point to the Secondary Vertex point, then α_{2D} is the angle between the $\boldsymbol{x}$ and the momentum vector, $\boldsymbol{p}$, of the B-meson.
ΔR	$\Delta R = \sqrt{(\varphi_x - \varphi_p)^2 + (\eta_x - \eta_p)^2}$, where ϕ is the azimuthal angle and η is the pseudorapidity.
L_{xy}	Scalar product in the transverse plane of $\boldsymbol{x} \cdot \hat{\boldsymbol{p}}^B$
t_0 significance	Proper decay length $t_0 = L_{xy} M_B / p_T^B$, divided by its uncertainty, σ_{t_0}.
χ^2_{xy}, χ^2_z	χ^2 computed between the measured PV and SV positions respectively in x, y and z.
Isolation $(I_{0.7})$	Ratio of $|p_T^B|$ over the sum of $|p_T^B|$ and of transverse momenta of all tracks within a cone $\Delta R \leq 0.7$ from the direction of the B-meson, excluding its decay products.
$|d_0^{\max}|$, $|d_0^{\min}|$	Maximum and minimum impact parameter in the transverse plane of the B-meson decay products to the primary vertex (used in absolute value).
$|D_{xy}^{\min}|$, $|D_z^{\min}|$	Minimum distance of the closest approach in xy plane between the B-meson vertex and the tracks in the event (used in absolute value).
p_T^B	The transverse momentum of the B-meson.
$|p_L^{\max}|$, $|p_L^{\min}|$	Maximum and minimum momentum of the two muon candidates along the B-meson direction.

Table 7.2: *The final list of discriminating variables.*
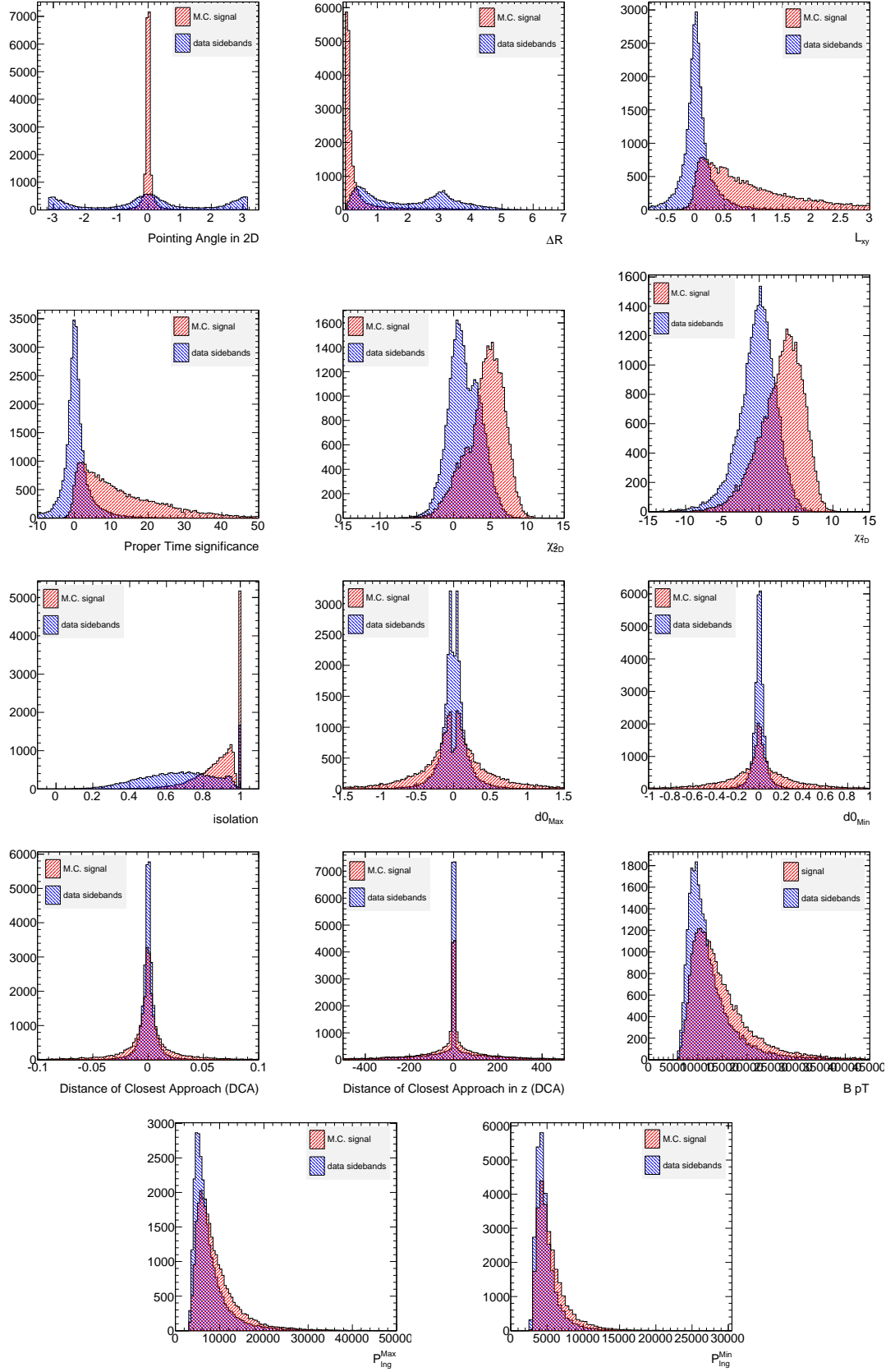
Figure 7.11: *The final list of discriminating variables, defined in Table 7.2. The variables are the α_{2D}, ΔR, L_{xy}, t_0, χ^2_{xy}, χ^2_z, $I_{\Delta R \leq 0.7}$, d_0^{max}, d_0^{min}, D_{xy}^{min}, D_z^{min}, p_T^B, p_L^{max}, p_L^{min}*

7.7   Pileup Effect on Isolation

The isolation variable usually serves as a good discriminating variable in B physics, since B particles are kinematically isolated from other tracks originating from the same primary vertex. However, the isolation variable is notorious for its strong correlation with the increasing pile-up conditions (as is the case with ATLAS). For this reason, a special definition of the isolation variable has been developed for the needs of this study. Detailed information on this definition can be found in the appendix B of [3]. The validation studies undertaken to ensure that the systematic uncertainties coming from this variable are under control, are being presented here.

The naive definition of the isolation variable, $I_{\Delta R}$, is given by:

$$I_{\Delta R} = \frac{p_T^{B_s^0}}{p_T^{B_s^0} + \sum_{\text{tracks}}^{\Delta R \leq 0.7} p_T}$$

where $p_T^{B_s^0}$ is the transverse momentum of the B-meson and the $\sum_{\text{tracks}}^{\Delta R \leq 0.7} p_T$ is the transverse momenta of all tracks within a cone $\Delta R \leq 0.7$ from the direction of the B-meson, excluding its decay products.

The extra selection criteria:

$$\hat{\chi}^2 = \left(\frac{d_0^{\text{PV}_B}}{\sigma_{d_0}^{\text{PV}_B}}\right)^2 + \left(\frac{z_0^{\text{PV}_B}}{\sigma_{z_0}^{\text{PV}_B}}\right)^2$$

where $d_0^{\text{PV}_B}, d_0^{\text{PV}_B}$ are the perigee and $\sigma_{d_0}^{\text{PV}_B}, \sigma_{z_0}^{\text{PV}_B}$ the perigee errors for tracks extrapolated to the primary vertex candidate. The primary vertex associated to the B-meson vertex is the one closest to the B-meson in the direction of z. In the hypothesis that there is only one PV, the perigee for all tracks will be distributed normally: $d_0/\sigma_{d_0} \sim \text{N}(0; 1), z_0/\sigma_{z_0} \sim \text{N}(0; 1)$, the $ln\hat{\chi}^2$ is expected to peak around 0. By setting the cut $ln\hat{\chi}^2 < 6.0$ in the distribution of $ln\hat{\chi}^2$, the tracks of the primary vertex that corresponds to the B_s^0 are separated from tracks that correspond to other primary vertices.

The validation procedure aims to test the efficiency isolation variable against the primary vertex multiplicity. It has to be ensured that the efficiency of the isolation variable does not depend on the number of primary vertices in the event. Accordingly, the straight forward and accurate way to study such a dependence (or independence) is by looking at the efficiency of the isolation variable for a fixed cut, as a function of the primary vertex multiplicity. It is expected that the naive definition will show dependence, while the improved definition will not. The result of the test is displayed in Figure 7.12 for MC (left) and data (right).

Indeed, the test demonstrates that the efficiency of the naive definition of the isolation variable, shows strong dependence with the primary vertex with its efficiency dropping by a factor of 2, for 5 primary vertices and by a factor of ~ 4, for 8 primary vertices. In comparison, the efficiency of the enhanced definition shows extremely mild dependence with the primary vertex multiplicity.

The test appears to be equally sound in both data and MC samples. Nevertheless, the absolute scale of the efficiency in data and MC appears to be different. This difference comes from different potential systematic sources, such as:

- fits in the side-band subtraction method,

- background contamination,
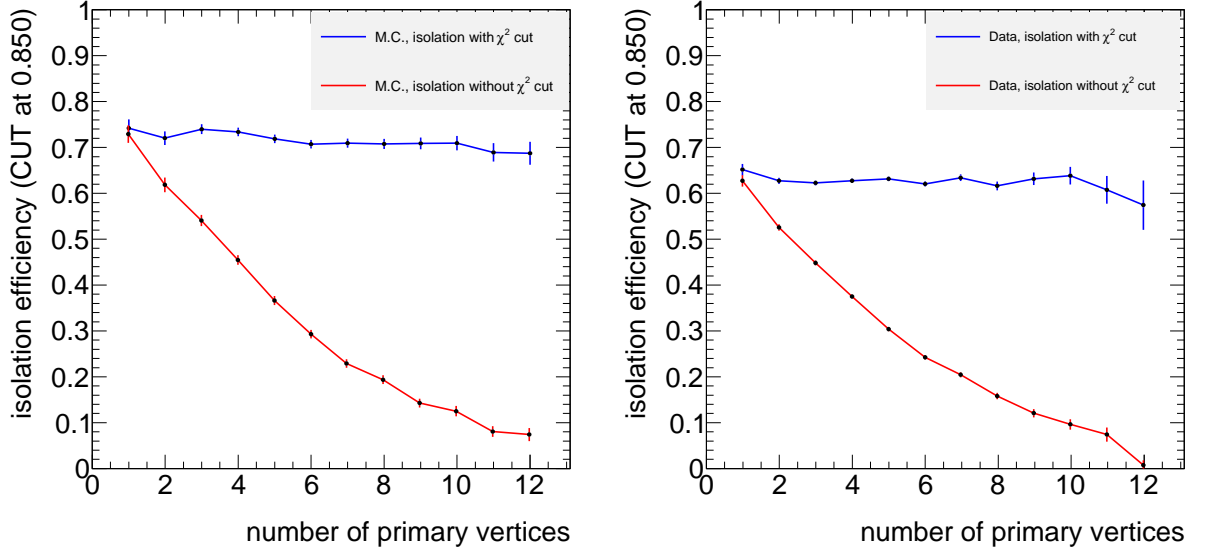
Figure 7.12: *The efficiency of the isolation variable for a fixed cut (Isolation variable $I_{\Delta R} > 0.85$), as a function of the primary vertex multiplicity. The left plot corresponds to the B_s^0 MC signal, while the right plot corresponds to the data.*

- difference in underlying event model between data and MC.

The errors of the efficiencies are treated accordingly. The number of selected events m is treated as a binomial random variable and the efficiency and its error are calculated by minimizing a maximum likelihood [116].

$$P(m; N, \epsilon) = \frac{N!}{m!(N-1)!}\epsilon^m(1-\epsilon)^{N-m} \text{ is the binomial probability}$$

where

N is the number of all trials

m is the number of successes

ϵ is the probability of success in each trial

The estimator of the efficiency is derived by:

$$\partial\left(\ln(\epsilon)\right)/\partial(\epsilon) = 0 \Rightarrow \hat{\epsilon} = m/N$$

Accordingly, the error of the efficiency can be calculated using an estimator for the variance of the efficiency estimator

$$\hat{\sigma}[\hat{\epsilon}] = \sqrt{\hat{V}[\hat{\epsilon}]} = \sqrt{\frac{\hat{\epsilon}(1-\hat{\epsilon})}{N}} = \frac{\sqrt{m(1-m/N)}}{N}$$

7.7.1   Re-weight of MC Events

As previously explained, generator-level (GL) and data-driven (DD) corrections have to be used in order to correct the (p_T^B, η_B) bias by MC generation and the modelling of the physics of the

generator accordingly. The final weight is used per event on the MC sample and is calculated by

$$W = \frac{1}{\text{GL}(\eta, p_T)}\text{DD}(p_T)\text{DD}(\eta)$$

where $\text{GL}(\eta, p_T)$ is derived from the binned (p_T, η) map of the GL selection efficiencies and $\text{DD}(p_T)$, $\text{DD}(\eta)$ are the DD weights derived from the p_T and η binned DD correction maps (see section 7.5.1).

7.7.2 Side-bands Subtraction in Reference Channel

In the pile-up studies of the isolation variable, the distribution of the isolation variable is used after the removal of the background, with the *side-band subtraction method*. The side-band subtraction method is typically used in order to eliminate the background under a signal peak using the distribution on the left and right bands (side-bands). Before applying the method an assumption must be made though: the kinematic variable distributions of the background in the signal region are the same with the ones in the side-bands. The method is performed in three steps.

- First, the peak region and the side-bands region has to be carefully selected. The peak region, should cover at least the $\sim 3\sigma$ region around the mean value of the peak while the side-bands region have to be broad enough to provide the needed statistics excluding on the same time regions of resonances.

- Then, an appropriate function $\mathcal{F}$ that fits the shape of the distribution has to be defined. The function is a sum of an $\mathcal{F}_b$ part that describes the background and an $\mathcal{F}_s$ part that describes the signal. In the case of resonances in the side-bands, the background function has to be modified so as to include them as well. Furthermore, the corresponding integrals of the function in the signal region, $\mathcal{I}_{\text{peak}}(\mathcal{F})$, in the left, $\mathcal{I}_{\text{left}}(\mathcal{F})$, and right side-band, $\mathcal{I}_{\text{right}}(\mathcal{F})$, have to be calculated, too.

- The wanted background subtracted distribution is finally given by

$$\mathcal{D}_{\text{subtracted}} = \mathcal{D}_{\text{peak}} - \frac{\mathcal{I}_{\text{peak}}(\mathcal{F})}{\mathcal{I}_{\text{left}}(\mathcal{F}) + \mathcal{I}_{\text{right}}(\mathcal{F})}(\mathcal{D}_{\text{left}} + \mathcal{D}_{\text{right}})$$

In our specific example of the $B^{\pm}$ reference channel, the fit model is rather complicated (see 7.10).

7.8 Data-MC Comparisons

A validation of the side-band subtracted data against the MC using the $B^{\pm}$ sample is performed (details in section F of [3]), aiming to extract the systematic uncertainties coming from the observed differences. The test is performed for all the potential discriminating variables that are used in the analysis, plus the hit multiplicity of the pixel layer hits for the two muons and the pile-up multiplicity.

The agreement is good in some variables, while in others the overall shapes of the distributions do not agree as well (see examples in Figure 7.13). The discrepancies are suspected to be originating from the side-band subtraction procedure. The assumption that side-bands can

Variable/Vertex type	3-prong	2-prong
α_{2D}	5.6284×10^{-21}	5.30564×10^{-11}
ΔR	0.0365444	9.39301×10^{-5}
t_0 significance	3.44806×10^{-6}	5.90699×10^{-15}
L_{xy}	0.00142891	0.638837
χ_z^2	1.64741×10^{-12}	4.83795×10^{-16}
χ_{xy}^2	5.94821×10^{-6}	1.62198×10^{-7}
$|d_0^{min}|$	0.000773118	-
$|d_0^{max}|$	6.82066×10^{-5}	-
Isolation $I_{\Delta R \leq 0.7}$	0	1.41145×10^{-10}
$|D_{xy}^{min}|$	0.115886	-
$|D_z^{min}|$	3.10501×10^{-14}	-
p_T^B	0.0801387	2.28735×10^{-14}
$|p_L^{max}|$	1.37693×10^{-15}	3.94263×10^{-12}
$|p_L^{min}|$	2.35725×10^{-11}	1.50892×10^{-10}

Table 7.3: *Kolmogorov-Smirnov test statistic of the shapes of the discriminating variables distributions. The 3-prong vertex corresponds to $B^\pm$, while the 2-prong one deals with variables that by construction differ between $B^\pm \to J/\psi K^\pm$ and $B_s^0 \to \mu^+\mu^-$ (e.g. secondary vertex resolution) and corresponds to the $B^\pm \to J/\psi K^\pm$, using only two muons in the fit.*

model the background in the signal region is not absolutely correct, since there are some partially reconstructed B decays in the left band. Quantitatively, the compatibility of the data-MC shapes is expressed using the Kolmogorov–Smirnov test statistic and is summarised in table 7.3. All the separation variables are used, but the observed discrepancies are accounted for as systematics.
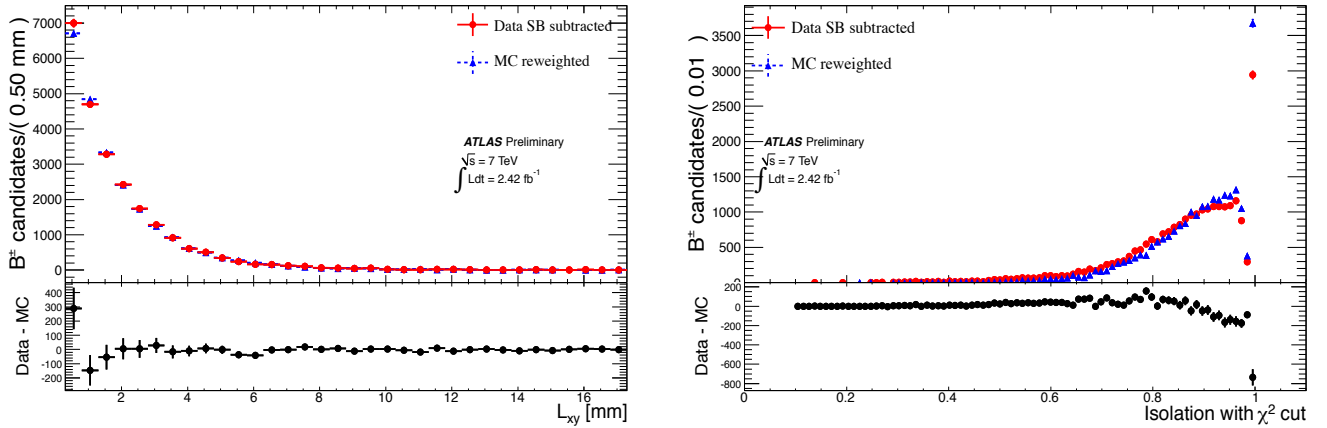
Figure 7.13: *Examples of data - MC comparisons for the reference channel of the variables of proper decay length (left) and isolation (right). The data (red dots) are side-band subtracted, while the MC (blue dots) are re-weighted, matched with the truth information and normalised to the number of data events in the signal region.*
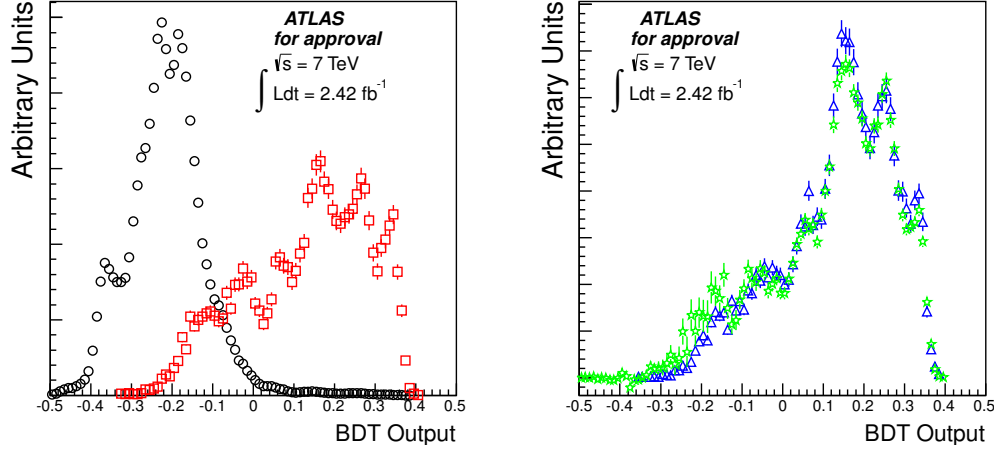
Figure 7.14: *Left: response of the BDT classifier for the signal* $B_s^0 \rightarrow \mu^+\mu^-$. *The data are represented with circles while the MC with squares. The output of BDT is performed by using 16270 signal events and 104052 background events (signal over background scale is 0.15). Right: response of the BDT classifier for the reference channel* $B^{\pm} \rightarrow J/\psi K^{\pm}$ *The data are represented with stars while the MC with triangles.*

7.9 Multivariate Analysis Optimisation

In order to achieve the best possible signal background discrimination, a large combination of multivariate classifiers, training sample definitions and input variables have been explored. The multivariate analysis tool (TMVA) being used is embedded in the ROOT framework [117] and the ranking of the performance of the different event selection strategies is achieved using the quantity

$$ \mathcal{P} = \frac{\epsilon_{\text{sig}}}{a/2 + \sqrt{N_{\text{bgr}}}} $$

where ϵ_{sig} is the signal efficiency and N_{bgr} is the background yield for a given set of cuts [1]. It is concluded that the *Boosted Decision Tree* (BDT) classifier provides the best performance and therefore, is used in the multivariate optimisation.

Several versions of the BDT classifier with different input parameters have also been studied in order to arrive at the best possible definition. The best tuning of the classifier, for the needs of this analysis, has been achieved by requiring 6000 trees, 300 minimum events, max depth equal to 2, boost type "AdaBoost" and "Separation Type" Gini Index (details of the Boosted Decision Tree configuration can be found in [118]). After the above tuning, the response of the BDT classifier shows good separation of signal and background, as shown in the left plot of Figure 7.14, while the right plot shows good agreement between data and MC for the reference channels, as expected.

7.9.1 Input Variables to the Classifier

The input variables of the classifier are the discriminating variables (studied in section 7.6) that show the maximum separation capabilities. The ranking of their separation power after the classifier treatment is shown in table 7.4, where the separation $\langle S^2 \rangle$ of a classifier y is defined

Variable	Separation
α_{2D}	5.68×10^{-1}
ΔR	5.35×10^{-1}
L_{xy}	5.22×10^{-1}
t_0 significance	5.22×10^{-1}
χ_z^2	3.40×10^{-1}
χ_{xy}^2	3.37×10^{-1}
$|d_0^{\min}|$	3.32×10^{-1}
Isolation $I_{\Delta R \leq 0.7}$	2.67×10^{-1}
$|d_0^{\max}|$	2.38×10^{-1}
$|D_{xy}^{\min}|$	1.38×10^{-1}
p_T^B	4.32×10^{-2}
$|D_z^{\min}|$	4.27×10^{-2}
$|p_L^{\max}|$	3.89×10^{-2}
$|p_L^{\min}|$	3.47×10^{-2}

Table 7.4: *Ranking of the input variables.*

by the integral

$$\langle S^2 \rangle = \frac{1}{2} \int \frac{\left(\hat{y}_S(y) - \hat{y}_B(y)\right)^2}{\hat{y}_S(y) + \hat{y}_B(y)} \, \mathrm{d}y$$

where $\hat{y}_S$ and $\hat{y}_B$ are the signal and background PDFs of y, respectively.

7.9.2 Validation of the Multivariate Analysis Procedure

Before using the classifier, however, we have to optimize the classifier behaviour with the use of extra variables and furthermore verify that its response is unbiased. The validation of the classifier's response includes the three tests that are discussed below.

- Test of BDT performance against a standard "cut and count".
  This study compares the performance of the BDT with that of a straight-forward cut and count method, using the same variables (pointing angle, isolation, proper time). The efficiency of the classifier is better than the one coming from the pure "cut and count", but the overall performance (taking into account the invariant mass window and the number of background events in the signal region) is slightly worse (see table 7.5). The two performances are compatible within the corresponding errors though which is a first indication that the classifier is behaving properly.

- Test of BDT output response by an increasing number of input variables.
  This study evaluates the evolution of the BDT against the number of variables that are progressively introduced. The study is done in five steps:

  1. The sequence of the variables follows the sequence of the ranking shown in table 7.4.

  2. The starting point is the use of the first three variables.

	ΔM (mass window in MeV/c^2)	Pointing angle in 2D cut	Isolation Cut	Proper Time cut	Signal efficiency	Number of bckg events
Cut & Count	105	0.03	0.830	0.3	0.0402	9.0 ± 2.0
BDT	116	0.06	0.825	0.4	0.0420	14 ± 3.3

Table 7.5: *Comparison of the BDT against a standard "cut and count" method.*

3. One variable is added each time, until all the variables have been used.

4. In each step the optimal cut is calculated.

5. In each step the turn-on distributions are plotted. For example, see Figure 7.15 for the variables α_{2D} and $I_{0.7}$.

The results show that the training of the classifier and its performance becomes better with an increasing number of separation variables.
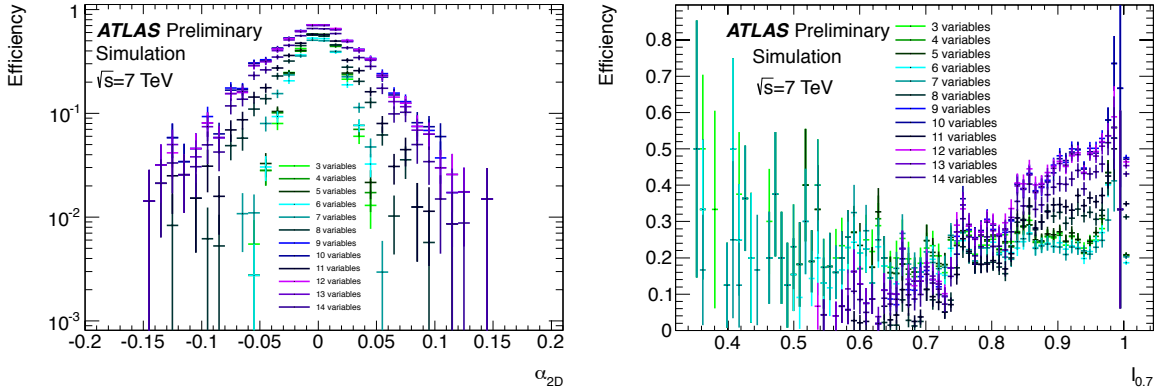
Figure 7.15: *Examples of distributions, α_{2D} (left) and $I_{\Delta R \leq 0.7}$ (right), as a function of the variables that are used in the classifier. The colour of the points shifts to "darker" tones as more variables are included in the classifier.*

- Verify that the classifier is impartial. Test with a fictitious mass of $6.5\,\mathrm{GeV}/c^2$ sample. Finally, a study of the mass dependence against the classifier response is performed. For this special training, a new $B_s^0 \to \mu^+\mu^-$ MC sample has been prepared with a shifted B_s^0 mass to $6.5\,\mathrm{GeV}/c^2$. The procedure is performed in three main steps, as described below:

1. This special MC sample together with data coming from the right side-band, is used for the training of the BDT.

2. Optimization is performed using the odd events.

3. The BDT output cut is applied in the full invariant mass range of the background sample, unblinding the signal mass window.

The result of the classifier is a smooth linear response in all the examined mass range that proves its unbiased behaviour. As shown in the left plot of Figure 7.16 in the case of the background, the response of the BDT output is smooth in the whole the mass range.

Also, the same behaviour is observed for the signal, as indicated in the right plot of the same Figure. This way, it is verified that the there is no secondary mass dependence which could introduce a systematic bias of the classifier.

7.10 $B^\pm \rightarrow J/\psi\,K^\pm$ **Event Yield**

The $B^\pm$ yield is one of the ingredients for the computation of the Br($B_s^0 \rightarrow \mu^+\mu^-$). The yield of the number of reference events, N_{ref}, is derived from a binned maximum likelihood fit to the invariant mass distribution in the range 5180 to 5380 MeV/c^2, as shown in Figure 7.17. According to the three mass resolution categories described in Section 7.4, the data are split into three parts and the fit is performed for each of them. For the extraction of systematic errors, the fit procedure is repeated for a different number of bins and different signal/background fit models. Moreover, an unbinned fit is performed. The results are summarised in table 7.6.

Category	yield $\pm$ stat. $\pm$ syst.	rel. stat.	rel. syst.	χ^2 fit prob.
1	4928 $\pm$ 67 $\pm$ 37	1.6%	0.9%	41%
2	1407 $\pm$ 39 $\pm$ 23	2.8%	1.6%	93%
3	1126 $\pm$ 34 $\pm$ 19	3.0%	1.7%	21%
All	6968 $\pm$ 86 $\pm$ 88	1.2%	1.3%	82%

Table 7.6: *The $B^\pm$ yield for the different mass resolution families.*

The combinatorial background is modelled as an exponential type:

$$C(m_{J/\psi K^\pm}) = \exp\left(\lambda\, m_{J/\psi K^\pm}\right) \tag{7.1}$$

where $m_{J/\psi\,K^\pm}$ is the measured $B^\pm$-meson invariant mass and λ (≤ 0) is a free parameter.
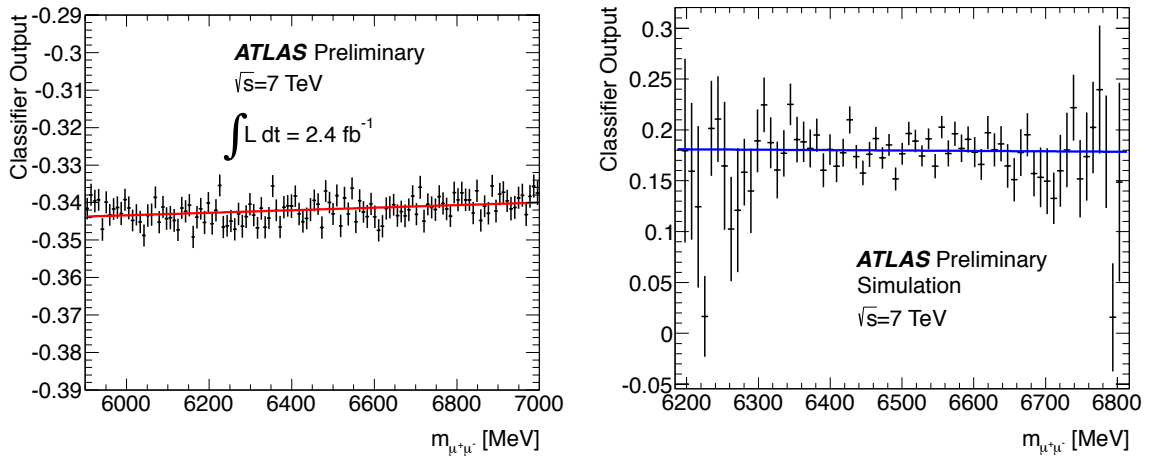
Figure 7.16: *Study of the dependence of the classifier output as a function of the di-muon invariant mass.*
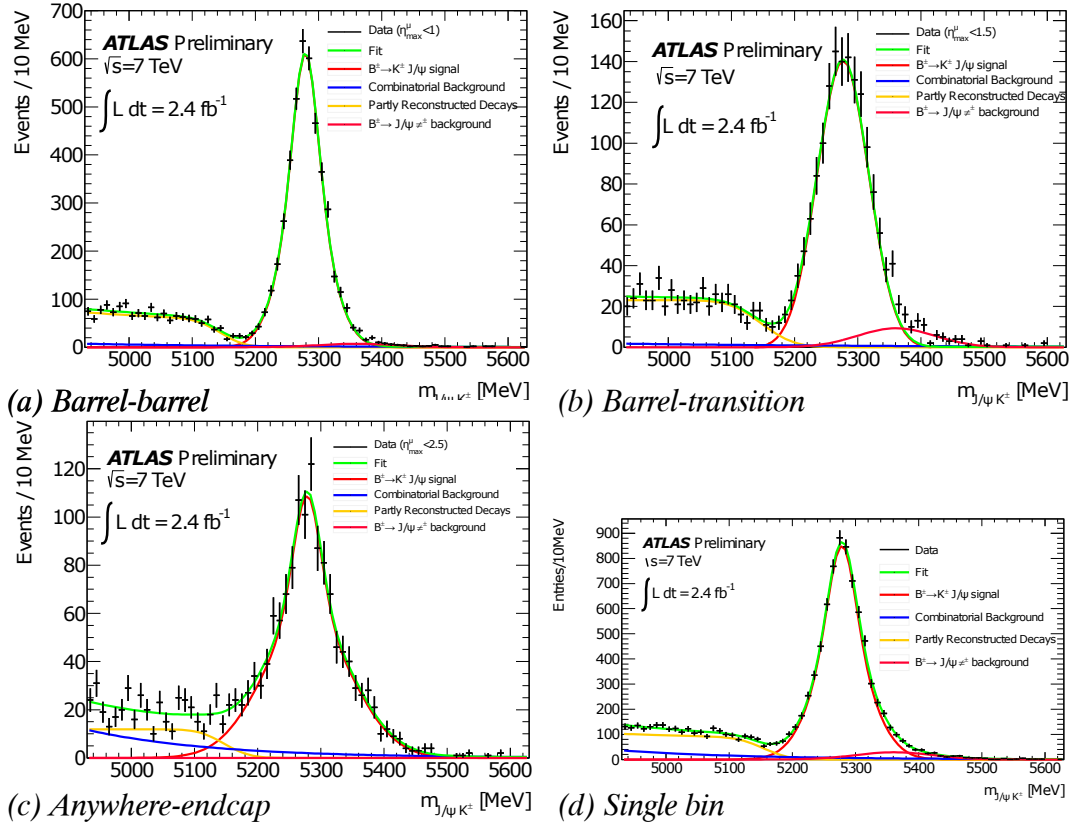
Figure 7.17: *Fit on the $B^{\pm}$ invariant mass spectrum in the different mass resolution categories, barrel-barrel (top-left), barrel-transition (top-right) anywhere-end-cap (bottom-left) and anywhere-anywhere (bottom-right). The solid red curve is the fit overlayed on top of binned data distribution (black circles) while he dotted green curve is the $B^{\pm} \to J/\psi\,K^{\pm}$ signal component.*

The partially reconstructed decay background is modelled as a step function plus an error function:

$$S(m_{J/\psi K^{\pm}}) = \text{erfc}\!\left(\frac{m_{J/\psi K^{\pm}} - \mu_S}{\sigma_S}\right) \tag{7.2}$$

where $\text{erfc}(x) = \frac{2}{\sqrt{\pi}} \int_x^{\infty} e^{-t^2} dt$ is the complementary error function, μ_S ($\sim 5130\,\text{MeV}/c^2$) and σ_S ($\sim 90\,\text{MeV}/c^2$) are respectively its mean and standard deviation.

The background due to wrong pion mass assignment (G_{π}) is assumed to be normally distributed with mean μ_{π} and standard deviation σ_{π}.

$$G_{\pi}(m_{J/\psi K^{\pm}}) = \exp\!\left(-\frac{(m_{J/\psi K^{\pm}} - \mu_{\pi})^2}{2\,\sigma_{\pi}^2}\right) \tag{7.3}$$

The $B^+ \to J/\psi\,K^+$ peak, is modelled as a Gaussian distribution,

$$G(m_{J/\psi K^{\pm}}, \delta m_{J/\psi K^{\pm}}) = \exp\!\left(-\frac{(m_{J/\psi K^{\pm}} - m_{B^{\pm}})^2}{2(s\,\delta m_{J/\psi K^{\pm}})^2}\right) \tag{7.4}$$

where, $m_{B^{\pm}}$ is the mean $B^{\pm}$ mass, and $\delta m_{J/\psi K^{\pm}}$ is the error on $m_{J/\psi K^{\pm}}$. Factor s is a scale factor, which allows for variations in the errors per event, and $\delta m_{J/\psi K^{\pm}}$ adjusts the overall width of the Gaussian distribution.

7.11 Systematic Uncertainties

There are two main contributions to the systematic uncertainties of the analysis. The first one comes from the uncertainty in the number of background events in the signal region and the other one comes from the uncertainties in the Single Event Sensitivity (SES). All the details can be found in [3], while the results are summarised in table 7.7.

The number of background events in the signal region is depending on the functional shape of the fit of the background that is used. Three different functions, linear, exponential, exponential+linear (arbitrary but reasonable fit models of the corresponding distribution), model the background and are used to estimate a systematic uncertainty in the calculation of the background events in the signal region which is 4%.

Concerning the uncertainties in SES, the dominant contribution comes from tje Br($B^\pm \to J/\psi K^\pm \to \mu^+\mu^- K^\pm$)$f_u/f_s$. The information of the Br($B^\pm \to J/\psi K^\pm$) = 1.014 ± 0.034 and the Br($J/\psi \to \mu^+\mu^-$ = (5.93 ± 0.06)% comes from the [4], while the $f_s/f_d = 0.267^{+0.021}_{-0.020}$ is calculated using $f_u/f_d = 1.052 \pm 0.029$ which is measured in LHCb [119]. Secondary contributions in the uncertainty comes from the $B^\pm$ yield uncertainty (±5.9%), the absolute $K^\pm$ tracking uncertainty (±5%) and the relative vertex efficiency in the signal and reference channel (±2%). Finally, the uncertainty of the relative efficiencies and acceptances is ±2.5% and the charge asymmetry uncertainty of ±1% is introduced since the produced MC for the reference sample is using only $B^+ \to JpsiK^+$ events.

PDG BR and f_s/f_d	9%
$K^\pm$ tracking efficiency	5%
Vertexing efficiency	2%
$B^\pm \to J/\psi K^\pm$ yield	1.5%
ϵA	1.4%
$K^\pm$ charge asym. in $B^\pm \to J/\psi K^\pm$	1%
Total (comb. in quadrature)	11%

Table 7.7: *Summary of the ΔSES/SES uncertainty due to the dominant sources of systematic uncertainty on the Single Event Sensitivity.*

7.12 Unblinding and Extraction of the Limit

The last step of the analysis before the extraction of the limit is the unblinding of the signal region. According to the mass resolution families (see 7.4), the signal region data are split into 3 bins. Figure 7.18 displays the B_s^0 invariant mass distributions for the selected candidates.

The extraction of the upper limit of Br($B_s^0 \to \mu^+\mu^-$) is obtained using the CLs method in [6] with a likelihood of the type:

$$\mathcal{L} = \text{Gauss}(\epsilon_{\text{obs}}|\epsilon, \sigma_\epsilon) \times \text{Gauss}\left(R_{\text{obs}}^{bgr}|R^{bgr}, \sigma_{R^{bgr}}\right) \times$$

$$\prod_{i=1}^{Nbin} \text{Poisson}\left(N_i^{obs}|\epsilon\epsilon_i BR + N_i^{bgr} + N_i^{b\to hh}\right) \times \text{Poisson}\left(N_{bgr,i}^{obs}|R^{bgr}R_i^{bgr}N_i^{bgr}\right) \times$$

$$\text{Gauss}\left(\epsilon_{i,obs}|\epsilon_i, \sigma_{\epsilon_i}\right)$$
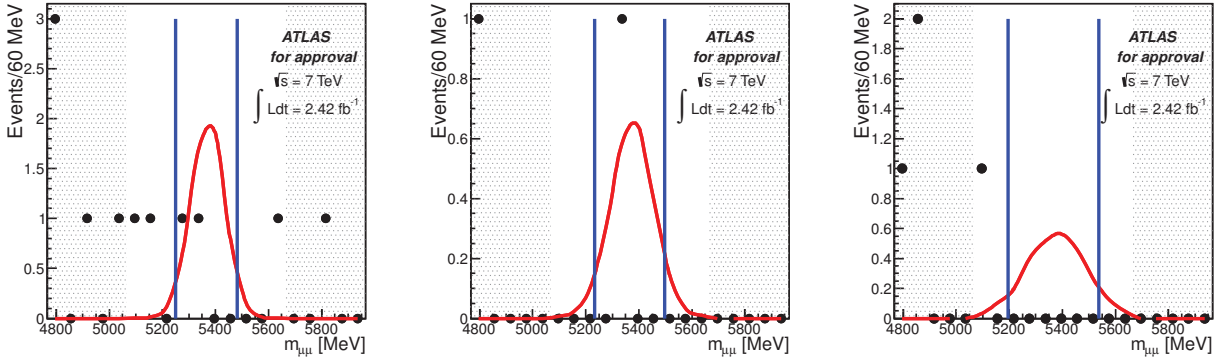
Figure 7.18: *The invariant mass distributions that correspond to the three mass resolution families. The data are represented by dots. The solid line represents the SM expectation where the branching ratio is multiplied by a factor of 10 so to make the comparison easier. The vertical lines correspond to the optimised ΔM cut.*

where

$\mathrm{Poisson}\left(N_i^{obs}|\epsilon\epsilon_iBR + N_i^{bgr} + N_i^{b\rightarrow hh}\right)$ describes the event count in the signal region

$\mathrm{Poisson}\left(N_{bgr,i}^{obs}|R^{bgr}R_i^{bgr}N_i^{bgr}\right)$ describes the event count in the bands region

$\mathrm{Gauss}\left(\epsilon_{i,obs}|\epsilon_i, \sigma_{\epsilon_i}\right)$ describes the relative efficiency

$\mathrm{Gauss}\left(\epsilon_{obs}|\epsilon, \sigma_{\epsilon}\right)$ describes the coherent correlated systematic uncertainties in SES

$\mathrm{Gauss}\left(R_{obs}^{bgr}|R^{bgr}, \sigma_{R^{bgr}}\right)$ describes the coherent correlated systematic background scaling factor

A limit on the branching fraction $\mathrm{Br}(B_s^0 \rightarrow \mu^+\mu^-)$ is been set using $2.4\mathrm{fb}^{-1}$ of integrated luminosity collected in 2011 by the ATLAS detector. The maximisation of the above likelihood induces the observed limit:

$$\mathrm{Br}\left(B_s^0 \rightarrow \mu^+\mu^-\right) < 2.2 \times 10^{-8}, \text{ at } 95\,\% \text{ CL} \tag{7.5}$$

Figure 7.19 displays the median CLs and the 1 and $2 \pm \sigma$ bands of the branching fraction. The data are compatible with SM expectations.
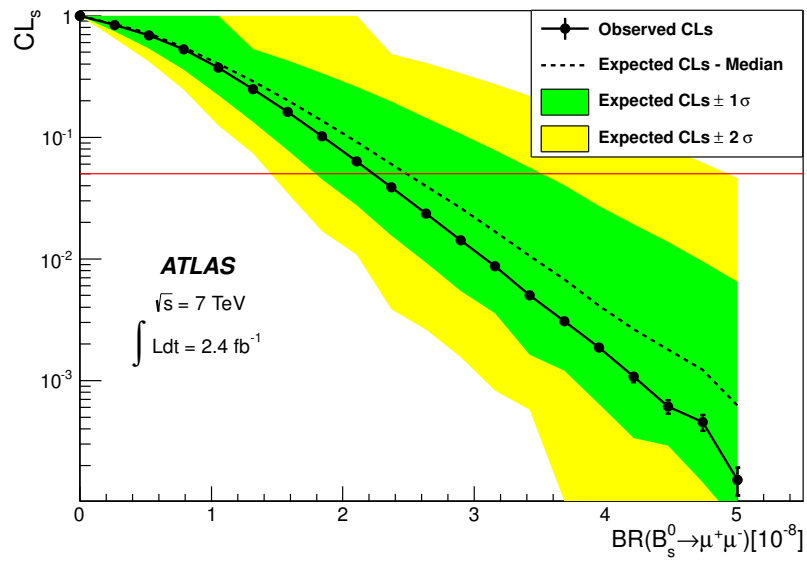
Figure 7.19: *The expected (dashed line) and observed (solid line) CLs as a function of Br($B_s^0 \to \mu^+\mu^-$). The horizontal red line indicates the 95% CL, the green and yellow bands correspond to the 1σ and 2σ predictions on the expectation.*

Part III

Data Viewer for ATLAS Detector Control System

Chapter 8

DCS Data Viewer, a Flexible Web Application

This chapter describes the design and the technical aspects of a web application that visualizes data of the ATLAS Detector Control System (DCS). In the beginning, the DCS and some basic concepts of data storage in ATLAS DCS are briefly introduced, next, an insight in the project's architecture is given and finally, the various programming techniques concerning the development of the application are explained in detail.

8.1 The ATLAS Detector Control System

The ATLAS Detector Control System (DCS) [120] is the system responsible for the coherent and safe operation of the detector and serves as a homogeneous interface to all sub-detectors and technical infrastructure of the experiment. It consists of different front-end systems and the Supervisory Control and Data Acquisition (SCADA) back-end system.

An current overview of the tasks and services of ATLAS DCS system can be found in [121]. "The DCS has the task to permit coherent and safe operation of ATLAS and to serve as a homogeneous interface to all sub-detectors and the technical infrastructure of the experiment. The DCS must bring the detector into any desired operational state, continuously monitor and archive the operational parameters, signal any abnormal behavior".

The DCS system, is organised in three functional horizontal layers, a *Local Control Station (LCS)* , a *Subdetector Control Station (SCS)* and a *Global Control Station (GCS)*. This is a modular and flexible hierarchy that models reliably the physical sub-detector parts and sub-systems of the ATLAS detector (see Figure 8.1).

The LCS layer propagates information concerning the condition of the sub-detectors and sub-systems. LCS can execute commands that are received from the upper levels of the hierarchy or it can perform its own specific actions.

The SCS layer forms the middle level of the hierarchy. Each sub-detector has a single control station which allows its full local control. At this level of the hierarchy, the sub-detectors establish connection with external systems like the magnet system, the LHC accelerator, the Detector Safety System and the Trigger and Data Acquisition (TDAQ) system.

The GCS layer is the top level of the hierarchy and it is in charge of the overall operation of the detector. In this level it is summarised all the available information of the *state* and

status of the various sub-detectors and sub-systems, as well as the various anomalies of the operation (alarms).
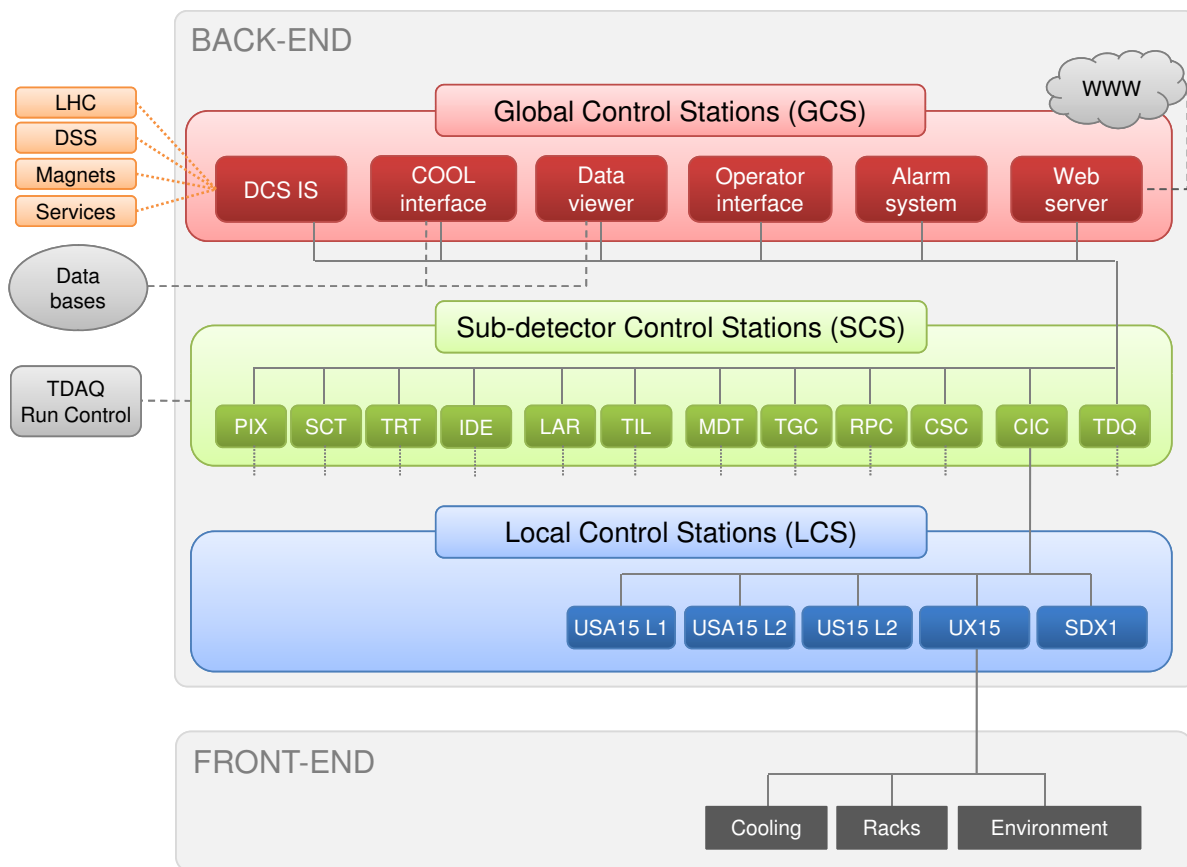
Figure 8.1: *The overall DCS architecture including the three functional horizontal layers, LCS, SCS, GCS, (adapted from [121]).*

8.1.1   Front-End System

The front-end system of the detector is composed of various components placed close to the detector or in rooms close to the detector cavern. It is connected directly to the detector hardware providing reading, digitization and in some cases processing of signals and transferring the data to the back-end. On the other side, it receives and executes commands coming from the back-end.

The equipment of the front-end consists of sensors, controllers, digitizers, processors and computer stand-alone-based systems. All the ATLAS front-end equipment has to respect several requirements such as radiation tolerance (radiation levels can reach up to 100 kGy/year in areas close to the interaction point), operation under strong magnetic field (magnetic field magnitude can reach up to 4 Tesla in ATLAS cavern),? large lifetime (the experiment will operate for more than a decade) and low cost.

8.1.2 Back-End System

The back-end is composed of different software components that communicate with the front-end and offer the supervisory control to the detector users. The back-end system, used by all the four LHC experiments, is implemented using a commercial SCADA package. On top of the SCADA package, a Joint Controls Project framework provides a set of software tools and guidelines and assures the back-end homogeneity over the different sub-systems, sub-detectors and LHC experiments.

The PVSS SCADA System In the mid-90s a major evaluation of SCADA products was performed in CERN by which concluded that the PVSS-II [122] of the Austrian company ETM (now absorbed by SIEMENS) should be used for the back-end system. PVSS-II is a highly modular, device oriented product with an event driven architecture. The different tasks are handled by functional modules called *managers* which constitute separate software processes. The central manager in PVSS-II is called *Event Manager* (EM) and is responsible for all the internal communications. A *Database Manager* (DM) provides an interface to a runtime database. Moreover, *User Interface* (UI) managers include a graphical editor, a database editor and the user interface of the application. Finally, the *Distribution Manager* (DM) connects different systems. The ATLAS back-end is composed of ∼ 150 of such SCADA systems. These control systems are connected in a *Distributed System* that has an hierarchical structure which allows scalable data access and event notification. The different ATLAS sub-detectors with the number of their corresponding systems and their archived parameters are listed in the table 8.1.

JCOP framework The Joint Controls Project (JCOP) [123] is a framework that provides a set of components and tools to ease the development of the detector control system in all four LHC experiments. A core tool provided by the JCOP is the *Finite State Machine* (FSM), a tool-kit that provides high level control by modeling the sub-detector parts and sub-systems as software objects and behaving following a finite state machine logic.

8.1.3 Flow of the Information

ATLAS DCS systems archive the important detector parameters to the ATLAS online database which, for security and performance reasons, is accessible only to systems within ATLAS Control Network (ATCN). Nevertheless, an offline database - a complete replica of the online database - is in place to serve users within the CERN General Public Network (GPN). Although the operational parameters are in the order of 10^6, the latency of the copy mechanism is not more than few seconds. The flow of the information of the data is shown in Figure 8.2.

8.1.4 Organization of Information Inside the Database

According to JCOP recommendations, each sub-detector or sub-system stores its important information into the database, by using the PVSS Oracle Archive and following a carefully designed database schema[1]. In each schema, an archived parameter is stored in an oracle column named *element_name* that belongs to a table named *ELEMENTS*. The element_name is a name that reflects the hardware information of the parameter. For example, the element_name

---

[1]schema, is the structure of a database system, that defines the tables, the fields and their relationship. It is a way to logically group database objects and assing permissions to database users. It is described in a formal language which is supported by the database management system (DBMS).

System	Component	# Servers (Appl.)	# Archived PVSS Parameters	# Total	# FSM Objects
Inner Detector	Pixel	11(12)	57k	1'086k	9.1k
	Silicon strips	11(11)	106k	1'265k	14.7k
	Transit. radiation	11(11)	69k	123k	13k
	Common services	7(8)	16k	494k	3.7k
Calorimeters	Liquid Argon	13(13)	27k	910k	8.3k
	Tile	5(5)	51k	719k	2.4k
Muon Spectrometer	Drift tubes	29(29)	214k	3'229k	19.2k
	Cathode strip	2(2)	1.3k	109k	0.6k
	Resistive plate	7(7)	139k	1'597k	2.5k
	Thin gap	7(7)	81k	1'225k	10k
	Common services	2(2)	0.7k	55k	0.04k
Forward det.		4(4)	4.9k	194k	0.9k
Common Services	Counting rooms	7(7)	23k	568k	4.7k
	Trigger and DAQ	2(2)	11k	386k	1.3k
	External+safety	4(6)	8.0k	144k	0.4k
	Global services	9(13)	1.2k	222k	0.4k
Total		131(139)	809k	12.3M	91.2k

Table 8.1: *Detector sub-system statistics. For each detector component, the # of server control stations and associated PVSS applications, the # of archived parameters, the total # of PVSS parameters, and the # of FSM objects are shown. (adapted from [121])*
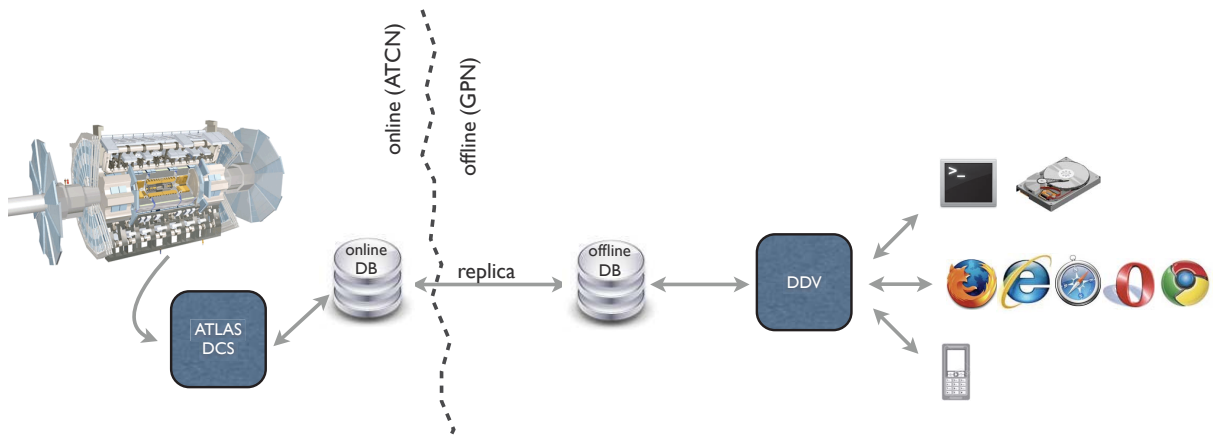
Figure 8.2: *Flow of the information. ATLAS sub-detectors write in the online database. DDV reads from the offline database that is a complete replica of the online database. Finally, the user accesses the data through the DDV interface.*

of a High Voltage power supply cable will include information of the mapping of the cable, the board that the cable belongs to, the crate that the board belongs to and the main crate that the crate belongs to. The element_name information is usually very useful for detector experts. For

example, in cases of technical problems of the front-end, this information points directly to the source of the problem.

Nevertheless, each element_name can have a more user friendly description. The table *ELEMENTS* keeps two other columns called *alias* and *comment* which are linked to the element_name and describe it using usually some geometric information of the detector (an example can be found in Table 8.2). The information of alias or comment is usually very useful to detector users and shifters which are not familiar with the technical infrastructure of the front-end.

Each triplet of *element_name*, *alias* and *comment* belongs to a single *element_id*.

Table Column	String Description
element_name	CAEN/PSMDT01/branchController11/Crate1/Board05/channel005.actual.iMon
comment	MDT PS EC ES1C16 HV Imon
alias	MDT/PS/EC/ES1C16/HV/Imon

Table 8.2: *Example of an element_name, comment and alias of an archived information.*

In the case of a Very Large Data Base (VLDB), like the one of ATLAS DCS, *partitioning* strategies (e.g. partitioning of data base tables) enhance the performance, manageability, and availability of the data base. In ATLAS, the table that keeps the archived information is called *ELEMENTS* table and it is automatically partitioned to 1 billion row tables which are called *EVENTHISTORY_X* tables (where X is a number like 000001, 00002 etc.).

8.2   DCS Data Viewer

Within the ATLAS Control Network (ATCN), the data of the detector can be visualised in real time by the DCS systems. This online monitoring covers the needs of the crew responsible for the detector operation. Notwithstanding this, a need for an offline, flexible and easily accessible tool for the visualisation of the ATLAS DCS data, is evident. The *DCS Data Viewer* (DDV) is a web based application designed to cover the offline monitoring needs by providing access to DCS historical data. The aim, the specifications and the architecture of the project are explained below.

8.2.1   Aim and Specifications

The DDV project aims at implementing a data viewing application that serves the offline needs of the ATLAS DCS data. It primarily targets users from the whole ATLAS collaboration and is accessible from the world wide web.

The detailed list of the specifications below was the starting point of the development and it went through several revisions driven by development expertise and end-user requests.

- Platform and browser independent project. Able to be accessed and used by users that work in Linux, Mac OS or windows. Compatible with most common browser technologies.

- Reasonable application startup time (e.g. less than 10 seconds).

- Small response time of queries (order of second for typical queries).

- All possible navigation mode options (element_name, alias, description).

- Multiple output formats (chart, tables, ascii and ROOT).

- Current configuration to be saved in XML format as option.

- Database protection mechanisms.

8.2.2 Project Architecture

The DDV service is based in a highly modular. Many different modules execute specific tasks, communicate through well defined interfaces and finally deliver the wanted output. The architecture is based on a *server–client* model which offers several advantages like *reduced network load* (only the results of the processes are transported), *flexibility* (new outputs and plugins are easily integrated), *efficiency* (work load is shared among the server and client software building blocks). Finally, along with the current trends in programming languages, instead of implementing DDV using a single language, a variety of different languages and technologies is used so that each DDV module is implemented in the programming language which is more suitable to accomplish its specific task. Hence, the implementation time is as minimum as possible and the future maintenance is facilitated.

The schematic Figure 8.3 illustrates the DDV architecture and shows the different software building blocks that it is composed of. The DDV server accepts requests concerning DCS information, connects and performs SQL requests to the ATLAS offline DB and finally returns the results in a form of a string or of a more structured output. The DDV Server is split in two main modules, one that deals with the *metadata*[2] and one that deals with the *data*. The DDV server can be called by the DDV client or any other external application, by well defined HTTP requests . The client is a browser independent web application which is the main interface of the project. It is composed of a *selection* module, that permits navigation through the DCS metadata, a *core* module that constructs the DDV server requests and handles the information of the corresponding responses, and an *output* module that offers different ways of visualisation of the data. A mechanism that saves the current configuration in XML files for a later use is also in place.

The ATLAS operational data are read from DCS and finally stored to a database which DDV accesses through its server. On the other side, the users' web browser is the DDV client which fetch the data from the DDV server via HTTP requests.

8.2.3 Software Tools and their Use by DDV

Below is the list of the software tools are used by DDV. Each of them is verified that meets many important requirements. It is popular among the other tools that do the same job, it has a large active community that maintains and expands it, it is already used by many different and diverse known applications, it has a short learning curve and it is free and open source.

Python The DDV server is decided to be written in *Python* programming language since it meets all of the wanted attributes. The implementation of the construction of the SQL requests, the manipulation of the data and the properly defined interface to external applications, are some examples that show that the programming of the serve needs to be developed in a structured way, by using a few sets of classes and methods. *Python* as an object oriented language

---

[2]Metadata are data concerning other data. Concerning the archived DCS information, the metadata can be a string–identifier that describes some hardware (e.g. of a temperature sensor) within the database.
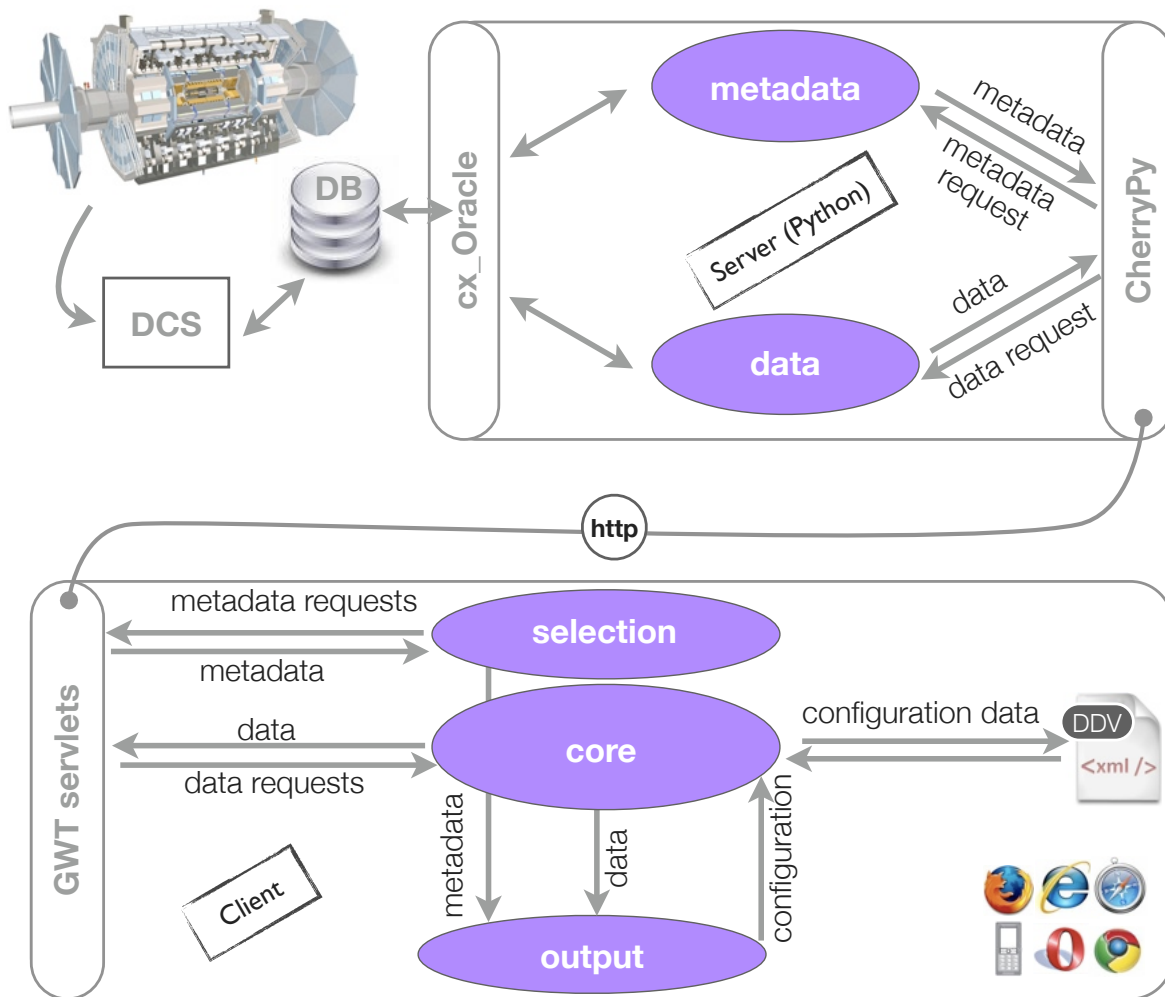
Figure 8.3: *The DDV server-client architecture.*

satisfies that need. Moreover, DDV server often needs to interact with the machine it is running on (e.g. read of configuration files, access to time information for performance tests, creationg of log files) and python language serves well since it offer many shell scripting facilities. Furthermore, since *Python* is on the market since 1980 and is growing fast, it includes many powerful toolkits, libraries and external frameworks like interfaces to databases and web used by DDV. Finally, due to its remarkably "clean" syntax the learning curve of the language is small, providing more time for the implementation of the application itself.

cx_Oracle   *cx_Oracle* [124] is a pythonic framework that conforms to the python database API specifications [125] and eases access to oracle databases. In DDV, *cx_Oracle* is used in the server side, it connects the project with the oracle database where the data are stored and all DDV SQL requests reach the database through *cx_Oracle* calls.

CherryPy   DDV server communicates with external applications by accepting properly defined HTTP requests. The server web interface is implemented using the *CherryPy* [126] which is a web application framework based on the python programming language. Its design allows an

easy and fast development of web applications while its configuration and plugin options permit building of complex sites. It works out of the box, is platform independent and can be either a web server itself or to be launched via any WSGI-enabled webserver (e.g. apache). *CherryPy* is used in the implementation of the web interface of the DDV server and is triggered by HTTP requests. Such request are coming either from DDV client or any other external application. In the latter case, calls to the server may be triggered from a command line permitting to use the tool in batch mode (see 8.2.4).

Although the main web interface of the DDV application is provided by the client and the server's web interface is used only as a communication port, it worth to be mentioned that *CherryPy* can be even used for implementing web applications, since it gathers several key desirable characteristics. It follows python conventions as much as possible and it is fairly simple (*hello wold* web page example is only few lines long). Cherrypy is *modular* and keeps a fast and clean core while powerful extensions permit high class web applications. It is proved to be *stable* and *optimized* since it is already several years in the market. Finally, it is open source, already quite popular and keeps a large active community.

SQLite   It is desirable that the access to the information of ATLAS DCS metadata is done in the most optimal way. Since the metadata information is relatively small (hundreds of Mega Bytes), the correct strategy is the storage of them ni the DDV server in a way that they can be fast and easily accessed .

SQLite is a software library that implements an SQL database engine. It is a cross-platform framework which has no external dependencies. It is fast, easy to use and supports quite big (tera-byte) databases. Since it does not require any configuration and all information can be stored in normal disk files, it is an ideal solution for electronic devices (like smartphones and MP3s) and middle-size websites. In DDV, an *SQLite* database is used in the server side, and keeps all the DCS metadata information. Furthermore, it is configured to work in *memory-mode* that means that instead of hard disk files, the information is stored in memory file objects. This mode optimizes the response time of the requests and is the one used by DDV.

RDBApi   *RDBApi* [127] is an interface implemented within the JCOP framework that allows access to the data stored by the PVSS archive manager in the oracle database. It is implemented in PL/SQL. RDBApi hides the complexity of the database and is organized in a generic way assuring at the same time the maximum possible performance. The RDBApi provides two main functionalities

1. provide database *triggers* that extend the pre-existing schema.

2. provide an interface that allows to access the DCS archives in database from an external application.

3. provide a mechanism that preserves the history of the *dpName/alias/comment element_id* mapping.

This mechanism, makes use of the oracle table called *ELEMENTS_ALL* which has the same structure as the PVSSs' *ELEMENTS* table with three additional columns, the *VALID_SINCE*, *VALID_TILL* (specifying the interval of validity of the entry) and the *WHAT* (indicating the nature of the change *alias/element_id/comment*). Whenever a change is triggered in the *ELEMENTS* table a copy/update is triggered in the *ELEMENTS_ALL* table.

The *RDBApi* is used by DDV server but only in the case that the requested item has more than one *element_id* in the requested period.

GWT Internet web browsers for general public appeared on scene in 1994 starting with Netscape Navigator and then Microsoft Internet Explorer, and followed by Opera, Safari, Mozilla Firefox and Chrome. Although these browsers share some important protocols and digital language, the browser universality issue still lurks in our days. Taking the above into consideration, the web developer framework of the client part of DDV was chosen carefully. *GWT* is an open source framework that allows developers to easily create and maintain web applications [128].

The GWT development is done in Java while the GWT creates the desirable universal Javascript code during a compilation step. The result is an AJAX based web application with browser-independent Java script. On the same time the development is kept in a type-based language (Java) that increases the testability and accelerates the debugging with the help of the eclipse platform [129].

Apache - Tomcat *Apache-Tomcat* [130] is a web server software implemented using the Java servlet technologies. It is released under *Apache Licence version 2* [131] and it is an open source software. Tomcat delivers HTML documents (usually including images, scripts and style sheets) to the web clients.

Except for *Tomcat* there are few other web servers (like boa, Zeus). However, *Tomcat* stays the most popular of the last decade. It collects many of the desired attributes, is light, fast, easy to use and is quite widely adopted wit a big community that debugs, expands and supports it.

In DDV *Tomcat* serves as a web server. The deployment of the application is done in three steps:

1. Initially, the generated GWT application files have to be placed in the server's d web application hosting path.

2. The desired prot has to be opened by configuring the servers' XML files.

3. Finally, the server has to be started by the appropriate command.

8.2.4 Technical Aspects of the Server

Metadata Organisation The ATLAS DCS *metadata* is information that refers to an archived parameter (*element_name*) that identifies that specific item in the Oracle tables. Besides, each *element_name* can have a *description* and an *alias* which are more user friendly definitions. The metadata information is copied from the database to an SQLite database cache within the DDV server.

The organization of metadata in SQLite file serves two different purposes. Firstly, the SQLite tables are configured to be stored in memory offering in this way the quickest possible response time of metadata queries. Secondly, all queries concerning metadata are performed exclusively inside DDV server keeping the database resources as available as possible.

It should be mentioned though that metadata information is not static. For example, it can happen that DCS experts change the alias or the comment of an element_name to a more user friendly description. Besides, during the long lifetime of the experiment, detector parts may be removed, exchanged or new front-end systems may be added. Such updates will

Figure 8.4: *Metadata are stored in SQLite tables hosted in DDV server. The update mechanism wakes up once every 24 hours.*

trigger changes in element_name tables and have to be taken into account by DDV. In order to keep the SQLite tables always up-to-date, an automatic mechanism that copies all the ATLAS DCS metadata information from the database to the SQLite tables is activated every 24 hours (see Figure 8.4). The total amount of metadata is nothing more than a couple of hundreds of megabytes and the whole update finishes within few seconds.

Below is an example of the SQL request concerning metadata information. The requested information is all the metadata of all types (element_name, alias, comment) that belong to the database schema of CSC.

```
SELECT element_name, alias, comment_ FROM atlas_pvssCSC.elements
ORDER by element_name
```

Data Retrieval In the case of data requests, the SQLite mechanism used for metadata cannot be used. The enormous number of archived items (order of 10^6) of the 9 main ATLAS sub-detectors, the 3 forward detectors and the common services, forbids the use of SQLite tables and in this case DDV acquires data directly from the DB. The pythonic server communicates with the DB using the *cx_Oracle* extension module. The SQL query that is formed contains the metadata of the chosen archived item, its element_name, the DB schema that this item belongs to and the requested time period. The DB response contains all the metadata types (element_name, comment, alias) of the requested item and its values with their timestamps within the requested period.

In order to achieve the optimal DB response time, many studies, concerning the *construction* of the SQL commands and the *performance* of the DB responses, have been performed. These studies ended up in two main results.

1. The response to SQL queries is faster if the request is split into two parts. A first SQL sub-request determines the *EVENTHISTORY* table that holds the recorded values of the item during the requested period. A second SQL sub-request uses the result of the first sub-request and directly asks for the values and their timestamps.

2. In case that the request includes more than one item, a faster DB response is achieved if the SQL command contains all the items. The other option of sending separate single-item SQL commands and merging the data of the result has been proven to be inefficient.

The performance optimisations of the query response time have been done with the help of the ATLAS database administrators.

Below is an example of a data SQL request. Since the structure of these SQL requests is developed for the needs of the DDV project, from here on, we are referring to these requests as *DDV custom* requests.

```
select 'eventhistory_'||lpad (archive#,8,'0')
from
( select archive#, start_time, end_time from atlas_pvssIDE.arc_archive A
  where A.group_name = 'EVENT'
  and  (A.end_time > to_date('31-01-2012 14:28','DD-MM-YYYY HH24:MI:SS') or A.end_time is null)
  intersect
  select archive#, start_time, end_time from atlas_pvssIDE.arc_archive A
  where   A.group_name = 'EVENT' and A.start_time < \
  to_date('01-02-2012 14:28','DD-MM-YYYY HH24:MI:SS')
)

select EN, AL, CO, TS, VN ,tsraw
from
(SELECT   b.element_name EN, b.alias AL, b.comment_ CO, a.ts as tsraw,
to_char(a.ts, 'dd-mm-yyyy hh24:mi:ss:ff3') TS, \
```

```
to_char(to_number(a.value_number),'9.999EEEE') VN
FROM   atlas_pvssIDE.eventhistory_00000052 a, atlas_pvssIDE.elements b
WHERE a.element_id = b.element_id and a.value_number != BINARY_DOUBLE_NAN
and (a.element_id = 3840338298153 OR a.element_id = 3840422184233)
and ts between to_date('31-01-2012 14:28','dd-mm-yyyy hh24:mi:ss' )
and to_date('01-02-2012 14:28','dd-mm-yyyy hh24:mi:ss' )
) ORDER BY  EN ,tsraw
```

Except for the main DDV custom requests, another DB interface is integrated inside DDV server that can be used to fetch the data, the RDB External API (see also 8.2.3). The main wanted feature of RDBApi is a function that resolves the *element_id/element_name/alias/comment* mapping at any specific time (schematically this is displayed in Figure 8.5). Nevertheless, since this intelligence comes with some performance cost (performance-related information can be found in Table 8.3, and graphically seen in Figure 8.6), the RDBApi is used by DDV only when it is needed.
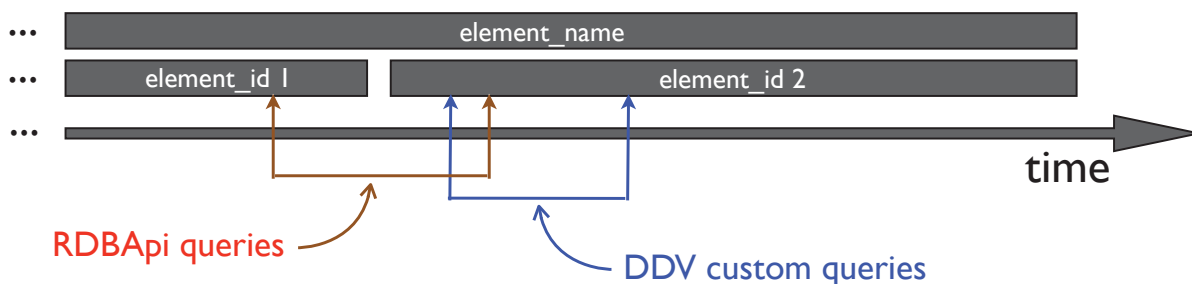
Figure 8.5: *The interfaces used to access the database. Changes in element_name happen quite rarely and usually for a serious reason. In the case that the element_name does not change within the requested time period, data requests are treated by the DDV custom DB query interface. In the other case, and only then, the RDBApi interface is used.*

Server Stand Alone Use   One interesting feature of the DDV tool is the *batch mode*. This mode offers the option of accessing DB information directly by calling the DDV sever (e.g. through a terminal) without the need of a browser or any other graphical environment. Following the original design, the interface of the *batch mode* is the same interface that is used by the DDV client. The server accepts HTTP requests which are decomposed to a meaningful DB request information with the use of the pythonic web framework *CherryPy*.

The incoming URL is composed of two parts. The first part is related to the information of the computer name that the DDV server is running and the port that it communicates through. The DDV official server is running in the computer with name *atlas-ddv.cern.ch* and its port is the *8089*. Accordingly, the first part of the URL is urlhttp://atlas-ddv.cern.ch:8089 . The second part of the URL has to do with the specific information of the DB requests. In case of a metadata request the URL keeps the information of the requested system name and schema it belongs to, while in the case of data requests the specific wanted items and the time period have to be included. Below there are listed few URL examples that cover most of the cases:

Metadata Requests, GET method:

[server]:[port]/metadata/[queryType]/[selectedSchema]/[system]/[pattern]

e.g. `http:/pcaticstest07:8089/metadata/element_name/atlas_pvssmdt/ATLMDTPS2/`
`*temp*`

Data requests, POST method:

[serverAddress]:[port]/multidata/getDataSafely

Rows	DDV custom response	RDBapi response
591	16	717
1477	64	720
2961	124	750
5918	185	780
8873	372	850
17734	550	1160
26596	740	1330
51102	1060	1930
68823	1430	2480
86544	1810	2860
100020	2080	3230
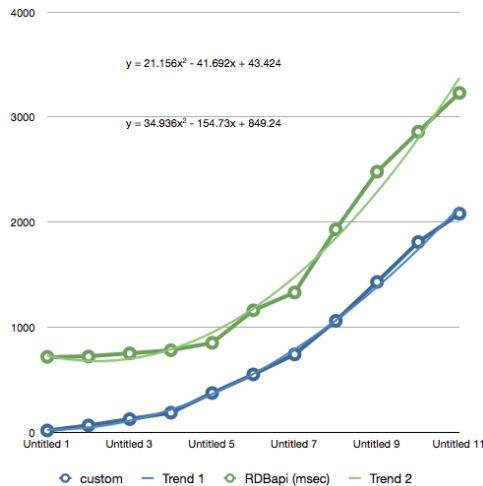
Figure 8.6: *The interfaces used to access the database. Changes in element_name happen quite rarely and usually for a serious reason. In the case that the element_name does not change within the requested time period, data requests are treated by the DDV custom DB query interface. In the other case, and only then, the RDBApi interface is used.*

Table 8.3: *Response time versus number of return DB rows. The line that corresponds to RDBApi is clearly higher than the one that corresponds to the custom requests showing no potential convergence.*

e.g. `http://pcaticstest07:8089/multidata/getDataSafely,queryInfo=atlas_ pvssdcs,comment_,CICRackControlLArgY0721A2Humidity,10-10-201012:0,11- 10-20100:0`

8.2.5   Technical Aspects of the Client

The client part of DDV is largely based on the Google Web Tool kit (GWT) framework for web framework. The client interface is organized in two main parts. The selection and configuration module (see Figure 8.7) is developed with the use of the GWT framework. With the use of the menu items, buttons, tables and other widgets the user enters the request selection criteria and a server request is constructed. The bottom part is independent of the GWT framework and hosts the output plugins.

Selection   The DDV client is designed to be as user friendly as possible. Carefully chosen widgets allow a quick selection with few mouse clicks in an intuitive way.

Time and date selection

The selection of time and date is done with the use of GWT plugins that are called *time picker* [132] and *date picker* [133] accordingly (see Figure 8.8).

Column based browsing

DDV provides an easy navigation mode (see Figure 8.9) through metadata using column-tree widgets. Since the metadata information is kept in the server in cache, the server
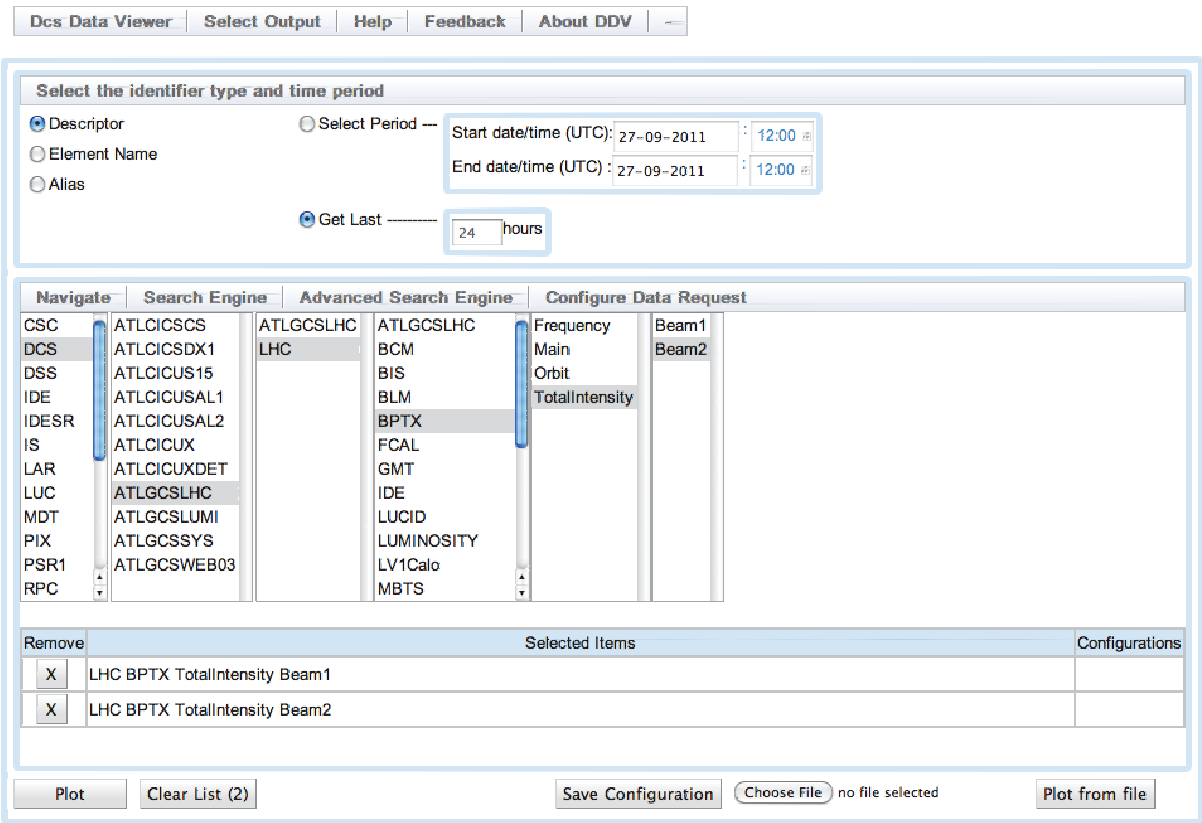
Figure 8.7: *The main browser window interface of DDV. The top part deals with the selection of the navigation mode and the start/end date and time. The middle part offers an easy navigation among the metadata with a column-tree view. The bottom part holds the action buttons like plot for a graphical display of data and save configuration for saving the current configuration in XML format.*
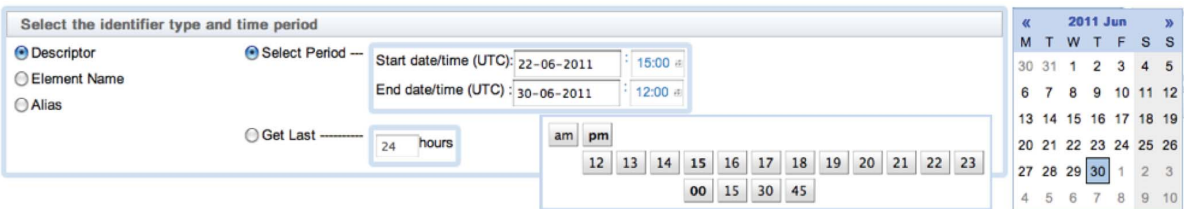
Figure 8.8: *Handy widgets for quick date and time selection, which can be done using exclusively mouse functions.*

response is prompt and in each request the result is returned back to the client in a fraction of a second.

Search Engine The *column list* is an easy navigation mode. However, the vast number of archived parameters can create difficulties to non-expert users. For such cases DDV provides a *Search Engine* for DCS metadata (see the corresponding interface in Figure 8.10). The user has to provide one or more strings that will be used as a pattern, separated with the wildcard

Figure 8.9: *The navigation is based on column-tree widgets. It is a user friendly technique that permits efficient browsing among the metadata.*

character "*" . In the DDV server side the search string is translated into a case insensitive SQL pattern which is sent as part of the database request. Apart from the user friendly search engine an *Advanced Search Engine* is in place that supports regular expressions.

8.2.6 Configuration

Despite the intuitive selection interface of the tool and the optimization of the response time in every action, the selection of the wanted items and the configuration of the final output may take some time. DDV offers a possibility of saving the current configuration to a file. In this way, users can save the current configuration and upload it at any time and quickly visualize the required information. The configuration file includes general information of the request (e.g. starting/ending time and date), the selected metadata information, the selected output, configuration of the selected output and relational queries information. The configuration file is chosen to be in XML standard which is simple, easy readable and at the same time flexible enough to accommodate future diverse needs.

Structure of Configuration Files   The structure of configuration file is described below.

- The configuration file begins with the The **XML declaration**. The encoding used is UTF-8. UTF stands for Unicode Transformation Format. In this format each character is encoded

Figure 8.10: *The search engine of DDV. The corresponding interface is kept simple and intuitive in use. The only input needed is a request string-pattern while the metadata results populate a table in the bottom.*

as a variable number of 1 to 4 octets and it is an efficient coding for unicode documents that use mostly US-ASCII characters. UTF-8 is the default encoding for XML.

```
\textbf{Example of the XML configuration file}
<?xml version="1.0" encoding="UTF-8" standalone="no"?>
```

- Under the declaration, the **root** element of the document is located which is *DDV*.

```
<DDV version="1.3">
```

- Under the root element, there are listed the **elements** of the selected DDV items and their relevant information. Each DDV element is called *DDVitem*, it has an **attribute** that is the *id* of the item and several **element contents**. Each element's contents can be grouped in three categories, contents that have to do with the selected item metadata (*elementName, queryType, schema*), the selected request time window (*selectHoursEnabled, selectHoursValue, startTime, endTime, startDate, endDate*) and information (*relQ.op1, relQ.val1, relQ.ANDOR, relQ.op2, relQ.val2*) concerning the relational queries (see 8.4.1).

```
<DDVitem ID="0">
  <elementName>LHC BPTX TotalIntensity Beam1 </elementName>
  <queryType>comment_</queryType>
  <schema>atlas_pvssDCS</schema>
  <selectHoursEnabled>False</selectHoursEnabled>
  <selectHoursValue>24</selectHoursValue>
  <startTime>12:0</startTime>
  <startDate>12-10-2011</startDate>
  <endTime>12:0</endTime>
  <endDate>13-10-2011</endDate>
  <relQ.op1> </relQ.op1>
  <relQ.val1> </relQ.val1>
  <relQ.ANDOR> </relQ.ANDOR>
  <relQ.op2> </relQ.op2>
  <relQ.val2> </relQ.val2>
</DDVitem>
```

8.3   DDV Outputs

DDV aims to offer to users several output options, which satisfy different needs. These outputs are connected with the DDV client with a thin, well defined interface. There are two main categories of outputs: visual outputs that appear on the browser and output-files that can be downloaded to the users disk.

8.3.1   Output Chart

The default output of DDV is a chart, implemented in form of a Java applet based on the JfreeChart [134] libraries. The user has an option to display the data as *time series* or one or two dimensional *histograms* when it is applicable. The configuration of the applet is done interactively in a flexible way.

Possible customizations within the applet for a *time series* plot include:

- toggling on/off showing the series' names,

- markers for individual data points,

- a cross hair and a table showing the cross hair coordinates,

- combining data on one common y-axis or display individual axes,

- showing dates in the plot,

- display y-axis using linear or logarithmic scale,

- zooming and unzooming.

Figure 8.11 shows two examples of the visualization of different sets of data series.

An option of the projection of the values to 1-D *histogram* is offered with configurable number of bins.

Finally, for the case of two selected items, the option of a time binned correlation plot in a 2-D *histogram* is offered with configurable number of time bins.

8.3.2   Output ROOT

Since many of the DDV users are familiar with the ROOT data analysis software, DDV offers a possibility to download the selected data in ROOT [117] format. These files consist of one *TTree* for every selected data series containing times and values of the contained data points. In this way the user can process the data flexibly in ROOT macros. Besides these trees, there is also a set of predefined TGraphs for the selected data included in the output file.

8.3.3   Output ASCII

The ASCII file format is a simple output format but still very desirable and highly universal. The output-file consists of three columns, the first column is the string that describes the archived parameter, the second column is a time-stamp of each occurred record and the third column is the recorded value. In case the request includes more than one item a separation line among them is used.

8.3.4   Output Table

The *data table* is a Java applet that displays the database response in table. The table consists of four columns. The first column is a string that describes the requested item, the second column keeps the date information of the archived entry, the third column keeps the time information of the archived entry and the fourth column holds the recorded value. The data table is implemented by using the *Jtable* [135] class of Java, that offers sorting options. In case of numeric values, the sorting is done in accessing order, while in the case of strings, it is done using alphabetical order.

8.4   Features

The deliberately modular design of the DDV tool in the initial phase of the development paid well back in the accomplishment of powerful features. These features aim to make the usage of the application even easier, to protect the DB from potentially dangerous requests and to provide an easy way to embed the tool in other web applications. They offer a new dimension to the use of DDV and establish it as the recommended tool for DCS data retrieval in ATLAS.
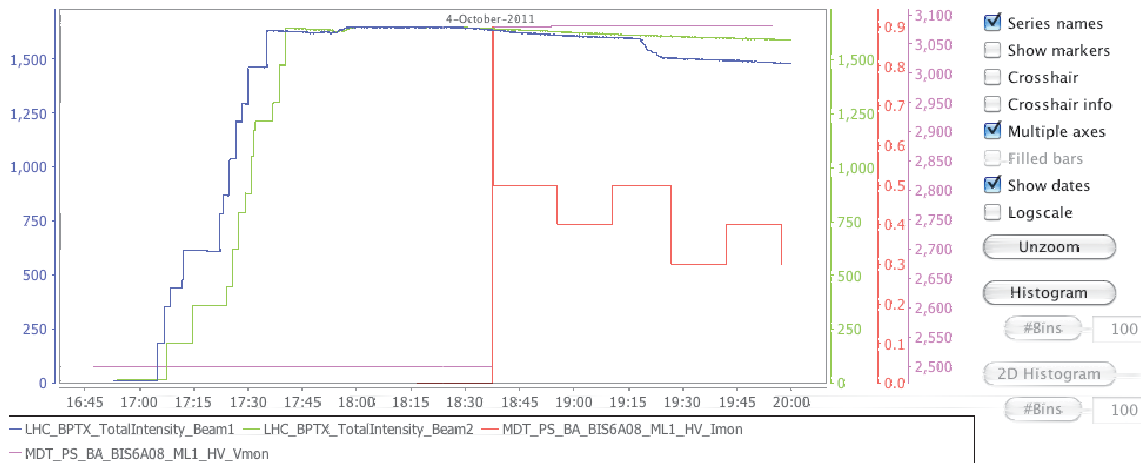
Figure 8.11: *JfreeChart, the default output of DDV. It offers several features like multiple axes, logarithmic scale, markers display, crosshair information, projection of data to 1D and 2D histograms (where applicable).*

8.4.1 Relational Queries

In some cases, users are not interested in all the data of a requested period, but in a subset of those data that satisfy some criteria. Typical example is the case of a *spike*, a value far higher or far lower than the usual value of a parameter.

DDV takes into consideration such needs and provides users with a *Relational Queries* mechanism. Users can specify an accepted range of values for the selected item(s). In this way, the database returns a subset of values for the requested item that belongs in this range. In case of multiple items, each one can be configured separately and can have its own accepted value region.

The *Relational Queries* mechanism, serves two different purposes. Firstly, the user can filter out only the useful information (e.g. case of spikes). Secondly, the database resources are used as little as possible since only a small fraction of rows that pass the requested criteria is returned back.

8.4.2 External Requests

With the use of *External Requests* the user can call DDV and at the same time provide the location of a configuration file that is pre-saved in the server. All the requested information is kept in the configuration file. In this way, a single call accompanied by the configuration file location as a url parameter, is enough to open a new browser window with an already populated chart, or to embed the plot into existing pages.

There are various examples of how such a feature can be useful, some of the most important of which are listed below.

- A simple use of the *External Request* feature is to add the URL as a bookmark in the browser.

- Since the *External Requests* are URL links, they can be embedded in any kind of *knowledge management* or *documentation* software, like *Twiki*.

• Finally, a more elaborate case-example would be the use of a *External Request* URL inside any other web application. For instance, the ATLAS *online monitoring* [136] web application which displays the detector status, can host a button-widget next to an important DCS parameter, which, if pressed, will pop up a new DDV browser window with the wanted information.

Finally, it is worth to be mentioned that the URL of external requests can have an extra argument called *mainPvisible*. If this argument is equal to *false* (*&mainPvisible=false*) the DDV browser window that pops up, appears only with the main *menu bar* and the output. In this way only the important information is displayed in the screen, leaving a lot of valuable active space. The full DDV window with the *menu bar*, the *selection* and *output* part can be easily retrieved by clicking the *+* button on the right of the *menu bar*.

8.4.3 Database Protection Mechanism

Intending to serve a high number of users, DDV aims to be more than an interface to the database data. DDV validates and certifies each request with a minimum-response-time cost and ultimately propagates it to the DB. This protection mechanism is organised in three levels and its decision diagram is displayed in Figure 8.12.

1. Firstly DDV applies *hard cuts*. Requests with time periods of more than 2 years or including more than 200 items are considered to be potentially dangerous for the DB and are declined. (Yet, if needed, the user could split the time window of the request in smaller parts or split the number of request items in smaller groups.)

2. A second protection mechanism performs a light test-request with a time period significantly shorter than the one requested. The number of returned rows is translated to a data rate (Hz) and by extrapolating to the full query time, a decision is made whether this request is acceptable or not.

3. Finally, a third kind of protection mechanism is in place to cover the cases that some unforeseen reason can cause the request pending for an irrational long time. In case DDV does not get any answer from the DB during 20 sec, the request is canceled before completion.
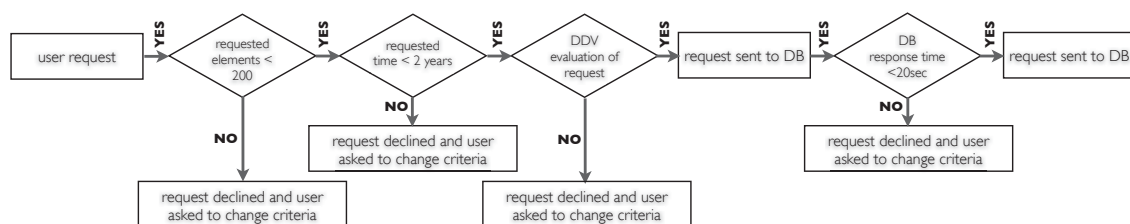
Figure 8.12: *Decision Diagram of the database protection mechanism.*

8.4.4 Logging

Log files are very useful for the analysis of a performance of a tool or for debugging a problem. All possible actions that are taken by the DDV server are archived in log files. Without a mechanism

that manages the *log* files, the disk of the DDV server would be filled up within few days. In order to prevent such situation, the linux *logrotate*, designed to facilitate the administration of big logging information, is used. Logrotate can automatically rotate, compress, remove or even email log files and all the relevant options are configured in a separate file.

```
DDV.log
{
        size 200k
        rotate 10
        create 777
        ifempty
}
```

The **size** *200K* specifies that the files will rotate when they reach the 200 kilobytes size, the **rotate** *10* specifies that each *log file* will be rotated 10 times before it is removed, the **create** *777* specifies that every user in the machine can have access to the *log* files and, finally, the *ifempty* declares that the *log* file will be rotated even if it is empty when the mechanism is triggered.

8.5   Production Setup as Service

Although the DDV application performs its tasks and the software parts it is composed of work coherently together, in order to be a stable service, its software has to be properly organised. The proper way to start or stop the DDV service is through its *shell scripts*. Concerning software management, *shell scripts* comparing with other programming languages, offer many advantages such as interactive running without compilation step, quick start, easy linkage of existing programs. DDV server and DDV client have their own shell scripts which are called *atlas-ddv-server* and *atlas-ddv-client* accordingly. There are 3 arguments accepted by the DDV shell scripts, *start*, *stop* and *status*. For example, the DDV server can be started by logging into the production machine with the appropriate user rights and entering the command:

```
/etc/init.d/atlas-ddv-server start
```

8.6   DDV Software Management

Although the writer of this thesis is the main developer, DDV is a result of a common effort of several people. Each developer builds up or debug its own piece of code, that usually performs a stand alone task of the application. At regular periods, the updates of the software are merged, providing a new release of the application. For a smooth and safe management of the code, the *SVN* [137] revision control system is used. In this way, the source code and the documentation, is maintained in current and historical versions, allowing branching practices until the final merging. Furthermore, the software management of DDV follows the good practice of coupling each stable SVN version with a release DDV package version (the version of the RPM, see C.2), allowing in this way, full control of the history of the deployed releases.

8.7   DDV Usage

DDV was announced as ATLAS central service in February of 2011. Since then, many people from the ALTAS collaboration, DCS experts or detector users, take advantage of the services

that DDV can provide. The current version is proven to be extremely stable, with a down–time kept at almost zero level. The number of different users per month reached over 150 few times, and an interest from other CERN experiments[3] for the usage of DDV is already expressed. The table 8.4 summarised important information concerning the usage of DDV the first three months of 2012, while the picture 8.13 illustrates the usage of the application from people all around the world.

Month	Unique visitors	# of visits	Pages	Hits	Bandwidth (MB)
January	64	111	4346	6557	211.29
February	66	97	3038	5345	256.71
March	94	173	5022	8914	408.00

Table 8.4: *The DDV usage of the three first months of 2012*
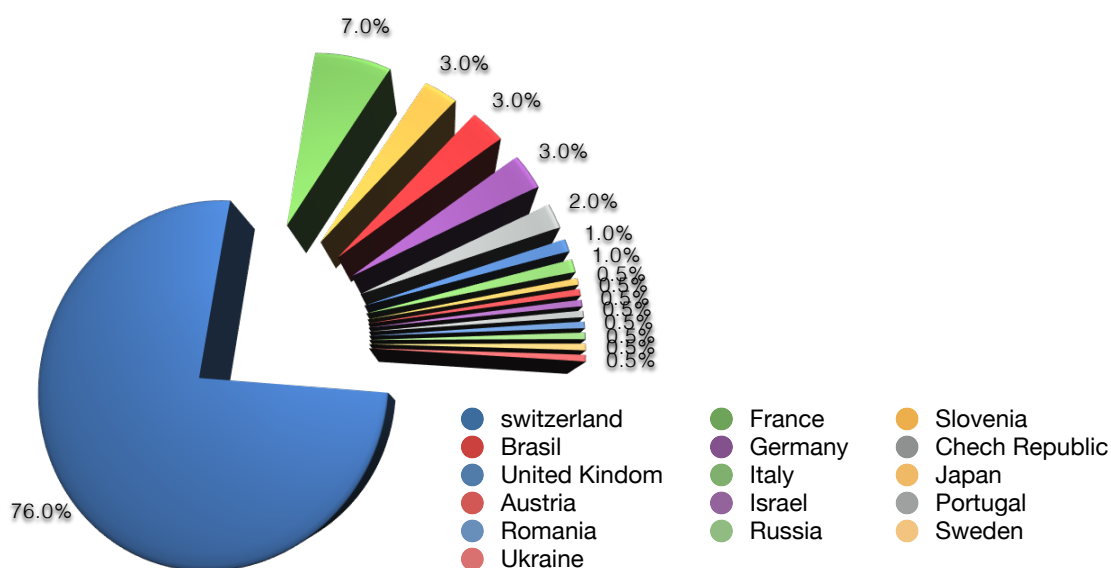
Figure 8.13: *The usage of DDV by the different countries during the winter of 2011–2012. Mainly the application is called from within CERN network but nevertheless, there is a 25% usage of the application from users in countries all around the world.*

---

[3]The DDV is already being used by the COMPASS [138] experiment in a trial mode. The adjustment of DDV software to the compass DCS information was easy due to the flexible design of DDV software and the fact that the COMPASS experiment uses the JCOP recommendations for the archiving of DCS data

Synopsis

The first part of the thesis is a study of the sensitivity of the ATLAS detector of the di-onia resonances. In this analysis, which is a first study of di-onia resonances within ATLAS, the desired final measurement is the $\mathrm{Br}(\chi_b \rightarrow J/\psi J/\psi)$. For the needs of this study, specific simulation data of the signal (statistics of 100k events) are being produced and studied. The initial preselection of the data provide a first reasonable skim of the events while all ATLAS recommended data quality criteria are fulfilled. Dedicated studies show that the best choice of trigger for this analysis is the *EF_2mu4_Jpsimumu*, which requires two muons of $4\,\mathrm{GeV}/c$ each, to have an invariant mass compatible with the mass of the J/ψ particle. A discrimination between the background and the signal is performed with the use of 6 separation variables, t_0, χ^2_{xyz}, χ^2_{ndf}, α_{2D}, p_{T}, $I_{\Delta R \leq 0,7}$. It follows the optimisation step with a simultaneous scan of all the discriminating variables which provides the optimum corresponding cut values. Before the performance of the sensitivity studies using LHC 2011 data, studies using the LHC 2010 data are performed. With the statistics of 2010 data and taking into consideration the [77, 84], the theoretically expected number of χ_b is $^{2010}N^{\mathrm{theory}}_{\chi_b} = 0.02$. By fitting the χ_b invariant mass distribution, the observed number of events in the signal region is $^{2010}N_{\mathrm{sig.\ region}} = 0.76 \pm 0.89_{\mathrm{stat}}$ which results in an upper limit of the $\mathrm{Br}(\chi_b \rightarrow J/\psi J/\psi)$ taking into consideration the optimal cut points calculated in the previous steps. The 2010 limit which is calculated with the Rolke method at 95% CL is $\mathrm{Br}(\chi_b \rightarrow J/\psi J/\psi) < 4.6 \times 10^{-3}$. The branching ratio limit is more than one order of magnitude higher than the theoretically expected value but it is not surprising due to the extremely low statistics of LHC 2010 data. Despite the big discrepancy, this is still a valuable measurement since it is the first measurement of this decay mode of the χ_b state in hadron colliders. In the case of 2011 LHC data, taking into consideration the [77, 84] the theoretically expected number of $^{2011}N^{\mathrm{theory}}_{\chi_b} = 2.2$ while by fitting the χ_b invariant mass distribution, the observed number of events in the signal region is $^{2011}N_{\mathrm{sig.\ region}} = 3.02 \pm 0.58_{\mathrm{stat}}$. By using the χ_b sidebands of LHC 2011 data, the measured effective cross section σ' of the signal ($\sigma' = N/L_{\mathrm{int}}$), is $\sigma'_{bgr} = (0.58 \pm 0.01)\,\mathrm{fb}$ while the theoretical value for the effective cross section of the signal based on [82] lie in the range $\sigma'_{bgr} = [0.23 - 1.47]\,\mathrm{fb}$. We conclude that the effective cross section of the measured background is comparable with the effective cross section of the expected signal, which indicates that the analysis has obtained the required sensitivity and that the expected statistics of the LHC 2012 data (even a fraction of them) should lead to a first observation.

The second part of this thesis, describes the measurement of the $\mathrm{Br}(B^0_s \rightarrow \mu^-\mu^+)$ using $2.4\,\mathrm{fb}^{-1}$ of the LHC ATLAS data. While the author has extensively contributed to some important steps of the study, the final measurement is a result of a work of many people (indicated in the main document accordingly). The analysis performed is *blind* and the $\mathrm{Br}(B^0_s \rightarrow \mu^-\mu^+)$ is measured with respect to a well reconstructed reference channel $B^\pm \rightarrow J/\psi K^\pm$, which minimise systematic uncertainties in the evaluation of relative efficiencies and acceptances, provides small statistical uncertainties and its branching ratio value is taken from PDG [4] . The background is mainly composed of a di–muon non-resonant part ($B \rightarrow \mu^+\mu^- X$) which is estimated

from side-bands interpolation, and a double fake resonant part which is estimated from simulations studies. A big list of 27 discriminating variables has been studied while a method to extract the minimum number of discriminating variables without loss of separation power is developed in order to be achieved a better control of the optimisation step and smaller systematic errors. The final list of discriminating variables is α_{2D}, ΔR, L_{xy}, t_0 significance, χ^2_{xy}, χ^2_z, $I_{\Delta R \leq 0,7}$, $|d_0^{\max}|$, $|d_0^{\min}|$, $|D_{xy}^{\min}|$, $|D_z^{\min}|$, p_T^B, $|p_L^{\max}|$, $|p_L^{\min}|$. These separation variables are used as an input in a multivariate analysis *Boosted Decision Tree* classifier, specifically tuned for the needs of this study. A special treatment of the MC–data discrepancies reduce the systematic error of acceptance and efficiency by tuning the simulation with generator level and data driven per event weights. Nevertheless, systematic uncertainties affect both the number of background events in the signal region (N_{BGR}) and the Single Event Sensitivity (SES). Instead of the N_{BGR}, in the analysis is used the τ (ratio between the background in the signal region and the background in the side-bands region) and its relative systematic uncertainty is 4%. In the case of SES, the main sources of uncertainties are the uncertainty of hte branching ratio of the reference channel and the difference in the b quark fragmentation probabilities, and the tatal $\delta(SES)/SES$ is 11.8%. Since it is proven that the invariant mass resolution is different for the different η regions, the yield of the reference channel is evaluated from carefully studied fit models in the three mass resolution categories accordingly. Finally, the number of observed B_s events in the signal region is 2,1,0 corresponding to the three mass resolution categories accordingly too. A proper statistical treatment, based on the CL_s method, is performed and a limit of the $\mathrm{Br}(B_s^0 \rightarrow \mu^- \mu^+) < 2.2 \times 10^{-8}$ at 95% CL is extracted.

The third part of the thesis described a data viewing application for ATLAS DCS data. The tool is called *Dcs Data Viewer* and it is the official ATLAS software that covers the needs of offline detector data visualisation. It is based in a server–client architecture where many different modules execute specific tasks. The server accepts requests of the client, communicates with the DB and reports back the results while the client is the main interface of the project which is composed of a *selection* module that permits navigation through the DCS information and an output module that offers different ways of visualisation of the data. It is a platform and browser independent project with reasonable application start–up and small response time of typical queries. It offers multiple output formats and its configuration can be saved in XML format. The project is in production since February 2011 with a downtime at zero levels. Due to it's intuitive and user friendly features, like the DCS metadata search engine, many detector users that are not DCS experts are using the tool. Furthermore, a CERN authentication mechanism in a combination with database protection algorithms within the DDV, allow exposure to hundreds of users in the world wide web. The proper organisation of the software of the tool in RPM packages with the combination of its simple configuration, make it integrable in other CERN experiments that follow the central DB archiving recommendations, for instance, the COMPASS experiment is already using the DDV. Currently 150 active users are using the tool from many countries all around the world.

Appendix A

Details on χ_b Analysis

A.1   Data and Monte Carlo Samples

The analysis uses 2010 and 2011 LHC data from pp collisions at $\sqrt{s} = 7\,\text{TeV}$.

DATA 2010

```
data10 7TeV.periodB.physics Muons.PhysCont.DAOD ONIAMUMU.repro05 v02/
data10 7TeV.periodD.physics Muons.PhysCont.DAOD ONIAMUMU.t0pro05 v02/
data10 7TeV.periodC.physics Muons.PhysCont.DAOD ONIAMUMU.t0pro05 v02/
data10 7TeV.periodF.physics Muons.PhysCont.DAOD ONIAMUMU.t0pro05 v02/
data10 7TeV.periodE.physics Muons.PhysCont.DAOD ONIAMUMU.t0pro05 v02/
data10 7TeV.periodH.physics Muons.PhysCont.DAOD ONIAMUMU.t0pro05 v02/
data10 7TeV.periodG.physics Muons.PhysCont.DAOD ONIAMUMU.t0pro05 v02/
data10 7TeV.periodI.physics Muons.PhysCont.DAOD ONIAMUMU.t0pro05 v02/
```

DATA 2011

```
data11 7TeV.periodB2.physics Muons.PhysCont.DAOD ONIAMUMU.repro08 v01/
data11 7TeV.periodD.physics Muons.PhysCont.DAOD ONIAMUMU.t0pro08 v01/
data11 7TeV.periodE.physics Muons.PhysCont.DAOD ONIAMUMU.t0pro08 v01/
data11 7TeV.periodF2.physics Muons.PhysCont.DAOD ONIAMUMU.t0pro08 v01/
data11 7TeV.periodF3.physics Muons.PhysCont.DAOD ONIAMUMU.t0pro08 v01/
data11 7TeV.periodG.physics Muons.PhysCont.DAOD ONIAMUMU.t0pro08 v01/
data11 7TeV.periodI.physics Muons.PhysCont.DAOD ONIAMUMU.t0pro08 v01/
data11 7TeV.periodJ.physics Muons.PhysCont.DAOD ONIAMUMU.t0pro08 v01/
data11 7TeV.periodK1.physics Muons.PhysCont.DAOD ONIAMUMU.t0pro08 v01/
data11 7TeV.periodK2.physics Muons.PhysCont.DAOD ONIAMUMU.t0pro08 v01/
data11 7TeV.periodK3.physics Muons.PhysCont.DAOD ONIAMUMU.t0pro08 v01/
data11 7TeV.periodK4.physics Muons.PhysCont.DAOD ONIAMUMU.t0pro08 v01/
```

MC of χ_b
Data for the simulated $\chi_b \to J/\psi J/\psi$ analysis channel are produced using Pythia and PythiaB. The statistics is 100.000 events.

Reconstruction software
The ATHENA release used is 17.0.2.10.
The ATHENA packages used are
PhysicsAnalysis/JpsiUpsilonTools-00-00-37
PhysicsAnalysis/BPhys/BPhysAnalysisTools-00-02-03
PhysicsAnalysis/BPhys/BPhysAnalysisSkeleton
PhysicsAnalysis/BPhys/JpsiUpsilonAlgs
PhysicsAnalysis/BPhys/BJpsiDecayAlgs

PhysicsAnalysis/BPhys/RareDecayAlgs
PhysicsAnalysis/BPhys/BPhysAnalysisObjects
PhysicsAnalysis/BPhys/BPhysDAOD
Tracking/TrkVertexFitter/TrkVertexAnalysisUtils
Tracking/TrkVertexFitter/TrkVKalVrtFitter
Trigger/TrigAnalysis/TrigEffJpsiTools

The algorithm used in the analysis is the *Bs2mumu* under the *RareDecayAls* adjusted accordingly to the χ_b needs.

A.2   The Preselection Variables

The variables before and after the preselection are displayed in Figure A.1 and A.2, respectively.
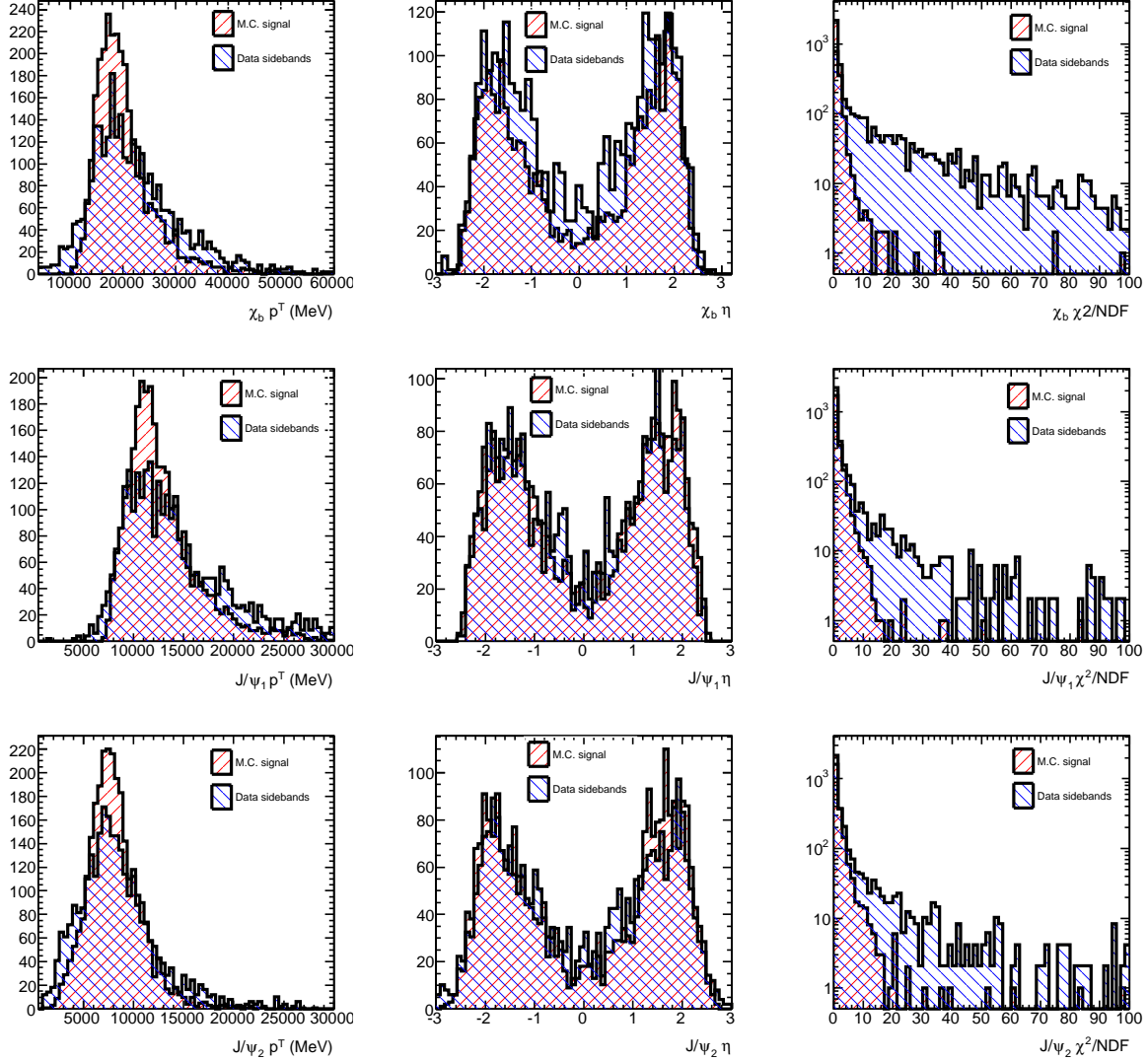
Figure A.1: *The variables used in the preselection step for MC signal (red) and data (blue). The variables are displayed **before** the preselection. In the first line the preselection variables of the χ_b particle, the momentum (left), the pseudorapidity (middle) and the χ^2/ndf (right) are presented. In the second line, the preselection variables of the J/ψ with the highest momentum between the two J/ψs of the decay of χ_b, momentum (left), the pseudorapidity (middle) and the χ^2/ndf (right) are shown. In the third line are presented the preselection variables of the J/ψ with the lowest momentum between the two J/ψs of the decay of χ_b, momentum (left), the pseudorapidity (middle) and the χ^2/ndf (right).*
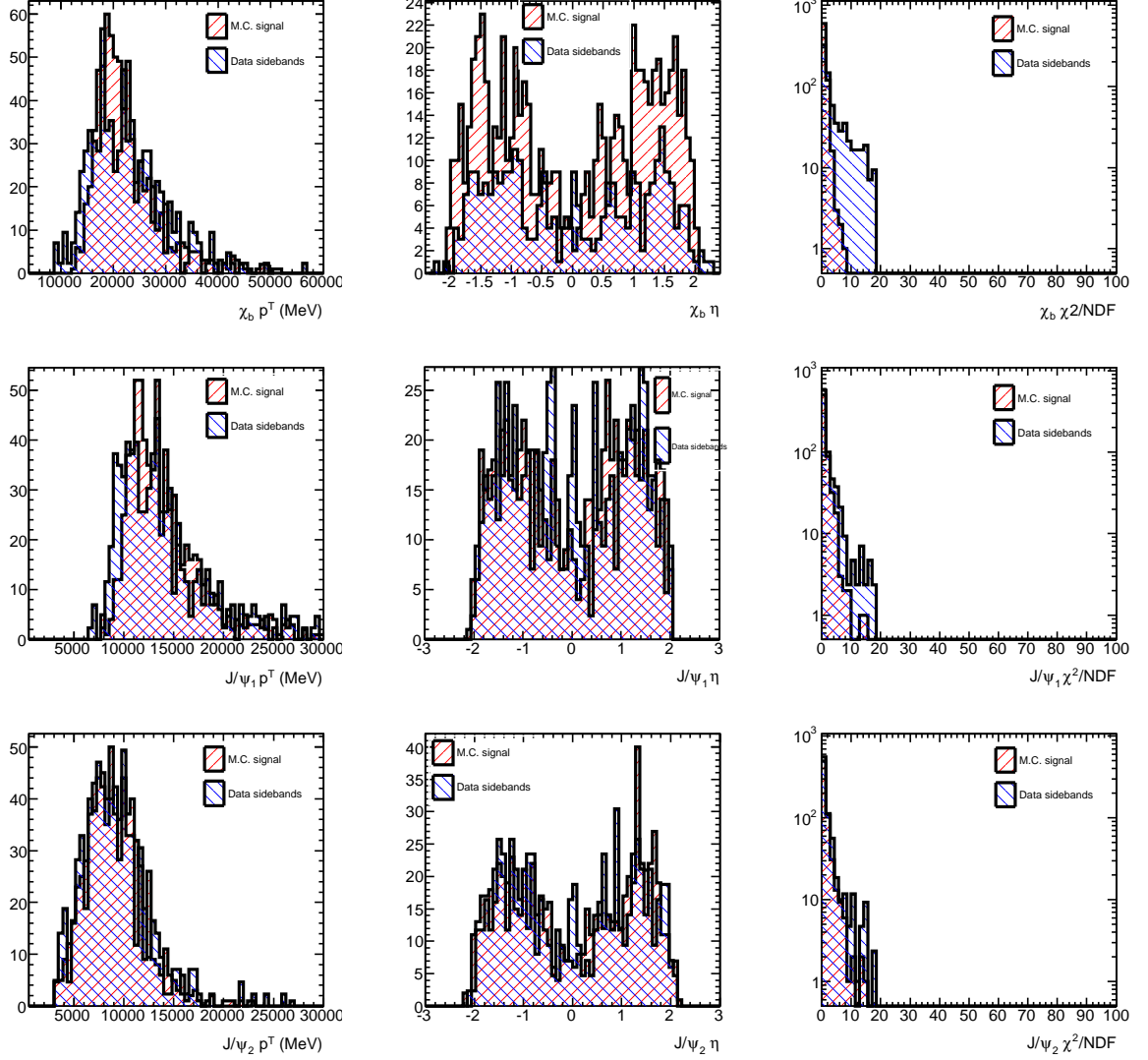
Figure A.2: *The variables used in the preselection step for MC signal (red) and data (blue). The variables are displayed **after** the preselection. In the first line the preselection variables of the χ_b particle, the momentum (left), the pseudorapidity (middle) and the χ^2/ndf (right) are presented. In the second line, the preselection variables of the J/ψ with the highest momentum between the two J/ψs of the decay of χ_b, momentum (left), the pseudorapidity (middle) and the χ^2/ndf (right) are shown. In the third line are presented the preselection variables of the J/ψ with the lowest momentum between the two J/ψs of the decay of χ_b, momentum (left), the pseudorapidity (middle) and the χ^2/ndf (right).*

A.3 Selection of the Isolation Variable Study

The distributions of different definitions of isolation are shown in Figure A.3. The selection of the definition with the best separation power is done with the help of the curves in Figure A.4.
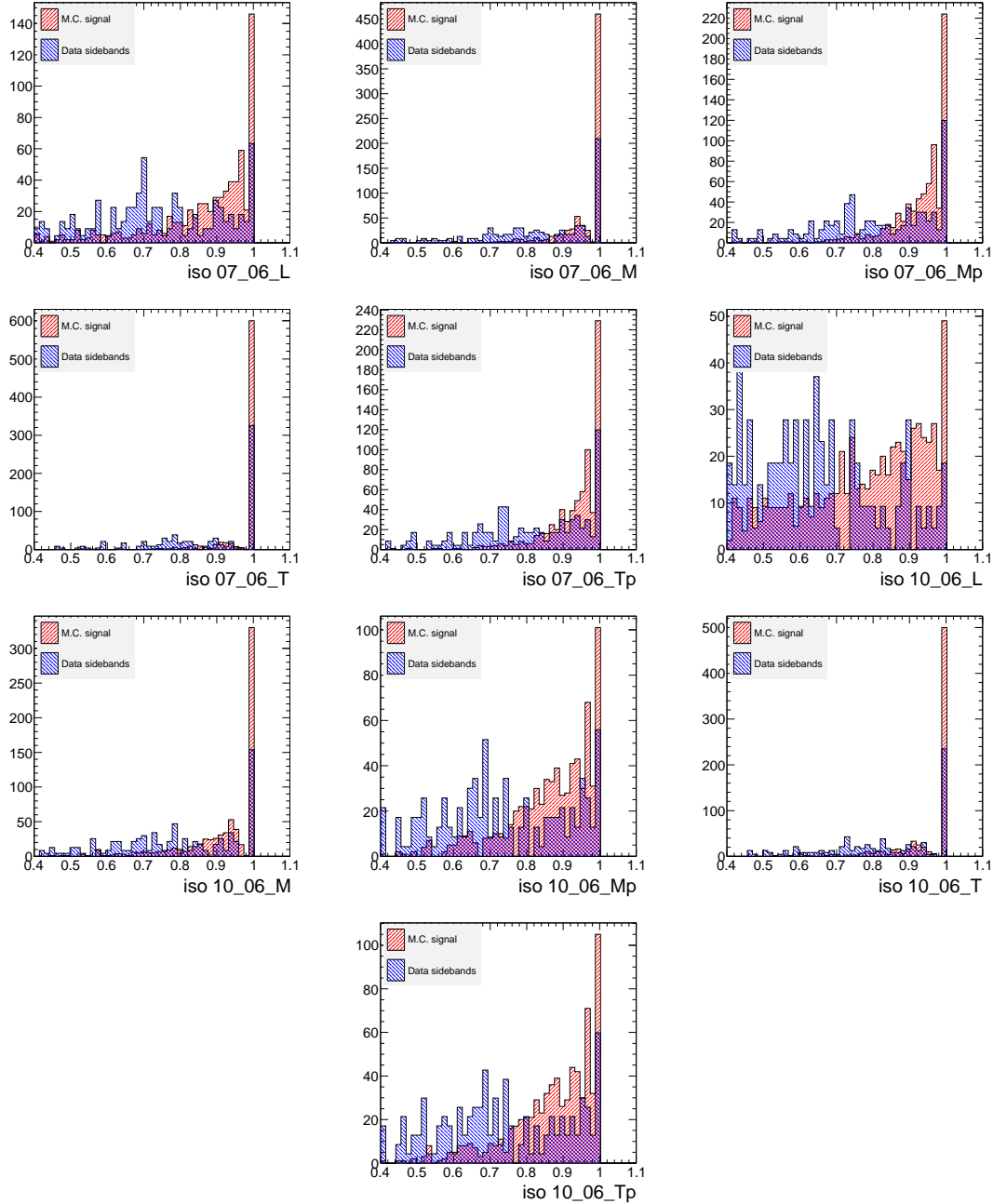
Figure A.3: *The distributions of the different definitions of the isolation variable that are studied. The definitions on the first row are the isolation_7_6_L (left), Isolation_7_6_M (middle), Isolation_7_6_Mp (right). The definitions on the second row are the isolation_7_6_T (left), Isolation_7_6_Tp (middle), Isolation_10_6_Mp (right). The definitions on the third row are the isolation_10_6_M (left), Isolation_10_6_Mp (middle), Isolation_10_6_T (right). The definitions on the fourht row are the isolation_10_6_Tp. The explanation of the definition is found in 5.8.*
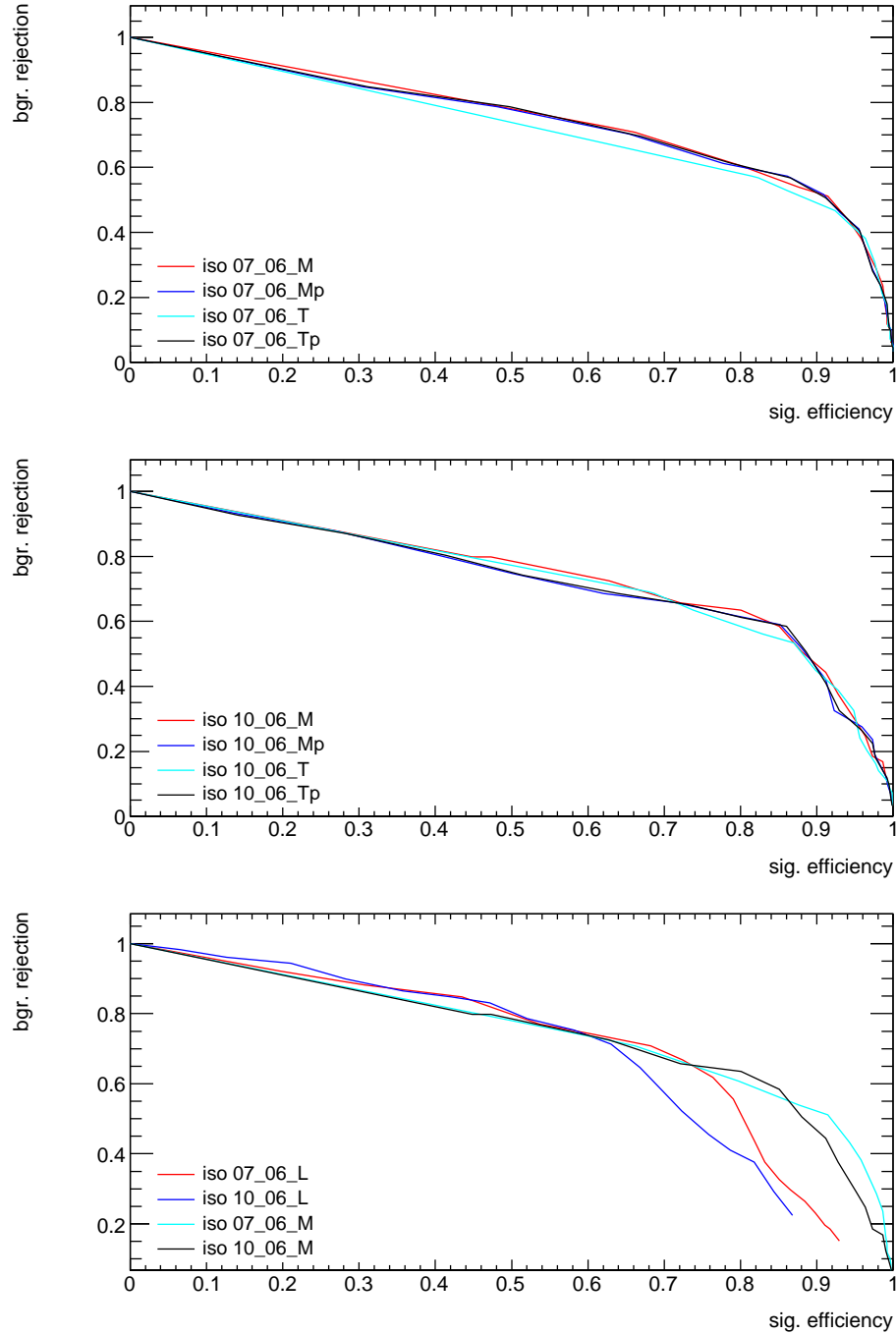
Figure A.4: *ROC curves of the study of the separation capabilities of the different isolation definitions. The Figure on the top shows that among the isolation_7_6_M, isolation_7_6_Mp, isolation_7_6_T, isolation_7_6_Tp, the definition of isolation_7_6_M shows better separation capabilities (its corresponding line is on the top). The Figure in the middle shows that among the isolation_10_6_M, isolation_10_6_Mp, isolation_10_6_T, isolation_10_6_Tp, the definition of isolation_10_6_M shows better separation capabilities (its corresponding line is on the top). The Figure on the bottom shows that among the isolation_7_6_L, isolation_10_6_L, isolation_7_6_M, isolation_10_6_M, the definition of isolation_10_6_L shows better separation capabilities in low efficiencies (its corresponding line is on the top), while the definition of isolation_7_6_M shows better separation capabilities in high efficiencies.*

A.4 Separation Variables

All the separation variables that were studied in the analysis are listed below and displayed in A.5:

- Pointing angle in 2D (α_{2D}) and 3D (α_{3D})
  If x is the vector from the Primary Vertex point to the Secondary Vertex point, then α_{2D} is the angle between the x and the momentum vector, p, of the B-meson. It is calculated in the transverse plane (α_{2D}) and in the 3-dimensional space (α_{3D}).

- $\Delta R = \sqrt{(\varphi_x - \varphi_p)^2 + (\eta_x - \eta_p)^2}$
  It is the distance ΔR in the $\eta\phi$ plane, where ϕ is the azimuthal angle and η is the pseudo-rapidity.

- χ^2_z, χ^2_{xy}, χ^2_{xyz} of PV-SV
  These variables are derived from the positions (PV − SV) and the covariance matrices ($\Sigma_{\mathrm{PV}}, \Sigma_{\mathrm{SV}}$) of the primary and secondary vertex. If $\Lambda = \mathrm{SV} - \mathrm{PV}$, we define $\chi^2 = \Delta^T \Lambda \Delta$, where $\Lambda = (\Sigma_{\mathrm{PV}} + \Sigma_{\mathrm{SV}})^{-1}$. These expressions, evaluated either for vectors in the xy plane (2D) or along z (1D) or in space (3D), are χ^2-like under the hypothesis that the PV and χ_b vertex coincide.

- $L_{xy} = x \cdot \hat{p}_B$ and its significance
  Where x is the vector from the Primary to the Secondary Vertex and $\hat{p}_B$ is the unitary momentum vector of the B-meson. The L_{xy} significance, which is $L_{xy}/\sigma_{L_{xy}}$, is calculated, too.

- Proper Time and Proper Time significance
  The proper time is defined as $t_0 = \dfrac{L_{xy} M_B}{p_T}$, where p_T, M_B are the transverse momentum and the mass of the B-meson, respectively. The Proper Time significance, t_0/σ_{t_0}, is calculated as well, where σ_{t_0} is the error of the proper time. The uncertainty of the proper time is calculated propagating the error of the L_{xy}, mass and p_T

$$\delta(t_0) = \sqrt{\left(\frac{M}{p_T}\right)^2 \left(\delta L_{xy}\right)^2 + \left(\frac{L_{xy}}{p_T}\right)^2 (\delta M)^2 + \left(\frac{L_{xy}M}{p_T}\right)^2 \left(\delta p_T\right)^2}$$

- χ^2 of the vertex fit of the B-meson

- Transverse Momentum, p_T, is the momentum of the B-meson in the xy plane

- Isolation
  is defined as the ratio of $|p_T^B|$ over the sum of $|p_T^B|$ and of the transverse momenta of all tracks within a cone $\Delta R < 0.7$ from the direction of the B-meson, excluding its decay products. Two definitions of the isolation variable are studied, one including the χ^2 compatibility cut and one not including it.
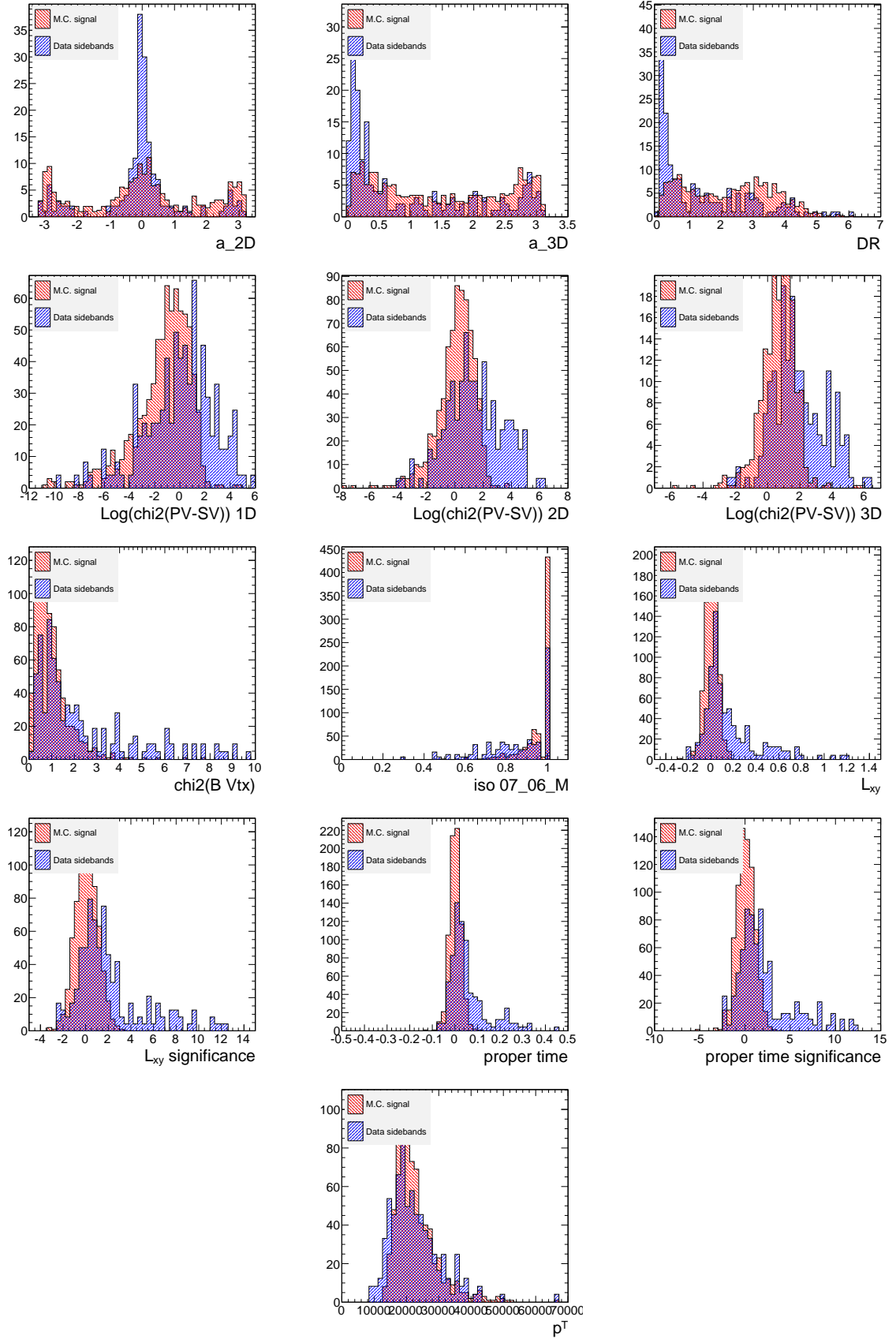
Figure A.5: *The variables displayed here are the* α_{2D}, α_{3D}, ΔR, χ_z^2, χ_{xy}^2, χ_{xyz}^2, *fit* χ^2, L_{xy}, L_{xy} *significance,* t_0, t_0 *significance,* p_T

A.5 The Pythia χ_b Generation File

```
#################################################################
# JOB OPTIONS FILE. THIS FILE IS TO DEMONSTRATE HOW THE USER CAN
# CHANGE THE PYTHIA PARAMETERS. IT DOES NOT NECESSARILY COMPLY TO
# THE ATLAS DEFAULTS FOR PHYSICS EVENT GENERATION.
#===============================================================
# Private Application Configuration option
from AthenaCommon.AppMgr import ServiceMgr
ServiceMgr.MessageSvc.OutputLevel = DEBUG
#---------------------------------------------------------------
# Event related parameters
#---------------------------------------------------------------
# Number of events to be processed (default is 10)
theApp.EvtMax = 100000
#---------------------------------------------------------------
# Algorithms Private Options
#---------------------------------------------------------------
from AthenaServices.AthenaServicesConf import AtRndmGenSvc
ServiceMgr += AtRndmGenSvc()
ServiceMgr.AtRndmGenSvc.Seeds = ["PYTHIA 4789899 989240512","PYTHIA_INIT 820021 2347532"]

from AthenaCommon.AlgSequence import AlgSequence
job=AlgSequence()
from Pythia_i.Pythia_iConf import Pythia
job +=Pythia()

job.Pythia.PythiaCommand = ["pysubs msel 0",              #user chooses decay
                    "pysubs msub 471 1",         #gg->bb~[3P0(1)]+g
                    "pysubs msub 474 1",         #qg->q+bb~[3P0(1)]
                    # Force chi_b ->J/psi J/psi
                    "pydat3 mdme 1521 1 0",        #chi_0b->gg
                    "pydat3 mdme 1520 1 1",        #chi_0b->Y+gamma
                    "pydat3 kfdp 1520 1 443",      #chi_0b->J/psi+gamma
                    "pydat3 kfdp 1520 2 443",      #chi_0b->J/psi+J/psi

                    # J/Psi Decays (close ee-pairs and random flavours production,
                    #and open only mumu pairs production.
                    "pydat3 mdme 860 1 0", ## 860 -> t
                    "pydat3 mdme 859 1 1", ## 859 -> mu
                    "pydat3 mdme 858 1 0", ## 858 -> e (so I open Jpsi to ee )

                    # Other stuff (pysubs ckin 3 3- mean that i demand pt > 3 GeV
                    # "pyinit pylistf 1",
                    "pyinit dumpr 0 3",
                    "pysubs ckin 3 3"]

from TruthExamples.TruthExamplesConf import DumpMC
job += DumpMC()
#------- Muon Trigger Cuts --------
BSignalFilter = Algorithm( "BSignalFilter" )
#------------- Level 1 Muon Cuts ----------------
BSignalFilter.LVL1MuonCutOn = 1 #in rel 12 was "true"
BSignalFilter.LVL1MuonCutPT = 6000.0
BSignalFilter.LVL1MuonCutEta = 2.5
#------------- Level 2 lepton cuts ------------------
# These will only function if LVL1 trigger used.
BSignalFilter.LVL2MuonCutOn = 1 #in rel 12 was "True"
BSignalFilter.LVL2MuonCutPT = 4000.0
BSignalFilter.LVL2MuonCutEta = 2.5
#
# End of job options file
#
#################### Pool Persistency ###########################################
from AthenaPoolCnvSvc.WriteAthenaPool import AthenaPoolOutputStream
Stream1 = AthenaPoolOutputStream( "Stream1" )
Stream1.OutputFile = "Chib.pool.root"
Stream1.ItemList += [ 'EventInfo#*', 'McEventCollection#*' ]
#################################################################################
```

Appendix B

Details on $B_s^0 \rightarrow \mu^+\mu^-$ Analysis

B.1 Data Preparation

The LHC data used in this analysis are ATLAS pp collision data at $\sqrt{s} = 7\,$TeV that correspond to an integrated luminosity of $2.4\,\text{fb}^{-1}$. The data that passed the trigger *EF_2mu4* are used while the $[5066, 5666]\,\text{MeV}/c^2$ invariant mass region is extracted from the data until the end of the analysis.

The MC data are generated with Pythia [86] using ATLAS MC 10 tune [139, 140]. The statistics of MC data for the signal channel is 200.000 events while for the reference channel is 500.000 events.

B.1.1 Data and MC Samples

DATA

The following 2011 (D)AOD s were used in the analysis:

```
data11 7TeV.periodB2.physics Muons.PhysCont.DAOD ONIAMUMU.repro08 v01/
data11 7TeV.periodD.physics Muons.PhysCont.DAOD ONIAMUMU.t0pro08 v01/
data11 7TeV.periodE.physics Muons.PhysCont.DAOD ONIAMUMU.t0pro08 v01/
data11 7TeV.periodF2.physics Muons.PhysCont.DAOD ONIAMUMU.t0pro08 v01/
data11 7TeV.periodF3.physics Muons.PhysCont.DAOD ONIAMUMU.t0pro08 v01/
data11 7TeV.periodG.physics Muons.PhysCont.DAOD ONIAMUMU.t0pro08 v01/
data11 7TeV.periodI.physics Muons.PhysCont.DAOD ONIAMUMU.t0pro08 v01/
data11 7TeV.periodJ.physics Muons.PhysCont.DAOD ONIAMUMU.t0pro08 v01/
data11 7TeV.periodK1.physics Muons.PhysCont.DAOD ONIAMUMU.t0pro08 v01/
data11 7TeV.periodK2.physics Muons.PhysCont.DAOD ONIAMUMU.t0pro08 v01/
data11 7TeV.periodK3.physics Muons.PhysCont.DAOD ONIAMUMU.t0pro08 v01/
data11 7TeV.periodK4.physics Muons.PhysCont.DAOD ONIAMUMU.t0pro08 v01/
```

MC Signal

The 2011 AOD signal MC sample was used in the analysis:

```
mc11 7TeV.108556.PythiaB Bs mu2p5mu2p5 mass6p5.merge.AOD.e955 a131 s1353 a133 r2780/
```

MC Reference Channel

The 2011 AOD reference MC sample was used in the analysis:

```
mc10 7TeV.108506.PythiaB Bplus Jpsi mu2p5mu2p5 Kplus.merge.AOD.e574 s933 s946 r2297 r2300/
```

B.1.2   Reconstruction Software

The reconstruction software used is Athena release 17.0.2.10. The packages *JpsiUpsilonTools*, *BPhysAnalysisObjects*, *JpsiUpsilonTools*,*JpsiUpsilonTools* of the B physics working group are used for easy reconstruction of *B* particles like *J/ψ* and *Y* and easy access to useful quantities. The package *TrkVertexAnalysisUtils* is used for the reconstruction of the primary and secondary vertices that are used in the analysis. The package *TrigEffJpsiTools* is used for the retrieval of the desirable Trigger information. The *RareDecayAlgs* is the main package developed especially for the rare decays studies. The versions of the packages that are used in this analysis are listed below.

```
JpsiUpsilonTools-00-00-36
BPhysAnalysisObjects-00-00-45
BPhysAnalysisTools-00-02-03
JpsiUpsilonTools-00-00-37 (only for the control sample)
RareDecayAlgs-00-00-15
RareDecayAlgs-00-00-19(only for the control sample)
TrkVertexAnalysisUtils-00-02-21
TrigEffJpsiTools-01-00-31
```

B.2   The Possible Discriminating Variables

Figures B.1 and B.2 show the discriminating variables that are studied and can be possibly used in analysis of the $B_s^0 \to \mu^+\mu^-$.
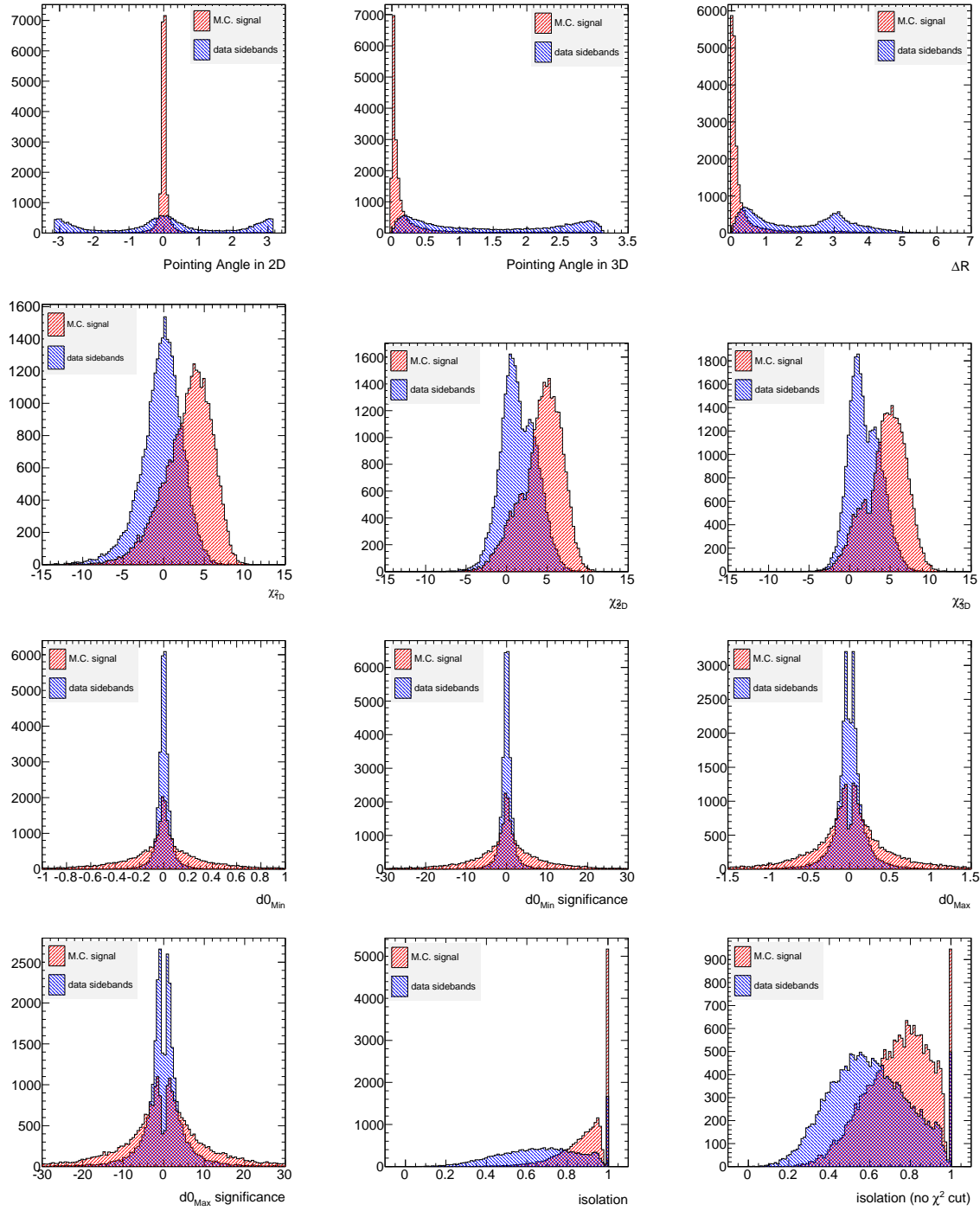
Figure B.1: *The discriminating variables (definitions for each of these variables can be found in Section 7.6.2). The variables displayed here are the α_{2D}, α_{3D}, ΔR, χ^2_z, χ^2_{xy}, χ^2_{xyz}, d_0^{min}, d_0^{min} significance, $|d_0^{max}|$, $|d_0^{max}|$ significance, $I_{\Delta R \leq 0.7}$, $I_{\Delta R \leq 0.7}$ without the χ^2 cut.*
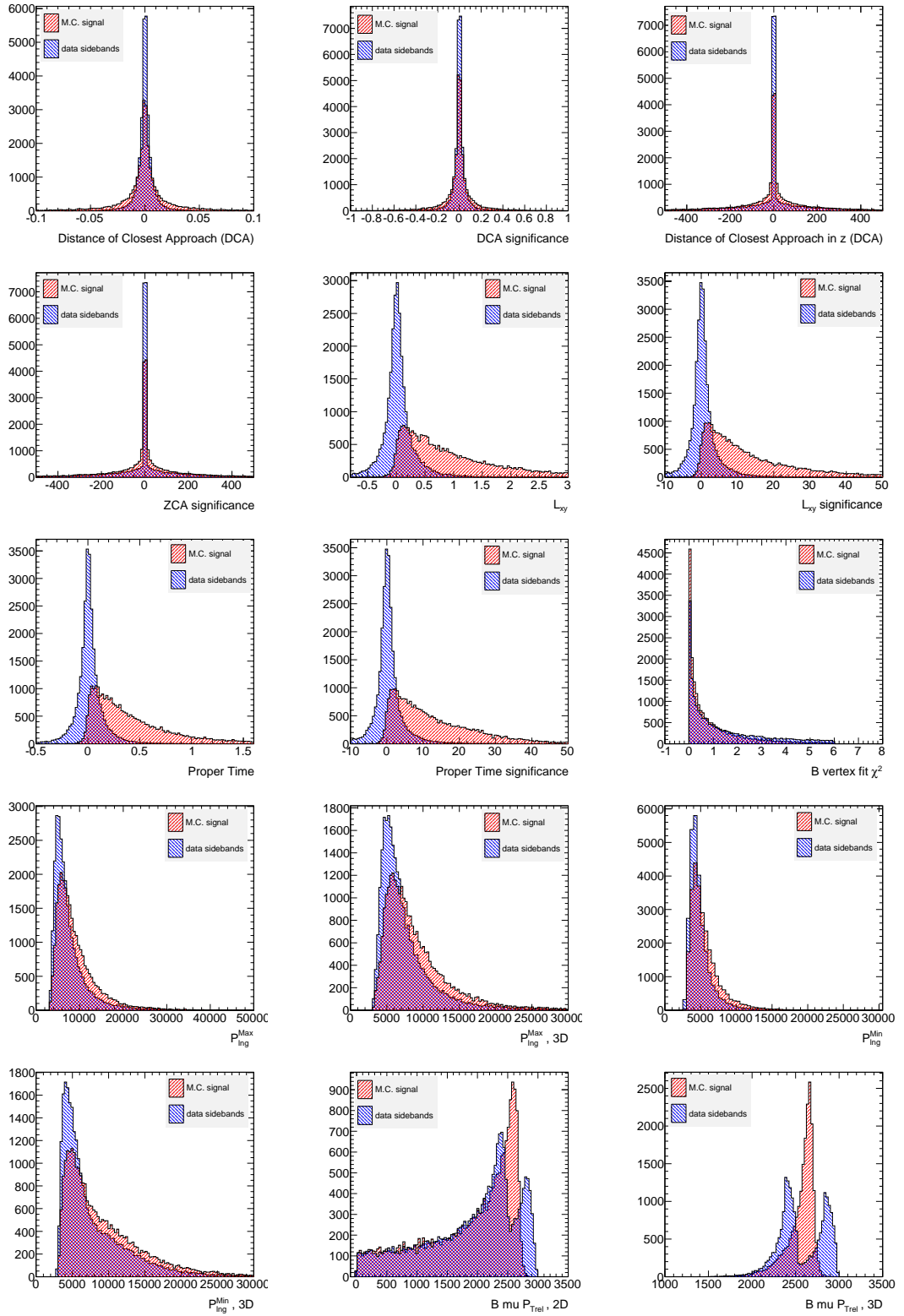
Figure B.2: *The discriminating variables (continuing from previous Figure). The variables displayed here are the D_{xy}^{min}, D_{xy}^{min} significance, D_z^{min}, D_z^{min}, significance, L_{xy}, L_{xy} significance, t_0, t_0 significance, fit χ_B^2, $|p_L^{max}|$, $|p_L^{min}|$(2D), $|p_L^{max}|$, $|p_L^{max}|$ (3D).*

B.3   Histograms related to the Discrimination Capabilities of the Variables

The following section presents some examples of how the discriminating variable that shows the best separation power is chosen, among a group of other discriminating variables. The method that is followed is based in the concepts developed in 7.6.6.

Two examples of the application of this method are shown in Figures B.3, B.4. The initial possible discriminating variables, are properly re-grouped in smaller groups of variables, that are highly correlated. This is done with the help of the correlation matrices (see 7.8).

Subsequently, within a group, the ranking of the variables according to their separation power, is done by looking at the curves:

1. ROC curves:
   The name stands for *Receiver Operating Characteristic curve* and it is defined as the plot of the true positive rate against the false positive rate for the different possible points of the cuts of a test. Generally, the ROC curve is related to the ratio of the benefit over the cost. Graphically, the ROC curve starts at point (0,1). This point declares zero (0%) signal efficiency, $\text{eff}_{\text{SIG}} = 0$ and maximum (100%), background rejection, $\text{rej}_{\text{BGR}} = 1$. The ROC curve stops at the point (1,0). This point declares maximum (100%) signal efficiency, $\text{eff}_{\text{SIG}} = 1$ and zero (0%) background rejection, $\text{rej}_{\text{BGR}} = 0$. If the same plot includes more than one ROC curve, the ROC curve that appears to be "higher" than the others, is the one that corresponds to the best benefit over cost ratio.

   The ROC curves are commonly used in high energy physics analysis. In this case, the benefit is the background rejection, and the cost is the signal efficiency. In the examples that follow, the curve that appears "on the top" of the other curves is the one that corresponds to the variable with the best separation power of this group and though, is the variable to be included in the final list of discriminating variables.

2. $\log(\text{rej}_{\text{BGR}})/\log(\text{eff}_{\text{SIG}})$ curves:
   In the most typical examples, the ROC curves of the separation variables are well separated in the plot and the selection of the best separation variable can be performed easily as explained above. Nevertheless, in some examples, the ROC curves appear to be almost not separable, especially in the small signal efficiency range. In such cases, a good resolution of the separation of the curves can be achieved by using the logarithmic values of the efficiencies and the rejections. Specifically, the curve $\log(\text{rej}_{\text{BGR}})/\log(\text{eff}_{\text{SIG}})$ is the one used in this analysis when the separation of the ROC curves is insignificant.

   It has to taken into notice though, that since the logarithm of the values is used, in the case of $\log(\text{rej}_{\text{BGR}})/\log(\text{eff}_{\text{SIG}})$ curves, the curve that is located *lower* than the rest of the group, is the one that offers the best separation power.
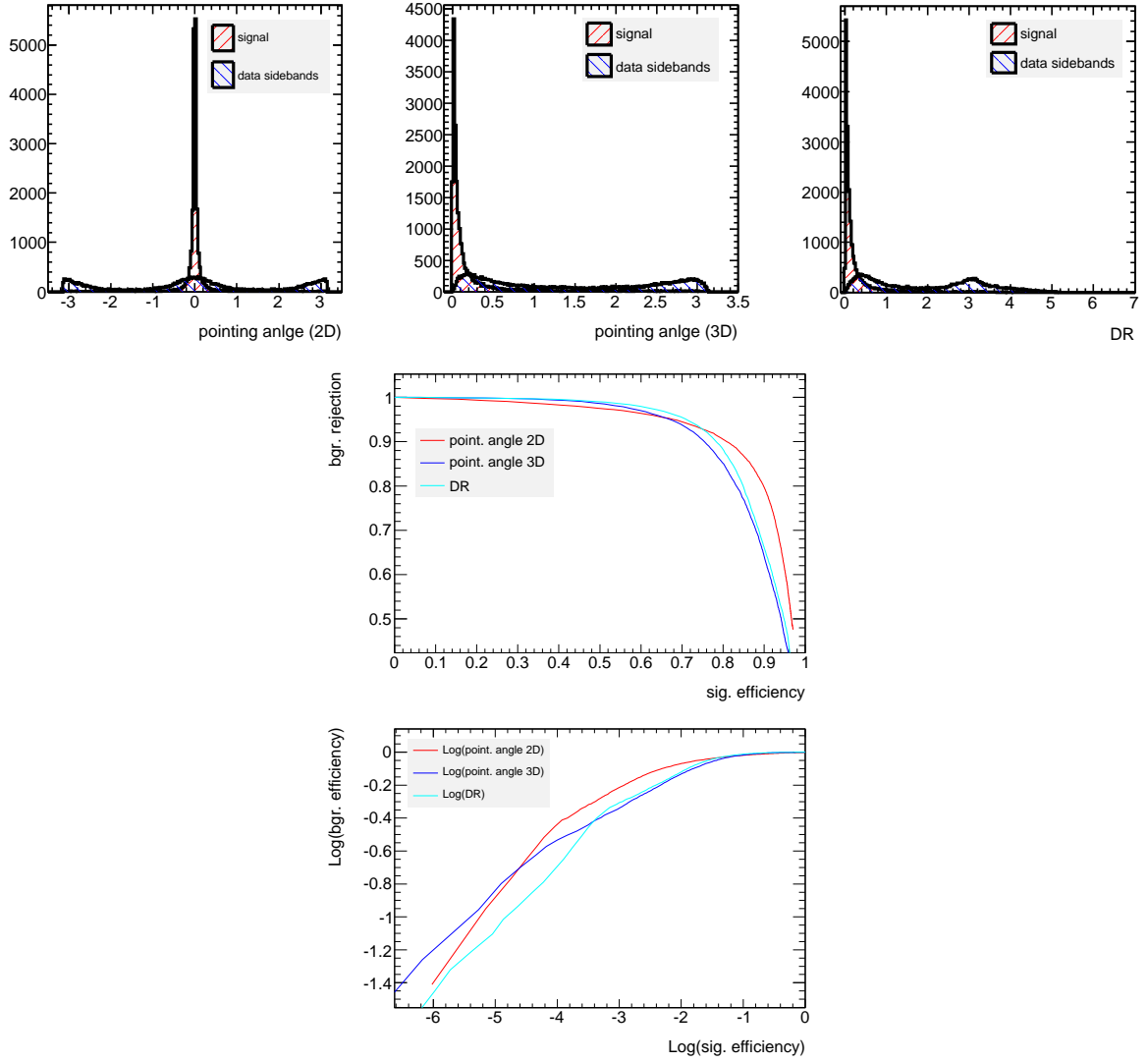
Figure B.3: *Pointing angle calculated in 2D (α_{2D}) (top left), pointing angle calculated in 3D (α_{3D}) (top middle), ΔR (top right). The ROC curves (second row) and $log(rej_{BGR})/log(eff_{SIG})$ curves (bottom) show clearly that in the high signal efficiencies, the line that is "higher" than the rest is the one that corresponds to the α_{2D} showing that this variable offers the best separation power than the rest of this group. Nevertheless, in small signal efficiencies, the lines seem to be entangled, and the decision can not be made by looking only at the ROC curves. By using the $log(rej_{BGR})/log(eff_{SIG})$ curves, we clearly notice that the "lower" line is the one that corresponds to the ΔR variable showing that this variable is the one that offers the best separation power than the rest of this group in the small signal efficiencies range. Finally, both the α_{2D} and ΔR variables have to be used, since they offer the best separation power in the higher and lower signal efficiency ranges accordingly.*
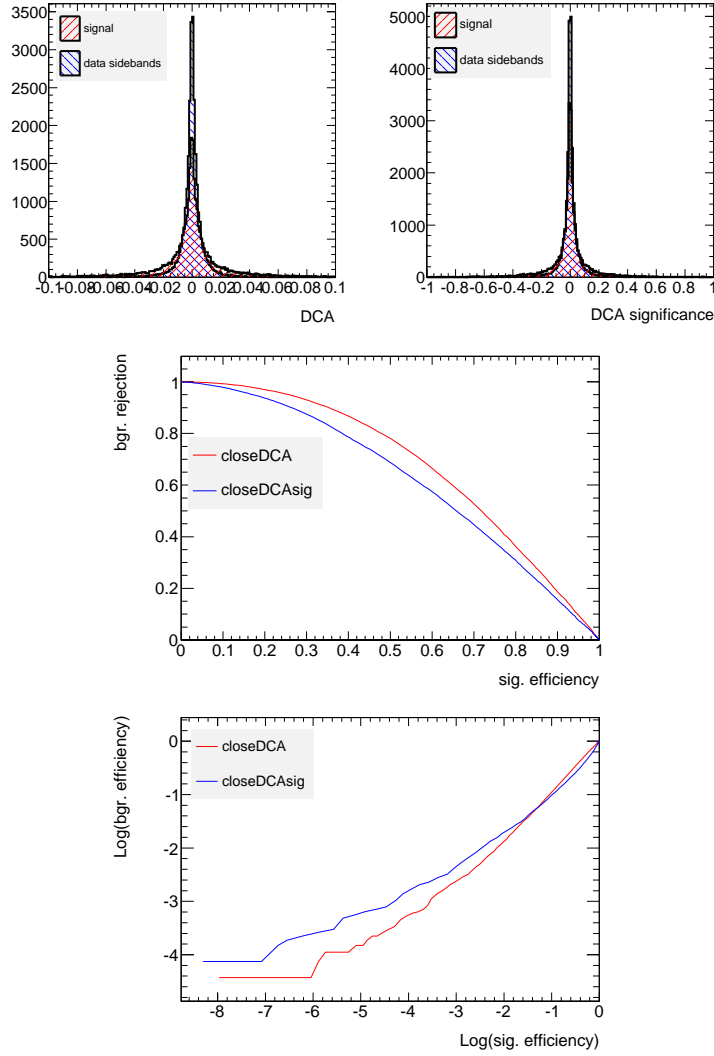
Figure B.4: *Distance of Closest Approach (DCA) (left), Distance of Closest Approach (DCA) significance (right). The ROC curves (second row) and $log(rej_{BGR})/log(eff_{SIG})$ curves (bottom), show that the DCA shows better separation power in all signal efficiency range.*

Appendix C

DCS Data Viewer Appendix

C.1   Example of DDV XML Configuration File

```
\textbf{Example of the XML configuration file}
<DDV version="1.3">
<!--DDV Configuration XML file-->
<DDVitem ID="0">
  <elementName>LHC BPTX TotalIntensity Beam1 </elementName>
  <queryType>comment_</queryType>
  <schema>atlas_pvssDCS</schema>
  <selectHoursEnabled>False</selectHoursEnabled>
  <selectHoursValue>24</selectHoursValue>
  <startTime>12:0</startTime>
  <startDate>12-10-2011</startDate>
  <endTime>12:0</endTime>
  <endDate>13-10-2011</endDate>
  <relQ.op1> </relQ.op1>
  <relQ.val1> </relQ.val1>
  <relQ.ANDOR> </relQ.ANDOR>
  <relQ.op2> </relQ.op2>
  <relQ.val2> </relQ.val2>
</DDVitem>
<DDVitem ID="1">
  <elementName>LHC BPTX TotalIntensity Beam2 </elementName>
  <queryType>comment_</queryType>
  <schema>atlas_pvssDCS</schema>
  <selectHoursEnabled>False</selectHoursEnabled>
  <selectHoursValue>24</selectHoursValue>
  <startTime>12:0</startTime>
  <startDate>12-10-2011</startDate>
  <endTime>12:0</endTime>
  <endDate>13-10-2011</endDate>
  <relQ.op1> </relQ.op1>
  <relQ.val1> </relQ.val1>
  <relQ.ANDOR> </relQ.ANDOR>
  <relQ.op2> </relQ.op2>
  <relQ.val2> </relQ.val2>
</DDVitem>
</DDV>
```

C.2   RPM Package Manager

The RPM [141] package management system was introduced by the end of 90s in *Red Had Linux*
distributions. While typically containing the compiled version of the software of an application,
it also comprises information of the installation procedure of the software and information of
post-install actions. The configuration of the RPM package is done in its *spec* file that includes
building steps, naming and versioning information and installation procedures. DDV server and
DDV client have their own RPM package *atlas-ddv-server.rpm*, *atlas-ddv-client.rpm* accordingly
(see appendix: C.3).

    The structure of the DDV server spec file is explained below:

The preamble

    The preamble is located on the top of the file. Its entries are listed one per line and start
with a tag with a colon followed by the relevant information. It keeps some useful infor-
mation of the package, including data of the developers, the version and the description.
In this first part of the *spec* file, some global variables are stored, such as the name
of the package and the destination place. The name of the package is called *atlas-ddv-
server-svn* and it is included in the filename of the package. The versioning of the DDV
rpm package follows the versioning of the DDV software in the SVN (SVN is the software
versioning control system that is used by most groups and communities in CERN). The
licence is the *zlib* permissive free software licence [142]. Since DDV rpms consist only of
non-binary files (source code, images, text files), the architecture is chosen to be *noarch*.

```
# Current developers:
# Charilaos.Tsarouchas@cern.ch
# Stefan.Schlenker@cern.ch
# mirjam.fehling@physik.uni-freiburg.de
# stefan.winkelmann@physik.uni-freiburg.de

%define name atlas-ddv-server-svn
%define version 1.0.0
%define unmangled_version 1.0.0
%define release 6
%define place /data/DDV/

Summary: A flexible data viewing application for ATLAS DCS data.
Name: %{name}
Version: %{version}
Release: %{release}
Source0: %{name}.tar.gz
Licence: zlib/libpng licence
Group: Development/Libraries
BuildRoot: %{_tmppath}/%{name}-%{version}-%{release}-buildroot
BuildArch: noarch
Prefix: %{_prefix}
Vendor: Charilaos.Tsarouchas@cern.ch
Url: https://twiki.cern.ch/twiki/bin/view/Atlas./AtlasDcsDdv

%description
The Dcs Data Viewer is an application for the viewing of ATLAS DCS data. The application
is split into two main parts, a server and a client.The client is written in java with
the help of GWT tool and is organised in a web panel that helps the user to access and
visualise data. The server is written in python and can be used without the client,
stand alone.
```

The prep Section

    The *prep* section prepares the package building process. The installation of the DDV

package does not need any special preparation. The only information entered here is the *setup* macro, which cleans up old installations, uncompresses and extracts files from the source.

```
%prep
%setup -n %{name}
```

The build Section

The *build* section is the section responsible for performing the building of the software. In DDV, the RPM does not include any software (just files) so there is not any information in this section.

```
%build
```

The install Section

It is executed like a shell script. In this case it creates the destination folder of the DDV server and copies there all the necessary files.

```
%install
%{__rm} -rf %{buildroot}
/bin/mkdir -p %{buildroot}%{place}
/bin/cp -a * %{buildroot}%{place}
```

The pre Section

The *pre* section deals with all the necessary steps that have to be done prior to the installation. Generally it is rarely used and DDV *spec* files do not need this section either.

```
%pre
```

The post Section

The *post* section includes scripts that are executed after the installation of the package. The post section covers the DDV needs by installing one *cron job* that is responsible for the daily update of metadata information and a second one that is responsible for the rotation of the log information of the server. In the same section the *start/stop* scripts of the service are installed in the appropriate place and a command is executed that starts the service.

```
%post
# Install the cron job
if [ -e /var/spool/cron/atlddvs ]; then
  sed -i ':^0-59/1.*/DDV_updateSqliteWatchdog.sh:d' /var/spool/cron/atlddvs
  cat /var/spool/cron/atlddvs |sed -e '/DDV_updateSqliteWatchdog/d' \
  > /var/spool/cron/atlddvs
fi
cat  /data/DDV/Server/setupServer/DDV_cronfile >> /var/spool/cron/atlddvs
echo ">>> DDV cronjobs installed... "
/bin/chown atlddvs:root /var/spool/cron/atlddvs
/bin/chmod 600 /var/spool/cron/atlddvs

#install Start/Stop script
/bin/chown -R atlddvs:zp /data/DDV
/bin/chmod -R g+rw /data/DDV
/usr/bin/install -o root -g root -m 755 /data/DDV/Server/setupServer/atlas-ddv-server \
/etc/init.d/atlas-ddv-server
/sbin/chkconfig --add atlas-ddv-server
/sbin/chkconfig atlas-ddv-server on
#stop the server in case it is running from previous installation
/sbin/service atlas-ddv-server stop || exit 0
sudo -u atlddvs /usr/bin/nohup /sbin/service atlas-ddv-server start >/dev/null || exit 0 &
echo ">>> DDV server started... "
```

The preun Section

The preun section is activated before the deletion of the package, which can happen, for example, during an update of a new release. The first action performed is to stop the service and thereafter to remove the relevant cron-job lines from the cron file.

```
%preun
if [ $1 -eq 0 ]; then
  /etc/init.d/atlas-ddv-server status | grep -q "running"
  status=$?

  # stopping DDV server
  if [ ${status} -eq 0 ]; then
      echo ">>> Stopping the DDV server service..."
      /sbin/service atlas-ddv-server stop || exit 0
  fi

   # Removing lines from cron job
   if [ -e /var/spool/cron/atlddvs ]; then
 echo ">>> Removing relative cron job lines for the atlddvs user ..."
 # sed -i ':^0-59/1.*/DDV_updateSqliteWatchdog.sh:d' /var/spool/cron/atlddvs
 cat /var/spool/cron/atlddvs |sed -e '/DDV_updateSqliteWatchdog/d' > /var/spool/cron/atlddvs
         cat /var/spool/cron/atlddvs |sed -e '/DDV_logrotate/d' > /var/spool/cron/atlddvs
    fi

fi

serv=`eval chkconfig --list atlas-ddv-server 2>/dev/null | awk -F" " '{print $1}'`
if [ "x${serv}" = "xatlas-ddv-server" ]; then
   echo ">>>Removing the atlas-ddv-server service from chkconfig..."
   /sbin/chkconfig --del atlas-ddv-server
fi
```

The postun Section

The postun section, is commonly used for a clean up after the package is removed. It removes the *start/stop* file.

```
%postun
if [ $1 -eq 0 ]; then
  /bin/rm -f /etc/init.d/atlas-ddv-server
fi
```

The clean Section

As the name suggests, the clean section deals with some clean up of the files that are not part of the applications build area.

```
%clean
%{__rm} -rf %{buildroot}
#install atlas-ddv-server %{buildroot}/etc/init.d/atlas-ddv-server
```

The files Section

The files section contains a list of files that are part of the package. It contains the *defattr* directives that allows setting of default attributes for files and directives.

```
%files
%defattr(-,root,root)
/data/DDV/
```

C.3   The DDV RPM .spec Files

The DDV server RPM .spec File

```
# Current developers:
# Charilaos.Tsarouchas@cern.ch
# Stefan.Schlenker@cern.ch
# mirjam.fehling@physik.uni-freiburg.de
# stefan.winkelmann@physik.uni-freiburg.de

%define name atlas-ddv-server-svn
%define version 1.0.0
%define unmangled_version 1.0.0
%define release 6
%define place /data/DDV/

Summary: A flexible data viewing application for ATLAS DCS data.
Name: %{name}
Version: %{version}
Release: %{release}
Source0: %{name}.tar.gz
License: zlib/libpng license
Group: Development/Libraries
BuildRoot: %{_tmppath}/%{name}-%{version}-%{release}-buildroot
BuildArch: noarch
Prefix: %{_prefix}
Vendor: Charilaos.Tsarouchas@cern.ch
Url: https://twiki.cern.ch/twiki/bin/view/Atlas./AtlasDcsDdv

%description
The Dcs Data Viewer is an application for the viewing of ATLAS DCS data. The application is split
into two main parts, a server and a client. The client is written in java with the help of GWT tool
and is  organised in a web panel that helps  the user to access and visualise data. The server is
written in python and can be used without the client, stand alone.

%prep
%setup -n %{name}
#%setup -n %{name}-%{unmangled_version}

%build

%install
%{__rm} -rf %{buildroot}

/bin/mkdir -p %{buildroot}%{place}
/bin/cp -a * %{buildroot}%{place}

%pre

%post
# Install the cron job
if [ -e /var/spool/cron/atlddvs ]; then
  sed -i ':^0-59/1.*/DDV_updateSqliteWatchdog.sh:d' /var/spool/cron/atlddvs
  cat /var/spool/cron/atlddvs |sed -e '/DDV_updateSqliteWatchdog/d' > /var/spool/cron/atlddvs
fi
cat  /data/DDV/Server/setupServer/DDV_cronfile >> /var/spool/cron/atlddvs
echo ">>> DDV cronjobs installed... "
/bin/chown atlddvs:root /var/spool/cron/atlddvs
/bin/chmod 600 /var/spool/cron/atlddvs

#install Start/Stop script
/bin/chown -R atlddvs:zp /data/DDV
/bin/chmod -R g+rw /data/DDV
/usr/bin/install -o root -g root -m 755 /data/DDV/Server/setupServer/atlas-ddv-server /etc/init.d/atlas-ddv-ser
/sbin/chkconfig --add atlas-ddv-server
/sbin/chkconfig atlas-ddv-server on
#stop the server in case it is running from previous installation
```

```
/sbin/service atlas-ddv-server stop || exit 0
sudo -u atlddvs /usr/bin/nohup /sbin/service atlas-ddv-server start >/dev/null || exit 0 &
echo ">>> DDV server started... "


%preun
if [ $1 -eq 0 ]; then
  /etc/init.d/atlas-ddv-server status | grep -q "running"
  status=$?

  # stopping DDV server
  if [ ${status} -eq 0 ]; then
      echo ">>> Stopping the DDV server service..."
      /sbin/service atlas-ddv-server stop || exit 0
  fi

   # Removing lines from cron job
   if [ -e /var/spool/cron/atlddvs ]; then
echo ">>> Removing relative cron job lines for the atlddvs user ..."
# sed -i ':^0-59/1.*/DDV_updateSqliteWatchdog.sh:d' /var/spool/cron/atlddvs
cat /var/spool/cron/atlddvs |sed -e '/DDV_updateSqliteWatchdog/d' > /var/spool/cron/atlddvs
        cat /var/spool/cron/atlddvs |sed -e '/DDV_logrotate/d' > /var/spool/cron/atlddvs
   fi

fi

serv=`eval chkconfig --list atlas-ddv-server 2>/dev/null | awk -F" " '{print $1}'`
if [ "x${serv}" = "xatlas-ddv-server" ]; then
   echo ">>>Removing the atlas-ddv-server service from chkconfig..."
   /sbin/chkconfig --del atlas-ddv-server
fi


%postun
if [ $1 -eq 0 ]; then
  /bin/rm -f /etc/init.d/atlas-ddv-server
fi

%clean
%{__rm} -rf %{buildroot}
#install atlas-ddv-server %{buildroot}/etc/init.d/atlas-ddv-server

%files
%defattr(-,root,root)
/data/DDV/
```

The DDV client RPM .spec file

```
# Current developers:
# mirjam.fehling@physik.uni-freiburg.de
# stefan.winkelmann@physik.uni-freiburg.de
# Stefan.Schlenker@cern.ch
# Charilaos.Tsarouchas@cern.ch


%define name atlas-ddv-client-svn
%define version 1.0.0
%define unmangled_version 1.0.0
%define release 6
%define place /data/DDV/Client/atlas-ddv-apache-tomcat-6.0.20/apache-tomcat-6.0.20/webapps/


Summary: A flexible data viewing application for ATLAS DCS data.
Name: %{name}
Version: %{version}
Release: %{release}
Source0: %{name}.tar.gz
License: zlib/libpng license
Group: Development/Libraries
BuildRoot: %{_tmppath}/%{name}-%{version}-%{release}-buildroot
BuildArch: noarch
Prefix: %{_prefix}
Vendor: Charilaos.Tsarouchas@cern.ch
Url: https://twiki.cern.ch/twiki/bin/view/Atlas./AtlasDcsDdv

%description
The Dcs Data Viewer is an application for the viewing of ATLAS DCS data. The
application is split into two main parts, a server and a client. The client is written in java with
the help of GWT tool and is  organised in a web panel that helps  the user to access and visualise
data.    The server is written in python and can be used without the client,
stand alone.


%prep
%setup -n %{name}
#%setup -n %{name}-%{unmangled_version}

%build

%install
%{__rm} -rf %{buildroot}

/bin/mkdir -p %{buildroot}%{place}
/bin/cp -a * %{buildroot}%{place}

%pre

%post
/bin/chown -R atlddvs:zp /data/DDV
/bin/chmod -R g+rw /data/DDV
/usr/bin/install -o root -g root -m 755 \
/data/DDV/Client/atlas-ddv-apache-tomcat-6.0.20/apache-tomcat-6.0.20/webapps/DDV/atlas-ddv-client \
/etc/init.d/atlas-ddv-client
/sbin/chkconfig --add atlas-ddv-client
/sbin/chkconfig atlas-ddv-client on
/sbin/service atlas-ddv-client start || exit 0

%preun
if [ $1 -eq 0 ]; then
  /etc/init.d/atlas-ddv-client status | grep -q "running"
  status=$?
  if [ ${status} -eq 0 ]; then
      echo "Stopping the DDV client service"
      /sbin/service atlas-ddv-client stop || exit 0
  fi
```

```
fi

serv=`eval chkconfig --list atlas-ddv-client 2>/dev/null | awk -F" " '{print $1}'`
if [ "x${serv}" = "xatlas-ddv-client" ]; then
    echo "Removing the atlas-ddv-client service from chkconfig"
    /sbin/chkconfig --del atlas-ddv-client
fi


%postun
if [ $1 -eq 0 ]; then
  /bin/rm -f /etc/init.d/atlas-ddv-client
fi




%clean
%{__rm} -rf %{buildroot}

%files
%defattr(-,root,root)
/data/DDV/Client/atlas-ddv-apache-tomcat-6.0.20/apache-tomcat-6.0.20/webapps/
```

The DDV apache-tomcat modified RPM .spec file

```
# Current developers:
# mirjam.fehling@physik.uni-freiburg.de
# stefan.winkelmann@physik.uni-freiburg.de
# Stefan.Schlenker@cern.ch
# Charilaos.Tsarouchas@cern.ch


## is exactly the same directory with the apache-tomcat-6.0.20
## BUT it is removed the "examples" directory for security reasons

%define name atlas-ddv-apache-tomcat-6.0.20-svn
%define version 1.0.0
%define unmangled_version 1.0.0
%define release 1
%define place /data/DDV/Client/atlas-ddv-apache-tomcat-6.0.20

Summary: tomcat apache engine for DDV needs.
Name: %{name}
Version: %{version}
Release: %{release}
Source0: %{name}.tar.gz
License: zlib/libpng license
Group: Development/Libraries
BuildRoot: %{_tmppath}/%{name}-%{version}-%{release}-buildroot
BuildArch: noarch
Prefix: %{_prefix}
Vendor: Charilaos.Tsarouchas@cern.ch
#Url: http://pysqlite.googlecode.com/

%description
Put shotrt discription here

%prep
#%setup -n DDV
%setup -n %{name}
#%setup -n %{name}-%{unmangled_version}

%build

%install
%{__rm} -rf %{buildroot}

mkdir -p %{buildroot}%{place}
cp -a * %{buildroot}%{place}


%clean
%{__rm} -rf %{buildroot}

%files
%defattr(-,root,root)
/data/DDV/Client/atlas-ddv-apache-tomcat-6.0.20
```

The update SQLite watchdog file

```bash
#!/bin/bash

export TNS_ADMIN=/etc/oracle/
export SQLPATH=/usr/lib/oracle/10.2.0.4/client64/bin
export PATH=$PATH:$SQLPATH
export ORACLE_HOME=/usr/lib/oracle/10.2.0.4/client64
export LD_LIBRARY_PATH=$LD_LIBRARY_PATH:$ORACLE_HOME/lib

#create the log file and modify permissions
touch /data/tsarouch/DDViewer/Server/setupServer/DDV.log
chmod 777 /data/tsarouch/DDViewer/Server/setupServer/DDV.log

#check if server is running...
ps efaux | grep python | grep DDV_UpdateSqliteTables
#if not found equals to 1 , start it

if [ $? -eq 1 ]
then
echo DDV UpdateSqliteTables is NOT running
python2.5 /data/DDV/Server/DDV_UpdateSqliteTables.py >> /data/DDV/Server/setupServer/DDV.log 2>&1 &
else
echo DDV server is running
fi
```

C.4 DDV Start/Stop Files

The Start/Stop file of the client

```
#! /bin/bash
#
# Start/stop file for atlas-ddv-client service
#
# chkconfig: 2345 99 00
# description: DDV application
# Start/Stop script for DDV client
# processname: atlas-ddv-client


#. /etc/init.d/functions


#
# Define useful CATALINA options
#
#CATALINA_PID="/data/DDV/Client/atlas-ddv-apache-tomcat-6.0.20/apache-tomcat-6.0.20/logs/tomcat.pid"
CATALINA_PID="/tmp/catalina.pid"
export CATALINA_PID

ATLAS_TOMCAT_DDV_PATH="/data/DDV/Client/atlas-ddv-apache-tomcat-6.0.20/apache-tomcat-6.0.20/bin"
ATLAS_DDV_SERVER_PATH="/data/DDV/Server/"

ServiceName="atlas-ddv-client"

#
# Check if service user exists
#
UserName=atlddvs

id=`id -u $UserName`
if [ $? -ne 0 ] ; then
        echo User $UserName doesn\'t exists\! Skiping action $@ on service atlas-ddv.
        exit 1
fi

start()
{
 if [ -e ${CATALINA_PID} ]; then
   /bin/rm ${CATALINA_PID}
 fi

 [ `id -u` != $id ] \
   && exec sudo -E -u atlddvs ${ATLAS_TOMCAT_DDV_PATH}/startup.sh || exit 2
 exec ${ATLAS_TOMCAT_DDV_PATH}/startup.sh

}

stop()
{
 if [ -e ${CATALINA_PID} ]; then
   /bin/rm ${CATALINA_PID}
 fi

 [ `id -u` != $id ] \
   && exec sudo -E -u atlddvs ${ATLAS_TOMCAT_DDV_PATH}/shutdown.sh || exit 2
 exec ${ATLAS_TOMCAT_DDV_PATH}/shutdown.sh
}

status()
{
 if [ -s "${CATALINA_PID}" ]; then
   ps -p `cat ${CATALINA_PID}` 1>/dev/null
   if [ $? -eq 0 ]; then
     echo "${ServiceName} (pid" `cat ${CATALINA_PID}`") is running..."
     exit 0
```

```
    else
     echo "${ServiceName} with pid" `cat ${CATALINA_PID}` "non existing but pid file ${CATALINA_PID} existing"
     exit 1
    fi
 else
    echo "${ServiceName} is stopped"
 fi
}

case "$1" in
  start)
        start
        ;;
  stop)
        stop
        ;;
  status)
        status
        ;;
  restart|reload)
        stop && start
        ;;
  condrestart)
        ;;
  *)
        echo $"Usage: $0 {start|status|stop}"
        exit 1
esac
```

The Start/Stop file of the server

```
#! /bin/bash
#
# Start/stop file for atlas-tomcat-ddv service
#
# chkconfig: 2345 99 00
# description: DDV application
# Start/Stop script for DDV server
# processname: atlas-ddv-server

#. /etc/init.d/functions



# --- define some variables
ATLAS_DDV_SERVER_PATH="/data/DDV/Server"
ServiceName="atlas-ddv-server"
UserName=atlddvs

# --- export some enviromental vars - for central ATLAS systems (voatlas53, voatlas120)
export ROOTSYS=/afs/cern.ch/sw/lcg/app/releases/ROOT/5.26.00/x86_64-slc5-gcc34-opt/root
export LD_LIBRARY_PATH=$ROOTSYS/lib:$PYTHONDIR/lib:$LD_LIBRARY_PATH
export PYTHONPATH=$ROOTSYS/lib:$PYTHONPATH
export LD_LIBRARY_PATH=$ROOTSYS/lib:$PYTHONDIR/lib:$LD_LIBRARY_PATH
export PYTHONPATH=$ROOTSYS/lib:$PYTHONPATH


# --- Check if service user (atlddvs) exists
id=`id -u $UserName`
if [ $? -ne 0 ] ; then
        echo User $UserName doesn't exists\! Skiping action $@ on service atlas-ddv.
        exit 1
fi


# --- Start function...
start()
{
    # if the user that starts DDV Server is not atlddvs:
    if [ `id -u` != $id ]; then
#sudo -E -u atlddvs python2.5 ${ATLAS_DDV_SERVER_PATH}/DDV_StartServer.py || exit 2
#sudo -E -u atlddvs /usr/bin/nohup python2.5  ${ATLAS_DDV_SERVER_PATH}/DDV_StartServer.py >/dev/null \
  || exit 2 &
sudo -E -u atlddvs /usr/bin/nohup python2.5 \
   ${ATLAS_DDV_SERVER_PATH}/DDV_StartServer.py > ${ATLAS_DDV_SERVER_PATH}/setupServer/DDV.log \
   || exit 2 &
    # if the user that starts DDV Server is atlddvs:
    else
        /usr/bin/nohup python2.5  ${ATLAS_DDV_SERVER_PATH}/DDV_StartServer.py  > \
        ${ATLAS_DDV_SERVER_PATH}/setupServer/DDV.log &
    fi
}


# --- Stop function...
stop()
{
    ps aux | grep python | grep  DDV_StartServer | grep -v grep | awk '{ print $2 }' | xargs -i kill {}
    echo DDV server stopped...
}


# --- Get Status function...
status()
{
    ps efaux | grep python | grep DDV_StartServer >>/dev/null
    if [ $? -eq 1 ]
       then
```

```
            echo DDV server is stopped....
        else
            echo DDV server running...
    fi
}



case "$1" in
  start)
        start
        ;;
  stop)
        stop
        ;;
  status)
        status
        ;;
  restart|reload)
        stop && start
        ;;
  condrestart)
        ;;
  *)
        echo $"Usage: $0 {start|status|stop}"
        exit 1
esac
```

C.5   RPM Package Manager

The RPM [141] package management system was introduced by the end of 90s in *Red Had Linux* distributions. While typically containing the compiled version of the software of an application, it also comprises information of the installation procedure of the software and information of *post-install* actions. The configuration of the RPM package is done in its *spec* file that includes building steps, naming and versioning information and installation procedures. DDV server and DDV client have their own RPM package *atlas-ddv-server.rpm*, *atlas-ddv-client.rpm* accordingly (see appendix: C.3).

The structure of the DDV server spec file is explained below:

The preamble

The preamble is located on the top of the file. Its entries are listed one per line and start with a tag with a colon followed by the relevant information. It keeps some useful information of the package, including data of the developers, the version and the description. In this first part of the *spec* file, some global variables are stored, such as the name of the package and the destination place. The name of the package is called *atlas-ddv-server-svn* and it is included in the filename of the package. The versioning of the DDV rpm package follows the versioning of the DDV software in the SVN (SVN is the software versioning control system that is used by most groups and communities in CERN). The licence is the *zlib* permissive free software licence [142]. Since DDV rpms consist only of *non-binary* files (source code, images, text files), the architecture is chosen to be *noarch*.

```
# Current developers:
# Charilaos.Tsarouchas@cern.ch
# Stefan.Schlenker@cern.ch
# mirjam.fehling@physik.uni-freiburg.de
# stefan.winkelmann@physik.uni-freiburg.de
```

```
%define name atlas-ddv-server-svn
%define version 1.0.0
%define unmangled_version 1.0.0
%define release 6
%define place /data/DDV/

Summary: A flexible data viewing application for ATLAS DCS data.
Name: %{name}
Version: %{version}
Release: %{release}
Source0: %{name}.tar.gz
Licence: zlib/libpng licence
Group: Development/Libraries
BuildRoot: %{_tmppath}/%{name}-%{version}-%{release}-buildroot
BuildArch: noarch
Prefix: %{_prefix}
Vendor: Charilaos.Tsarouchas@cern.ch
Url: https://twiki.cern.ch/twiki/bin/view/Atlas./AtlasDcsDdv

%description
The Dcs Data Viewer is an application for the viewing of ATLAS DCS data. The application
is split into two main parts, a server and a client.The client is written in java with
the help of GWT tool and is organised in a web panel that helps the user to access and
visualise data. The server is written in python and can be used without the client,
stand alone.
```

The prep Section

The *prep* section prepares the package building process. The installation of the DDV package does not need any special preparation. The only information entered here is the *setup* macro, which cleans up old installations, uncompresses and extracts files from the source.

```
%prep
%setup -n %{name}
```

The build Section

The *build* section is the section responsible for performing the building of the software. In DDV, the RPM does not include any software (just files) so there is not any information in this section.

```
%build
```

The install Section

It is executed like a shell script. In this case it creates the destination folder of the DDV server and copies there all the necessary files.

```
%install
%{__rm} -rf %{buildroot}
/bin/mkdir -p %{buildroot}%{place}
/bin/cp -a * %{buildroot}%{place}
```

The pre Section

The *pre* section deals with all the necessary steps that have to be done prior to the installation. Generally it is rarely used and DDV *spec* files do not need this section either.

```
%pre
```

The post Section

The *post* section includes scripts that are executed after the installation of the package.

The post section covers the DDV needs by installing one *cron job* that is responsible for the daily update of metadata information and a second one that is responsible for the rotation of the log information of the server. In the same section the *start/stop* scripts of the service are installed in the appropriate place and a command is executed that starts the service.

```
%post
# Install the cron job
if [ -e /var/spool/cron/atlddvs ]; then
  sed -i ':^0-59/1.*/DDV_updateSqliteWatchdog.sh:d' /var/spool/cron/atlddvs
  cat /var/spool/cron/atlddvs |sed -e '/DDV_updateSqliteWatchdog/d' \
  > /var/spool/cron/atlddvs
fi
cat  /data/DDV/Server/setupServer/DDV_cronfile >> /var/spool/cron/atlddvs
echo ">>> DDV cronjobs installed... "
/bin/chown atlddvs:root /var/spool/cron/atlddvs
/bin/chmod 600 /var/spool/cron/atlddvs

#install Start/Stop script
/bin/chown -R atlddvs:zp /data/DDV
/bin/chmod -R g+rw /data/DDV
/usr/bin/install -o root -g root -m 755 /data/DDV/Server/setupServer/atlas-ddv-server \
/etc/init.d/atlas-ddv-server
/sbin/chkconfig --add atlas-ddv-server
/sbin/chkconfig atlas-ddv-server on
#stop the server in case it is running from previous installation
/sbin/service atlas-ddv-server stop || exit 0
sudo -u atlddvs /usr/bin/nohup /sbin/service atlas-ddv-server start >/dev/null || exit 0 &
echo ">>> DDV server started... "
```

The preun Section

The preun section is activated before the deletion of the package, which can happen, for example, during an update of a new release. The first action performed is to stop the service and thereafter to remove the relevant cron-job lines from the cron file.

```
%preun
if [ $1 -eq 0 ]; then
  /etc/init.d/atlas-ddv-server status | grep -q "running"
  status=$?

  # stopping DDV server
  if [ ${status} -eq 0 ]; then
      echo ">>> Stopping the DDV server service..."
      /sbin/service atlas-ddv-server stop || exit 0
  fi

   # Removing lines from cron job
   if [ -e /var/spool/cron/atlddvs ]; then
  echo ">>> Removing relative cron job lines for the atlddvs user ..."
  # sed -i ':^0-59/1.*/DDV_updateSqliteWatchdog.sh:d' /var/spool/cron/atlddvs
  cat /var/spool/cron/atlddvs |sed -e '/DDV_updateSqliteWatchdog/d' > /var/spool/cron/atlddvs
        cat /var/spool/cron/atlddvs |sed -e '/DDV_logrotate/d' > /var/spool/cron/atlddvs
   fi

fi

serv=`eval chkconfig --list atlas-ddv-server 2>/dev/null | awk -F" " '{print $1}'`
if [ "x${serv}" = "xatlas-ddv-server" ]; then
  echo ">>>Removing the atlas-ddv-server service from chkconfig..."
   /sbin/chkconfig --del atlas-ddv-server
fi
```

The postun Section

The postun section, is commonly used for a clean up after the package is removed. It removes the *start/stop* file.

```
%postun
if [ $1 -eq 0 ]; then
  /bin/rm -f /etc/init.d/atlas-ddv-server
fi
```

The clean Section

As the name suggests, the clean section deals with some clean up of the files that are not part of the applications build area.

```
%clean
%{__rm} -rf %{buildroot}
#install atlas-ddv-server %{buildroot}/etc/init.d/atlas-ddv-server
```

The files Section

The files section contains a list of files that are part of the package. It contains the *defattr* directives that allows setting of default attributes for files and directives.

```
%files
%defattr(-,root,root)
/data/DDV/
```

List of Tables

List of Figures

Bibliography

[1] G. Punzi, "Sensitivity for searches of new signal and its optimisation," *SLAC Stanford*, 2003.

[2] A. J. Burasm, G. Isidory, P. Paradisi, "Edms versus cpv in bs,d mixing in two higgs doublet models with mfv," *Phys. Lett.*, vol. **B694**, pp. 402–409, 2011.

[3] The ATLAS Collaboration, *ATL-COM-PHYS-2011-1619*, 2011.

[4] C. Amsler *et al. Phys. Lett.*, vol. **B667**, 2008.

[5] Elisa Musto, "The search for the rare decay $B_s \to \mu^+ \mu^-$ with the ATLAS detector at LHC," *Thesis*, 2011.

[6] A. L. Read , *J Phys*, vol. **G28**, pp. 2693–2704, 2002.

[7] Lichtenberg, Don Bernett and S. P. Rosen, "Developments in the quark theory of hadrons," 1980.

[8] O. W. Greenberg, *Phys. Rev. Lett.*, vol. **13**, 20, 1964.

[9] J. J. Aubert, *Phys. Rev. Lett.*, vol. **33**, 1404, 1974.

[10] J. Augustin *et al. Phys. Rev. Lett.*, vol. **33**, 1406, 1974.

[11] S. D. Drell, *Scientific American*, vol. **50**, 1975.

[12] D. Griffiths, *Introduction to Elementary Particles.* Physics Textbook, Wiley-VCH, 2008.

[13] E. Stueckelberg *Helv. Phys. Act*, vol. **A14**, pp. 588–594, 1941.

[14] S. D. Drell, S. L. Glashow, *Nucl. Phys.*, vol. **22**, 579, 1961.

[15] Wolfgang Pauli, *Rev. Mod. Phys.*, vol. **13**, pp. 203–232, 1941.

[16] S. Weinberg, *Phys. Rev. Lett.*, vol. **19**, p. 1264, 1967.

[17] G. Hooft and M. J. G. Veltman, *Nucl. Phys.*, vol. **B44**, 189, 1972.

[18] D. Griffiths, *Introduction to Elementary Particles.* Physics Textbook, Wiley-VCH, 2008.

[19] N.Arkani-Hamed, A.G. Cohen, and H. Georgi, *Phys. Lett.*, vol. **B513**, pp. 232–240, 2001.

[20] S. Dawson, *Phys. Rev. Lett.*, vol. **62**, 579, pp. 1232–1235, 1989.

[21] R. R. Wilson, *FERMILAB-TM-0763*, 1978.

[22] "Rencontres de Moriond, ." `http://moriond.in2p3.fr/`, 2012.

[23] R. Barate *et al. Phys. Lett.*, vol. **B565**, 61, 2003.

[24] CDF Collaboration, *Phys. Lett.*, vol. **103**, 52, 2009.

[25] D0 Collaboration, *Phys. Rev. Lett.*, vol. **102**, 2009.

[26] J. Wess, Zumino, *Phys. Lett.*, vol. **B49**, 52, 1974.

[27] A. Djouadi, *hep-ph/9901246v1*, 1999.

[28] A. ARbeg, M. Battoglia, F. Mahmoudi, *CERN-PH-TH*, 2011.

[29] The D0 Collaboration, *New J. Phys.*, vol. **9** 335, 2007.

[30] The ATLAS Collaboration, *JINST*, vol. **3**, S08003, 2008.

[31] The CMS Collaboration, *JINST*, vol. **3**, S08004, 2008.

[32] The ALICE Collaboration, *JINST*, vol. **3**, S08002, 2008.

[33] The LHCb Collaboration, *JINST*, vol. **3**, S08005, 2008.

[34] The TOTEM Collaboration, *JINST*, vol. **3**, S08007, 2008.

[35] The LHCf Collaboration, *CERN-LHCC-2006-004, LHCF-TDR-001*, 2006.

[36] A. P. G. Kane, *Perspectives on LHC physics*. World Scientific, 2008.

[37] A. G. *et al.*, "Expected performance of the atlas experiment - detector, trigger and physics," *CERN-OPEN- 2008-020, arXiv:0901.0512*, 2009.

[38] "ATLAS Inner Detector," *ATLAS-TDR-005, CERN-LHCC-97-017*, 1997.

[39] "Status and performance of the atlas pixel detector," *ATL-COM-INDET-2012-015*, 2012.

[40] A. Abdesselam *et al. JINST*, vol. **3**, P10006, 2008.

[41] E. Hines *et al. ATL-INDET-PROC-2011-035*, 2011.

[42] ATLAS Collaboration, *JINST*, vol. **3**, S08003, 2008.

[43] "Atlas muon spectrometer, technical design report," *CERN/LHCC/97-22*, 1997.

[44] W. Lavrijsen, *ATLAS-TDR-006, CERN-LHCC-97-018*, 1997.

[45] ATLAS Collaboration, *CERN/LHCC/98-14*, 1998.

[46] S. Gonzalez, "The atlas trigger system," *NCHEP99*, 1999.

[47] The ATLAS Collaboration, *ATL-DAQ-CONF-2007-007*, 2007.

[48] The ATLAS Collaboration, *ATL_PHYS_PUB_2009-000*, 2009.

[49] G. Duckeck *et al. CERN-LHCC-2005-022*, 2005.

[50] Jike Wang, *PRAMANA journal of physics CERN-LHCC-2005-022, ATL-INDET-PROC-2012-001*, 2012.

[51] S. Aefsky, *Science Direct, ATL-MUON-PROC-2011-003*, 2011.

[52] C. K. Foster, *The Grid: Blueprint for a New computing infrastructure*. Elsevier, 2003.

[53] E.D. and Feldman, "Quarkonium," *Scientific American*, vol. **66**, May 1982.

[54] T. S. D. Besson, "Upsilon spectroscopy: Transitions in the bottomonium system,"

[55] J. Aubert *et al. Phys. Rev. Lett.*, vol. **33**, p. 1404, 1974.

[56] B. Martin and G. Shaw, *Particle Physics*. 1993.

[57] D. H. Perkins, *Introduction to Elementary Particles High Energy Physics*. 2000.

[58] E. Eichten *et al. Phys. Rev.*, vol. **D17**, pp. 3090–3117, 1978.

[59] D. S. J.C. Collins and G. Sterman, *High Energy Physics*. 1988.

[60] C. Chang, "The atlas trigger system," *Nucl. Phys.*, vol. **B172**, p. 425, 1980.

[61] R.Baier and R. Ruckl, "The atlas trigger system," *Phys. Lett.*, vol. **B102**, p. 364, 1981.

[62] E. L. Berger and D. L. Jones, *Phys. Rev.*, vol. **D23**, p. 1521, 1981.

[63] F. Abe *et al. Phys. Rev. Lett.*, vol. **69**, p. 3704, 1992.

[64] H. Fritzsch, *Phys. Lett.*, vol. **B67**, p. 217, 1977.

[65] A. Abulencia *et al. Phys. Rev. Lett.*, vol. **98**, 2007.

[66] G. T. Bodwin, E. Braaten and G. P. Lepage *Phys. Rev.*, vol. **D51**, 1995.

[67] Price, D.D. , "Studies of quarkonium production and polarisation with early data at atlas," *CERN-THESIS-2008-098*, 2008.

[68] Jian-Wei Qiu, *arXiv:hep-ph/0610437v1*, 2006.

[69] A. Affolder *et al. Phys. Rev. Lett.*, vol. **85**, p. 2826, 2000.

[70] K. Abe *et al. Phys. Rev. Lett.*, vol. **89**, 2002.

[71] BABAR Collaboration, B. Aubert *Phys. Rev.*, vol. **D72**, 2005.

[72] P. Cho and A. K. Leibovich, *Phys. Rev.*, vol. **D53**, p. 1996, 2008.

[73] F. Yuan, C.-F. Qiao, and K.-T. Chao, *Phys. Rev.*, vol. **D56**, 1997.

[74] V.V. Kiselev, A. K. Likhoded, and M.V. Shevlyagin, *Phys. Lett.*, vol. **B332**, p. 411, 1994.

[75] J. P. Ma and Z. G. Si, *Phys.Rev.*, vol. **D70**, 2004.

[76] A.E. Bondar and V.L. Chernyak, *Phys. Lett.*, vol. **B612**, 2005.

[77] V.V. Braguta, A.K. Likhoded and A.V. Luchinsky, *Phys. Rev.*, vol. **D72**, 2005.

[78] V. V. Braguta, *arXiv:hep-ph/0701234v1*, 2007.

[79] T. Huang and F. Zuo, *arXiv:hep-ph/0702147v2*, 2007.

[80] K.Y.Liu, Z.G.He and K.T.Chos, *Phys. Lett.*, vol. **B557**, p. 45, 2002.

[81] G. T. Botwin, J. Lee, C. Yu, *Physical Review*, vol. **D77**, 2008.

[82] V.V. Braguta, A.K. Likhoded and A.V.Luchinsky, *Physical Review*, vol. **D80**, 2009.

[83] J. Zhang, H. Dong, F. Feng, *arXiv:1108.0890v3*, 2011.

[84] V.V. Braguta, A. K. Likhoded, A. V. Lunchinsky, *Physics of Atomic Nuclei*, vol. **73**, 6, pp. 1054–1068, 2009.

[85] W. A. Rolke, A. M. Lopez, J. Conrad, *Nucl. Instrum. Meth.*, vol. **A551**, pp. 493–503, 2004.

[86] T. Sjostrand, S. Mrenna, and P. Z. Skands, "Pythia 6.4 physics and manual," *arXiv:hep-ph/0603175*, 2006.

[87] Thesis, Fanouria Antoniou, "Study of the potential of measuring χ_{b0} using the decay $\chi_b \rightarrow J/\psi J/\psi$ in ATLAS experiment," *NTUAthens*, 2008.

[88] M. Smizanska, "Pythiab, interface to pythia6 dedicated to simulation of beauty events'," 2005.

[89] S. Hassani, L. Chevalier, E. Lancon, J. F. Laporte, R. Nicolaidou and A. Ouraou, *Nucl. Instrum. Meth.*, vol. **A572**, p. 77, 2007.

[90] D. Adams *et al. ATL-SOFT-2003-007*, 2003.

[91] V. Kostyukhim, *ATLAS ATL-PHYS-2003-031*, 2003.

[92] R. Aaij *et al. ATLAS-CONF-2010-036*, 2010.

[93] A. Cerri *et al. ATL-COM-PHYS-2011-1619*, 2011.

[94] The ATLAS Collaboration, *ATLAS-COM-CONF-2011-130*, 2011.

[95] "Atlas luminosity calculator." `https://atlas-lumi-calc.cern.ch`.

[96] G.J. Feldman, R. Cousins, *Phys. Rev.*, vol. **D57**, pp. 3873–3889, 1998.

[97] K. J. Hirata *et al. Phys. Lett.*, vol. **B280**, 1992.

[98] E. K *et al. Phys. Rev. Lett.*, vol. **90**, 2003.

[99] Kearns, Z. Kajita, T. Totsuka, *Y. Scientific American,*, vol. **68**, August 1999.

[100] D. Griffiths, *Introduction to Elementary Particles*. Physics Textbook, Wiley-VCH, 2008.

[101] N. Cabibbo, *Phys. Rev. Lett.*, vol. **10**, p. 531, 1963.

[102] S. L. Glashow, J. Iliopoulos, L. Maiani, *D2. Rev. Lett.*, vol. **D53**, p. 1585, 1970.

[103] M. Kobayashi, K. Maskawa, *Progress in Theoretical Physics*, vol. **49**, p. 652, 1973.

[104] S. L. Glashow, *Nuclear Physics*, vol. **22**, p. 579, 1961.

[105] L. Wolfenstein, *Phys. Rev. Lett.*, vol. **51**, p. 1945, 1983.

[106] S. P. Martin, "A supersymmetry primer," *hep-ph/9709356v6*, 201.

[107] C. D. Carone and R. T. Hamilton, *Phys. Lett.*, vol. **B301**, p. 196, 1993.

[108] M. Gronau and D. London, *Phys. Rev.*, vol. **D55**, p. 2845, 1997.

[109] V. Abazov *et al. Phys. Lett.*, vol. **23**, 2011.

[110] T. Aaltonen *et al. Phys. Rev. Lett.*, vol. **107**, 2011.

[111] S. Chatrchyan *et al. Phys. Rev. Lett.*, vol. **107**, p. 2011, 2008.

[112] R. Aaij *et al. Phys. Rev. Lett.*, vol. **708**, p. 55, 2011.

[113] The ATLAS Collaboration, *ATL-COM-PHYS-2012-136*, 2012.

[114] Michael J. Morello, *FERMILAB-CONF-11-091-E-PPD*, 2012.

[115] W. Lavrijsen, "The Athena Startup Kit, Computing in High Energy and Nuclear Physics," *La Jolla, California*, 2003.

[116] G. Cowan, "Error analysis for efficiency," *Phys. Rev. Lett.*, 2008.

[117] "Root documentation." `http://root.cern.ch/root/doc/RootDoc.html`.

[118] A. Hoecker, P. Speckmayer, J. Stelzer, J. Therhaag, E. von Toerne, H. Voss, *arXiv:physics/0703039*, 2009.

[119] The LHCb collaboration, "The lhcb collaboration, measurement of *b* hadron production fractions in 7tev *pp* collisions," *arXiv:1111.2357v1*, 2011.

[120] A. Barriuso Poy, H. Boterenbrood, H. Burckhart, J. Cook, V. Filimonov, *et al.*, "The detector control system of the ATLAS experiment," *JINST*, vol. 3, p. P05006, 2008.

[121] S. Schlenker *et al. ICALEPCS, Conf. Proc. MOBAUST02*, 2011.

[122] "PVSS-II." `http://www.pvss.com`.

[123] O. Holme *et al. ICALEPCS, Conf.Proc.C051010:WE2.1-6O*, 2005.

[124] "cxoracle documentation." `http://cx-oracle.sourceforge.net/html/index.html`.

[125] "Python database api." `http://www.python.org/dev/peps/pep-0249/`.

[126] "Cherrypy documentation." `http://docs.cherrypy.org/stable/`.

[127] "Rdbapi." `http://j2eeps.cern.ch/wikis/display/EN/JCOP+Framework+RDBAPI`.

[128] "Gwt api reference." `http://code.google.com/webtoolkit/doc/latest/RefGWTClassAPI.html`.

[129] "eclipse." `http://www.eclipse.org/`.

[130] `http://tomcat.apache.org/`.

[131] `http://www.apache.org/licencies/`.

[132] `http://code.google.com/p/gwt-incubator-lib/`.

[133] `http://code.google.com/p/gwt-datepicker/`.

[134] D. Gilbert, "Jfreechart documentation," *http://www.jfree.org/jfreechart/*.

[135] "Java Table." `http://docs.oracle.com/javase/1.4.2/docs/api/javax/swing/JTable.html`.

[136] `https://atlasop.cern.ch/dcs`.

[137] B. W. F. C. Michael Pilato, Ben Collins-Sussman, "Version control with subversion," *ISBN 0-596-00448-6*, 2004.

[138] The Compass Collaboration, *CERN-PH-EP/2007-001, hep-ex/0703049*, 2007.

[139] A. Buckley, "Atlas monte carlo generator tunes to lhc data," *Nuclear Science Symposium Conference Record (NSS/MIC)*, vol. EEE 167-173, 2010.

[140] G. Aad *et al. New J. Phys.*, vol. **13**, 2011.

[141] "Rpm." `http://www.rpm.org/`.

[142] `http://www.gzip.org/zlib/zlib_license.html`.